Time-dependent analysis and amplitude analysis of B0 ! K0s K0s K0s decays with the BABAR experiment

Simon Sitt

UNIVERSITÉ PIERRE ET MARIE CURIE - PARIS 6
École doctorale 517 "Particules, Noyaux et Cosmos "

THÈSE
Spécialité: Physique des particules

Présentée par

SITT Simon

Pour obtenir le grade de Docteur de l'Université Paris VI

Time-dependent analysis and amplitude analysis of $\mathrm{B}^0 \to \mathrm{K}^0_\mathrm{s}\mathrm{K}^0_\mathrm{s}\mathrm{K}^0_\mathrm{s}$ decays with the *BABAR* experiment

Soutenue le 29 Septembre 2010

Jury :

Rapporteurs:	Stéphane Monteil
	Christian Weiser
Examinateurs:	Tim Gershon
	Emi Kou
	Reynald Pain (Président du jury)
Directeur de thèse:	Eli Ben-Haim

Abstract

Two independent analyses of the decay channel $\mathrm{B}^0 \to \mathrm{K}^0_\mathrm{s}\mathrm{K}^0_\mathrm{s}\mathrm{K}^0_\mathrm{s}$ have been performed on a data sample of 468 millions of $\mathrm{B\bar{B}}$ pairs recorded by the *BABAR* detector at the PEP-II B factory at SLAC National Laboratory.
The first analysis is a phase-space-integrated time-dependent analysis to extract the CP violation parameters $\mathcal{S}$ and $\mathcal{C}$ from the two sub-modes $\mathrm{B}^0 \to 3\mathrm{K}^0_\mathrm{s}(\pi^+\pi^-)$ and
$\mathrm{B}^0 \to 2\mathrm{K}^0_\mathrm{s}(\pi^+\pi^-)\mathrm{K}^0_\mathrm{s}(\pi^0\pi^0)$ simultaneously and to compare them to the charmonium measurements. The result is

- $\mathcal{S} = -0.94^{+0.24}_{-0.21} \pm 0.06$
- $\mathcal{C} = -0.17^{+0.18}_{-0.18} \pm 0.04$,

where the first uncertainty is statistical and the second is systematical. The result is compatible within uncertainties with the Standard Model prediction and the charmonium modes measurements.
The second analysis is a time-integrated amplitude (or Dalitz plot) analysis to extract the inclusive branching fraction and the branching fractions of the resonant modes that contribute to the decay. The result of the first amplitude analysis of this decay channel is

- $\mathcal{B}(\mathrm{B}^0 \to \mathrm{K}^0_\mathrm{s}\mathrm{K}^0_\mathrm{s}\mathrm{K}^0_\mathrm{s}) = (6.18 \pm 0.47 \pm 0.14 \pm 0.06) \times 10^{-6}$
- $\mathcal{B}(\mathrm{B}^0 \to \mathrm{f}_0(980)\mathrm{K}^0_\mathrm{s};\ \mathrm{f}_0(980) \to \mathrm{K}^0_\mathrm{s}\mathrm{K}^0_\mathrm{s}) = (2.69^{+1.25}_{-1.18} \pm 0.35 \pm 1.87) \times 10^{-6}$
- $\mathcal{B}(\mathrm{B}^0 \to \mathrm{f}_0(1710)\mathrm{K}^0_\mathrm{s};\ \mathrm{f}_0(1710) \to \mathrm{K}^0_\mathrm{s}\mathrm{K}^0_\mathrm{s}) = (0.50^{+0.46}_{-0.23} \pm 0.04 \pm 0.12) \times 10^{-6}$
- $\mathcal{B}(\mathrm{B}^0 \to \mathrm{f}_2(2010)\mathrm{K}^0_\mathrm{s};\ \mathrm{f}_2(2010) \to \mathrm{K}^0_\mathrm{s}\mathrm{K}^0_\mathrm{s}) = (0.54^{+0.21}_{-0.20} \pm 0.03 \pm 0.44) \times 10^{-6}$
- $\mathcal{B}(\mathrm{B}^0 \to \mathrm{Nonresonant};\ \mathrm{K}^0_\mathrm{s}\mathrm{K}^0_\mathrm{s}\mathrm{K}^0_\mathrm{s}) = (13.31^{+2.23}_{-2.30} \pm 0.55 \pm 2.77) \times 10^{-6}$
- $\mathcal{B}(\mathrm{B}^0 \to \chi_{\mathrm{c}0}\mathrm{K}^0_\mathrm{s};\ \chi_{\mathrm{c}0} \to \mathrm{K}^0_\mathrm{s}\mathrm{K}^0_\mathrm{s}) = (0.46^{+0.25}_{-0.16} \pm 0.01 \pm 0.19) \times 10^{-6}$,

where the first uncertainty is statististal, the second is systematical and the third corresponds to Dalitz plot model uncertainties. No significant contribution of the controversial $\mathrm{f_X}(1500)$ resonance has been found.

Key words:

BaBar	B meson
time-dependent CP asymmetry	penguin
Dalitz plot analysis	K meson
Branching ratio	$\mathrm{B}^0 \to \mathrm{K}^0_\mathrm{s}\mathrm{K}^0_\mathrm{s}\mathrm{K}^0_\mathrm{s}$

Abstract

Deux analyses indépendantes du canal de désintegration $\mathrm{B}^0 \to \mathrm{K}^0_\mathrm{s}\mathrm{K}^0_\mathrm{s}\mathrm{K}^0_\mathrm{s}$ ont été effectuées, utilisant un échantillon de 468 millions de paires $\mathrm{B\bar{B}}$ enregistrées par le détecteur *BABAR* auprès de l'usine à B PEP-II à SLAC National Laboratory.
La première analyse est dépendant du temps et integrée sur l'espace de phase. Son but est d'extraire simultanément des deux sous-canaux $\mathrm{B}^0 \to 3\mathrm{K}^0_\mathrm{s}(\pi^+\pi^-)$ et
$\mathrm{B}^0 \to 2\mathrm{K}^0_\mathrm{s}(\pi^+\pi^-)\mathrm{K}^0_\mathrm{s}(\pi^0\pi^0)$, les paramètres $\mathcal{S}$ et $\mathcal{C}$ de violation de CP. Il est intéressant de comparer les valeurs mesurées avec les mesures des modes charmonium. Le résultat obtenu est

- $\mathcal{S} = -0.94^{+0.24}_{-0.21} \pm 0.06$
- $\mathcal{C} = -0.17^{+0.18}_{-0.18} \pm 0.04$,

où la première incertitude est statistique et la deuxième est systématique. Ce résultat est compatible avec la prédiction du modèle standard et les mesures des modes charmonium.
La deuxième analyse est une analyse en amplitude (ou dans le plan de Dalitz). Elle est intégrée sur le temps. Son but est d'extraire le rapport de branchement total, ainsi que les rapports de branchement des modes résonnants partiels. C'est la première fois que cette analyse est effectuée pour le canal étudié. Le résultat est

- $\mathcal{B}(\mathrm{B}^0 \to \mathrm{K}^0_\mathrm{s}\mathrm{K}^0_\mathrm{s}\mathrm{K}^0_\mathrm{s}) = (6.18 \pm 0.47 \pm 0.14 \pm 0.06) \times 10^{-6}$
- $\mathcal{B}(\mathrm{B}^0 \to \mathrm{f}_0(980)\mathrm{K}^0_\mathrm{s};\ \mathrm{f}_0(980) \to \mathrm{K}^0_\mathrm{s}\mathrm{K}^0_\mathrm{s}) = (2.69^{+1.25}_{-1.18} \pm 0.35 \pm 1.87) \times 10^{-6}$
- $\mathcal{B}(\mathrm{B}^0 \to \mathrm{f}_0(1710)\mathrm{K}^0_\mathrm{s};\ \mathrm{f}_0(1710) \to \mathrm{K}^0_\mathrm{s}\mathrm{K}^0_\mathrm{s}) = (0.50^{+0.46}_{-0.23} \pm 0.04 \pm 0.12) \times 10^{-6}$
- $\mathcal{B}(\mathrm{B}^0 \to \mathrm{f}_2(2010)\mathrm{K}^0_\mathrm{s};\ \mathrm{f}_2(2010) \to \mathrm{K}^0_\mathrm{s}\mathrm{K}^0_\mathrm{s}) = (0.54^{+0.21}_{-0.20} \pm 0.03 \pm 0.44) \times 10^{-6}$
- $\mathcal{B}(\mathrm{B}^0 \to \mathrm{Nonresonant};\ \mathrm{K}^0_\mathrm{s}\mathrm{K}^0_\mathrm{s}\mathrm{K}^0_\mathrm{s}) = (13.31^{+2.23}_{-2.30} \pm 0.55 \pm 2.77) \times 10^{-6}$
- $\mathcal{B}(\mathrm{B}^0 \to \chi_{\mathrm{c}0}\mathrm{K}^0_\mathrm{s};\ \chi_{\mathrm{c}0} \to \mathrm{K}^0_\mathrm{s}\mathrm{K}^0_\mathrm{s}) = (0.46^{+0.25}_{-0.16} \pm 0.01 \pm 0.19) \times 10^{-6}$,

où la première incertitude est statistique, la deuxième est systématique et la troisième est liée au modèle de l'amplitude. Aucun signal statistiquement significatif de la résonance controversée $\mathrm{f_X}(1500)$ n'a été observé.

Mots clés:

BaBar	méson B
asymmetrie de CP dépendante du temps	penguin
analyse en amplitude	méson K
Rapport d'embranchement	$\mathrm{B}^0 \to \mathrm{K}^0_\mathrm{s}\mathrm{K}^0_\mathrm{s}\mathrm{K}^0_\mathrm{s}$

Résumé en français

Le contexte théorique

Le modèle standard (MS) décrit les interactions fondamentales en dehors de la gravitation, à savoir les interactions électro-faible et forte. La physique des saveurs joue un rôle particulier, puisque la saveur est conservée dans l'interaction forte mais pas dans l'interaction faible. Des particules à saveur non nulle (étranges, charmées, belles ...) peuvent être produites (par paires) par les interactions fortes ou électro-magnétiques, mais ne peuvent se désintégrer que par l'interaction faible. Dans le MS les quarks ne sont pas en même temps des états propres de masse et de saveur, et la matrice unitaire de Cabbibo-Kobayashi-Maskawa (CKM) décrit les couplages faibles dans la base des états propres de masse. La matrice CKM peut être décrite par quatre paramètres, dont trois paramètres réels et une phase. La phase permet d'accommoder la violation de CP dans le MS. Cette dernière a été observée pour la première fois en 1964 dans la désintégration des kaons neutres et pourrait partiellement expliquer l'asymétrie entre matière et antimatière dans l'Univers. Une fois mesurés ces quatre paramètres, la théorie devient prédictive et permet de comparer les résultats de mesures expérimentales indépendantes avec leur prédictions théoriques. Ceci permet de tester les hypothèses qui ont été admises en construisant le MS, par exemple l'existence d' exactement 3 familles de particules. L'unitarité de la matrice CKM de traduit par 6 relations qui peuvent être interprétées géométriquement comme reliant les côtés de triangles. Un de ces triangles, dont les angles sont appelés α, β et γ, n'est pas plat et est appelé *triangle d'unitarité*. La raison d'être des usines à B, dont *BABAR* et Belle, est la mesure de ce triangle, et en particulier de l'angle β par le biais de la violation de CP dans le secteur des mésons B neutres. Les mésons neutres portant de la saveur (K^0, D^0, B^0) peuvent se transformer en leur anti-particule ($\overline{\mathrm{K}}^0$, $\overline{\mathrm{D}}^0$, $\overline{\mathrm{B}}^0$) par le biais de diagrammes en boîte. Dans le cas des mésons B neutres, certains couplages aux vertex de ces diagrammes portent la phase β. En mesurant la violation de CP dépendant du temps on peut avoir accès a cette phase : on observe l'interférence entre des B^0 qui se désintègrent dans un état final propre de CP, $\mathrm{f_{CP}}$, et des B^0 qui oscillent d'abord en $\overline{\mathrm{B}}^0$ et se désintègrent ensuite dans le même état final $\mathrm{f_{CP}}$. Au cas où un seul diagramme contribue à ces désintégrations, ce qui est le cas avec une bonne approximation dans la désintégration $\mathrm{B}^0 \to \mathrm{J}/\psi\,\mathrm{K}^0_\mathrm{s}$, le paramètre $\mathcal{S}$ correspond à $-\eta_{\mathrm{CP}}\sin(2\beta)$, où η_{CP} est la valeur propre de $\mathrm{f_{CP}}$ pour l'opérateur CP.
Avec davantage de données, une approche permettant de tester le MS consiste à mesurer indépendamment les côtés et les angles du triangle d'unitarité dans des processus différents, et à vérifier que toutes ces observables sont compatibles avec un seul triangle. Une incompatibilité pourrait signer la manifestation d'une nouvelle physique (NP). Cette thèse s'inscrit dans le contexte de ces recherches en analysant un canal supprimé dans le MS et qui pourrait être sensible à une nouvelle physique, car l'amplitude de désintégration dominante passe par

une boucle (pingouin) qui pourrait inclure des contributions virtuelles de particules inconnus dans le MS.

Le cadre de travail: L'expérience *BABAR*

Le travail de recherche exposé dans cette thèse a été réalisé dans le cadre de l'expérience *BABAR*, collaboration internationale regroupant des institutions de dix pays. Le détecteur *BABAR* est placé auprès du collisionneur PEP-II du SLAC National Laboratory, en Californie (Etats-Unis). PEP-II est une usine à B, constituée d'un double anneau de stockage d'électrons et positrons. Les énergies des faisceaux sont ajustés à la résonance $\Upsilon(4S)$, dont la masse est très légèrement supérieure au seuil de production des paires $\mathrm{B\bar{B}}$; des mésons B sont ainsi produits à un taux très élevé. La production dans un état cohérent et le fait que le $\Upsilon(4S)$ est boosté dans le système du laboratoire, permettent la réalisation de mesures dépendant du temps en étiquetant la saveur des mésons B. Le détecteur *BABAR* a été conçu pour enregistrer les produits des désintégrations des mésons B avec d'excellentes performances en termes d'efficacité et de résolution. La période de prise de données de l'expérience *BABAR* a commencé en 1999, s'est prolongée jusqu'en 2008 et a permis d'enregistrer 465 millions de paires $\mathrm{B\bar{B}}$. La richesse et la qualité de la production scientifique de la collaboration *BABAR* contribuent grandement aux succès actuels de la physique des saveurs. Cette thèse comprend d'une part deux analyses de physique complémentaires du canal de désintégration $\mathrm{B^0 \to K^0_s K^0_s K^0_s}$ et rend compte de deux études concernent la performance du détecteur *BABAR*. Il s'agit d'une part d'une étude des effects de l'irradiation du détecteur de traces en silicium (SVT), qui utilise des mesures de bruit en fonction de la tension de dépletion pour en déduire la dose absorbée, et d'autre part d'une étude de la différence entre simulation et données dans la reconstruction dee π^0, qui utilise des données et des désintegrations $\mathrm{D^0 \to K^\pm \pi^\pm \pi^0}$ et $\mathrm{D^0 \to K^\pm \pi^\pm}$ simulées. Les deux analyses de physique sont détaillés ci-dessous.

Analyses de physique

Aspects théoriques et expérimentaux du mode $B^0 \to K^0_s K^0_s K^0_s$

L'angle β a été mesuré avec une haute précision par les expériences *BABAR* et Belle dans les modes $\mathrm{B \to c\bar{c}K^{(*)}}$ qui sont insensibles à des contributions possibles d'une nouvelle physique. L'intérêt de l'analyse dépendant du temps est de comparer cette valeur a celle obtenu dans le canal $\mathrm{B^0 \to K^0_s K^0_s K^0_s}$ qui est supprimé dans le MS et qui procède par un diagramme en boucle, dit "pingouin". Cette boucle pourrait inclure des contributions de particules virtuelles venant d'une "nouvelle physique", qui, par un couplage avec une phase différente, pourraient modifier la valeur de β. Comme l'état final est état propre de CP, il est possible d'extraire les paramètres $\mathcal{S}$ et $\mathcal{C}$ sans prendre en compte les résonances intermédiaires dans $\mathrm{K^0 \overline{K}^0}$. Cependant il n'y a a priori aucune raison d'avoir les mêmes $\mathcal{S}$ et $\mathcal{C}$ pour tous les états intermédiaires, qui son aussi états propres de CP (par exemple $\mathrm{f_0(980)K^0_s}$). Dans un scénario idéal, une analyse en amplitude et dépendante du temps permettrait de séparer

ces contributions, mais avec 200 événements $\mathrm{B}^0 \to 3\mathrm{K}^0_\mathrm{s}(\pi^+\pi^-)$ attendus, c'est impossible. La façon d'extraire le plus d'information possible des données, consite à faire deux analyses complémentaires : une analyse dépendant du temps mais intégrée sur le plan de Dalitz afin d'extraire les paramètres $\mathcal{S}$ et $\mathcal{C}$ inclusifs, et une deuxième analyse en amplitude intégrée sur le temps qui nous indique pour quelles contributions on a moyenné dans l'analyse dépendant du temps. Un autre aspect de l'analyse en amplitude est qu'elle peut contribuer à élucider le statut de la résonance controversée $\mathrm{f_X}(1500)$ qui a été observée par *BABAR* et Belle dans les canaux $B^0 \to K^+K^-K^0_s$ et $B^+ \to K^+K^-K^+$: du fait de la conservation du moment cinétique, il ne peut y avoir que des résonances intermédiaires de spin pair. En conséquence, une observation de cette résonance dans $\mathrm{B}^0 \to \mathrm{K}^0_\mathrm{s}\mathrm{K}^0_\mathrm{s}\mathrm{K}^0_\mathrm{s}$ serait en faveur d'une résonance scalaire et une non-observation en faveur d'une résonance vectorielle, comme cela a été suggéré par l'observation d'une résonance vectorielle par BES.
Un point particulier de ce canal avantageux pour l'analyse, mais nécessitant l'utilisation de techniques non-standard, est la présence de trois bosons identiques dans l'état final imposant la symétrisation de l'amplitude. Cela mène à un plan de Dalitz avec une densité d'évènements six fois plus élevée que dans le cas de trois particules différentes. Il en résulte une beaucoup plus grande sensibilité aux interférences entre résonances et malgré la statistique très limitée l'analyse reste faisable.

Analyse dépendant du temps du canal $\mathrm{B}^0 \to \mathrm{K}^0_\mathrm{s}\mathrm{K}^0_\mathrm{s}\mathrm{K}^0_\mathrm{s}$

L'analyse utilise un ajustement de vraisemblance généralisé. La fonction de vraisemblance contient une description du temps propre $\Delta\mathrm{t}$ qui dépend de la saveur d'étiquetage et qui est fonction de $\mathcal{S}$ et $\mathcal{C}$, et des variables qui servent à mieux séparer statistiquement signal et bruits de fond. Une sélection préalable permet d'enrichir les données en signal. De plus la masse invariante de la résonance χ_{c0} est exclue afin d'éviter une contribution charmée. Le point crucial de l'analyse est la reconstruction précise du vertex de désintégration du B côté signal afin de mesurer $\Delta\mathrm{t}$. Comme les K^0_s ont un temps de vie non-négligeable et sont neutres, ce vertex est reconstruit de façon indirecte en à l'aide d'un ajustement global des trois K^0_s en utilisant des contraintes géométriques. Pour assurer une bonne qualité d' ajustement, nous demandons qu'au moins un de ces K^0_s soit de bonne qualité, evaluée par le nombre d'impacts des pions chargés provenant de sa désintégration dans le détecteur de vertex. Nous analysons les deux modes $\mathrm{B}^0 \to 3\mathrm{K}^0_\mathrm{s}(\pi^+\pi^-)$ et $\mathrm{B}^0 \to 2\mathrm{K}^0_\mathrm{s}(\pi^+\pi^-)\mathrm{K}^0_\mathrm{s}(\pi^0\pi^0)$ simultanément pour extraire les paramètres communs $\mathcal{S}$ et $\mathcal{C}$. L'analyse est réalisée en aveugle, ce qui veut dire que l'outil d'analyse est complètement validé en utilisant des données simulées avant de d'y passer les données. L'analyse de 3261 candidats dans le canal $\mathrm{B}^0 \to 3\mathrm{K}^0_\mathrm{s}(\pi^+\pi^-)$ et de 7209 candidats dans le canal $\mathrm{B}^0 \to 2\mathrm{K}^0_\mathrm{s}(\pi^+\pi^-)\mathrm{K}^0_\mathrm{s}(\pi^0\pi^0)$ permet de trouver respectivement 201^{+16}_{-15} évènements et 62^{+14}_{-13} évènements de signal. Les paramètres de violation de CP trouvés dans les données sont

$$\begin{aligned} \mathcal{S} &= -0.935^{+0.238}_{-0.214} \pm 0.06\,, \\ \mathcal{C} &= -0.166^{+0.180}_{-0.178} \pm 0.03 \end{aligned}$$

La Fig. 0.1 montre des ${}_s\mathcal{P}lots$ de l'asymétrie de CP dans les données. La deuxième erreur

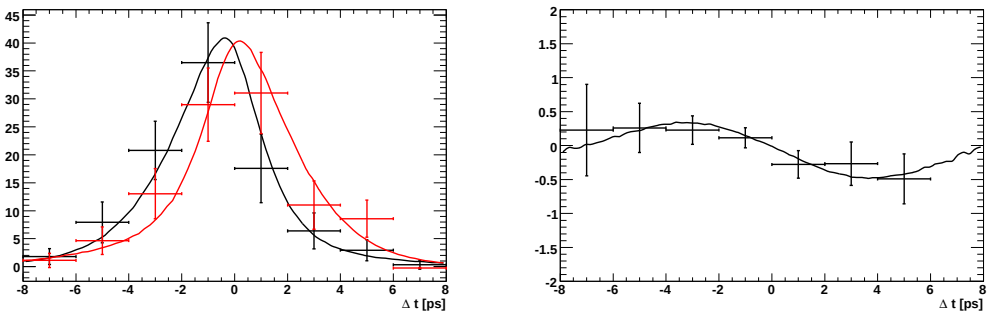

Figure 0.1: ${}_s\mathcal{P}lots$ pour $\Delta\mathrm{t}$ côté signal. A gauche sont montrées les distributions du temps propre $\Delta\mathrm{t}$ pour des mésons B côté signal (étiquetés comme B^0 en noir et des mésons B étiqueté comme $\bar{\mathrm{B}}^0$ en rouge). La figure de droite montre l'asymétrie dépendant du temps.

correspond à l'incertitude systématique et inclut des incertitudes dûes à la statistique limitée des données simulées, aux différences entre simulations et données, au biais de l'ajustement, à l'incertitude des paramètres de violation de CP des bruits de fond et au veto utilisé pour rejeter les contributions de charmonium. L'incertitude dominante qui est due au vertexing sans traces directes venant du vertex de désintégration du méson B, est évaluée en estimant les différences entre simulation et données dans un échantillon de contrôle $\mathrm{B}^0 \to \mathrm{J}/\psi\,\mathrm{K}^0_\mathrm{s}$.

Analyse en amplitude du canal $\mathrm{B}^0 \to \mathrm{K}^0_\mathrm{s}\mathrm{K}^0_\mathrm{s}\mathrm{K}^0_\mathrm{s}$

Afin d'étudier le contenu résonant, nous réalisons une analyse en amplitude du canal $\mathrm{B}^0 \to \mathrm{K}^0_\mathrm{s}\mathrm{K}^0_\mathrm{s}\mathrm{K}^0_\mathrm{s}$ en utilisant le modèle isobar pour extraire les modules et phases des amplitudes qui contribuent. Contrairement à l'analyse dépendant du temps, on n'utilise que des événements $\mathrm{B}^0 \to 3\mathrm{K}^0_\mathrm{s}(\pi^+\pi^-)$ afin de réduire les bruits de fond et les événements de signal qui ne sont pas correctement reconstruits. Comme mentionné plus haut, l'amplitude est symétrisée, ce qui est réalisé en construisant le plan de Dalitz avec les variables non ambigües de la masse minimale s_min et la masse maximale s_max. Comme c'est la première analyse en amplitude de ce canal, les contributions résonantes ne sont pas connues. Pour trouver un modèle du signal qui prend en compte toutes les contributions statistiquement significatives, on commence par un modèle de base qui inclut toutes les contributions de spin pair trouvées dans l'analyse *BABAR* de $\mathrm{B}^0 \to \mathrm{K}^+\mathrm{K}^-\mathrm{K}^0_\mathrm{s}$, sauf le $\mathrm{f}_\mathrm{X}(1500)$ controversé: $\mathrm{f}_0(980)$, $\chi_{\mathrm{c}0}$ et contribution non résonante. On utilise ensuite une méthode de vraisemblance dans laquelle on balaye l'espace bidimensionel des paramètres (masse et largeur) d'une résonance supplémentaire. On cherche des régions de vraisemblance accrue qui correspondent à la masse et à la largeur de résonances connues. On applique d'abord cette méthode pour une résonance scalaire supplémentaire et on trouve une contribution de la $f_0(1710)$, illustré par la Fig. 0.2. Aucune contribution de $\mathrm{f}_\mathrm{X}(1500)$ n'est visible. Ensuite $f_0(1710)$ est ajoutée au modèle et on répéte la procédure pour une éventuelle résonance tensorielle. On trouve une contribution de la $f_2(2010)$, illustré par la Fig. 0.2. Avec ce modèle, qui comprend main-

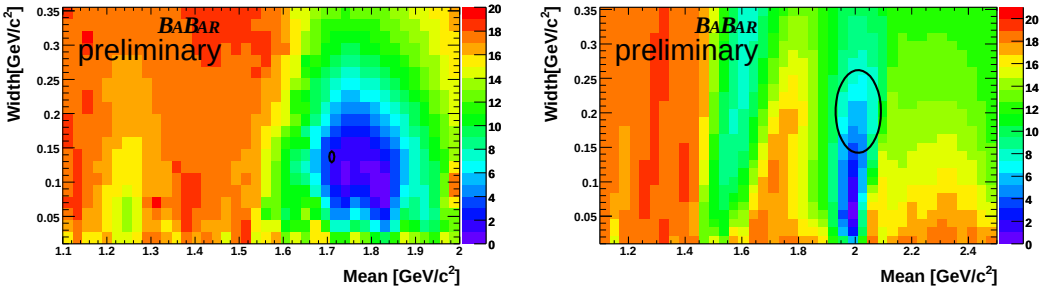

Figure 0.2: Vraisemblance traduite en χ^2 ($-2\Delta\log\mathcal{L}$) en fonction de la masse et de la largeur d'une résonance scalaire additionnelle (à gauche) et d'une résonance tensorielle (à droite). Des régions de vraisemblance accrue correspondent à des petites valeurs de $-2\Delta\log\mathcal{L}$ (le maximum correspond à $-2\Delta\log\mathcal{L} = 0$). Les ellipses indiquent les valeurs mesurées des résonances $\mathrm{f}_0(980)$ et $\mathrm{f}_2(2010)$ issus de la Ref. [1].

tenant $\mathrm{f}_0(980)$, χ_{c0}, $f_0(1710)$, $f_2(2010)$ et une contribution non résonante nous effectuons l'ajustement final aux données. L'utilisation de la vraisemblance généralisé avec 505 candidats fournit 200 ± 15 événements de signal $\mathrm{B}^0 \to \mathrm{K}^0_\mathrm{s}\mathrm{K}^0_\mathrm{s}\mathrm{K}^0_\mathrm{s}$ et 305 ± 18 événements de bruit de fond (les incertitudes sont statistiques seulement). Les projections du résultat de l'ajustement sur les axes du plan de Dalitz sont montrées sur la Fig. 0.3. Nous traduisons les

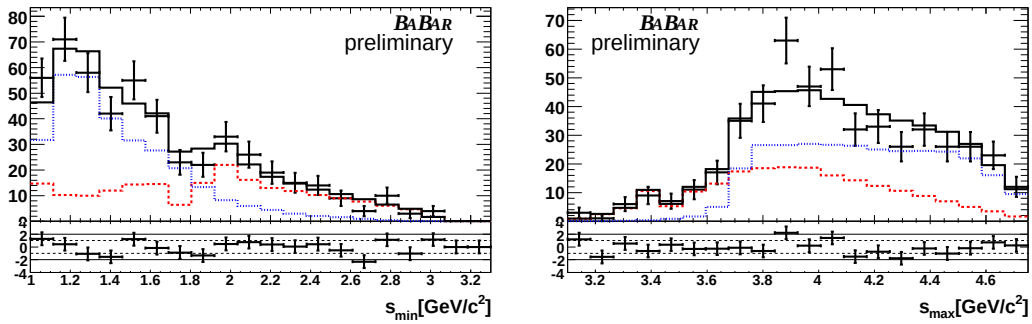

Figure 0.3: Projections du résultat de l'ajustement sur les axes du plan de Dalitz($\mathrm{s}_{\mathrm{min}}$ à gauche et $\mathrm{s}_{\mathrm{max}}$ à droite). Les données sont indiquées avec leurs barres d'erreur. La ligne rouge tireté (pointillée bleue) correspond au signal (bruit de fond) et la ligne noire correspond au modèle total.

magnitudes et phases des contributions au modèle en fractions isobares (FF), les valeurs étant résumées dans le Tab. 0.1. I existe une deuxième solution à l'ajustement, différant de celle qui correspond au maximum par presque deux écart-types. Les valeurs correspondantes sont également montrées. En utilisant les fractions et le rapport de branchement inclusif obtenu par le nombre d'évènements signal nous calculons les rapports de branchement individuels. Les valeurs obtenues pour la meilleure solution sont montrées dans le Tab. 0.2. Les

Table 0.1: Résumé des fractions isobars et des phases relatives. Les erreurs sont statistiques seulement. La signification statistique a été évaluée par la variation de la vraisemblance quand la contribution est retiré du modèle ($\mathrm{Significance} = \sqrt{-2\Delta\log\mathcal{L}}$). Tous les modes résonants ont une signification statistique de moins de 5 écart-types.

Mode	Solution 1	Solution 2
FF $\mathrm{f_0}(980)\mathrm{K_s^0}$	$0.44^{+0.20}_{-0.19}$	$1.03^{+0.22}_{-0.17}$
Phase [rad]$\mathrm{f_0}(980)\mathrm{K_s^0}$	0.09 ± 0.16	1.26 ± 0.17
Significance [σ]$\mathrm{f_0}(980)\mathrm{K_s^0}$	3.3	-
FF $\mathrm{f_0}(1710)\mathrm{K_s^0}$	$0.07^{+0.07}_{-0.03}$	$0.09^{+0.05}_{-0.02}$
Phase [rad] $\mathrm{f_0}(1710)\mathrm{K_s^0}$	1.11 ± 0.23	0.36 ± 0.20
Significance [σ]$\mathrm{f_0}(1710)\mathrm{K_s^0}$	3.7	-
FF $\mathrm{f_2}(2010)\mathrm{K_s^0}$	$0.09^{+0.03}_{-0.03}$	0.10 ± 0.02
Phase [rad] $\mathrm{f_2}(2010)\mathrm{K_s^0}$	2.50 ± 0.20	1.58 ± 0.22
Significance [σ]$f_2(2010)K_s^0$	3.3	-
FF$\chi_{\mathrm{c0}}\mathrm{K_s^0}$	$0.07^{+0.04}_{-0.02}$	0.07 ± 0.02
Phase [rad]$\chi_{\mathrm{c0}}\mathrm{K_s^0}$	0.63 ± 0.47	-0.24 ± 0.52
Significance [σ]$\chi_{c0}K_s^0$	4.2	-
FF NR	$2.15^{+0.36}_{-0.37}$	$1.37^{+0.26}_{-0.21}$
Phase [rad] NR	0.0	0.0
Significance [σ]NR	8.2	-
Total FF	$2.84^{+0.71}_{-0.66}$	$2.66^{+0.35}_{-0.27}$

Table 0.2: Résumé des mesures des rapports de branchement. Les nombres ont été obtenus en multipliant les fractions isobars correspondantes, obtenus dans la meilleure solution, avec le rapport de branchement inclusif de $\mathrm{B}^0 \to \mathrm{K}^0_\mathrm{s}\mathrm{K}^0_\mathrm{s}\mathrm{K}^0_\mathrm{s}$. La première incertitude est statistique, la deuxième est systématique et la troisième correspond aux incertitudes liées au modèle du plan de Dalitz.

Mode	$\mathcal{B}(\mathrm{B}^0 \to \mathrm{Mode})[10^{-6}]$
Inclusive $\mathcal{B}(\mathrm{B}^0 \to \mathrm{K}^0_\mathrm{s}\mathrm{K}^0_\mathrm{s}\mathrm{K}^0_\mathrm{s})$	$6.186 \pm 0.475 \pm 0.145 \pm 0.067$
$\mathrm{f}_0(980)\mathrm{K}^0_\mathrm{s},\ \ \mathrm{f}_0(980) \to \mathrm{K}^0_\mathrm{s}\mathrm{K}^0_\mathrm{s}$	$2.696^{+1.250}_{-1.188} \pm 0.357 \pm 1.874$
$\mathrm{f}_0(1710)\mathrm{K}^0_\mathrm{s},\ \ \mathrm{f}_0(1710) \to \mathrm{K}^0_\mathrm{s}\mathrm{K}^0_\mathrm{s}$	$0.502^{+0.461}_{-0.235} \pm 0.043 \pm 0.129$
$\mathrm{f}_2(2010)\mathrm{K}^0_\mathrm{s},\ \ \mathrm{f}_2(2010) \to \mathrm{K}^0_\mathrm{s}\mathrm{K}^0_\mathrm{s}$	$0.543^{+0.214}_{-0.204} \pm 0.034 \pm 0.440$
$\mathrm{NR},\ \ \mathrm{K}^0_\mathrm{s}\mathrm{K}^0_\mathrm{s}\mathrm{K}^0_\mathrm{s}$	$13.315^{+2.234}_{-2.302} \pm 0.554 \pm 2.779$
$\chi_{\mathrm{c}0}\mathrm{K}^0_\mathrm{s},\ \chi_{\mathrm{c}0} \to \mathrm{K}^0_\mathrm{s}\mathrm{K}^0_\mathrm{s}$	$0.462^{+0.252}_{-0.165} \pm 0.015 \pm 0.197$

incertitudes systématiques comprennent des incertitudes liées aux paramètres de la fonction de vraisemblance, à l'efficacité de reconstruction, aux bruits de fonds négligés, au biais de l'ajustement et au nombre de paires de $\mathrm{B\bar{B}}$ produits dans PEP-II . Les incertitudes liées au modèle de l'amplitude sont dues aux erreurs sur les mesures des masses et des largeur des contributions résonantes et aux contributions résonantes statistiquement non-significatives qui n'ont pas été incluses dans le modèle. La plus grande incertitude dans le modèle est dûe à la mesure peu précise de la $f_2(2010)$.

Discussion des résultats physiques

L'analyse dépendant du temps a permis de trouver des paramètres $\mathcal{S}$ et $\mathcal{C}$ qui sont compatibles à un écart-type avec la prédiction du MS. L'analyse en amplitude a permis de mesurer pour la première fois les modes résonants contribuant à la désintégration $\mathrm{B}^0 \to \mathrm{K}^0_\mathrm{s}\mathrm{K}^0_\mathrm{s}\mathrm{K}^0_\mathrm{s}$ et trouve des contributions de $\mathrm{f}_0(980)$, $\chi_{\mathrm{c}0}$, $f_0(1710)$, $f_2(2010)$ et une contribution non resonante. Les deux analyses sont statistiquement très limitées : dans l'analyse dépendante du temps cela se traduit par le fait que la limite du domaine physique ($\mathcal{S}^2 + \mathcal{C}^2 \leq 1$), est à moins d'un écart-type de l'incertitude. Dans l'analyse en amplitude, aucune contribution résonante n'a une signification statistique supérieur a 5 écart-types.

Acknowledgments

I thank Stéphane Monteil and Christian Weiser for having accepted to be referees and Tim Gershon, Emi Kou and Reynald Pain for having accepted to be members of the jury for my thesis.

I am grateful to Pacal Debu and Reynald Pain for hosting me at the LPNHE during my thesis.

I want to especially thank my supervisor Eli, who was always available, for exceptional three years, for the very friendly and efficient working atmosphere (even when deadlines are close) and for all he taught me.

A special thanks goes to my collaborator at SLAC, Matt Graham, for his help, his very efficient way of doing things and for the great atmosphere we had in our small analysis group.

I would also like to thank:

The *BABAR* group at LPNHE: Jacques Chauveau, Eli Ben-Haim, José Ocariz, Alejandro Perez, Jennifer Prendki, Pablo del Amo Sanchez, Giovanni Calderini and Giovanni Marchiori. Jacques who was always there for advice and willing to do the final reading of this document. José for the many interesting discussions and his inputs. Alejandro for his help and the great time we spent together at SLAC and elsewhere. Pablo for his help, in particular for the π^0 efficiency study, the many physics and non-physics discussions over lunch and his inputs to the analyses. Giovanni C., with whom I did the SVT radiation damage study, for giving me the chance to do a hardware-related study.

The whole *BABAR* collaboration, in particular the Charmless 3-Body B Decays Analysis Working Group, and Tim Gershon, Tom Latham and Enrico Robutti for their attention and valuable comments during the internal review of the analyses.

The theorists and experimentalist who helped us when we got confused with quantum mechanics: Sébastien Descôtes-Genon, Emi Kou, Patrick Roudeau, Alain Le Yaouanc and Zoltan Ligeti.

Achille Stocchi for his inputs to the SuperB study.

The whole staff of the LPNHE, in particular fellow graduate students and my "parrain" Jean-Michel.

My family and friends who always supported me during this thesis and before.

Contents

Part I

Introduction

1.1 CP violation

When a particle and a antiparticle are created in pair from energy, it is intuitive to think that they behave and decay in the same way. Why wouldn't they? They are exactly the same, except the quantum numbers have changed signs. The quantum mechanical operator that transforms a particle into its anti-particle is the charge conjugation C. It changes the sign of all internal quantum numbers (charge, baryon number, lepton number, strangeness, charm, beauty, truth) while leaving the mass, energy, momentum and spin untouched. While C is conserved in the strong and electromagnetic interaction, this is not the case for the weak interaction. For instance, if one applies C on a left-handed neutrino, as the spin is conserved in the transformation, the result is a left-handed anti-neutrino, but left-handed anti-neutrinos do not exist and C is therefore maximally violated.
An operation that turns a left-handed neutrino into a right-handed anti-neutrino does not only need to invert the internal quantum numbers, but also the spin of the particle. This is done by the parity operator P that does the transformation $\vec{\mathrm{x}} \rightarrow -\vec{\mathrm{x}}$, i.e. the spin is inverted.
The combined operation of charge conjugation and parity (CP) reproduces what we observe in nature: it turns left-handed particles into right-handed anti-particles. While C and P are maximally violated in the weak interaction, their combination was expected by most physicists to be an exact symmetry. This assumption has been proven wrong in 1964 when Cronin, Fitch, Christenson and Turlay [2] showed experimentally that neutral $\mathrm{K}^0_{\mathrm{L}}$ mesons do not always decay to CP eigenstates with a CP eigenvalue of -1 (three pions in the final state) as expected, but that a small fraction also decays to final states with CP eigenvalue of +1 (two pions).
If CP is not an exact symmetry of nature, particles and anti-particles can decay differently. This is why CP violation (CPV) is a candidate to explain cosmological observations that find no sign of free anti-matter, while the Big Bang theory assumes creation of an equal amount of matter and anti-matter out of energy [3].
In the standard model of particle physics (SM), CP violation can be accommodated by a non-zero weak phase in the Lagrangian (see Sec. 2.1). In the SM picture, CP violation is an interference effect that can be measurable when several amplitudes with different phases contribute to the transition amplitude of a decay (see Sec. 2.2.3). In the case of neutral flavored mesons, a second amplitude that can lead to interference is engendered by "mixing" (see Sec. 2.2.2). In the case of the neutral B mesons, the oscillation frequency between B^0 and it's anti-particle $\bar{\mathrm{B}}^0$ is of the same order of magnitude as the lifetime of these particles. As a result the interfering amplitudes are of comparable sizes which makes the $B^0\bar{B}^0$ system a privileged laboratory for measuring CP violating effects. From an experimental point of view, to measure a difference between the decays of B^0 and $\bar{\mathrm{B}}^0$, one needs to identify the flavor of the B meson under study, as both neutral B mesons have access to the same final state. The experimental setup in the B factories is optimized for this kind of measurement, as the $\mathrm{B}^0\bar{\mathrm{B}}^0$ system is produced in a coherent L=1 state through the decay of the $\Upsilon(4\mathrm{S})$ resonance. In this coherent state, there is always exactly one B^0 and one $\bar{B}^0$. When one of them, $\mathrm{B}_{\mathrm{tag}}$, decays to a flavor specific state, the other one, B_{CP}, has at the same moment the opposite flavor. As neutral B mesons oscillate as a function of time, one also needs to measure the time Δt between the decays of $\mathrm{B}_{\mathrm{tag}}$ and B_{CP}. To provide precise measurements

of Δt (see Sec. 7.4) the B factories have been designed as asymmetric e^+e^- colliders. Her the $\Upsilon(4S)$ is boosted in the laboratory frame and the short-lived B mesons ($\sim$1.5 ps) travel an average distance of 256 μm, which is measurable in the detector. As the boost in known, Δt can be measured through the distance between the decay vertices of B_{tag} and B_{CP}.

1.2 Flavor physics and charmless-3-body B decays

The flavor sector of the SM is strongly constrained by the CKM formalism that describes flavor couplings. The unitarity of the CKM matrix implies relations between the matrix elements that can be geometrically interpreted as unitarity triangles (UT). This means once two angles or sides of a UT are measured, the theory becomes predictive. *CP* violation in the B meson system is directly linked to the flavor coupling and gives access to UT properties (see Sec. 2.2.3). Together with other measurements [4] [5], the UT can be over constrained and used to test the SM (see Fig. 2.5). If the different measurements are not compatible with one single UT, this can be a sign of new physics (NP) contributions (see Sec. 3.1). Given that all current measurements agree with the SM, NP contributions are expected to be small. This is why the search of NP is most promising in processes where the SM contribution is small.
$b \to s$ charmless-3-body B decays are good candidates for the search of NP, as they are suppressed in the SM and dominated by loop diagrams (penguin diagrams, see Sec. 3.1) that could have virtual contributions from NP particles.
$B^0 \to K^0_s K^0_s K^0_s$ is a privileged channel for the search of NP: not only it is experimentally clean (see Sec. 7.3) but also it is impaired by small theoretical uncertainties (see Sec. 3.2.1). Additionally the final state is *CP* definite (see Sec. 3.2.2) and the *CP* violation parameters can be measured without an amplitude analysis. Independently, an amplitude analysis can provide information on the m_{KK} spectrum. In particular, the unclear nature for the controversial $f_X(1500)$ resonance (see Sec. 3.2.3) can be constrained because only even-spin resonances are permitted due to angular momentum conservation. An observation of this resonance would make a scalar nature more likely and in case of non-observation a vector nature would be favored. Our reconstruction method is common to both the time-dependent *CP* violation analysis (TDCPV) and the amplitude analysis, and so are also most analysis techniques (Chap. 7).

1.3 Overview

In part II we describe the theoretical and experimental context of this work. A general introduction to *CP* violation in the B meson system in the context of the SM is given in Chap. 2, while more detailed information on charmless 3-body B decays with focus on $B^0 \to K^0_s K^0_s K^0_s$ can be found in Chap. 3. In the following Chap. 4, the *BABAR* detector and the PEP-II collider are presented. This part also includes detector-related studies: in Chap. 5 we present a radiation damage study oft the silicon vertex detector and in Chap. 6 a study of the π^0 reconstruction efficiency.
Part III represents the core of this work, where the analysis techniques are presented in Chap. 7 while the time-dependent analysis is described in Chap. 8 and the amplitude analysis

is described in Chap. 9.
Part IV concludes this work with the prospectives of the time-dependent analysis in the context of the SuperB project.

Part II

Theoretical and experimental context

2 Quark mixing and CP violation

2.1 Quark Mixing and CKM matrix

In the SM[1], interactions between elementary particles are mediated by gauge bosons. These gauge bosons are associated with the invariance of the Lagrangian under abelian and non-abelian gauge transformations [6].
The weak interaction is mediated by the $\mathrm{W}^{\pm}$ and Z^0 bosons that are generated by the non-abelian SU(2) flavor group. The quark content of the SM are three left-handed flavor doublets and six right-handed flavor singlets. Each doublet consists of one up-type quark and one down-type quark.

$$\begin{pmatrix} \mathrm{u} \\ \mathrm{d} \end{pmatrix} \begin{pmatrix} \mathrm{c} \\ \mathrm{s} \end{pmatrix} \begin{pmatrix} \mathrm{t} \\ \mathrm{b} \end{pmatrix} . \tag{2.1}$$

The part of the Lagrangian that describes flavor changing charged currents between quarks is

$$\mathcal{L}_{\mathrm{CC}} = -\frac{\mathrm{g}}{2} \cdot \begin{pmatrix} \bar{\mathrm{u}} & \bar{\mathrm{c}} & \bar{\mathrm{t}} \end{pmatrix}_{\mathrm{L}} \gamma^{\mu} \mathrm{V}_{\mathrm{CKM}} \begin{pmatrix} \mathrm{d} \\ \mathrm{s} \\ \mathrm{b} \end{pmatrix}_{\mathrm{L}} \mathrm{W}_{\mu}^{+} + \mathrm{h.c.} , \tag{2.2}$$

where (u,c,t) are the up-type left-handed quarks, (d,s,b) are the down-type left-handed quarks, g is the $\mathrm{SU}(2)_{\mathrm{L}}$ coupling constant and W_{μ} is the W boson field operator. Flavor changing neutral currents are not allowed in the SM and right-handed quarks are not subject to flavor changing transitions as they are singlets. By convention one works with mass eigenstates, but the couplings between quarks mix flavors, and the quark mass eigenstates are not the quark flavor eigenstates. The matrix $\mathrm{V}_{\mathrm{CKM}}$

$$\mathrm{V}_{\mathrm{CKM}} = \begin{pmatrix} \mathrm{V}_{\mathrm{ud}} & \mathrm{V}_{\mathrm{us}} & \mathrm{V}_{\mathrm{ub}} \\ \mathrm{V}_{\mathrm{cd}} & \mathrm{V}_{\mathrm{cs}} & \mathrm{V}_{\mathrm{cb}} \\ \mathrm{V}_{\mathrm{td}} & \mathrm{V}_{\mathrm{ts}} & \mathrm{V}_{\mathrm{tb}} \end{pmatrix} \tag{2.3}$$

is the unitary matrix that describes quark mixing in the Cabbibo-Kobayashi-Maskawa formalism [7]. In other words $\mathrm{V}_{\mathrm{CKM}}$ gives the SU(2) flavor couplings in the basis where the quark mass matrix is diagonal and real. The non-diagonal terms of the matrix allow flavor changing transitions between quarks, i.e. transitions between quarks from different flavor doublets.
A priori a 3x3 unitary complex matrix has 9 degrees of freedom, i.e. it can be parameterized with three angles and 6 phases. By redefining the phases of the quark fields, this parameterization can be reduced to three mixing angles and a single phase.

[1] This section is non-exhaustive, a detailed description of the Standard Model of particle physics (SM) can be found in [6]

With such a particular quark field phase convention, the mixing matrix can be written in the so-called "standard parameterization" [8]:

$$\mathrm{V_{CKM}} = \begin{pmatrix} \mathrm{c_{12}c_{13}} & \mathrm{s_{12}c_{13}} & \mathrm{s_{13}e^{-i\delta}} \\ -\mathrm{s_{12}c_{23}} - \mathrm{c_{12}s_{23}s_{13}e^{i\delta}} & \mathrm{c_{12}c_{23}} - \mathrm{s_{12}s_{23}s_{13}e^{i\delta}} & \mathrm{s_{23}c_{13}} \\ \mathrm{s_{12}s_{23}} - \mathrm{c_{12}c_{23}s_{13}e^{i\delta}} & -\mathrm{c_{12}s_{23}} - \mathrm{s_{12}c_{23}s_{13}e^{i\delta}} & \mathrm{c_{23}c_{13}} \end{pmatrix} . \tag{2.4}$$

This single phase δ allows the possibility of CP violation in the SM [7] but CP violation is not a necessary feature of the SM. There could be further "accidental" symmetries such as two quarks of the same charge could have the same mass, or the value of one of the angles could be zero or $\pi/2$ or the phase itself could be zero. In these scenarios, the number of parameters could be reduced even further and CP violation would no longer be possible.
Experimental data shows that there is a hierarchy among the matrix elements and that the matrix is dominated by its diagonal terms. This means that transitions inside flavor doublets are preferred. An experimentally more convenient parameterization has been proposed by Wolfenstein [9]:

$$\mathrm{V_{CKM}} = \begin{pmatrix} 1 - \frac{\lambda^2}{2} & \lambda & \mathrm{A}\lambda^3(\rho - \mathrm{i}\eta) \\ -\lambda & 1 - \frac{\lambda^2}{2} & \mathrm{A}\lambda^2 \\ \mathrm{A}\lambda^3(1 - \rho - \mathrm{i}\eta) & -\mathrm{A}\lambda^2 & 1 \end{pmatrix} + \mathcal{O}(\lambda^4) , \tag{2.5}$$

where the parameters A, λ, ρ and η are defined with respect to the standard parameterization as follows

$$\begin{aligned} \mathrm{s_{12}} &\equiv \lambda , \\ \mathrm{s_{23}} &\equiv \mathrm{A}\lambda^2 , \\ \mathrm{s_{13}e^{-i\delta}} &\equiv \mathrm{A}\lambda^3(\rho - \mathrm{i}\eta) \equiv \tfrac{\mathrm{A}\lambda^3}{1-\lambda^2/2}(\bar{\rho} - \mathrm{i}\bar{\eta}) . \end{aligned} \tag{2.6}$$

The advantage is that we know from experimental data that the λ parameter is small ($\lambda \simeq |\mathrm{V_{us}}| \simeq 0.22$), and the Taylor development of the matrix elements that is shown in Eq. 2.5 is sufficiently accurate for most experimental and phenomenological considerations. The unitarity of the CKM matrix ($\mathrm{VV^\dagger} = \mathrm{V^\dagger V} = 1$) implies 9 constraints among the matrix elements, 3 that result from the normalization of the columns and 6 that result from the vanishing product of pairs of different columns and rows.
Three of them are of particular interest for the study of CP violation, as they are more sensitive to the non-reducible CKM phase:

$$\mathrm{V_{ud}V_{us}^*} + \mathrm{V_{cd}V_{cs}^*} + \mathrm{V_{td}V_{ts}^*} = 0 , \tag{2.7}$$

$$\mathrm{V_{us}V_{ub}^*} + \mathrm{V_{cs}V_{cb}^*} + \mathrm{V_{ts}V_{tb}^*} = 0 , \tag{2.8}$$

$$\mathrm{V_{ud}V_{ub}^*} + \mathrm{V_{cd}V_{cb}^*} + \mathrm{V_{td}V_{tb}^*} = 0 . \tag{2.9}$$

A null sum of three complex numbers can be interpreted geometrically as a triangle in the complex plane. Equations 2.7, 2.8 and 2.9 are the basis of the so-called unitarity triangles. In the following we concentrate on the third triangle as it is related to $\mathrm{B^0\bar{B}^0}$ mixing (via $\mathrm{V_{td}V_{tb}^*}$, see 2.2.2), charmed semileptonic and charmless B decays. If we divide 2.9 by $\mathrm{V_{cd}V_{cb}^*}$ we get a convention-independent definition of the unitarity triangle (UT)

$$\frac{\mathrm{V_{ud}V_{ub}^*}}{\mathrm{V_{cd}V_{cb}^*}} + 1 + \frac{\mathrm{V_{td}V_{tb}^*}}{\mathrm{V_{cd}V_{cb}^*}} = 0 . \tag{2.10}$$

Using 2.5 it can be shown that all sides of this triangle are of the same order of magnitude. The vertices are exactly (0,0), (1,0) and ($\bar{\rho}$,$\bar{\eta}$), where $\bar{\rho} + \mathrm{i}\bar{\eta} = -\frac{\mathrm{V_{ud}V_{ub}^*}}{\mathrm{V_{cd}V_{cb}^*}}$ is phase definition independent. The triangle is shown in Fig. 2.1.

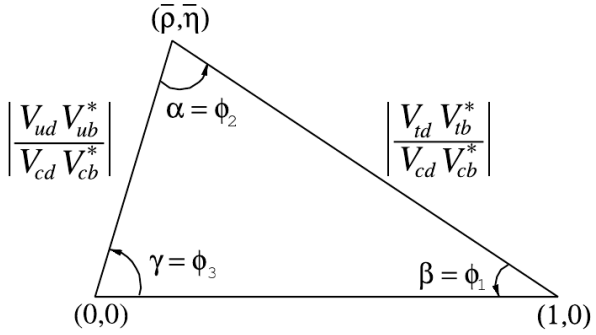

Figure 2.1: Sketch of the unitarity triangle. The coordinates $\bar{\rho}$ and $\bar{\eta}$ are defined in Eq. 2.6

The angles α, β and γ are defined as

$$\alpha \equiv \arg\left(-\frac{\mathrm{V_{td}V_{tb}^*}}{\mathrm{V_{ud}V_{ub}^*}}\right) \ , \quad \beta \equiv \arg\left(-\frac{\mathrm{V_{cd}V_{cb}^*}}{\mathrm{V_{td}V_{tb}^*}}\right) \ , \quad \gamma \equiv \arg\left(-\frac{\mathrm{V_{ud}V_{ub}^*}}{\mathrm{V_{cd}V_{cb}^*}}\right) \ , \tag{2.11}$$

The UT is of particular experimental and theoretical interest, as it can be over-constrained by independent measurements. There are three sides and three angles that can be measured, but a triangle is already well defined with three out of this six constraints. One of the main goals of the B factories is to make as many independent measurements as possible: If the SM is valid, all these independent measurements should be compatible with the same triangle, whereas if this is not the case, this is a sign of non-SM contributions to the decay amplitudes. We show the current experimental constraints of the UT in Sec. 2.2.4.

2.2 CP violation in the B meson system

2.2.1 Introduction

B mesons have the heaviest quark that forms bound states, the b quark, as valence quark. Studying decays of heavy flavored mesons, e.g. in semi-leptonic decays, can give yield information of CKM elements [6]. Another way to measure CKM elements is through mixing induced phenomena. The neutral B mesons have a lifetime $\tau = 1.530 \pm 0.009$ ps that is of the same order of magnitude as their oscillation period ($\mathrm{T} = \frac{1}{\Delta \mathrm{m_d}} = \frac{1}{0.51\ \mathrm{ps^{-1}}} = 1.96\mathrm{ps}$). The probability that a neutral B meson oscillates before decaying is $\sim 18.8\%$.

2.2.2 The neutral B system, mixing and time dependent CP asymmetry

Mixing in the neutral B system

The neutral B^0 meson and its CP conjugate the $\bar{\mathrm{B}}^0$ meson are defined by their flavor contents $(\bar{\mathrm{b}}\mathrm{d})$ and $(\mathrm{b}\bar{\mathrm{d}})$, respectively. While the B^0 and $\bar{\mathrm{B}}^0$ mesons are produced via the strong and electro-magnetic interactions, we know from their lifetime that the decay proceeds via the weak interaction. Before its decay, the development in time of the physical B meson $\mathrm{B}^0_{\mathrm{phys}}$ is governed by its effective Hamiltonian. As there are flavor-non-conserving weak processes that connect the flavor eigenstates, the effective Hamiltonian is non-diagonal in the $\{\mathrm{B}^0, \bar{\mathrm{B}}^0\}$ base [10]:

$$\mathrm{H}_{\mathrm{eff}} = \begin{pmatrix} \mathrm{H}_0 & \mathrm{H}_{12} \\ \mathrm{H}_{21} & \mathrm{H}_0 \end{pmatrix} = \mathrm{M} - \frac{\mathrm{i}}{2}\Gamma = \begin{pmatrix} \mathrm{M}_0 & \mathrm{M}_{12} \\ \mathrm{M}^*_{21} & \mathrm{M}_0 \end{pmatrix} - \frac{\mathrm{i}}{2}\begin{pmatrix} \Gamma_0 & \Gamma_{12} \\ \Gamma^*_{21} & \Gamma_0 \end{pmatrix} \tag{2.12}$$

The assumption of CPT invariance constrains the diagonal terms of the matrices to be the same. The effective Hamiltonian is not Hermitian to take into account the decay of the particle. The real part describes oscillation between flavor eigenstates and the imaginary part the decay. Feynman representations of weak transitions between B^0 and $\bar{\mathrm{B}}^0$ are shown in Fig. 2.2. It results that the mass eigenstates of the neutral B meson system are a superposition

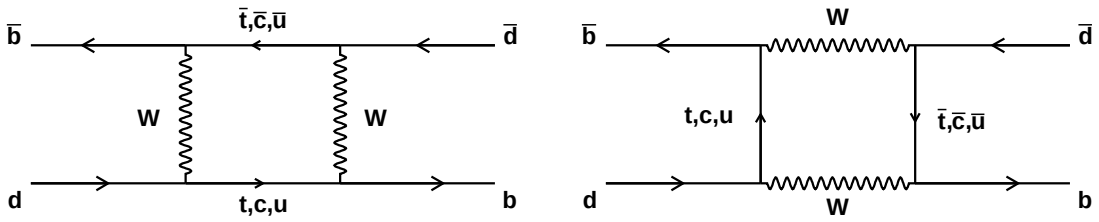

Figure 2.2: Box Feynman diagrams weakly mediated transitions between B^0 and $\bar{\mathrm{B}}^0$ flavour eigenstates

of B^0 and $\bar{\mathrm{B}}^0$ flavor eigenstates. They are called $\mathrm{B}_{\mathrm{L(ight)}}$ and $\mathrm{B}_{\mathrm{H(eavy)}}$ with mass eigenvalues M_{L} and M_{H} and width eigenvalues Γ_{L} and Γ_{H}.

$$|\mathrm{B_L}\rangle = \mathrm{p}|\mathrm{B}^0\rangle + \mathrm{q}|\bar{\mathrm{B}^0}\rangle, \quad |\mathrm{B_H}\rangle = \mathrm{p}|\mathrm{B}^0\rangle - \mathrm{q}|\bar{\mathrm{B}^0}\rangle \,, \tag{2.13}$$

where p and q are complex numbers that satisfy $|\mathrm{p}|^2 + |\mathrm{q}|^2 = 1$. The mass and width differences are defined as follows:

$$\Delta \mathrm{m_d} = \mathrm{M_H} - \mathrm{M_L}, \quad \Delta\Gamma = \Gamma_{\mathrm{H}} - \Gamma_{\mathrm{L}} \,, \tag{2.14}$$

where $\Delta \mathrm{m_d}$ is positive by definition and corresponds to the mixing frequency. The ratio of the q and p parameters is given by

$$\frac{\mathrm{q}}{\mathrm{p}} = -\frac{\Delta \mathrm{m_d} - \frac{\mathrm{i}}{2}\Delta\Gamma}{2(\mathrm{M}_{12} - \frac{\mathrm{i}}{2}\Gamma_{12})} \,. \tag{2.15}$$

All the information of the time development of the system is contained in the Hamiltonian, i.e the oscillation of the physical B meson $\mathrm{B}^0_{\mathrm{phys}}$ between flavor eigenstates through weak interaction can be described by the eigenvalues of the Hamiltonian and the q and p parameters.

$$|\mathrm{B}^0_{\mathrm{phys}}(\mathrm{t})\rangle = \mathrm{g}_+(\mathrm{t})|\mathrm{B}^0\rangle - \frac{\mathrm{q}}{\mathrm{p}}\mathrm{g}_-(\mathrm{t})|\bar{\mathrm{B}}^0\rangle \tag{2.16}$$

$$|\bar{\mathrm{B}}^0_{\mathrm{phys}}(\mathrm{t})\rangle = \mathrm{g}_+(\mathrm{t})|\bar{\mathrm{B}}^0\rangle - \frac{\mathrm{p}}{\mathrm{q}}\mathrm{g}_-(\mathrm{t})|\mathrm{B}^0\rangle \tag{2.17}$$

with

$$\mathrm{g}_\pm(\mathrm{t}) \equiv \frac{1}{2}(\mathrm{e}^{-\mathrm{i}\mathrm{M}_\mathrm{H}\mathrm{t}-\frac{1}{2}\Gamma_\mathrm{H}\mathrm{t}} \pm \mathrm{e}^{-\mathrm{i}\mathrm{M}_\mathrm{L}\mathrm{t}-\frac{1}{2}\Gamma_\mathrm{L}\mathrm{t}}) \tag{2.18}$$

Eq. 2.16 describes that a B^0 meson of definite quark content at a time t=t', will oscillate with a definite probability amplitude into its *CP* conjugate $\bar{\mathrm{B}}^0$ at a time t=t". By doing so, the amplitude picks up the weak phase contained in $\frac{\mathrm{q}}{\mathrm{p}}$. This weak phase comes from the complex coupling constants between quarks corresponding to the CKM matrix elements in the box diagram Fig. 2.2. All three up-type quarks should contribute, as they all couple with a factor $\sim \lambda^6$. When integrating over the internal degrees of freedom it turns out that each contribution is weighted by its mass [11]. As a result the non-top-quark contributions can be neglected and the weak phase in $\frac{\mathrm{q}}{\mathrm{p}}$ corresponds to the phase in $(\mathrm{V}_{\mathrm{td}}\mathrm{V}^*_{\mathrm{tb}})^2$,

$$\frac{\mathrm{q}}{\mathrm{p}} = \mathrm{e}^{-\mathrm{i}2\beta} \tag{2.19}$$

where β is the angle of the unitarity triangle given in Eq. 2.11. This phase can be measured when both B^0 and $\bar{\mathrm{B}}^0$ decay to a common *CP* definite final state, e.g. $\mathrm{J}/\psi\,\mathrm{K}^0_\mathrm{s}$ or $\mathrm{f}_0(980)\mathrm{K}^0_\mathrm{s}$, by measuring the time-dependent *CP* asymmetry, as described in Sec. 2.2.3.

2.2.3 Different types of CP violation in the B mesons system

In Sec. 2.1 we have seen that there is a non-reducible phase in weak coupling. In the following we show how this phase generates observable *CP* violating effects in particle decays. If we look at a transition amplitude with a phase from strong coupling δ (*CP* even) and phase from weak coupling ϕ (*CP* odd), it transforms as follows:

$$\mathrm{A}_1\mathrm{e}^{\mathrm{i}(\delta+\phi)} \xrightarrow{\mathcal{CP}} \mathrm{A}_1\mathrm{e}^{\mathrm{i}(\delta-\phi)} \,. \tag{2.20}$$

This phase shift is not observable as the probability is $\propto \mathrm{A}_1^2$ before and after transformation. Single phases have no physical meaning; they are chosen arbitrarily. The situation is different when several amplitudes with different weak phases contribute to a transition. Only one of the phases can be chosen arbitrarily, but the phase difference has physical meaning and can lead to observable effects. If we look at the sum of two amplitudes

$$\mathrm{A} = \mathrm{A}_1\mathrm{e}^{\mathrm{i}(\delta_1+\phi_1)} + \mathrm{A}_2\mathrm{e}^{\mathrm{i}(\delta_2+\phi_2)} \,, \tag{2.21}$$

and its *CP* conjugate

$$\bar{\mathrm{A}} = \mathrm{A}_1\mathrm{e}^{\mathrm{i}(\delta_1-\phi_1)} + \mathrm{A}_2\mathrm{e}^{\mathrm{i}(\delta_2-\phi_2)} \,, \tag{2.22}$$

the expectation values of A and $\bar{\mathrm{A}}$ are not the same:

$$|\mathrm{A}|^2 - |\bar{\mathrm{A}}|^2 = -4|\mathrm{A}_1||\mathrm{A}_2|\sin(\delta_1 - \delta_2)\sin(\phi_1 - \phi_2). \tag{2.23}$$

The decay rate of a particle is proportional to the square of the magnitude of the underlying transition amplitude. To observe CP asymmetry in particle decays, at least 2 amplitudes with different weak phases need to contribute to the decay. Eq. 2.23 also tells us that to observe direct CP asymmetries, the strong phases and their difference need to be non-zero. To measure CP asymmetries, one can reconstruct the decay of particles from a flavor eigenstate to a final state f that is a CP eigenstate. The decay amplitudes of a particle P and its CP conjugate $\bar{\mathrm{P}}$ to a multi particle final state f and its CP conjugate $\bar{\mathrm{f}}$ are defined as

$$\mathrm{A_f} = \langle \mathrm{f}|\mathcal{H}|\mathrm{P}\rangle \ , \ \bar{\mathrm{A}}_\mathrm{f} = \langle \mathrm{f}|\mathcal{H}|\bar{\mathrm{P}}\rangle \ , \ \mathrm{A}_{\bar{\mathrm{f}}} = \langle \bar{\mathrm{f}}|\mathcal{H}|\mathrm{P}\rangle \ , \ \bar{\mathrm{A}}_{\bar{\mathrm{f}}} = \langle \bar{\mathrm{f}}|\mathcal{H}|\bar{\mathrm{P}}\rangle, \tag{2.24}$$

where $\mathcal{H}$ is the Hamiltonian governing weak interactions.
CP violation in decay or *direct* CP violation is defined by

$$\frac{\bar{\mathrm{A}}_{\bar{\mathrm{f}}}}{\mathrm{A_f}} \neq 1 \ . \tag{2.25}$$

Direct CP violation can be observed by measuring decay rates, in other words by counting events. The direct CP asymmetry is defined as

$$\mathcal{A}_{\mathrm{CP}} = \frac{\mathcal{B}(\bar{\mathrm{B}} \to \bar{\mathrm{f}}) - \mathcal{B}(\mathrm{B} \to \mathrm{f})}{\mathcal{B}(\bar{\mathrm{B}} \to \bar{\mathrm{f}}) + \mathcal{B}(\mathrm{B} \to \mathrm{f})} = \frac{|\bar{\mathrm{A}}_{\bar{\mathrm{f}}}/\mathrm{A_f}|^2 - 1}{|\bar{\mathrm{A}}_{\bar{\mathrm{f}}}/\mathrm{A_f}|^2 + 1} \ . \tag{2.26}$$

This is the only possible source of CP asymmetries for charged mesons as there is no mixing. There are two other types of CP asymmetry that can be observed in neutral meson systems only. The difference is that in neutral meson systems weakly mediated box diagrams (see. Fig. 2.2 in Sec. 2.2.2) can generate a second amplitude. The first of the mixing-induced types of CP violation is CP violation in mixing and is defined as:

$$\frac{|\mathrm{q}|}{|\mathrm{p}|} \neq 1 \ . \tag{2.27}$$

It can be observed if the probability of a B^0 to oscillate to a $\bar{\mathrm{B}}^0$ is different from the probability of the $\bar{\mathrm{B}}^0$ to oscillate to a B^0. This type of CP violation was observed in the neutral K system [12] [13]. In the case of neutral B and K mesons $\frac{|\mathrm{q}|}{|\mathrm{p}|} \approx 1$ to good approximation and CP violation in mixing is negligible with respect to the sensitivity of the B factories.
The CPV observed in the neutral B meson system is in the interference between decay without mixing and decay with mixing, i.e. in the interference between $\mathrm{B}^0 \to \bar{\mathrm{B}}^0 \to \mathrm{f_{CP}}$ and $\mathrm{B}^0 \to \mathrm{f_{CP}}$ where B^0 and $\bar{\mathrm{B}}^0$ can decay to the same CP definite final state $\mathrm{f_{CP}}$. The three types of CP violation are presented schematically in Fig. 2.3. If we want to measure CP asymmetry in the interference between decays with and without mixing of neutral B mesons, we need to take into account that the neutral B mesons oscillate over time. If we know the flavor of the B meson under study at a given time before or after its decay, we have all the information for a complete description of the oscillation according to Eq. 2.16. The B factories

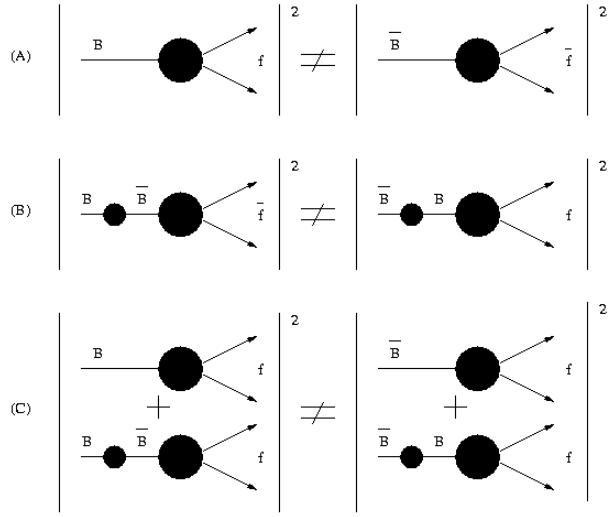

Figure 2.3: Schematic representation of the 3 types of *CP* violation: Direct *CP* violation (A), *CP* violation in mixing (B) and *CP* violation in the interference between decays with and without mixing (C).

are optimized for this kind of measurement, as they produce pairs of $\mathrm{B^0\bar{B}^0}$ via the $\Upsilon(4s)$ resonance and the pairs are created in a coherent L=1 state S:

$$\mathrm{S(t=0)} = \frac{\mathrm{B^0\bar{B}^0 - \bar{B}^0B^0}}{\sqrt{2}} \,. \tag{2.28}$$

In other words, in this coherent quantum state, there is always exactly one $\mathrm{B^0}$ and one $\mathrm{\bar{B}^0}$. If one of the mesons decays in a flavor-dependent way, the flavor of the other meson is known at the exact same instant; it is flavour tagged (see Sec. 7.3.4). In the following we call the B meson that decays in a flavor specific way $\mathrm{B_{tag}}$ and the B meson that decays to an exclusive *CP* definite final state $\mathrm{B_{CP}}$.
What the B factories measure in this context is $\Delta\mathrm{t}$, the time between the decay of the $\mathrm{B_{tag}}$ and the $\mathrm{B_{CP}}$. $\Delta\mathrm{t}$ is measured by a precise vertex measurement, a schematic presentation is shown in Fig. 2.4, for more detailed information see Sec. 7.4. Using the flavor-tag and the $\Delta\mathrm{t}$ measurement, the time-dependent *CP* asymmetry can be defined as:

$$\mathcal{A}_{\mathcal{CP}}(\Delta\mathrm{t}) = \frac{\mathcal{B}(\mathrm{B_{tag=B^0}}(\Delta\mathrm{t}) \to \mathrm{f_{CP}}) - \mathcal{B}(\mathrm{B_{tag=\bar{B}^0}}(\Delta\mathrm{t}) \to \mathrm{f_{CP}})}{\mathcal{B}(\mathrm{B_{tag=B^0}}(\Delta\mathrm{t}) \to \mathrm{f_{CP}}) + \mathcal{B}(\mathrm{B_{tag=\bar{B}^0}}(\Delta\mathrm{t}) \to \mathrm{f_{CP}})} \,. \tag{2.29}$$

Using the time-dependent decay rate of a tagged neutral B meson [14]

$$\mathrm{R_{q_{tag}}}(\Delta\mathrm{t}) = \frac{\mathrm{e}^{-|\Delta\mathrm{t}|/\tau}}{4\tau}[1 + \frac{\mathrm{q_{tag}}}{2} + \mathrm{q_{tag}}(\mathcal{S}\mathrm{sin}(\Delta\mathrm{m_d}\Delta\mathrm{t}) - \mathcal{C}\mathrm{cos}(\Delta\mathrm{m_d}\Delta\mathrm{t}))], \tag{2.30}$$

where $q_{tag} = +1(-1)$ when the B_{tag} is identified as $B^0(\bar{B}^0)$, this expression can be written in a simpler form

$$\mathcal{A}_{\mathcal{CP}}(\Delta\mathrm{t}) = \mathcal{S}\mathrm{sin}(\Delta\mathrm{m_d}\Delta\mathrm{t}) - \mathcal{C}\mathrm{cos}(\Delta\mathrm{m_d}\Delta\mathrm{t}) \,, \tag{2.31}$$

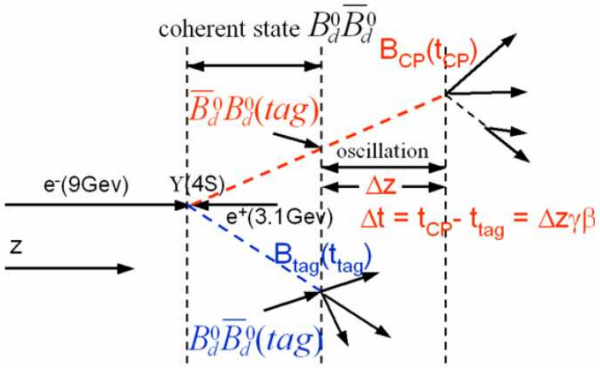

Figure 2.4: Schematic presentation of the Δt measurement. The time measurement is done via precise measurements of the decay vertices of the signal B_{CP} that decays into a CP eigenstate and the B_{tag} that decays in a flavor specific way. The separation in space along the boost direction Δz can then be used to calculate the proper time $\Delta t \equiv t_{CP} - t_{tag}$, as the boost of the $B^0\bar{B}^0$ system is known from the beam energies. The time development of the B_{CP} between the time it is tagged and its decay is described by Eq. 2.16. Δt can be negative if the B_{CP} decay occurs before the B_{tag} decay.

with

$$\mathcal{S} = \frac{2\mathrm{Im}\lambda}{1+|\lambda|^2}\ ,\ \mathcal{C} = \frac{1-|\lambda|^2}{1+|\lambda|^2}\ ,\ \lambda = e^{-i\Phi_{mix}}\frac{\bar{A}_f}{A_f}\ , \tag{2.32}$$

where Φ_{mix} is the mixing phase. The coefficients $\mathcal{S}$ and $\mathcal{C}$ describe mixing induced and direct CP violation respectively. If $\mathcal{C}$ is non-zero, there is direct CP violation ($\mathcal{C} = -\mathcal{A}_{CP}$). If $\mathcal{S}$ is non-zero, there is mixing-induced CP violation. If we look at a decay that proceeds through a single diagram, CP violation being an interference effect, there is no direct CP violation and $\mathcal{C}$ is expected to be zero. The mixing-induced CP violation for the same scenario yields according to Eq. 2.19:

$$\mathcal{S} = -\eta_{CP}\sin(2\beta)\ , \tag{2.33}$$

where η_{CP} is the CP eigenvalue of the final state. This means when only one Feynman diagram contributes to the decay, the mixing angle Φ_{mix} is given by the CKM angle 2β. In reality, there is no B decay that proceeds through only one Feynman diagram and a comparison of measurements from different decay mode and with theory predictions is often done using the "effective mixing angle" $2\beta_{eff}$ [15]:

$$\mathcal{S} = \sqrt{1-\mathcal{C}^2} - \eta_{CP}\sin(2\beta_{eff}) \tag{2.34}$$

2.2.4 Experimental status of the CKM parameters

The current status of the constraints on the CKM matrix is shown in 2.5. The best constraint on a parameter of the UT triangle comes from the β measurement of the B factories. The so-called "golden channel" $B^0 \to J/\psi K_s^0$ provides a precise measurement, as it has a relatively

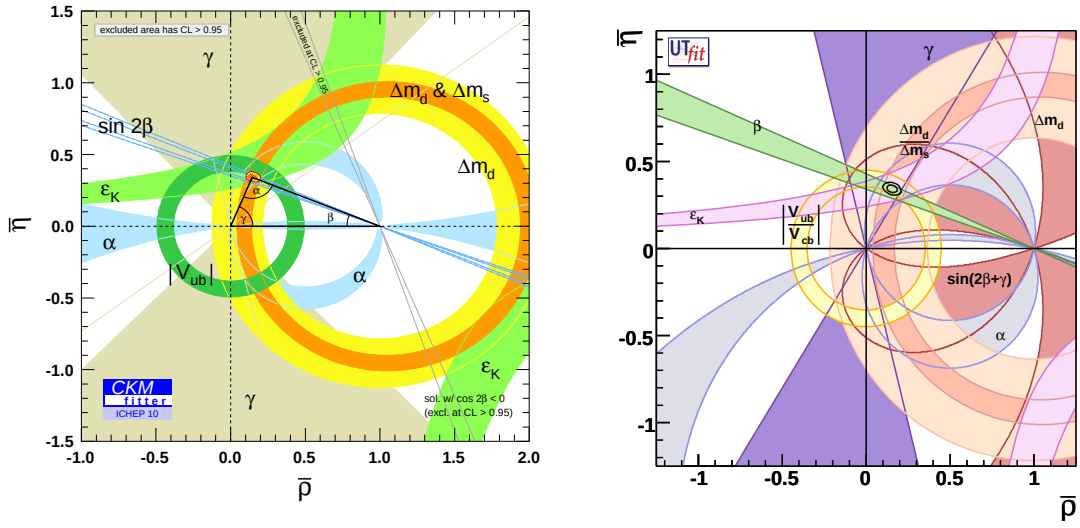

Figure 2.5: Global fit of the UT showing the current experimental and theoretical constraints on the sides and angles, by the CKMFitter group [4] on the left and by the UTFit group [5] on the right . The CKMFitter fit is updated with the results available at the ICHEP conference in 2010, the UTFit fit includes the summer 2010 results before ICHEP. The strongest experimental constraints on the UT come from the B factories, in particular with the β measurement. As can be seen all the currents constraints are compatible with the same triangle, all the allowed regions overlap around the apex of the triangle. This means that the current experimental data are compatible within the experimental and theoretical uncertainties with the SM picture.

large BF ($\sim 4 \cdot 10^{-4}$) and diagrams other than the one shown in Fig. 2.6 carry the same weak phase (compare Sec. 3.1).Also it is experimentally very clean due to the reconstruction of the narrow J/ψ resonances from leptons and the clean experimental signature of the K^0_s decay into charged pions. The final *BABAR* measurement is shown in Fig. 2.6. The world average including other $\mathrm{b} \to \mathrm{c\bar{c}s}$ channels (e.g. $\chi_{\mathrm{c}0}\mathrm{K}^0_\mathrm{s}$) is

$$\sin(2\beta)_{\mathrm{b}\to\mathrm{c\bar{c}s}} = 0.672 \pm 0.023, \tag{2.35}$$

the error includes both statistical and systematical uncertainties.

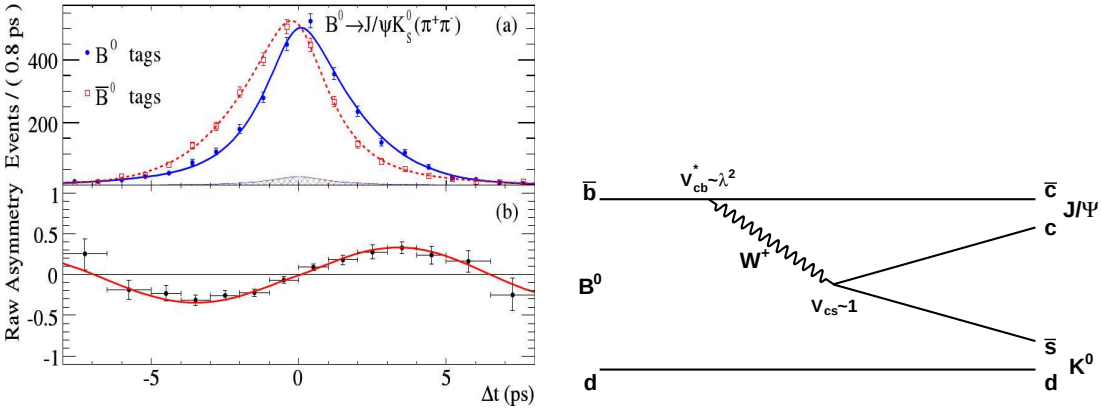

Figure 2.6: On the left: final result from *BABAR* [16] on the time-dependent CP asymmetry in the $\mathrm{B}^0 \to \mathrm{J/\psi\,K}^0_\mathrm{s}$ channel. In the top plot are the $\Delta\mathrm{t}$ distributions for both tags. In the bottom plot the resulting time dependent CP asymmetry. It clearly can be seen that the time-evolution differs between B^0 and $\bar{\mathrm{B}}^0$ mesons. On the right: dominating tree-level Feynman diagram for the same process.

3 Charmless 3-body B decays and $B^0 \to K^0_s K^0_s K^0_s$

This chapter is divided into two parts. In the first one, in Sec. 3.1 and Sec. 3.2, we present the theoretical and experimental interest in analyzing the decay channel $\mathrm{B}^0 \to \mathrm{K}^0_\mathrm{s}\mathrm{K}^0_\mathrm{s}\mathrm{K}^0_\mathrm{s}$ and put it in the larger context of the search for new physics in charmless 3-body B decays. The second part, Sec. 3.3, concentrates on the Dalitz plot (DP) formalism.

3.1 Search for new Physics in b $\to$s Penguin dominated modes

The CKM phase β has been measured to high precision in $\mathrm{B} \to \mathrm{c\bar{c}K}^{(*)}$ decays by the means of the time-dependent CP violation (TDCPV) parameter $\mathcal{S}$ in the decay of neutral B mesons. This is possible for decays that are dominated by only one amplitude, or, in case several decay amplitudes contribute, if all contributing amplitudes have the same CP-odd phase. The decay amplitudes of neutral B mesons can have contributions from "tree" diagrams where a charged $\mathrm{W}^\pm$ is radiated and then couples to quarks that contribute to the final state, or from "penguin" diagrams where a $\mathrm{W}^\pm$ is emitted and then reabsorbed by the same quark line creating a loop in the diagram. In Fig. 3.1 are shown tree and penguin diagrams contributing to the "golden mode" $\mathrm{B}^0 \to \mathrm{J}/\psi\,\mathrm{K}^0_\mathrm{s}$. In penguin diagrams the contribution to the loop scales

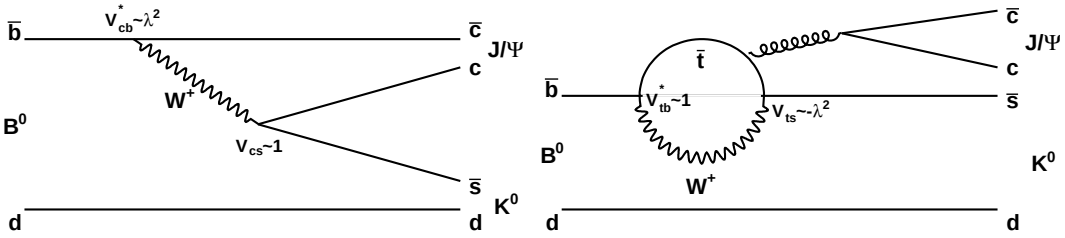

Figure 3.1: Feynman diagrams of tree (right) and penguin (left) diagrams that contribute to the amplitude of the decay $\mathrm{B}^0 \to \mathrm{J}/\psi\,\mathrm{K}^0_\mathrm{s}$. As the loop in the penguin diagram is dominated by the top quark contribution, the SM phase in the weak coupling is the same as for the tree diagram. As result the measurement of $\mathcal{S}$ provides a clean measurement of the UT angle β (Sec. 2.2.3).

with the mass of the virtual particle, i.e. the top quark dominates the loop in the SM picture. In a new physics scenario non-SM heavy particles could contribute as virtual particle to the

loop. If this non-SM particle couples with a new CP violating phase, the measured value of the TDCPV parameters $\mathcal{S}$ and $\mathcal{C}$ can deviate from the SM prediction. Candidates for such particles are for instance squarks from a super symmetric model that could have sizable contributions [17]. In many decays, penguin diagrams contribute to the final state, but they are suppressed by a factor $\mathcal{O}(0.2-0.3)$ [18] compared to the tree diagram(s) that contribute as well and have SM couplings. In this way possible effects from non-SM couplings in the loop are drowned in the SM contributions. On the other hand, in charmless 3-body B decays, in the absence of $\mathrm{b} \to \mathrm{c}$ amplitudes, the $\mathrm{b} \to \mathrm{s}$ penguin contributions are often comparable to the tree diagrams, or can even dominate the decay, as it is the case for $\mathrm{B}^0 \to \mathrm{K}^0_\mathrm{s}\mathrm{K}^0_\mathrm{s}\mathrm{K}^0_\mathrm{s}$, see Sec. 3.2. Here, possible contributions from beyond SM physics are not drowned in tree diagram contributions to the decays. Over the last years the B factories have explored the domain of charmless quasi two body (Q2B) decays and three body decays. Q2B decays proceed through an intermediate 2-body state, before reaching 3-body (or in general multi-body) final state. In 3-body decays a Q2B mode consists of a final state particle and a resonance, e.g. $\mathrm{B}^0 \to \mathrm{f}_0(980)\mathrm{K}^0_\mathrm{s}$, where the $\mathrm{f}_0(980)$ then decays to kaons or pions. In most cases the TDCPV analysis of a 3-body decay needs to take into account the phase-space dependence, the Dalitz plot (DP), as the final state in not CP definite. The CPV parameters $\mathcal{S}$ and $\mathcal{C}$ can only be defined for CP definite final states and, in case the 2-body intermediate states are CP definite, even if the final state in the detector in not CP definite, a model of the DP can be used to describe these intermediate states. This is the case for instance for the decay $\mathrm{B}^0 \to \mathrm{K}^0_\mathrm{s}\pi^+\pi^-$, where the final state itself is not a CP eigenstate, but intermediate states such as $\mathrm{B}^0 \to \mathrm{f}_0(980)\mathrm{K}^0_\mathrm{s}$ or $\mathrm{B}^0 \to \rho_0(770)\mathrm{K}^0_\mathrm{s}$ are. Many of the Q2B modes that contribute to charmless 3 body B decays are penguin-dominated and good candidates for the search of NP at loop level, such as $\mathrm{B}^0 \to \mathrm{f}_0(980)\mathrm{K}^0_\mathrm{s}$ or $\mathrm{B}^0 \to \Phi\mathrm{K}^0_\mathrm{s}$. Dalitz plot analyses have been performed for many charmless 3-body B decays. For instance TD DP analysis have been performed for $\mathrm{B}^0 \to \mathrm{K}^0_\mathrm{s}\pi^+\pi^-$ [19], $\mathrm{B}^0 \to \rho\pi$ [20] and $\mathrm{B}^0 \to \mathrm{K}^+\mathrm{K}^-\mathrm{K}^0_\mathrm{s}$ [21]. It is also interesting to study the 3-body decays of charged B mesons, as a DP analysis allows to measure the relative strong phases between the Q2B modes, direct CP violation and the resonant Q2B BF's can be extracted. Analyses have been done for the modes $\mathrm{B}^+ \to \pi^+\pi^-\pi^+$ [22], $\mathrm{B}^+ \to \mathrm{K}^+\pi^+\pi^-$ [23] and $\mathrm{B}^+ \to \mathrm{K}^+\mathrm{K}^-\mathrm{K}^+$ [24]. All these analyses are statistically limited by the low branching fraction (BF) of $10^{-5}-10^{-6}$ and have only become possible after several years of running of the B factories. A compilation of results from $\mathrm{b} \to \mathrm{s}$ penguin decays is shown in Fig. 3.2. There is a tendency of the penguin modes to lie on the left of the value measured in $\mathrm{B} \to \mathrm{c\bar{c}K}^{(*)}$ decays, but the naive average is less than 3σ away from the $\mathrm{B} \to \mathrm{c\bar{c}K}^{(*)}$ value. The true significance is hard to estimate, as all of these penguin channels have mode-dependent and for some cases sizable theoretical uncertainties in the SM prediction (see Sec. 3.2).

3.2 Particularities of the decay $B^0 \to K^0_s K^0_s K^0_s$

The decay mode $\mathrm{B}^0 \to \mathrm{K}^0_\mathrm{s}\mathrm{K}^0_\mathrm{s}\mathrm{K}^0_\mathrm{s}$ is considered as a "golden" $\mathrm{b} \to \mathrm{s}$ penguin mode, as it has small theoretical uncertainties and is experimentally clean.
As we will show in Sec. 3.2.2 the final state is CP even. As a result, from the experimental

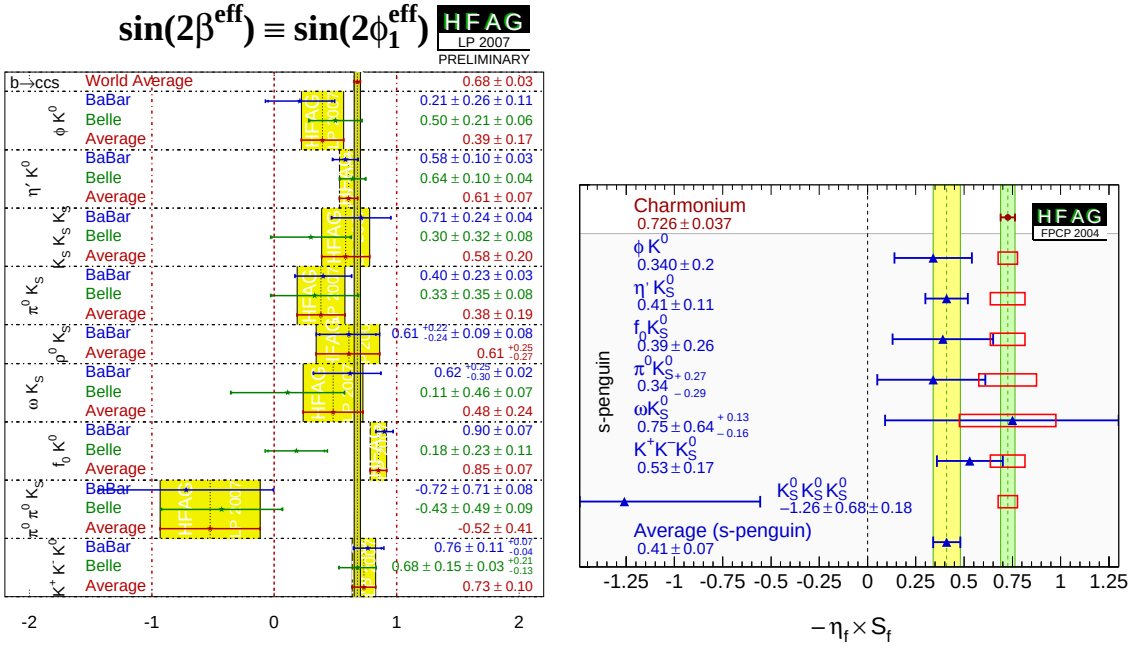

Figure 3.2: On the left, compilation of $\sin(2\beta_{\rm eff})$ (defined in Eq. 2.34) measurements for $\mathrm{b} \to \mathrm{s}$ penguin decays before the beginning of this work by the HFAG group [25]. On the right a similar compilation from 2004 is given for comparison, the latter showing a disagreement between $\mathrm{B} \to \mathrm{c\bar{c}K}^{(*)}$ and $b \to s$ penguin decays, where a clear shift to the left of penguin-dominated decays is seen. The red boxes show an estimation of the theoretical uncertainties that have been updated since then (see Fig. 3.4). In 2007, with more data, this disagreement has become less important. The analysis of more data, including this thesis, will show if the disagreement was a statistical fluctuation or if it is due to NP processes.

point of view, the TDCPV parameters can be extracted without a DP analysis. On the other hand, several Q2B modes are expected to contribute to the signal and there is no reason why the Q2B CPV parameters should be the same for all of them. By performing a phase-space integrated analysis of the TDCPV of the channel, one averages over these contributions. The ideal scenario would be to do a TD DP analysis, but with expected $\sim$200 signal events this is not feasible. The best we can do, is to perform a phase-space integrated analysis of the TDCPV parameters and a time-integrated DP analysis to extract the Q2B fit fractions. This way we can measure the phase space integrated values of the TDCPV parameters and the the DP analysis tells us what this phase space looks like. That is the maximal information we can extract from the complete *BABAR* dataset. The approach also allows us to use the additional channel where one of the K^0_s decays to neutral pions for the TDCPV analysis in order to increase the statistics for the measurement that would complicate the DP analysis due to a larger fraction of wrongly reconstructed events and therefore we do not use K^0_s

decaying to neutral pions in the latter. Given the small number of signal events, all these measurements are limited by the statistical uncertainties. Still especially the DP analysis can provide useful information, in particular concerning the controversial $\mathrm{f_X}(1500)$ resonance because only even spin resonances are allowed to contribute to the final state. These subjects will be developed in the following sections.

3.2.1 Theoretical predictions for TDCPV parameters of the decay $B^0 \to K^0_s K^0_s K^0_s$

The dominating SM Feynman diagram for the decay is shown in Fig. 3.3. As other contri-

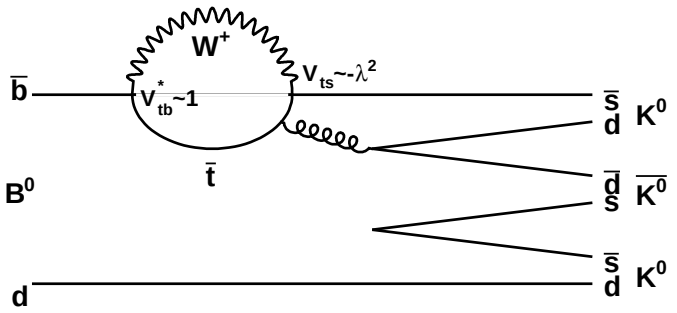

Figure 3.3: Feynman diagram that dominates the decay amplitude. Other contributions are suppressed by (at least) λ^2. As can be seen the weak coupling has the same phase as the decay $\mathrm{B^0 \to J/\psi K^0_s}$ shown in Fig. 3.1

butions are suppressed by (at least) λ^2, assuming that this is the only significant SM diagram is a good approximation. The TDCPV parameters $\mathcal{S}$ and $\mathcal{C}$ are expected to have the same values as in the golden mode $\mathrm{B^0 \to J/\psi K^0_s}$, i.e. $\mathcal{S} = -\eta_{\mathrm{CP}} \sin(2\beta) \stackrel{\eta_{\mathrm{CP}}=1}{=} -\sin(2\beta)$ and $\mathcal{C} = 0$. The theoretical prediction of penguin-dominated modes is shown in Fig. 3.4. Clearly the mode $\mathrm{B^0 \to K^0_s K^0_s K^0_s}$ has particularly small theoretical uncertainties. The predictions include short-distance and long-distance corrections [26] [27]. The short distance corrections are calculated via a factorization approach using NLO effective Wilson coefficients. They are due to "tree-pollution" from $\mathrm{b \to u\bar{u}s}$ contributions to the penguin-dominated modes. These tree contributions carry the weak phase γ and could hence give a shift in S, but as they are usually color-suppressed, this shift is expected to be small. Nevertheless for some modes, e.g. for $\rho^0 \mathrm{K^0_s}$ and $\omega \mathrm{K^0_s}$, there is dynamical enhancement of the tree-pollution. For instance in the penguin-dominated decay $\mathrm{\bar{B}^0 \to \omega \bar{K}^0}$, the decay can occur through the color allowed weak tree amplitude $\mathrm{\bar{B}^0 \to K^{*-} \pi^+}$ and then re scatter as $\mathrm{K^{*-} \pi^+ \to \omega \bar{K}^0}$. This tree amplitude is comparable to the penguin amplitude. The prediction suffers from large uncertainties, e.g. from the experimental uncertainty on γ and from the fact that the size of the tree contribution is not exactly known. Other uncertainties are associated the quark masses, the renormalization scale and form factors. The long-distance corrections, namely final state re-scattering effects are estimated by including resonant contributions between kaon pairs in the final state. As an example we show in Fig. 3.5 the Feynman diagrams of the main

contributions of final state re-scattering in $\phi \mathrm{K}_\mathrm{s}^0$. If one of the couplings in these diagrams carries a weak phase, the value of $\mathcal{S}$ is modified. In case of charmless intermediate states the coupling involves $\mathrm{V_{ub}V_{us}^*} \sim \mathrm{A}\lambda^4 \mathrm{e}^{\mathrm{i}\gamma}$, i.e. the weak phase γ.

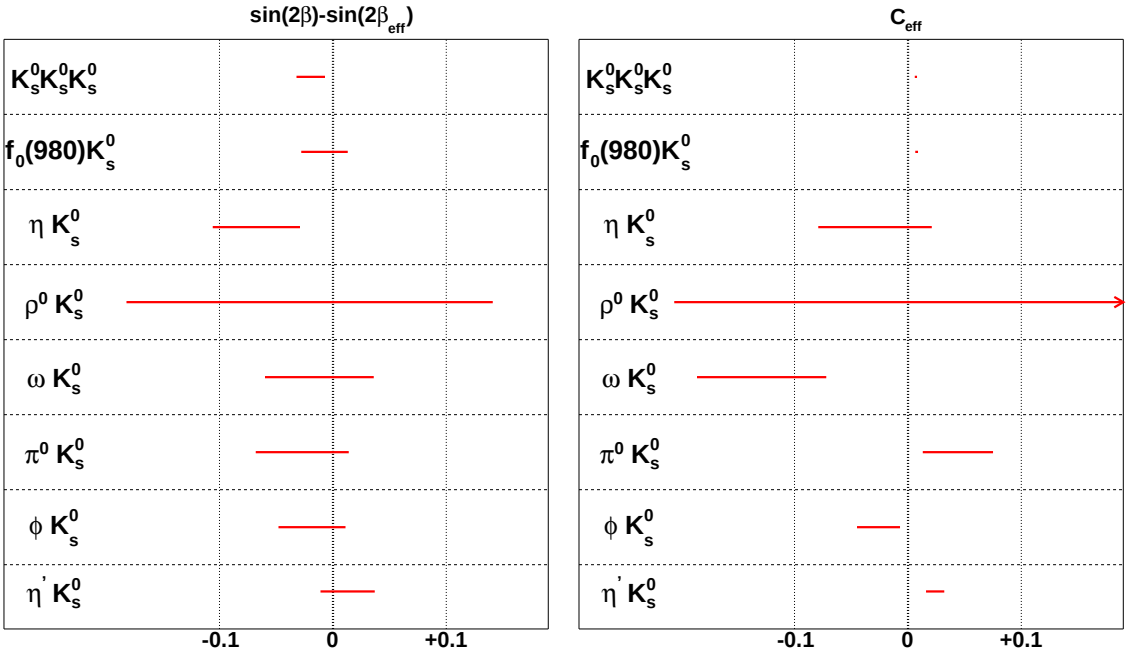

Figure 3.4: Shift of the central values of $\mathcal{S}$ and $\mathcal{C}$ with theoretical uncertainties, for $\mathrm{B}^0 \to \mathrm{K_s^0 K_s^0 K_s^0}$ [26] and for the other penguin-dominated modes [27]. β_{eff} was defined in Eq. 2.34.

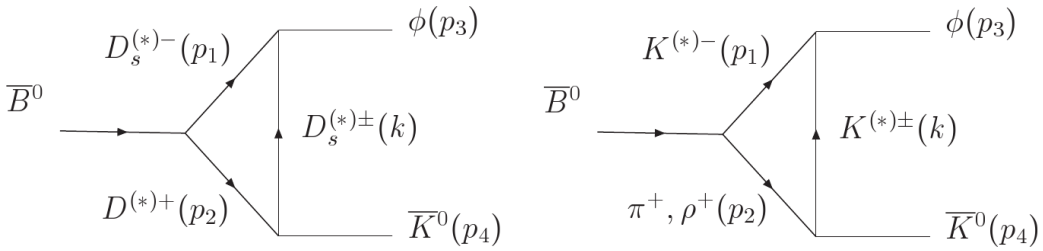

Figure 3.5: Final state rescattering contributions to $\bar{B}^0 \to \phi \bar{K}^0$

3.2.2 Restrictions on the final state due to angular momentum conservation

We look at the $\mathrm{K_s^0 K_s^0 K_s^0}$ final state in a quasi two body way, i.e. we describe the system as constructed of two subsystems, the $(\mathrm{K_s^0 K_s^0})$ with angular momentum L and the bachelor $\mathrm{K_s^0}$ with angular momentum L' relative to the $(\mathrm{K_s^0 K_s^0})$ system. As the $\mathrm{K_s^0}$ are pseudoscalars

($\mathrm{J^P} = 0^-$) they have no intrinsic angular momentum and hence obey Bose statistics and the ($\mathrm{K^0_s K^0_s}$) wave function must be symmetric, as result only even values of L are allowed. This is a strong constraint for an amplitude analysis, as an intermediate resonance that decays to a pair of $\mathrm{K^0_s}$ is necessarily of even spin. The CP eigenvalue of the system can be calculated:

$$\begin{aligned} \mathrm{CP(K^0_s K^0_s)} &= C(K^0_s K^0_s) \times P(K^0_s K^0_s) = \mathrm{C(K^0_s)^2 \times P(K^0_s)^2 \times (-1)^L} && (3.1) \\ &= \mathrm{CP(K^0_s)^2 = +1}\ , && (3.2) \end{aligned}$$

where the assumption is that the $\mathrm{K^0_s}$ are *CP* eigenstates. Neglecting CPV in $\mathrm{K^0_s}$ decays, which is a good approximation, K^0_s mesons are a CP eigenstate with eigenvalue +1.
The mother particle B^0, as its daughter particles, is a pseudoscalar, i.e. its angular momentum $\vec{\mathrm{J_B}}$ is zero and there are no intrinsic angular momenta in the final state. Angular momentum conservation imposes that L' is even-valued:

$$\vec{\mathrm{J_B}} = \vec{\mathrm{L}} + \vec{\mathrm{L}}' = 0 \Rightarrow \vec{\mathrm{L}}' = -\vec{\mathrm{L}}\ . \tag{3.3}$$

The *CP* eigenvalue of the $K^0_s K^0_s K^0_s$system is the same as the *CP* eigenvalue of a single K^0_s:

$$\begin{aligned} \mathrm{CP(K^0_s K^0_s K^0_s)} &= \mathrm{CP(K^0_s K^0_s) \times CP(K^0_s) \times (-1)^{L'}} && (3.4) \\ &= \mathrm{CP(K^0_s) = +1}\ . && (3.5) \end{aligned}$$

For more details and other $\mathrm{B^0 \to P^0 P^0 X^0}$ decays see [28].

3.2.3 The controversial $f_X(1500)$ resonance

Other charmless 3-body B decays studies with two kaons in the final state, including the *BABAR* [24] and BELLE [29] analyses of $\mathrm{B^+ \to K^+ K^- K^+}$ and the *BABAR* analysis of $\mathrm{B^0 \to K^+ K^- K^0_s}$ [21], have observed the contribution of a resonance $\mathrm{f_X(1500)}$ that they assumed to be scalar. The nature of this resonance is unclear. Tab. 3.1 gives its measured mass and width, Fiq. 3.6 shows the corresponding spectra of the $\mathrm{m_{KK}}$ invariant mass. The $\mathrm{f_X(1500)}$ is

Mass[GeV/c^2]	Width[GeV/c^2]	Measurement
1539 ± 20	257 ± 33	[24]
1524 ± 14	136 ± 23	[29]

Table 3.1: $\mathrm{f_X(1500)}$ mass and width measurements by *BABAR* and BELLE.[21] used the same values as [24].

assumed to be dominated by its quarkonium content, i.e. $|\mathrm{f_X(1500)}\rangle = \cos\theta|\bar{\mathrm{s}}\mathrm{s}\rangle + \sin\theta|\bar{\mathrm{n}}\mathrm{n}\rangle$, where θ is the mixing angle and $\bar{\mathrm{n}}\mathrm{n} = \frac{\bar{\mathrm{u}}\mathrm{u}+\bar{\mathrm{d}}\mathrm{d}}{\sqrt{2}}$. There are two main theoretical scenarios [30] concerning the nature of the $\mathrm{f_X(1500)}$ that give different predictions for direct CPV. In the first scenario, the $\mathrm{f_X(1500)}$ is the ground state, while in the second scenario, it is the first radial excitation. In the latter scenario the direct *CP* violation is expected to be small (3.5% for the $\bar{\mathrm{n}}\mathrm{n}$ component), while it is expected to be sizeable for the former (24% for the $\bar{\mathrm{n}}\mathrm{n}$

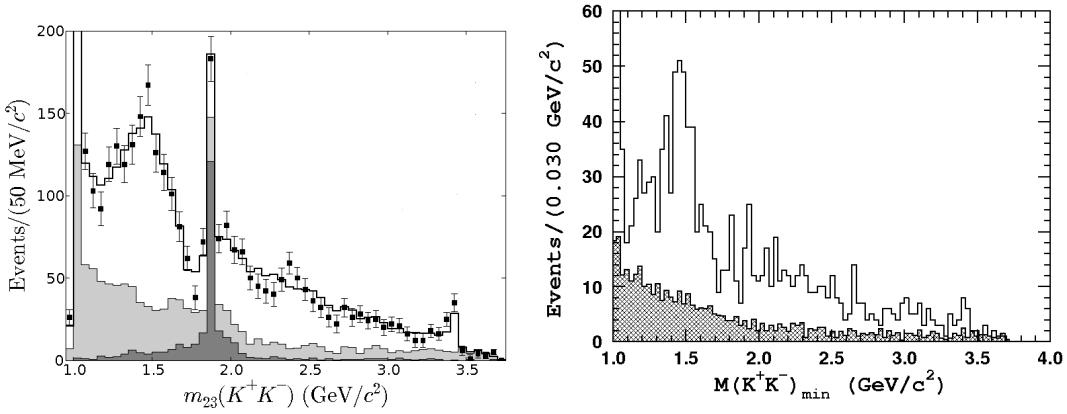

Figure 3.6: Projections of the $\mathrm{m_{KK}}$ invariant mass from the $\mathrm{B^{\pm} \to K^{\pm}K^{+}K^{-}}$ *BABAR* analysis [24] on the left and the Belle analysis [29] on the right. Due to interference the fitted values of the masses do not necessarily coincide with the peaks in the mass spectra.

component). If the $\mathrm{f_X(1500)}$ contributes to the decay of $\mathrm{B^0 \to K^0_s K^0_s K^0_s}$ this would have an impact on the $\mathcal{C}$ measurement and possibly the $\mathcal{S}$ measurement, as we measure an average of the $\mathcal{C}$ and $\mathcal{S}$ parameters of all the contributing resonances.
Another interesting aspect is that lattice QCD studies [31] indicate that the mass of the lightest scalar glueball lies at $\sim$1.5-1.7 GeV, and the $\mathrm{f_X(1500)}$ would be a candidate. This hypothesis could be tested using semi-leptonic decays or decays that include a J/ψ in the final state [32]. The scalar nature of the $\mathrm{f_X(1500)}$ is also controversial. The BES collaboration has observed a vector resonance at the same invariant mass in the KK spectrum [33]. If the $\mathrm{f_X(1500)}$ is a scalar resonance, it should contribute to the final state in $\mathrm{B^0 \to K^0_s K^0_s K^0_s}$. An observation would confirm the scalar nature, while a non-observation would play in favor of a vector resonance. Even though the decay channel is statistically limited, especially for an amplitude analysis, the result of the present study has more weight than other statistically comparable analyses, as here vector contributions are forbidden by angular momentum conservation.

3.3 3-body decays

3.3.1 Kinematics and Dalitz plot formalism

A Dalitz Plot (DP) is a purely kinematical description of a three body decay. In the case of this work, a spin-zero $\mathrm{B^0}$ meson with momentum $\mathrm{p_B}$ and mass $\mathrm{m_B}$ decays into three $\mathrm{K^0_s}$ pseudoscalar mesons with four-momenta $\mathrm{p_1}$, $\mathrm{p_2}$ and $\mathrm{p_3}$, masses $\mathrm{m_1}$, $\mathrm{m_2}$ and $\mathrm{m_3}$ and energies $\mathrm{E_1}$, $\mathrm{E_2}$ and $\mathrm{E_3}$. A priori there are 12 unknowns among the components of the four-momentum vectors of the particles in the final state. This number can be reduced by including several constraints:

- The masses of all final state particles are known (three constraints)
- Energy-momentum is conserved for the individual rows in the four-vectors (four constraints)

This leaves us with with 5 independent variables. Defining the invariant mass variable:

$$\mathrm{s_{ij}} = (\mathrm{p_i} + \mathrm{p_j})^2 \,, \tag{3.6}$$

energy-momentum conservation implies the following relation

$$\mathrm{s_{12}} + \mathrm{s_{23}} + \mathrm{s_{13}} = \mathrm{m_B^2} + \mathrm{m_1^2} + \mathrm{m_2^2} + \mathrm{m_3^2} \,, \tag{3.7}$$

where we can see that the third invariant mass is fully determined by the other two. In the $\mathrm{B^0}$ rest frame we can write

$$\begin{aligned} \mathrm{s_{ij}} &= (\mathrm{p_B} - \mathrm{p_k})^2 = \mathrm{m_B^2} + \mathrm{m_k^2} - 2\mathrm{m_B E_k} & (3.8) \\ &= (\mathrm{p_i} + \mathrm{p_j})^2 = \mathrm{m_i^2} + \mathrm{m_j^2} + 2\mathrm{E_i E_j} - 2|\vec{\mathrm{p_i}}||\vec{\mathrm{p_j}}|\cos(\theta_{\mathrm{ij}}) & (3.9) \end{aligned}$$

where $\cos(\theta_{\mathrm{ij}})$ is the angle between the 3-momenta $\vec{\mathrm{p_i}}$ and $\vec{\mathrm{p_j}}$. $\cos(\theta_{\mathrm{ij}})$ is a helicity angle and will be used later on to define the square Dalitz plot (Sec. 3.3.7). In the $\mathrm{B^0}$ rest frame, due to momentum conservation, the K^0_s momenta lie in a plane with arbitrary inclination and the relative angles between them are determined by their energy (compare Eq. 3.8). As we are not interested in the inclination of this plane that corresponds to three degrees of freedom, two quantities are sufficient to describe the kinematics of the decay, for instance two invariant masses. The two-dimensional scatter-plot of two invariant masses, for instance $\mathrm{s_{12}}, \mathrm{s_{13}}$, is called a Dalitz plot (DP). From now on we choose ($\mathrm{s_{12}}$,$\mathrm{s_{13}}$) to parametrize the DP.

The decay of a particle is described by its decay rate $\mathrm{d}\Gamma$, which is the probability of decay per unit of time to a given final state. The decay rate takes into account the phase space of the decay, meaning that in principle one needs to integrate over all momenta in the final state. We saw earlier, that all the kinematical information is contained for, instance in, $\mathrm{s_{12}}$ and $\mathrm{s_{13}}$ and we can write

$$\mathrm{d}\Gamma \propto |\mathcal{A}|^2 \mathrm{d s_{12} d s_{13}} \tag{3.10}$$

where all the decay dynamics are described by the amplitude $\mathcal{A}$. What we actually need to model for a Dalitz plot analysis, is $\mathcal{A}(\mathrm{s_{12}}, \mathrm{s_{13}})$ and what we observe is $|\mathcal{A}(\mathrm{s_{12}}, \mathrm{s_{13}})|^2$. In other words, a Dalitz plot displays the decay probability as a function of two squared invariant masses, which constitute the phase-space of the decay.
To get a better insight of the decay kinematics we look at the DP boundaries, which can be calculated using Eq. 3.8. When the two particles 1 and 2 are flying back to back, the maximum of their invariant mass $\mathrm{s_{12}}$ for a given mass $\mathrm{s_{23}}$ is reached. The invariant mass is minimal when they fly parallel in the same direction. Close to the kinematical limits of the DP, one of the invariant masses takes a small value, while in the central region of the DP all invariant masses have comparable values. The momentum of the particles vary as a function of the DP position and from Eq. 3.8 one can see that the momentum of one of the particles

reaches low values when approaching the DP corners. This variation of momentum has an impact of the reconstruction efficiency, i.e. the reconstruction efficiency depends on the DP position and this dependence is used to compute the acceptance corrected (signal) Dalitz plot (see Sec. 9.3).

3.3.2 The isobar model

The isobar model [34] describes $\mathcal{A}$ as a sum of quantum mechanical amplitudes

$$\mathcal{A}(\mathrm{s}_{12},\mathrm{s}_{13}) = \sum_{\mathrm{j}=1}^{\mathrm{N}} \mathrm{c_j F_j}(\mathrm{s}_{12},\mathrm{s}_{13}) \,, \tag{3.11}$$

$$\overline{\mathcal{A}}(s_{12},s_{13}) = \sum_{\mathrm{j}=1}^{\mathrm{N}} \bar{\mathrm{c}}_\mathrm{j} \overline{\mathrm{F}}_\mathrm{j}(\mathrm{s}_{12},\mathrm{s}_{13}) \,, \tag{3.12}$$

where $\mathrm{F_j}(\mathrm{s}_{12},\mathrm{s}_{13})$ are Dalitz plot dependent dynamical amplitudes (propagators) described in the following, and $\mathrm{c_j}$ are complex coupling constants that contain the relative weak magnitudes and phases of the different decay channels. $\overline{\mathcal{A}}$ is the decay amplitude of the CP conjugate state, i.e. the $\bar{\mathrm{B}}^0$. A Dalitz plot or amplitude analysis aims for extracting these coupling constants. This is feasible when there is interference between the different isobars, i.e. they occupy, at least partly, the same phase space. The interference pattern that is an observable gives access to the underlying dynamics.
One possible parameterization of the complex coupling constants is:

$$\mathrm{c_i} = \mathrm{a_i} \mathrm{e}^{\mathrm{i}(\delta_\mathrm{i}+\phi_\mathrm{i})}(1+\frac{\mathrm{b_i}}{\mathrm{a_i}}) \tag{3.13}$$

$$\bar{\mathrm{c}}_\mathrm{i} = \mathrm{a_i} \mathrm{e}^{\mathrm{i}(\delta_\mathrm{i}-\phi_\mathrm{i})}(1-\frac{\mathrm{b_i}}{\mathrm{a_i}}) \tag{3.14}$$

where δ_i are CP even (or strong) phases and ϕ_i are CP odd (or weak) phases. In this work we perform a CP averaged DP analysis, i.e. we set $\phi_\mathrm{i} = \mathrm{b_i} = 0$ or $\mathrm{c_i} = \bar{\mathrm{c}}_\mathrm{i}$. This means we do not use any tagging information for the amplitude analysis. All the weak phase dependence is contained in $\mathrm{c_j}$, and $\mathrm{F_j}(\mathrm{s}_{12},\mathrm{s}_{13})$ contains strong dynamics only, therefore

$$\mathrm{F_j}(\mathrm{s}_{12},\mathrm{s}_{13}) = \overline{\mathrm{F}}_\mathrm{j}(\mathrm{s}_{12},\mathrm{s}_{13}) \,. \tag{3.15}$$

The resonance dynamics are contained within the $\mathrm{F_j}$ term, which is represented by the product of the invariant mass and angular distributions,

$$\mathrm{F_j^L}(\mathrm{s}_{12},\mathrm{s}_{13}) = \mathrm{R_j}(\mathrm{m}) \times \mathrm{X_L}(|\vec{\mathrm{p}}^{\,\star}|\,\mathrm{r}) \times \mathrm{X_L}(|\vec{\mathrm{q}}\,|\,\mathrm{r}) \times \mathrm{T_j}(\mathrm{L},\vec{\mathrm{p}},\vec{\mathrm{q}}), \tag{3.16}$$

where

- $\mathrm{m} \equiv \sqrt{\mathrm{s_{ij}}}$ is the invariant mass of the two decay products of the resonance;
- $\mathrm{R_j}(\mathrm{x})$ is the resonance mass term or "lineshape" (e.g. Breit–Wigner);

- $\mathrm{T_j}(\mathrm{L}, \vec{\mathrm{p}}, \vec{\mathrm{q}})$ is the angular probability distribution;
- $\mathrm{X_L}$ are the barrier factors with parameter r, described below;
- $\vec{\mathrm{p}}^{\star}$ is the momentum of the bachelor particle[1] evaluated in the rest frame of the B;
- $\vec{\mathrm{p}}$ and $\vec{\mathrm{q}}$ are the momenta of the bachelor particle and one of the resonance daughters respectively, both evaluated in the rest frame of the resonance,
- L is the orbital angular momentum between the resonance and the bachelor.

$|\mathcal{A}(\mathrm{s_{12}}, \mathrm{s_{13}})|^2$ needs to be normalized to be used as a PDF. The integral $|\mathcal{A}(\mathrm{s_{12}}, \mathrm{s_{13}})|^2 \mathrm{ds_{12}ds_{13}}$ can be expressed as a function of bilinear terms $\langle \mathrm{F_\mu F^*_\nu} \rangle$, that are computed by a numerical integration.

$$|\mathcal{A}(\mathrm{s_{12}}, \mathrm{s_{13}})|^2 \mathrm{ds_{12}ds_{13}} = \sum_{\mu\nu} (\mathrm{c_\mu c^*_\nu} + \mathrm{\overline{c}_\mu \overline{c}^*_\nu}) \langle \mathrm{F_\mu F^*_\nu} \rangle \ , \tag{3.17}$$

where

$$\langle \mathrm{F_\mu F^*_\nu} \rangle = \int_{\mathrm{DP}} \mathrm{F_\mu F^*_\nu d(s_{12}, s_{13})} \ . \tag{3.18}$$

The model is approximate in the sense that it assumes that there is only one point-like interaction between the particles in the final state, and the strength of this coupling is given by the coupling constants $\mathrm{c_j}$. Final state re-scattering effects are neglected. The model also violates unitarity and for precision measurements the K-matrix formalism [35] is better adapted to describe the s-wave contribution, as it is based on the unitarity of the S-matrix. In this work the advantages of using the isobar formalism, namely the fact that *BABAR* simulation for charmless 3-body decays is generated using the isobar model and its relatively easy implementation, outweighs the advantages of the K-matrix formalism.
To summarize, by fitting $|\mathcal{A}|^2$ we have access to the underlying amplitude $\mathcal{A}$. By modeling the total 3-body amplitude using the isobar model, we have access to the relative amplitudes and phases as we are sensitive to the effects of the interference between them. It is important to mention that this is a relative measurement as what we measure is the normalized distribution of $|\mathcal{A}|^2$ and we have to choose one magnitude and phase arbitrarily. The numerical values of the magnitudes and phases have no physical meaning, only the phase differences and the fit fractions do (fit fraction is defined in Sec. 3.3.8).

3.3.3 Mass term description

We use the following mass term descriptions:

[1] It is not straight-forward to define a bachelor particle when there are three identical particles. When we symmetrize the amplitude in Sec. 3.3.6, we use the minimum and the maximum of the invariant masses to uniquely define a DP position. Only two 4-momenta are used to calculate an invariant mass; the particle corresponding to the 4-momentum that is not used for the calculation of the minimum (or the maximum) invariant mass is defined as the bachelor particle. The particles corresponding to the 4-momenta that have been used for the calculation are called daughter particles of the resonance

- The Relativistic Breit-Wigner (RBW) [12] line-shape is the relativistic generalization of the commonly used Breit-Wigner mass term formula and is given by:

$$\mathrm{R_j^J(m)} = \frac{1}{(\mathrm{m_j^0})^2 - \mathrm{m}^2 - \mathrm{i m_j^0 \Gamma_j^J(m)}} \,, \tag{3.19}$$

where m is the invariant mass of the two-daughter combination, $\mathrm{m_j^0}$ is the resonance pole mass and $\mathrm{\Gamma_j^J(m)}$ is the mass-dependent width, defined by

$$\mathrm{\Gamma_j^J(m)} = \mathrm{\Gamma_j^0} \left(\frac{|\mathbf{q}|}{|\mathbf{q_0}|} \right)^{2\mathrm{J}+1} \left(\frac{\mathrm{m_j^0}}{\mathrm{m}} \right) \mathrm{X_J^2}(|\mathbf{q}|\mathrm{r_j}) \,, \tag{3.20}$$

where $\mathrm{\Gamma_j^0} = \mathrm{\Gamma_j^J(m_j^0)}$ is the resonance decay width, the $|\mathbf{q_0}|$ symbol denotes the value of $|\mathbf{q}|$ when $\mathrm{m} = \mathrm{m_j^0}$ and J is the spin of the resonance.

- The Flatté line-shape [12] is a phenomenological description that takes into account the opening of thresholds which is not accounted for by the RBW mass term description. We use this description for the $\mathrm{f_0(980)}$ resonance whose main decay modes are $\mathrm{f_0(980)} \rightarrow \pi\pi$ and $\mathrm{f_0(980)} \rightarrow \mathrm{KK}$. The mass of the KK system at rest is $\sim 1GeV$, i.e. within the width of the resonance. Events that decay through the $\mathrm{f_0(980)}$ resonance with masses below this threshold proceed essentially to the $\pi\pi$ final state, while events above threshold can also decay to the KK final state. This behavior leads to an asymmetric mass term that is described by the Flatté line-shape given by

$$\mathrm{R_j^J(m)} = \frac{1}{(\mathrm{m_j^0})^2 - \mathrm{m}^2 - \mathrm{i m_j^0}(\mathrm{\Gamma_{\pi\pi}(m)} + \mathrm{\Gamma_{KK}(m)})} \,, \tag{3.21}$$

where the symbols previously defined are used. The decay widths of the resonance in the $\pi\pi$ and KK final states are given by:

$$\mathrm{\Gamma_{\pi\pi}(m)} = \mathrm{g_\pi} \left(\frac{1}{3}\sqrt{1 - 4\mathrm{m}^2_{\pi^0}/\mathrm{m}^2} + \frac{2}{3}\sqrt{1 - 4\mathrm{m}^2_{\pi^+}/\mathrm{m}^2} \right) \,, \tag{3.22}$$

$$\mathrm{\Gamma_{KK}(m)} = \mathrm{g_K} \left(\frac{1}{2}\sqrt{1 - 4\mathrm{m}^2_{\mathrm{K}^+}/\mathrm{m}^2} + \frac{1}{2}\sqrt{1 - 4\mathrm{m}^2_{\mathrm{K}^0}/\mathrm{m}^2} \right) \,, \tag{3.23}$$

where $\mathrm{g_\pi}$ and $\mathrm{g_K}$ are coupling constants for which the following values from the BES experiment [36] are used

$$\begin{array}{rcl} \mathrm{g_\pi} & = & 0.165\,\mathrm{GeV/c^2}, \\ \mathrm{g_K} & = & 0.695\,\mathrm{GeV/c^2}. \end{array} \tag{3.24}$$

- Non-resonant (NR) contributions to the decay are described by an effective model. It is almost flat with a slight rise at low mass that can account for the tails of resonances far below threshold, e.g. $\mathrm{f_0(600)}$:

$$\mathrm{NR(m)} = \mathrm{A e^{\alpha m}} \,. \tag{3.25}$$

The values for the mass term parameters can be found in the amplitude analysis chapter (Chapter. 9, Tab. 9.2).

3.3.4 Barrier factors

The functions $\mathrm{X_J}$ are the nuclear *Blatt-Weisskopf penetration factors* [37]. They are semi-classical and are motivated by the potential $\hbar \mathrm{J}(\mathrm{J}+1)/(2\mathrm{m}\rho^2)$ occurring in the Schrödinger equation, expressed in the spherical coordinates, for the scattering of a particle with orbital angular momentum $\mathrm{J} > 0$ in a central field. The repulsive potential is equivalent to a rotation energy, and can thus be denoted as *centrifugal barrier*. For growing J or decreasing radial distance ρ, the centrifugal barrier increases, which entails a decreasing transition probability. One empirically determines a radial distance, called *interaction radius*, r, of the resonance, which separates an outside region (with respect to the centrifugal barrier), with little interaction, from an inside region where the interaction between the particles is strong [38]. The transition coefficients of the centrifugal barrier are the Blatt-Weisskopf factors. They are derived using spherical Bessel and Hankel functions and read from the lowest orbital momenta (spins):

$$\begin{aligned} \mathrm{X_{J=0}(z)} &= 1\,, \\ \mathrm{X_{J=1}(z)} &= \sqrt{\frac{1+\mathrm{z_0^2}}{1+\mathrm{z^2}}}\,, \\ \mathrm{X_{J=2}(z)} &= \sqrt{\frac{\mathrm{z_0^4}+3\mathrm{z_0^2}+9}{\mathrm{z^4}+3\mathrm{z^2}+9}}\,, \end{aligned} \tag{3.26}$$

where $\mathrm{z_0}$ represents the value of z (which is equal to $|\tilde{\mathrm{q}}|\mathrm{r}$ or $|\tilde{\mathrm{p}}^*|\mathrm{r}$ in Eq. 3.16) when the invariant mass is equal to the pole mass of the resonce. This factor only has an effect for $\mathrm{J} > 0$, i.e. in this work it is only used for the $\mathrm{f_2}(2010)$ resonance (see Chap. 9).

3.3.5 Angular distribution

The angular distribution depends on the spin of the resonance. For a B meson decay into a scalar resonance there is no preferential direction and the angular distribution is given by

$$\mathrm{T_j(J=0,\vec{p},\vec{q}) = 1}\,. \tag{3.27}$$

For a tensor particle it is given by

$$\mathrm{T_j(J=2,\vec{p},\vec{q}) = \frac{4}{3}[(3(\vec{p}\cdot\vec{q})^2 - (|\vec{p}||\vec{q}|)^2]}\,. \tag{3.28}$$

It this work it is not important which one of the daughters is chosen for this calculation, this is to say $\vec{\mathrm{q}}$ can be the momentum of either resonance daughter. As the amplitude is symmetric under exchange of any pair of $\mathrm{K^0_s}$, the two possible choices are equivalent (see Sec. 3.3.7).

3.3.6 Symmetrized amplitude

In the decay $\mathrm{B^0 \to K^0_s K^0_s K^0_s}$ it is not straightforward to model the amplitude for two reasons. Firstly, the dynamics of intermediate resonances are described in terms of the flavor states

K^0 and $\overline{\mathrm{K}}^0$, that we do not reconstruct in the detector. Secondly the three particles in the final state are identical, and the amplitude needs to be symmetrized to take this into account. When we reconstruct neutral kaons in a detector, we detect the mass eigenstates K^0_s and K^0_L. In the case of this analysis we reconstruct K^0_s that have *CP* eigenvalue +1, as we reconstruct them from pairs of pions. Our requirements on the decay length remove basically all K^0_L that decayed to two pions.
The reconstructed K^0_s are superpositions of K^0 and $\overline{\mathrm{K}}^0$:

$$\mathrm{K}^0_\mathrm{s} = \frac{1}{\sqrt{2}}(\mathrm{K}^0 + \overline{\mathrm{K}}^0)\ . \tag{3.29}$$

We want to write down the decay amplitude

$$\mathcal{A}[\mathrm{B}^0 \to \mathrm{K}^0_\mathrm{s}(\mathrm{p}_1)\mathrm{K}^0_\mathrm{s}(\mathrm{p}_2)\mathrm{K}^0_\mathrm{s}(\mathrm{p}_3)] = \langle \mathrm{K}^0_\mathrm{s}(\mathrm{p}_1)\mathrm{K}^0_\mathrm{s}(\mathrm{p}_2)\mathrm{K}^0_\mathrm{s}(\mathrm{p}_3)|\mathrm{H}_\mathrm{Eff}|\mathrm{B}^0\rangle \tag{3.30}$$

where we distinguish the three K^0_s by their momenta. To describe intermediate resonances, we project on the flavor states:

$$\begin{aligned}&\mathrm{K}^0_\mathrm{s}(\mathrm{p}_1)\mathrm{K}^0_\mathrm{s}(\mathrm{p}_2)\mathrm{K}^0_\mathrm{s}(\mathrm{p}_3) = \\ &\frac{1}{\sqrt{2}}[\mathrm{K}^0(\mathrm{p}_1) + \overline{\mathrm{K}}^0(\mathrm{p}_1)]\frac{1}{\sqrt{2}}[\mathrm{K}^0(\mathrm{p}_2) + \overline{\mathrm{K}}^0(\mathrm{p}_2)]\frac{1}{\sqrt{2}}[\mathrm{K}^0(\mathrm{p}_3) + \overline{\mathrm{K}}^0(\mathrm{p}_3)]\end{aligned} \tag{3.31}$$

and develop the equation. We get

$$\begin{aligned}\mathcal{A}[\mathrm{B}^0 \to \mathrm{K}^0_\mathrm{s}(\mathrm{p}_1)\mathrm{K}^0_\mathrm{s}(\mathrm{p}_2)\mathrm{K}^0_\mathrm{s}(\mathrm{p}_3)] \ &\propto\ \langle \mathrm{K}^0(\mathrm{p}_1)\mathrm{K}^0(\mathrm{p}_2)\mathrm{K}^0(\mathrm{p}_3)|\mathrm{H}_\mathrm{Eff}|\mathrm{B}^0\rangle && (3.32)\\ &+\ \langle \overline{\mathrm{K}}^0(\mathrm{p}_1)\mathrm{K}^0(\mathrm{p}_2)\mathrm{K}^0(\mathrm{p}_3)|\mathrm{H}_\mathrm{Eff}|\mathrm{B}^0\rangle \\ &+\ \langle \overline{\mathrm{K}}^0(\mathrm{p}_1)\overline{\mathrm{K}}^0(\mathrm{p}_2)\mathrm{K}^0(\mathrm{p}_3)|\mathrm{H}_\mathrm{Eff}|\mathrm{B}^0\rangle && (3.33)\\ &+\ \langle \mathrm{K}^0(\mathrm{p}_1)\overline{\mathrm{K}}^0(\mathrm{p}_2)\mathrm{K}^0(\mathrm{p}_3)|\mathrm{H}_\mathrm{Eff}|\mathrm{B}^0\rangle \\ &+\ \langle \overline{\mathrm{K}}^0(\mathrm{p}_1)\mathrm{K}^0(\mathrm{p}_2)\overline{\mathrm{K}}^0(\mathrm{p}_3)|\mathrm{H}_\mathrm{Eff}|\mathrm{B}^0\rangle && (3.34)\\ &+\ \langle \mathrm{K}^0(\mathrm{p}_1)\mathrm{K}^0(\mathrm{p}_2)\overline{\mathrm{K}}^0(\mathrm{p}_3)|\mathrm{H}_\mathrm{Eff}|\mathrm{B}^0\rangle \\ &+\ \langle \overline{\mathrm{K}}^0(\mathrm{p}_1)\overline{\mathrm{K}}^0(\mathrm{p}_2)\mathrm{K}^0(\mathrm{p}_3)|\mathrm{H}_\mathrm{Eff}|\mathrm{B}^0\rangle && (3.35)\\ &+\ \langle \overline{\mathrm{K}}^0(\mathrm{p}_1)\overline{\mathrm{K}}^0(\mathrm{p}_2)\overline{\mathrm{K}}^0(\mathrm{p}_3)|\mathrm{H}_\mathrm{Eff}|\mathrm{B}^0\rangle.\end{aligned}$$

Due to strangeness conservation, all terms that do not contain exactly two K^0 and one $\overline{\mathrm{K}}^0$ vanish when they are contracted, and this yields the expression:

$$\begin{aligned}\mathcal{A}[\mathrm{B}^0 \to \mathrm{K}^0_\mathrm{s}(\mathrm{p}_1)\mathrm{K}^0_\mathrm{s}(\mathrm{p}_2)\mathrm{K}^0_\mathrm{s}(\mathrm{p}_3)] \ &=\ (\frac{1}{2})^{3/2}\{\langle \overline{\mathrm{K}}^0(\mathrm{p}_1)\mathrm{K}^0(\mathrm{p}_2)\mathrm{K}^0(\mathrm{p}_3)|\mathrm{H}_\mathrm{Eff}|\mathrm{B}^0\rangle && (3.36)\\ &+\ \langle \mathrm{K}^0(\mathrm{p}_1)\overline{\mathrm{K}}^0(\mathrm{p}_2)\mathrm{K}^0(\mathrm{p}_3)|\mathrm{H}_\mathrm{Eff}|\mathrm{B}^0\rangle \\ &+\ \langle \mathrm{K}^0(\mathrm{p}_1)\mathrm{K}^0(\mathrm{p}_2)\overline{\mathrm{K}}^0(\mathrm{p}_3)|\mathrm{H}_\mathrm{Eff}|\mathrm{B}^0\rangle\}.\end{aligned}$$

We identify three paths from the initial state to the final state:

$$\begin{aligned}\mathcal{A}_1[\mathrm{B}^0 \to \overline{\mathrm{K}}^0(\mathrm{p}_1)\mathrm{K}^0(\mathrm{p}_2)\mathrm{K}^0(\mathrm{p}_3)] \ &=\ \langle \overline{\mathrm{K}}^0(\mathrm{p}_1)\mathrm{K}^0(\mathrm{p}_2)\mathrm{K}^0(\mathrm{p}_3)|\mathrm{H}_\mathrm{Eff}|\mathrm{B}^0\rangle && (3.37)\\ \mathcal{A}_2[\mathrm{B}^0 \to \overline{\mathrm{K}}^0(\mathrm{p}_2)\mathrm{K}^0(\mathrm{p}_3)\mathrm{K}^0(\mathrm{p}_1)] \ &=\ \langle \mathrm{K}^0(\mathrm{p}_1)\overline{\mathrm{K}}^0(\mathrm{p}_2)\mathrm{K}^0(\mathrm{p}_3)|\mathrm{H}_\mathrm{Eff}|\mathrm{B}^0\rangle && (3.38)\\ \mathcal{A}_3[\mathrm{B}^0 \to \overline{\mathrm{K}}^0(\mathrm{p}_3)\mathrm{K}^0(\mathrm{p}_1)\mathrm{K}^0(\mathrm{p}_2)] \ &=\ \langle \mathrm{K}^0(\mathrm{p}_1)\mathrm{K}^0(\mathrm{p}_2)\overline{\mathrm{K}}^0(\mathrm{p}_3)|\mathrm{H}_\mathrm{Eff}|\mathrm{B}^0\rangle, && (3.39)\end{aligned}$$

where the index n in $\mathcal{A}_n$ stands for the momentum that comes from the $\overline{\mathrm{K}}^0$.
The coherent sum in Eq. 3.36 corresponds to formula (2.24) in [26]:

$$\begin{aligned}\mathcal{A}[\mathrm{B}^0 \to \mathrm{K}^0_\mathrm{s}(\mathrm{p}_1)\mathrm{K}^0_\mathrm{s}(\mathrm{p}_2)\mathrm{K}^0_\mathrm{s}(\mathrm{p}_3)] &= \frac{1}{2}^{3/2}\{\mathcal{A}_1[\mathrm{B}^0 \to \overline{\mathrm{K}}^0(\mathrm{p}_1)\mathrm{K}^0(\mathrm{p}_2)\mathrm{K}^0(\mathrm{p}_3)] \\ &+ \mathcal{A}_2[\mathrm{B}^0 \to \overline{\mathrm{K}}^0(\mathrm{p}_2)\mathrm{K}^0(\mathrm{p}_3)\mathrm{K}^0(\mathrm{p}_1)] \\ &+ \mathcal{A}_3[\mathrm{B}^0 \to \overline{\mathrm{K}}^0(\mathrm{p}_3)\mathrm{K}^0(\mathrm{p}_1)\mathrm{K}^0(\mathrm{p}_2)]\}.\end{aligned} \tag{3.40}$$

We show a simple example to illustrate how this amplitude translates into the isobar model. In the case when there is only the f_0 resonance, we can write isobar amplitudes with $\{\mathrm{K}^0, \overline{\mathrm{K}}^0\}$ resonances only:

$$\mathcal{A}_1 = \mathrm{c_{f_0}} \cdot \mathrm{F_{f_0}(p1, p2)} + \mathrm{c_{f_0}} \cdot \mathrm{F_{f_0}(p1, p3)} \tag{3.41}$$
$$\mathcal{A}_2 = \mathrm{c_{f_0}} \cdot \mathrm{F_{f_0}(p2, p3)} + \mathrm{c_{f_0}} \cdot \mathrm{F_{f_0}(p1, p2)} \tag{3.42}$$
$$\mathcal{A}_3 = \mathrm{c_{f_0}} \cdot \mathrm{F_{f_0}(p1, p3)} + \mathrm{c_{f_0}} \cdot \mathrm{F_{f_0}(p2, p3)} \tag{3.43}$$

We insert Eqs. 3.41, 3.42 and 3.43 into Eq. 3.40 and obtain the total amplitude of this simplified decay,

$$\mathcal{A}[\mathrm{B}^0 \to \mathrm{K}^0_\mathrm{s}(\mathrm{p}_1)\mathrm{K}^0_\mathrm{s}(\mathrm{p}_2)\mathrm{K}^0_\mathrm{s}(\mathrm{p}_3)] \sim \mathrm{c_{f_0}}\cdot\mathrm{F_{f_0}(p1, p2)}+\mathrm{c_{f_0}}\cdot\mathrm{F_{f_0}(p1, p3)}+\mathrm{c_{f_0}}\cdot\mathrm{F_{f_0}(p2, p3)}. \tag{3.44}$$

For now we have only used the fact that we do not know if a given K^0_s comes from an intermediate K^0 or $\overline{\mathrm{K}}^0$. To distinguish between the different K^0_s we have used the momenta as label. In reality, as the three K^0_s are identical particles, there is no way to distinguish them. It is completely arbitrary which momentum is noted momentum 1, 2 or 3. In case of non-distinguishable particles, in our case bosons, the amplitude needs to be symmetrized by summing all the possible permutations of the momenta. We have 3!=6 possibilities to exchange the labels of the K^0_s. A DP point is well defined by two invariant masses. We can decide, for instance, to look at the DP that is defined by the invariant masses s_{12} and s_{23}. In this case the symmetrized amplitude is given by

$$\begin{aligned}\mathcal{A}^{\mathrm{sym}}(\mathrm{s_{12}, s_{13}}) = \sum_{\mathrm{k=1}}^{\mathrm{N}} \mathrm{c_k}[\mathcal{A}(\mathrm{s_{12}, s_{13}}) &+ \mathcal{A}(\mathrm{s_{13}, s_{12}}) + \\ \mathcal{A}(\mathrm{s_{12}, s_{23}}) &+ \mathcal{A}(\mathrm{s_{23}, s_{12}}) + \\ \mathcal{A}(\mathrm{s_{13}, s_{23}}) &+ \mathcal{A}(\mathrm{s_{23}, s_{13}})].\end{aligned} \tag{3.45}$$

Eq. 3.45 describes the six-fold ambiguity of placing a given event on the DP. To illustrate the meaning of the sum of six terms, we can consider the simple case where there is only a contribution from one resonance, for instance $\mathrm{f_0(980)K^0_s}$. This resonance will give three bands along the three edges of the Dalitz plane. If we compute the amplitude for a point in the resonance band, the six terms correspond to 2 contributions from each of the 3 $\mathrm{f_0(980)K^0_s}$ bands. In the following, we order the invariant masses from the biggest one

$s_{\max} = \max(s_{12}, s_{13}, s_{23})$ to the smallest one $s_{\min} = \min(s_{12}, s_{13}, s_{23})$. With this approach, each candidate has a uniquely defined position on the Dalitz plot that, explicitly, is given in terms of $s_{\max}$ versus $s_{\min}$. Using this convention, the surface of the resulting Dalitz plane is a sixth of the surface obtained with a random numbering of the final state particles, as can be seen on the left hand side of Fig. 3.7. Another way to look at this problem is to say that each event engender 6 points in the Dalitz plane due to the exchange degeneracy. An interesting feature of this 6-fold Dalitz plane defined in terms of $s_{\max}$ versus $s_{\min}$ is that each s_{ij} band is "bounced back" by the inner symmetry axis. Therefore a narrow resonance will give a broken band (with two break points) instead of one straight band. In the case where the flavor of the B is known at some measured time $\Delta\mathrm{t}$ wrt the decay, the decay rate over the Dalitz plot can be written according to the usual equation used in time dependent Dalitz plot analysis. The fact that the $3\mathrm{K}^0_\mathrm{s}$ final state comes from the two intermediate states $\mathrm{K}^0\mathrm{K}^0\bar{\mathrm{K}}^0$ and $\mathrm{K}^0\bar{\mathrm{K}}^0\bar{\mathrm{K}}^0$ does not influence any expression as both give the final state of $3K^0_s$. The $\mathcal{A}$ and $\overline{\mathcal{A}}$ amplitudes are defined with respect to the flavor of the decaying B meson.

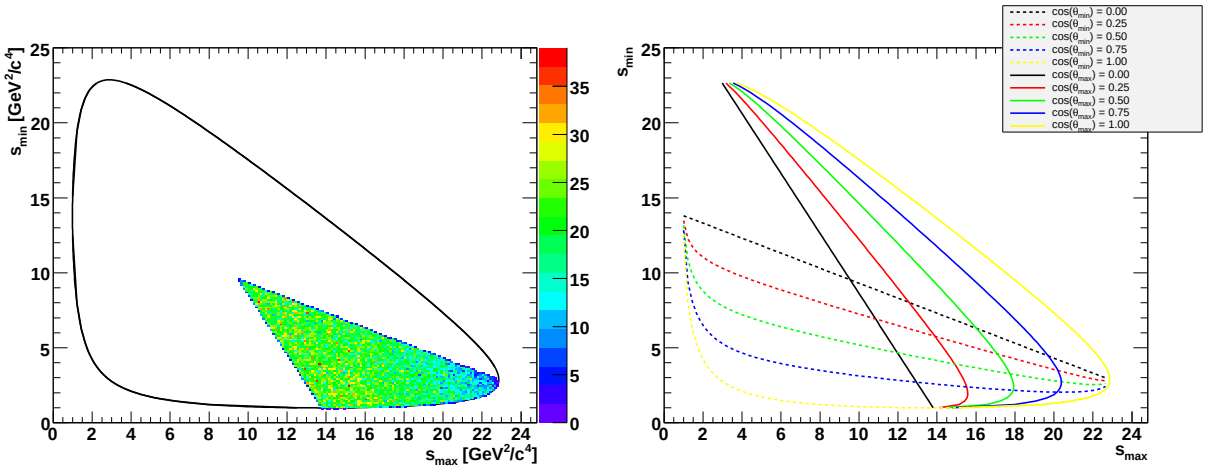

Figure 3.7: On the left are shown events taken from phasespace Monte Carlo after symmetrization. The black line is kinematical limit of the regular DP. On the right we show iso-helicity lines in the regular Dalitz plot. The lines intersect in the region of the symmetrized Dalitz plot and give a uniquely defined square Dalitz position.

3.3.7 Square Dalitz plot (SDP)

We use two-dimensional binned PDFs in our model to describe the phase-space dependent reconstruction efficiency and to model the Dalitz plot continuum PDF. When the phase-space boundaries of the DP do not coincide with the histogram boundaries this may introduce biases. We therefore define $\mathrm{h}_{\min}$ and $\mathrm{h}_{\max}$ as $\cos\theta_{\min}$ and $\cos\theta_{\max}$, respectively, and apply the transformation

$$\mathrm{ds}_{\min}\,\mathrm{ds}_{\max} \longrightarrow |\mathrm{J}|\,\mathrm{dh}_{\min}\,\mathrm{dh}_{\max}\ , \tag{3.46}$$

which defines the square Dalitz plot (SDP). $\mathrm{h_{min}}$ and $\mathrm{h_{max}}$ are given by

$$\mathrm{h_{min}} = \cos(\theta_{\mathrm{min}}(\mathrm{s_{min}}, \mathrm{s_{max}})) = \\ -\frac{-2\mathrm{s_{max}} - \mathrm{s_{min}} + \mathrm{m_B^2} + 3\mathrm{m_K^2}}{(\frac{\mathrm{s_{min}} - 4\mathrm{m_K^2}}{\mathrm{s_{min}}})^{\frac{1}{2}} \cdot (\mathrm{m_B^4} - 2\mathrm{m_B^2 s_{min}} - 2\mathrm{m_B^2 m_K^2} + \mathrm{s_{min}^2} - 2\mathrm{m_K^2 s_{min}} + \mathrm{m_K^4})^{\frac{1}{2}}} \tag{3.47}$$

$$\mathrm{h_{max}} = \cos(\theta_{\mathrm{max}}(\mathrm{s_{min}}, \mathrm{s_{max}})) = \\ \frac{-2\mathrm{s_{min}} - \mathrm{s_{max}} + \mathrm{m_B^2} + 3\mathrm{m_K^2}}{(\frac{\mathrm{s_{max}} - 4\mathrm{m_K^2}}{\mathrm{s_{max}}})^{\frac{1}{2}} \cdot (\mathrm{m_B^4} - 2\mathrm{m_B^2 s_{max}} - 2\mathrm{m_B^2 m_K^2} + \mathrm{s_{max}^2} - 2\mathrm{m_K^2 s_{max}} + \mathrm{m_K^4})^{\frac{1}{2}}} \tag{3.48}$$

J is the Jacobian of the transformation. The value of the Jacobian J as function of the SDP variables is shown in Fig. 3.8, both $\mathrm{h_{min}}$ and $\mathrm{h_{max}}$ range between 0 and 1. While J is straightforward to obtain, the backward transformation

$$\mathrm{dh_{min}}\,\mathrm{dh_{max}} \longrightarrow \frac{1}{|\mathrm{J}|}\,\mathrm{ds_{min}}\,\mathrm{ds_{max}}\,, \tag{3.49}$$

cannot be solved analytically. We use a numerical procedure involving the Newton method. We solve to a precision of 10^{-7} for the null problem. Each point is calculated individually, but we use a lookup table that provides initial values close to the solution to accelerate the calculation. The squares of the invariant masses $\mathrm{s_{min}}$ and $\mathrm{s_{max}}$ and the Jacobian as functions of the SDP variables are shown in Fig. 3.8. The Jacobian goes to high values when approaching the kinematical limit where both $\mathrm{h_{min}}$ and $\mathrm{h_{max}}$ have the value one. This can be understood by the means of the iso-helicity lines in Fig. 3.7, a high density of iso-helicity lines corresponds to a numerically large Jacobian. This does not present a problem, as the kinematical limit itself is not permitted, and the formula to calculate the Jacobian in analytical.

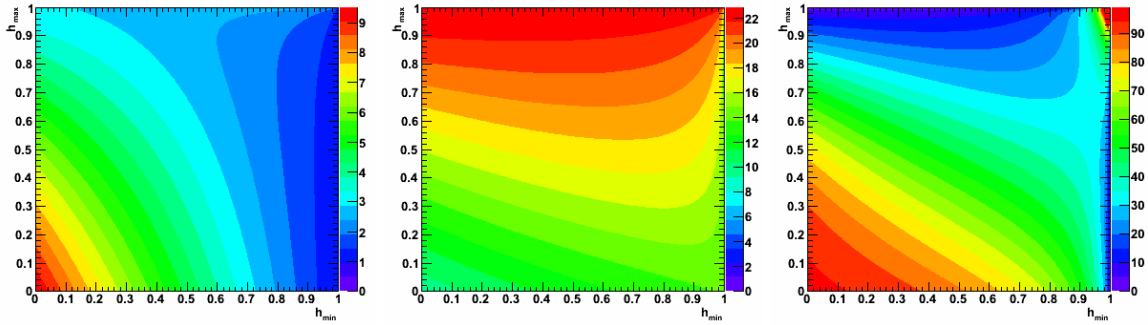

Figure 3.8: Square Dalitz plot maps of $\mathrm{s_{min}}$ (left), $\mathrm{s_{max}}$ (right) and the Jacobian of the transformation $(\mathrm{s_{min}}, \mathrm{s_{max}}) \to (\mathrm{h_{min}}, \mathrm{h_{max}})$ (right) as functions of the SDP variables.

3.3.8 Observables

The aim of the DP analysis presented in this work is to measure the branching fractions of the Q2B modes that contribute to the decay along with the relative strong phases between the Q2B modes. While the phase difference can be obtained in a straight-forward way from the measurements of the δ_{i} parameters of the isobar model, the branching fraction measurements are somewhat more complicated. The relevant observable for this measurement, that we multiply with the inclusive branching fraction to obtain the Q2B branching fraction, is the so-called relative isobar fraction $\mathrm{FF(j)}$ (or fit fraction) of a resonance j that is usually defined as follows:

$$\mathrm{FF(j)} = \frac{(|\mathrm{c_j}|^2 + |\overline{\mathrm{c}}_{\mathrm{j}}|^2)\langle \mathrm{F_j F_j^*}\rangle}{\sum_{\mu\nu}(\mathrm{c}_\mu \mathrm{c}_\nu^* + \overline{\mathrm{c}}_\mu \overline{\mathrm{c}}_\nu^*)\langle \mathrm{F}_\mu \mathrm{F}_\nu^*\rangle} \,, \tag{3.50}$$

In the present case, this definition has no physical meaning. As we have three identical particles in the final state, any resonance is allowed to decay into any pair of $\mathrm{K_s^0}$. To take this into account in the model, we implement three times the same "technical" resonance, see Eq. 3.44, but each decaying to a different pair. Due to the symmetrization we only look at one sixth of the regular DP, but all the three "technical" resonances have contributions in the part we look at. Consequently the physical fit fraction is the sum of the three resonances in the model[2]:

$$\mathrm{FF(j)} = \frac{\sum_{\mu=\mathrm{j}}^{\mathrm{j+2}} \sum_{\nu=\mathrm{j}}^{\mathrm{j+2}} (\mathrm{c}_\mu \mathrm{c}_\nu^* + \overline{\mathrm{c}}_\mu \overline{\mathrm{c}}_\nu^*)\langle \mathrm{F}_\mu \mathrm{F}_\nu^*\rangle}{\sum_{\mu\nu}(\mathrm{c}_\mu \mathrm{c}_\nu^* + \overline{\mathrm{c}}_\mu \overline{\mathrm{c}}_\nu^*)\langle \mathrm{F}_\mu \mathrm{F}_\nu^*\rangle} \,, \tag{3.51}$$

where the "self interference" term is taken into account by the non-diagonal terms in the numerator. It has been checked by assigning negligible widths to resonances in a toy model, that in case there is no interference between different resonances, the sum of the fit fractions is 1. When there is interference, the sum of all fit fractions can deviate significantly from unity.

[2]This formula is somewhat simplified for better readability. As it is written it is only valid for j=1,4,7,...

4 The PEP-II 2 B-Factory and the *BABAR* Detector

4.1 An asymmetric e^+e^- collider as a B factory

In Cha. 2 we briefly sketched the physics-driven design requirements of a B Factory: since b quarks are produced in particle-antiparticle pairs, one of the B mesons produced can be used to determine the flavor of the other one, thus enabling the measurement of time-dependent asymmetries in the decay of a B^0 and its anti-particle $\bar{\mathrm{B}}^0$.
Very good conditions for such measurements can be provided by an $\mathrm{e}^+\mathrm{e}^-$ collider with the center-of-mass energy tuned to the $\Upsilon(4\mathrm{S})$ resonance, which decays almost uniquely to $\mathrm{B}^0_\mathrm{d}\bar{\mathrm{B}}^0_\mathrm{d}$ and $\mathrm{B}^+_\mathrm{u}\mathrm{B}^-_\mathrm{u}$ pairs with equal probabilities. In Fig. 4.1 we show a scan in terms of beam energy where the enhancement of the cross-section due to the $\Upsilon(4\mathrm{S})$ can be seen. The resonance "sits" on a flat distribution of continuum events. The precise knowledge of the kinematical

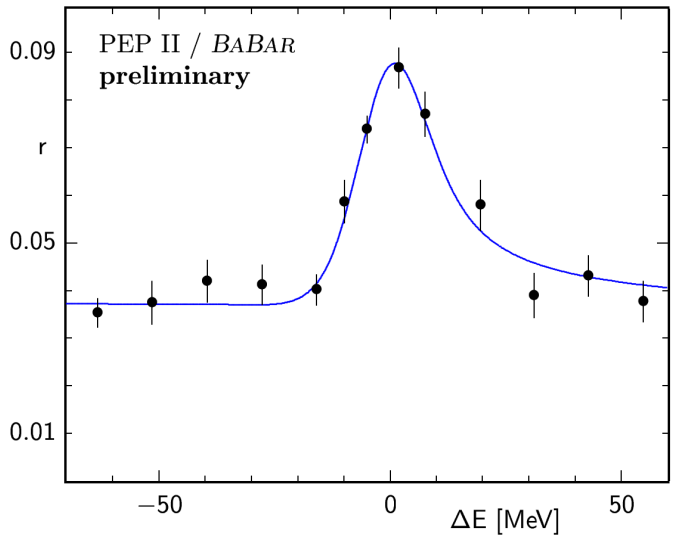

Figure 4.1: Number of multi-hadron events normalized to the number of Bhabha-scattering events as function of the energy difference between the energy in the center of mass and the invariant mass of the $\Upsilon(4\mathrm{S})$ resonance.

state of the $\mathrm{e}^+\mathrm{e}^-$ system allows for a complete reconstruction of the event and naturally provides us with background discriminating variables (Sec. 7.5). In addition, running at the $\Upsilon(4\mathrm{S})$ resonance implies that the neutral B mesons are produced in a quantum mechanical

state of entanglement, which greatly helps in the tagging process by forcing the two particles to remain a particle-antiparticle pair for as long as both exist. In a hadronic environment, such a statement is no longer true[1] and the tagging efficiencies (Sec. 7.3.4) fall dramatically for two reasons: firstly, the higher track multiplicity is an obstacle to finding the particle whose charge uniquely identifies the flavor of $\mathrm{B_{tag}}$; secondly, determining the flavor of $\mathrm{B_{rec}}$ requires establishing the flavor of $\mathrm{B_{tag}}$, evolving it back to the production point, and then forward to the $\mathrm{B_{rec}}$ decay vertex, thus depending strongly on the accuracy in the inference of the production point.
These properties, together with a large data sample consisting of $\sim 10^8$ $\mathrm{B\overline{B}}$ pairs, are the necessary ingredients for *BABAR*'s main physics goals: precisely measuring the *CP* violating time-dependent asymmetries and constraining the CKM matrix elements. Secondary physics interests are rare B decays, such as the subject of this thesis, charm and τ physics, and QCD and two-photon physics. Other quantum electrodynamic processes, such as muon pair production, are mostly filtered due to their large cross-sections, some of them being used for calibration and luminosity measurement purposes. Specifically, the integrated luminosity is calculated to great accuracy by examining the accumulated samples of $\mathrm{e^+e^-} \rightarrow \mathrm{e^+e^-}\,(\gamma)$, $\mathrm{e^+e^-} \rightarrow \mu^+\mu^-\,(\gamma)$ and $\mathrm{e^+e^-} \rightarrow \gamma\gamma$, processes for which the cross-sections are extremely well understood thanks to QED.
The constraints posed to the accelerator configuration by the difficulties of time-dependent analyses and the high luminosities needed to achieve the desired sample size are discussed in the next section.

4.2 PEP-II and the B Factory

For the time-dependent *CP* violating asymmetries arising in neutral B mesons to be measured, an asymmetric collider is required. The boost of the B mesons in the laboratory frame allows the distance between the decay vertices of the two mesons to be measured, from which the time between the decays of the two particles can be inferred.
The asymmetry is achieved by injecting into the PEP-II storage rings 9.0 GeV $\mathrm{e^-}$ and 3.1 GeV $\mathrm{e^+}$ beams which, upon collision, result in a boost of $\beta\gamma = 0.56$ along the $\mathrm{e^-}$ beam direction in the laboratory frame for the center-of-mass of the particles produced. The center-of-mass energy is tuned to the $\Upsilon(4\mathrm{S})$ mass, 10.58 GeV, for 90% of the running time, the remaining 10% being set 40 MeV below the resonance peak. The first sample, known as the *on-peak sample*, contains the $\mathrm{B\overline{B}}$ events, whereas the second one, called the *off-peak sample*, is recorded for background characterization purposes. The light quark processes $\mathrm{e^+e^-} \rightarrow \mathrm{q\overline{q}},\ \mathrm{q} = \mathrm{u,d,s,c}$ which constitute the most prominent background to the $\mathrm{B\overline{B}}$ events are the only hadronic reactions allowed below the $\Upsilon(4\mathrm{S})$ threshold.
The injection is carried out using the two mile long Stanford Linear Accelerator, which diverts a fraction of the accelerated electrons to produce positrons in collision with a high-Z stationary target. These are then directed back to the linear accelerator to be brought to their nominal energy before entering the storage rings. Once there, the electrons and the positrons, which circulate in bunches along physically separated rings, are collided in one Interaction

[1] An exception is "same side" tagging.

Region, in which the *BABAR* detector is located.

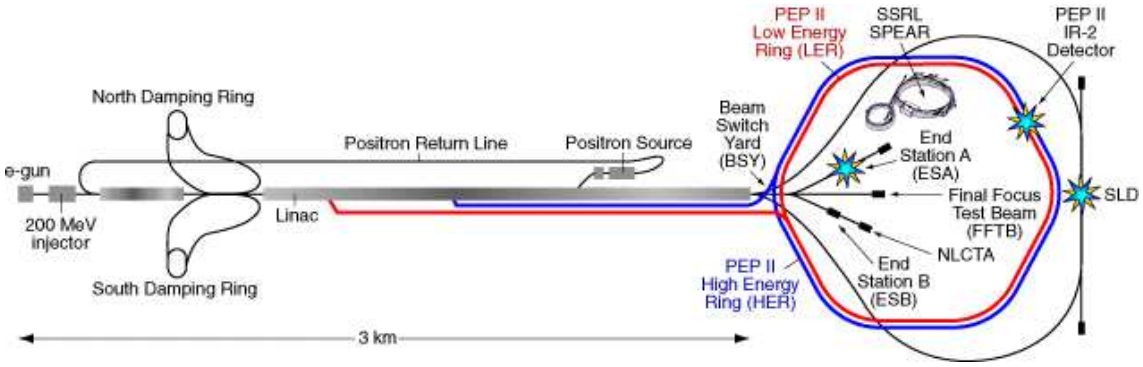

Figure 4.2: The linear accelerator at SLAC and the PEP-II collider.

4.2.1 The Interaction Region

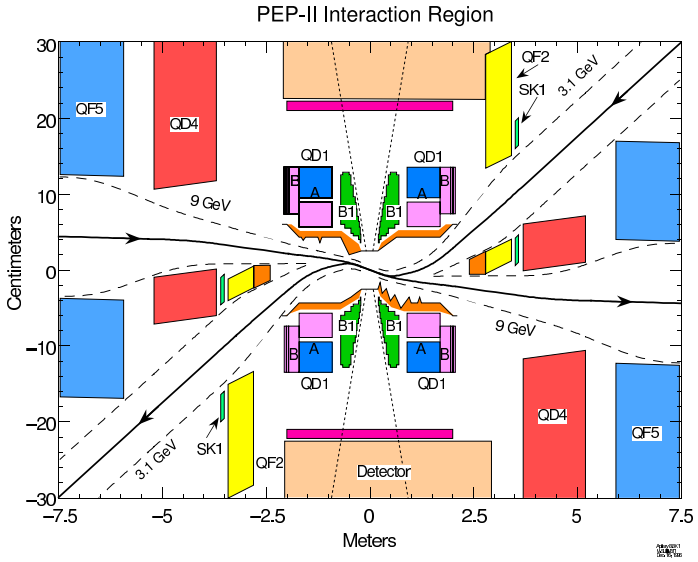

Figure 4.3: Schematic view of the Interaction Region. Observe the strong bending needed to make the two beams collide head-on, that results in the most prominent machine background: synchroton radiation.

The Interaction Region is heavily instrumented with magnets that focus the beams before the collision, directs them so that there is no crossing angle between them, and finally separates them before a given bunch of particles collides with a second bunch from the other

beam (see Figure 4.3). The quadrupole magnets labeled QD and QF, situated outside the *BABAR* detector, focus the high and low energy beams. The dipoles labeled B1 are responsible for bringing the beams together and separating them immediately afterwards. This is the reason why they need to be close to the interaction point; in fact, within the detector volume.

4.2.2 Machine backgrounds

By "machine backgrounds" we refer to the radiation that reaches different parts of the detector as a consequence of being immersed in an accelerator environment. They should be avoided as they lead to degradation of the performance of the detector, due to the sustained radiation damage, and they produce large dead times in which the different systems of the detector are unable to accept any real physics event because they are processing and flushing out the spurious signals. In *BABAR*, there are three main sources of machine backgrounds. In order of decreasing importance these are: synchroton radiation, beam-gas interactions and radiative Bhabha scatterings.
The synchroton radiation is a direct consequence of the rather complex optics discussed before, and especially of the dipoles inside the detector, as it is caused by the bending of the beams so close to the interaction point. The geometry of the crossing has been designed to minimize the probability of those photons, and the electromagnetic showers that they produce, impacting the detector. Copper masks are also used to prevent them from interacting with the beam pipe and creating further debris. This kind of background scales with the currents going through each of the storage rings. Increases in luminosity stemming from higher currents bring this background as an undesired side effect.
Interactions of the beam with gas molecules present in the beam pipe often lead to particles in the beam acquiring a momentum outside the range that can be focused by the optics. These lost particles may then hit the beam pipe and produce an electromagnetic shower that spreads over the detector. Collimators are employed to prevent any of these from occurring close to the detector.
Finally, radiative Bhabha scatterings of electrons and positrons may cause one of them to hit the pipe inside the detector and produce an electromagnetic shower that spreads over our measuring instrument. Such a background scales with luminosity, and may prove to be important as the luminosity is increased towards the end of the lifetime of the experiment.

4.2.3 Trickle injection

The currents stored in the rings can be topped up once every two or three hours, during which the voltage is ramped down in the detector to prevent any background from affecting it. A new injection is only arranged when the instantaneous luminosity falls below a preestablished threshold. It can also be made continuously at a low rate, in which case the resulting machine backgrounds must be dealt with. In successive tests during late 2003 and early 2004, it was shown that these backgrounds could be kept to a manageable level, and the default operation mode has involved such trickle injection ever since, greatly helping to improve the delivered luminosity (see Fig. 4.4).

4.2.4 Performance

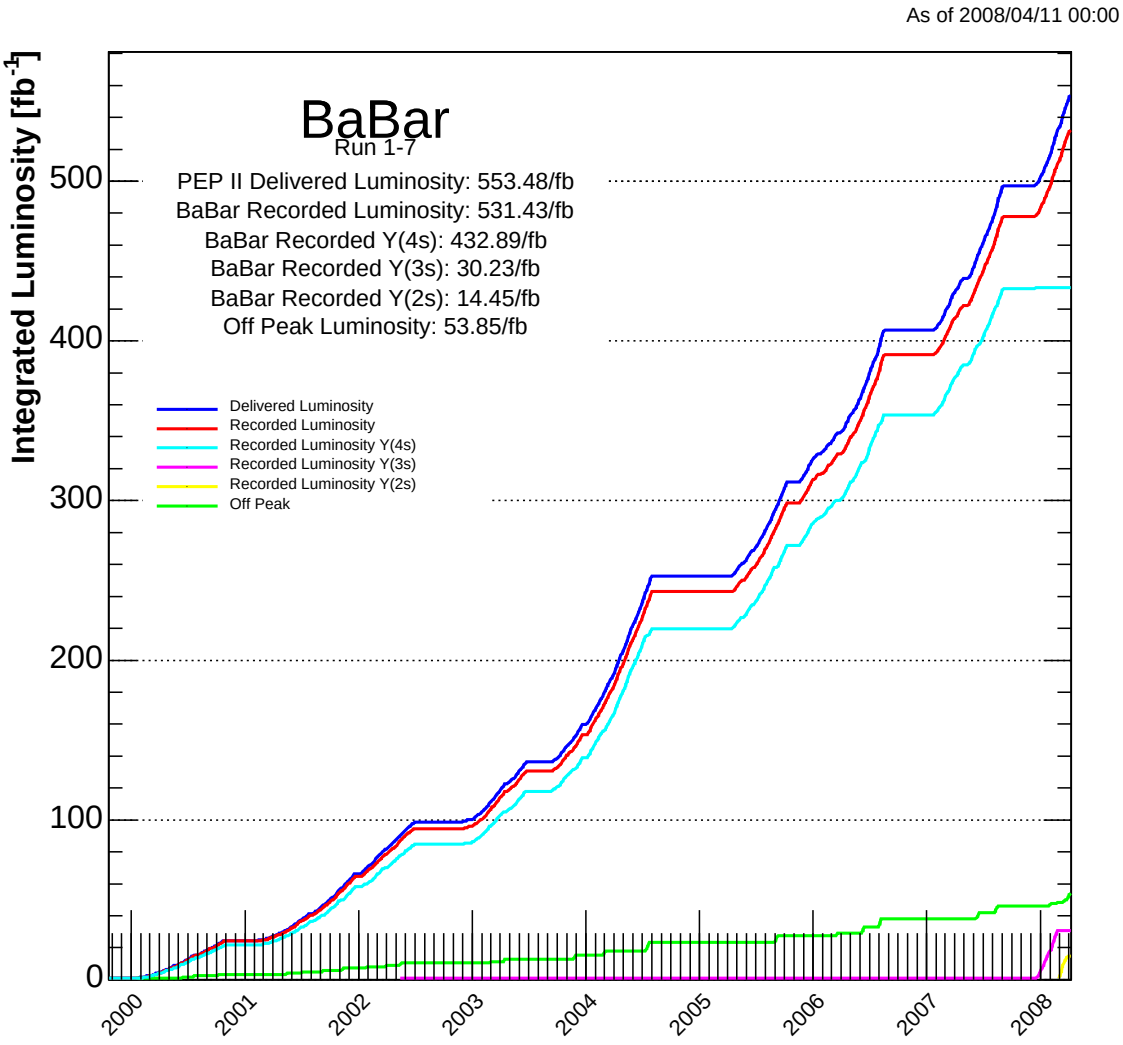

Figure 4.4: Plot showing the evolution of the integrated luminosity as delivered by PEP-II (dark blue) and recorded by *BABAR* (red) for the whole data taking period. The plot also shows the fractions recorded on the $\Upsilon(4S)$ (light blue), $\Upsilon(3S)$ (magenta), $\Upsilon(2S)$ (yellow), and off-peak (green).

The design luminosity and accelerator parameter goals were met by PEP-II within the first year of running, and they have been improving ever since (Fig. 4.4). Tab. 4.1 compares the design goals with the typical values achieved at the end of running in April 2008 and also shows the records of beam current and luminosity. In total 553.48 fb^{-1} have been delivered.

Parameters	Design	Typical	Best
Energy HER/LER (GeV)	9.0/3.1	9.0/3.1	-
Current HER/LER(A)	0.75/2.15	1.9/2.9	2.069/3.213
# of bunches	1658	1722	-
Bunches spacing (ns)	4.2	8.4	-
σ_{Lx} (μm)	110	120	-
σ_{Ly} (μm)	3.3	5.6	-
σ_{Lz} (mm)	9	9	-
Luminosity ($10^{33}\mathrm{cm}^{-2}\mathrm{s}^{-1}$)	3.0	9.0	12.07
Luminosity (pb^{-1}/day)	130	700	858.4

Table 4.1: PEP-II beams parameters. Values are given for both design and typical colliding beam operation in April 2008. σ_{Lx}, σ_{Lz} and σ_{Lz} refer to horizontal, vertical and longitudinal RMS size of the luminous region. The last column shows the best achieved luminosities and beam currents.

4.3 The *BABAR* detector

In this section we state the main requirements on the *BABAR* detector resulting from the physics under study, describing each subsystem and its performance in later sections. A detailed description of the detector can be found in [39].
The physics goals stated in Sec. 4.1 lead to an asymmetric collider, and therefore, since a uniform acceptance in the center-of-mass system is preferred, to an asymmetric detector as well, with its center displaced from the interaction point by 37 cm. It should also comply with the following requirements:

- A high reconstruction efficiency for charged and neutral particles of momenta above 60 MeV/c and 20 MeV/c, respectively.
- Good momentum resolution or charged particles in the momentum range 60 MeV/c to 4 GeV/c. Low momentum particles are important, among other reasons, because they are copiously produced by D^* mesons decaying to D mesons.
- Good photon energy and angular resolutions, in order to reconstruct π^0 and η particles.
- Excellent particle identification capabilities, as these are crucial to the tagging procedure. In particular, electrons and muons should be reliably identified, and hadrons such as $\mathrm{p}, \mathrm{K}, \pi$ should be distinguished.
- Excellent vertex resolution, so that the typical distances associated to a time-dependent analysis, $\beta\gamma\mathrm{c}\tau_{\mathrm{B}^0} \lesssim 250\ \mu\mathrm{m}$, are resolved. It is also desirable for D and τ physics, since these particles also exhibit displaced vertices.
- Dead times as short as possible, so that higher luminosities can be handled without problems.

- Radiation resistance, in order for the efficiencies of the subsystems not to degrade badly over the lifetime of the experiment.

The final design of the detector consists of five subsystems: the silicon vertex tracker (SVT), which provides the accuracy needed to reconstruct the displaced vertices of the B mesons and other particles with similar lifetimes; the drift chamber (DCH), the main tracking device; the detector of internally reflected $Cerencov$ light (DIRC), whose input for particle identification is essential; the electromagnetic calorimeter (EMC), that allows for exclusive studies of final states containing π^0 and other neutral particles; and the flux return (IFR), instrumented first with resistive plate chambers (RPC) and more recently with limited streamer tubes (LST), which serve as muon detectors and as a primitive hadronic calorimeter e.g. for the K^0_L. All but the last two subsystems are immersed in a uniform axial 1.5 T magnetic field necessary to measure the transverse momentum from the curvature of the tracks. Fig. 4.5 shows the whole detector, specifying each subsystem.
The convention adopted in *BABAR* for the coordinate system follows a standard spherical-polar coordinate system centred on the interaction point (IP), the z axis being parallel to the e^- beam direction, and θ and ϕ being the usual polar and azimuthal angles. The cartesian axes form a right-handed system with the x axis pointing outwards from the PEP-II ring and the y axis pointing upwards. The cartesian coordinate definitions can also be found graphically in Fig. 4.6.

4.4 Silicon Vertex Tracker

4.4.1 Physics requirements

The Silicon Vertex Tracker is located just outside the beam pipe, at around 3 cm from its center. Its position makes it crucial in the determination of decay vertices of B and D mesons and τ leptons. To achieve the necessary resolution in Δt, a resolution of 80 $\mu\mathrm{m}$ must be attained in z for single-vertex measurements. In the xy plane, distances of $\sim$100 μm must be resolved for the correct reconstruction of secondary vertices such as those from D and τ decays. The z axis is defined in the direction of the electron beam, the orientation of the x and y axes can be seen in the bottom plot of Fig. 4.6.
The SVT is also responsible for the tracking of low momentum particles, since for $\mathrm{p_t}$ <120 $\mathrm{MeV/c}$ they are unlikely to reach the drift chamber or produce enough hits in it. This is particularly relevant to the reconstruction of the D^* decay into a low momentum pion and a D meson, which is important in itself and for tagging purposes.
Finally, the SVT also plays a role in particle identification through its own measurements of the rate of energy loss, and by giving the best determination of the polar angle of high momentum tracks, which is a necessary input to fully exploit the DIRC.

4.4.2 Design

Although maximum coverage is desirable, the B1 dipoles situated inside the detector (see Fig. 4.3) and some support structures limit the SVT acceptance to the polar angles 20.1° <

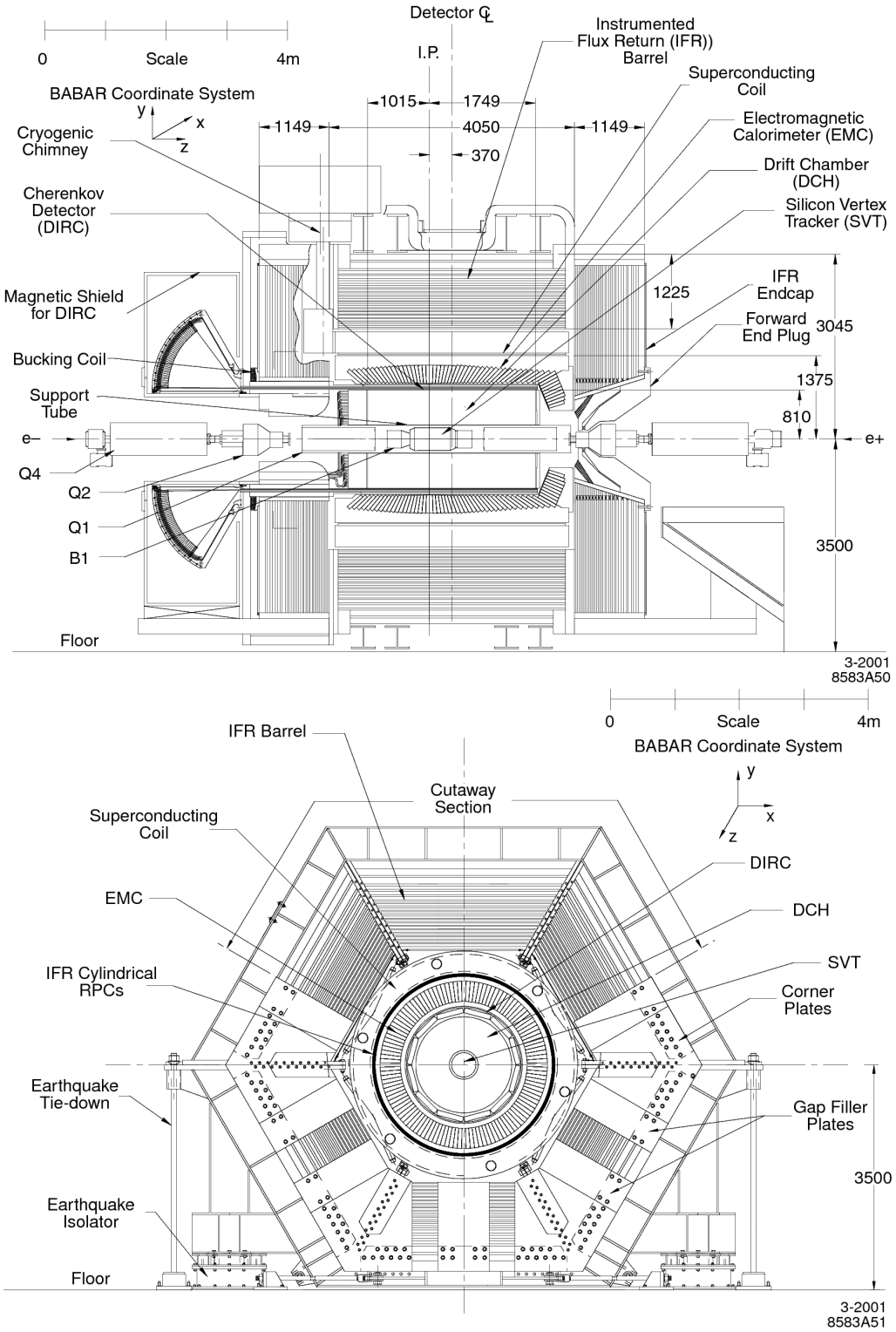

Figure 4.5: Lateral (top) and front (bottom) view of the detector, with all the subsystems clearly indicated.

θ <150.2°, which still comprises 90% of the solid angle in the centre-of-mass system. Another constraint on the SVT design is that it must be able to withstand the irradiation associated with being so close to the beam pipe, while still keeping the amount of material as low as possible to avoid multiple Coulomb scattering.

The SVT is composed of five layers of double-sided silicon strips (see Fig. 4.6), with the strips on the outside being parallel to the beam and on the inside perpendicular, thus providing simultaneous measurements of ϕ and z, respectively, for each hit.

The first three layers are composed of 6 modules each, slightly tilted to provide complete coverage. Layers 4 and 5, having 16 and 18 modules respectively, produce the overlap between neighboring strips by alternating the radii at which they are located. The strips in the two outermost layers are arch-shaped, in contrast to the three innermost, in order to reduce the material a track goes through while providing complete coverage. The two innermost layers are particularly important in determining the polar angle of a track, while the role of the two outermost is to help in matching tracks to those found by the DCH. The third layer provides extra information for low momentum tracks that may not reach the drift chamber.

To be able to meet the resolution goals, the local and global alignment of the SVT is crucial. The local alignment, of the different modules relative to each other, is only necessary after accesses to the detector. It is carried out by fitting tracks from cosmic rays and $\mathrm{e^+e^-} \rightarrow \mu^+\mu^-$ events. Global alignment, of the SVT with respect to the rest of the detector, is done at the beginning of each run, by minimizing the differences between the SVT and DCH tracks in a small sample of events.

4.4.3 Performance

The efficiency in track reconstruction of the SVT as measured in data on di-muon events is 97%, after excluding the defective strips. A good example of the efficiency of low momentum tracking in the SVT is *BABAR*'s measurement for $\mathrm{D^0} - \overline{\mathrm{D}}^0$ mixing [40], in which extraordinarily large samples of $\mathrm{D^*}$ mesons decaying to a charged pion and a D meson are needed in order to tag the flavor of the neutral meson and detect the minute oscillation.

The spatial resolution of the SVT hits can be evaluated by fitting high momentum tracks without the hit in the layer under inspection and comparing the hit with the intersection of the fitted track. The residuals are divided by the uncertainty on the track determination to get the resolution. This is found to be better than 40 μm, implying a vertex resolution better than 70 μm.

4.5 Drift Chamber

4.5.1 Physics requirements

The drift chamber is the main tracking system in the *BABAR* detector and it is therefore expected to measure the momenta and polar angles of the tracks efficiently and precisely over a wide range of momenta, $0.12 < \mathrm{p_t} < 5.0$ GeV/c. It provides one of the main inputs to the Level-1 trigger and plays a key role in the extrapolation of tracks into the DIRC, EMC and

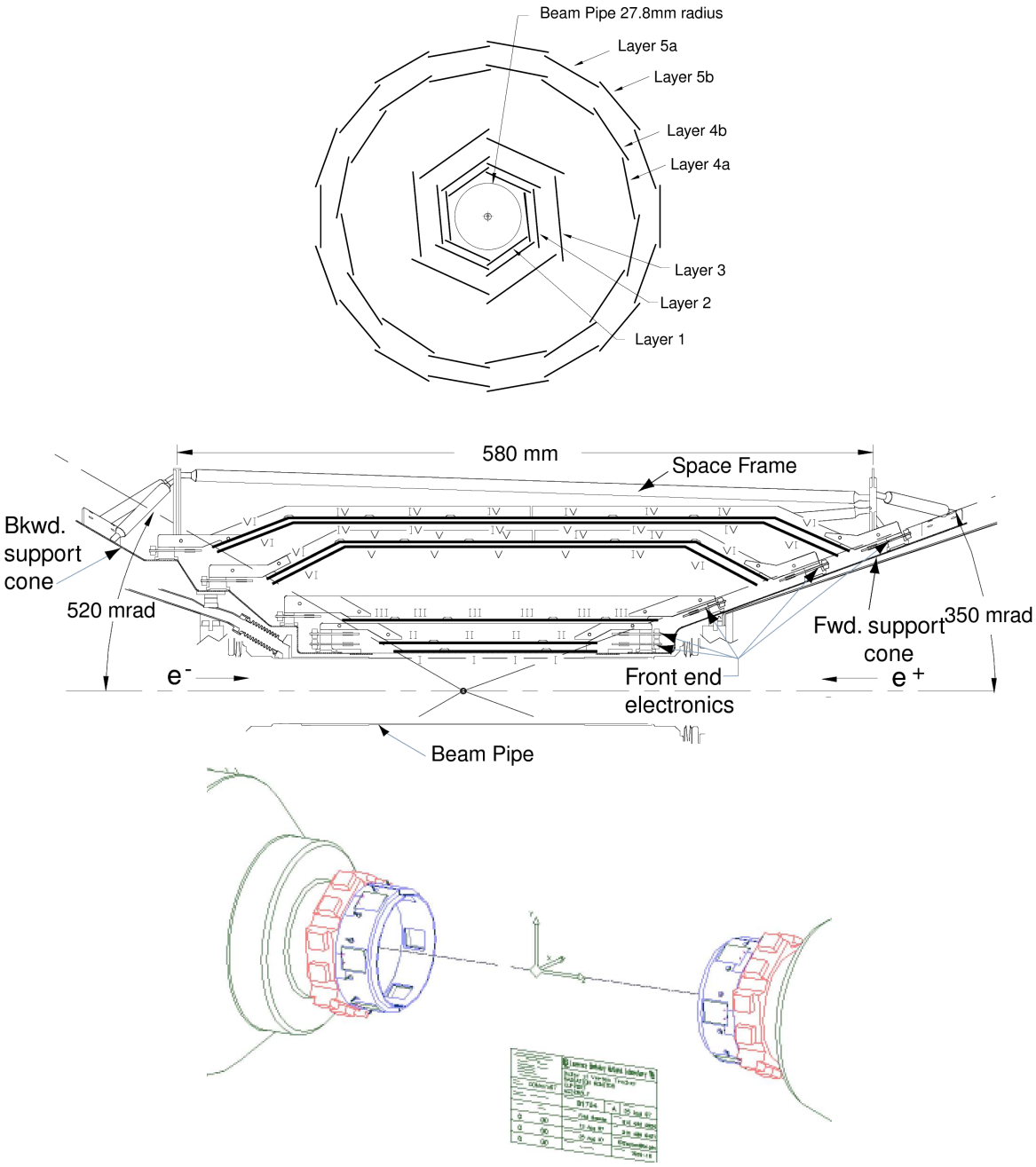

Figure 4.6: End (top) and side (middle) views of the Silicon Vertex Tracker, in which the five layer structure and the arch shape of the outer layers can be appreciated. Sensors (bottom) are mounted in two rings , one at each end of the support cone. The backward side is to the left, the forward side is to the right. Each ring holds 6 diodes (blue) and 12 thermistors (red). The diodes measure the instantaneous and integrated dose, the thermistors measure the temperature. The diodes in the midplane (x0z-plane) have later been replaced with diamonds.

IFR. Thus, the solid angle coverage must be as complete as possible whilst minimizing the amount of material that the particles have to traverse.
The DCH must achieve a resolution of $\sigma_{\mathrm{p_t}}/\mathrm{p_t} < 0.3\ \%$ in order to reconstruct B and D candidates. Furthermore, a spatial resolution of 140 $\mu\mathrm{m}$ is needed. The vertexing of long-lived particles such as the $\mathrm{K^0_s}$, present in the golden mode and in the channel analyzed in this thesis, as well as in many other final states studied with time-dependent analyses, requires the drift chamber to measure longitudinal positions to better than 1 mm.
Finally, the DCH also bears the responsibility for particle identification for momenta $\mathrm{p_t} <$ 700 $\mathrm{MeV/c}$, for which the DIRC is is not effective, and for tracks that fall outside the acceptance of the latter in the forward region. K/π separation is attained with a precision of 7% on $\mathrm{dE/dx}$ measurements.

4.5.2 Design

The DCH is a 276 cm long cylinder located immediately outside the SVT, with inner and outer radii of 23.6 and 80.9 cm respectively and displaced towards the forward direction to increase the center-of-mass acceptance. A mixture of helium and isobutane in a ratio 4:1 fills the chamber, with additional small amounts of water vapor (0.3 $\%$) to extend the lifetime of the device.
The DCH is formed from 40 layers of hexagonal drift cells, with each group of 4 layers

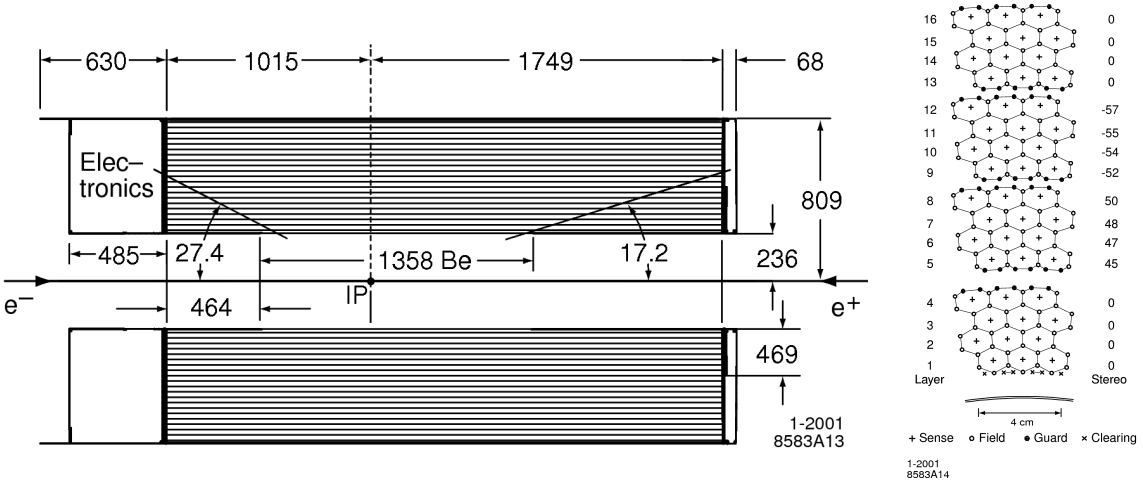

Figure 4.7: Side view of the drift chamber (left) and cell layout in first four superlayers (right). The angle in mrad of the stereo layers with the z axis is written on the right of each layer.

organized into a superlayer. The cells consist of a sense wire in the center, with a diameter of 20 $\mu\mathrm{m}$ and kept at 1930 V, surrounded by 6 field wires, of 80 and 120 $\mu\mathrm{m}$ diameters, that are grounded. Each layer of cells is staggered with respect to the previous one, which allows the left-right ambiguity in the measurements to be resolved. Longitudinal positions are measured by orienting of the layers at a small angle to the z axis. Their arrangement

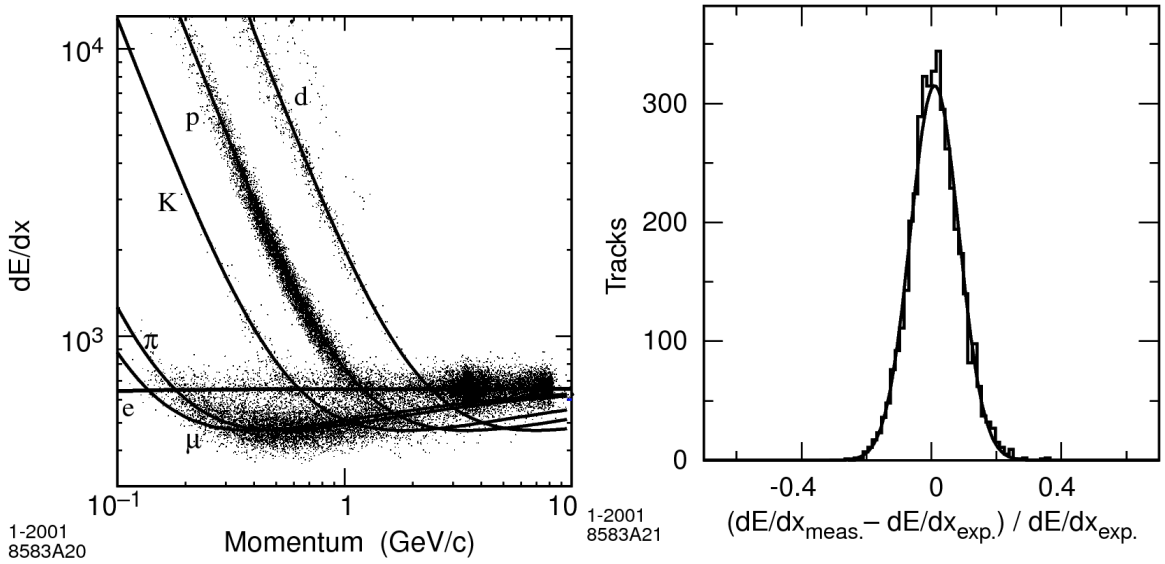

Figure 4.8: On the left, DCH $\mathrm{dE/dx}$ measurements and the Bethe-Bloch predictions [39]. On the right, difference between the measured and expected energy loss $\mathrm{dE/dx}$ for $\mathrm{e^{\pm}}$ from Bhabha scattering, measured in the DCH at a operating voltage of 1960 V. The curve represents a Gaussian fit to data with a resolution of 7.5$\%$.

is as follows: superlayers alternate between axial (A) and stereo (U,V) superlayers forming a pattern AUVAUVAUVA, with the angle of the stereo layers with respect to the z axis increasing outwards from 45 to 76 mrad. Altogether, the whole volume of gas and the wires represent only 0.28 $\%$ of a radiation length for tracks with normal incidence.

4.5.3 Performance

When a charged particle goes through the chamber, it ionizes some of the molecules in the gas. The charges then start drifting due to the electric field, which is locally quasi-cylindrical around each sense wire. Collisions with further gas molecules result in a gain of $\sim 5 \times 10^4$. The time taken for the charge to arrive at the wire translates into a distance from the wire. That drift time, however, requires cell-by-cell calibration, which is performed by fitting high momentum $\mu^+\mu^-$ and $\mathrm{e^+e^-}$ tracks while omitting the cell being calibrated. The total charge deposited, which is used to calculate $\mathrm{dE/dx}$, also needs calibration.
The track reconstruction efficiency can be estimated from the sample of tracks that traverse both tracking devices, the DCH and the SVT. After correcting for fake SVT tracks, the ratio of the number of tracks reconstructed in the DCH over those observed in the SVT is found to be (96$\pm$1)$\%$.

The $\mathrm{dE/dx}$ value for a given track is calculated as the truncated mean of the 80$\%$ lowest measurements $\mathrm{dE/dx}$ measurements for the track, since these follow a Landau distribution whose mean diverges. Fig. 4.8 shows the $\mathrm{dE/dx}$ measurements in the DCH as a function of the momentum, and the corresponding Bethe-Bloch expectations [1]. A good separation

between pions and kaons is achieved below $0.7\,\mathrm{GeV}/c$ momentum, above which the DIRC has the main responsibility for particle identification. This is also demonstrated in practice in *BABAR*'s last measurement of $\mathrm{B}^0 \to \mathrm{h}^+\mathrm{h}^-$ (where $\mathrm{h} = \mathrm{K}, \pi$) [41], where the DCH is used to provide particle identification of forward tracks falling outside the acceptance of the DIRC[2]. The dE/dx resolution on electrons is 7.5%, almost at the design value (7%). The resolution on $\mathrm{p_t}$ is, as shown in Figure 4.8, very close to the design value too.

4.6 Detector of Internally Reflected $Cerencov$ light

4.6.1 Physics requirements

Particle identification is essential to *BABAR*, since its physics programme consists of measuring CP violating asymmetries in a variety of channels. In neutral modes, the measurement of these asymmetries necessitates the determination of the flavor of the other B in the event, which is done through the correlation of the charges of certain particles with the flavor of the parent meson. These correlations depend on the particle species, making their identification mandatory (see Sec. 7.3.4). It is also crucial to avoid contamination in the isolation of final states, since similar channels, like $\mathrm{B}^0 \to \mathrm{K}^+\pi^-$ and $\mathrm{B}^0 \to \pi^+\pi^-$, have different asymmetries.

More specifically, above 700 $\mathrm{MeV/c}$, the drift chamber is no longer able to distinguish kaons from pions, which the DIRC aims to separate at 4 σ significance up to a momentum of 4.2 $\mathrm{GeV/c}$. For the muons, the DIRC must complement the IFR, whose effectiveness falls for momenta below 750 $\mathrm{MeV/c}$.

Finally, given its location between the drift chamber and inside the calorimeter, it must be small to minimize the size of the most expensive part of the detector, the calorimeter, and it amounts to only a fraction of a radiation length (see below).

4.6.2 Design

When a particle travels faster than the speed of light in the medium that surrounds it, $\mathrm{v/c} = \beta \geq 1/\mathrm{n}$, it emits $Cerencov$ photons at an angle $\cos\theta_\mathrm{C} = 1/\mathrm{n}\beta$ with the direction of the particle. Hence, provided that its trajectory is known accurately enough, a measurement of the direction of these photons establishes the speed of the particle. Given the space constraints sketched above, the instrumentation to detect them must lie outside the main body of the detector. Internal reflection on a plane surface is used to preserve the angle of these photons while directing them towards the photomultiplier tubes (see Figure 4.9). Forward moving photons are reflected in a mirror, allowing the DIRC instrumentation to occupy only the less populated backward end of the detector.

The material used to confine the photons is quartz (n=1.474) shaped in bars that are only 17 mm thick and 35 mm wide, but as long as 4.9 m. They amount to 17% of a radiation

[2]Unlike in this example, most analyses in *BABAR* which require particle identification do not use the information from each subdetector separately, and instead draw on a combination of information from the DIRC and the DCH and SVT dE/dx measurements, as described in Sec. 7.3.3.

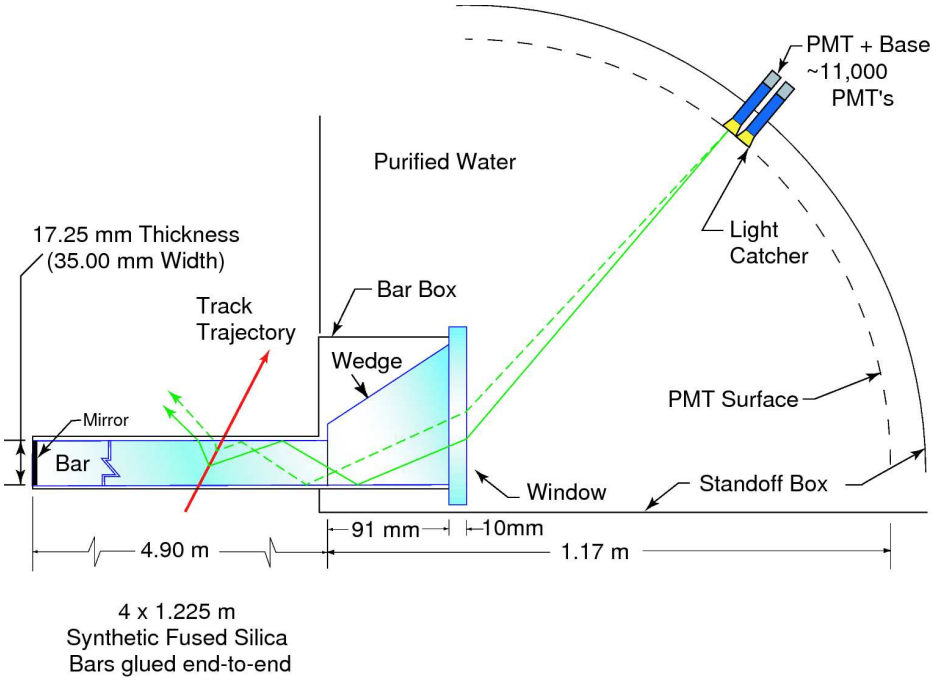

Figure 4.9: Diagram illustrating the operating principles of the DIRC.

length for a normally incident particle. In the backward end of the detector, the photons go through a wedge-shaped quartz piece and then into a water filled expansion region, known as the standoff box, after which they meet the photomultiplier tubes. The role of the wedge is to reflect photons arriving at large angles, thereby reducing the area of the standoff box that needs to be instrumented at the cost of introducing ambiguities in the angle.
The photomultiplier tubes, of which there are 10752, are surrounded by "light catchers", increasing the detection area. Also, the standoff box is magnetically shielded to avoid disturbances in the tubes.

4.6.3 Performance

The angle and time resolution can be calibrated from dimuon events. The $Cerencov$ angle resolution for a track turns out to be 2.5 mrad, giving over 4 σ separation at 3 $\mathrm{GeV/c}$ (see Fi. 4.10). Fig. 4.10 also shows the mass peak of the decay $\overline{\mathrm{D}}^0 \rightarrow \mathrm{K}^+\pi^-$ with and without the kaon/pion separation provided by the DIRC.

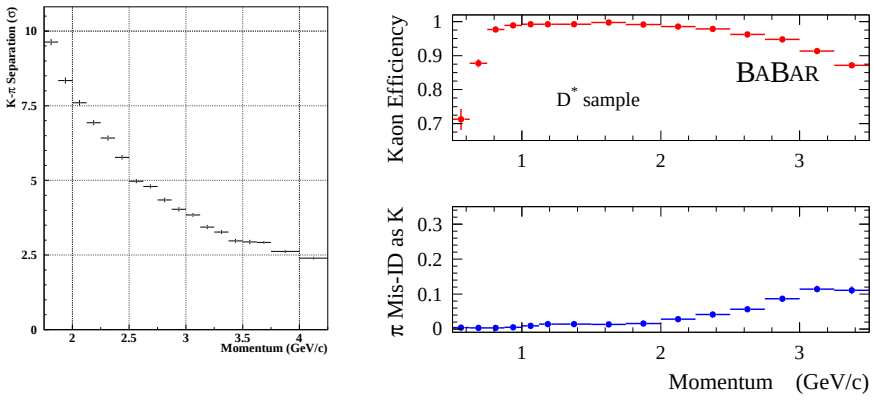

Figure 4.10: On the left: $\mathrm{K}-\pi$ separation (in σ units) of the DIRC as a function of the track momentum; and on the right: efficiency and misidentification probability of the selection of charged kaons as a function of track momentum, both obtained from a data sample of $\mathrm{D}^{*+} \to \mathrm{D}^0(\to \mathrm{K}^-\pi^+)\pi^+$ decays.

4.7 Electromagnetic Calorimeter

4.7.1 Physics requirements

A number of *CP* eigenstates within *BABAR*'s physics goals contain π^0's in the final state. Many others involve η particles or photons directly, such as $\mathrm{b} \to \mathrm{s}\gamma$, in which the spectrum is quite hard. Some QED processes, such as $\mathrm{e}^+\mathrm{e}^- \to \mathrm{e}^+\mathrm{e}^-\gamma$ or $\mathrm{e}^+\mathrm{e}^- \to \gamma\gamma$ are also important for calibration or luminosity measurement purposes. Therefore, *BABAR* must be able to reconstruct photons over a wide range of energies, from $20\,\mathrm{MeV}$ up to $4\,\mathrm{GeV}$.
The EMC must also be efficient in identifying electrons, as they are important for flavor tagging and semi-leptonic B decays, and no other system can provide accurate particle identification information for them.

4.7.2 Design

The EMC is formed from 6580 Thallium doped Cesium Iodide crystals arranged in a barrel and a forward endcap . The material was chosen due to its high light yield and small Molière radius, which imply good energy and angular resolutions, respectively. The crystal size varies from 16 radiation lengths in the backward direction to 17.5 radiation lengths in the forward endcap, since these receive impacts from the more energetic Lorentz-boosted particles. The crystals are tilted in such a way that they face the interaction point. Their exposed area is $\sim 5\ \mathrm{cm}^2$ (c.f. their Molière radius, $3.8\ \mathrm{cm}$), so a typical electromagnetic shower will spread over several crystals. Figure 4.11 shows a schematic view of the subdetector.

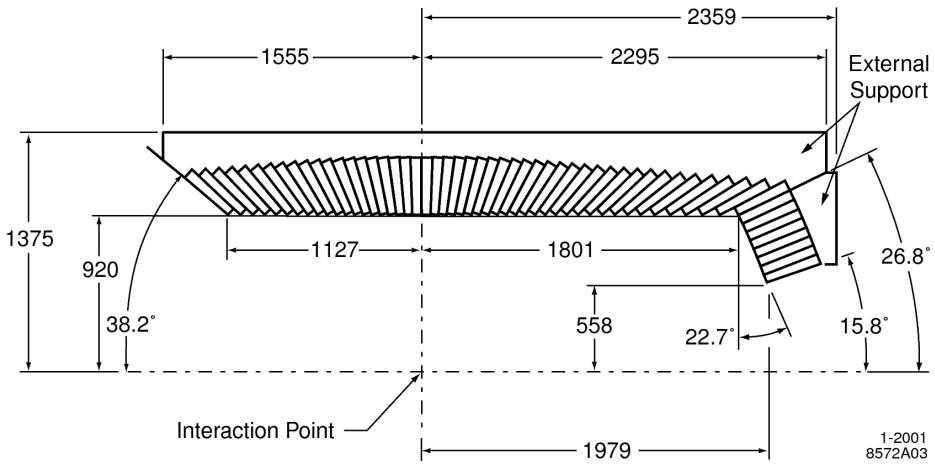

Figure 4.11: Side view on the Electromagnetic Calorimeter.

4.7.3 Performance

The calibration of the electromagnetic calorimeter involves determining the relation between the light yield and the energy deposited in the crystal, and between the cluster energy and the total energy of the incident particle. The light yield dependence on the energy varies from crystal to crystal, and may change over time due to radiation damage. It is calibrated for low energies using 6.13 MeV photons from a radioactive source, and in the high energy range by using Bhabha scattering events, for which the polar angle precisely determines the energy of the particle. Crystal leakage and absorption of energy by the material at the front of the crystals or between them leads to the need for the calibration of the cluster energy. This is applied during the off-line reconstruction and is derived from samples of π^0 and η mesons. The photon energy and angular resolutions of the EMC are also extracted from the calibrations, and are found to be parameterized, respectively (see Fig. 4.12), by

$$\frac{\sigma_{\mathrm{E}}}{\mathrm{E}} = \frac{\mathrm{a}}{(\mathrm{E(GeV)})^{1/4}} \oplus \mathrm{b} \tag{4.1}$$

$$\sigma_\theta = \sigma_\phi = \frac{\mathrm{c}}{\mathrm{E(GeV)}} + \mathrm{d}\,, \tag{4.2}$$

where the first sum is in quadrature, and $\mathrm{a} = (2.3 \pm 0.3)\%$, $\mathrm{b} = (1.85 \pm 0.12)\%$, $\mathrm{c} = 3.87 \pm 0.07$ and $\mathrm{d} = 0.00 \pm 0.04$.

4.8 Instrumented Flux Return

4.8.1 Physics requirements

The golden mode, $\mathrm{J/\psi\,K^0_s}$, involves muons, as the J/ψ is reconstructed in the channels $\mathrm{e^+e^-}$ and $\mu^+\mu^-$. Their detection is also essential for semi-leptonic physics and for the tagging al-

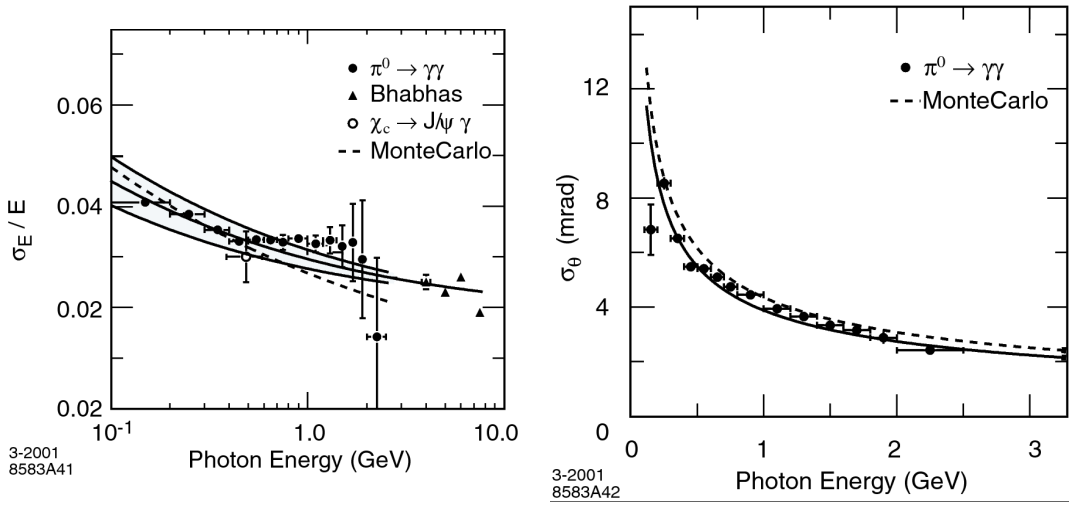

Figure 4.12: Photon energy (left) and angular (right) resolutions achieved by the electromagnetic calorimeter [39].

gorithms. Particle identification information on muons is desirable for momenta from about 1 $\mathrm{GeV/c}$.

Muons are heavier than electrons, making bremsstrahlung a far less effective energy loss mechanism for them. Since they have relatively long lifetimes and do not participate in nuclear interactions either, they are very penetrating particles. Therefore, the best choice is to place a dedicated subdetector outside the rest of the instruments.

In *BABAR*, the outer part of the detector plays the role of the flux return for the solenoid, at the same time as it provides a support structure. Interleaved between the steel plates of the flux return, instruments can be placed to turn it into a muon detector and a primitive hadron calorimeter, in charge of detecting neutral hadrons, mainly $\mathrm{K_L^0}$. These feature in a number of modes of interest, due to them having an opposite *CP* eigenvalue to the best experimentally suited modes containing a $\mathrm{K_S^0}$.

4.8.2 Design

The steel of the flux return, which is distributed in layers of increasing thickness from the inner to the outer sides, serves the purpose of filtering the muons and absorbing the neutral hadrons. Between the steel sheets, in the barrel and the endcaps, there are 19 and 18 gaps, respectively, which host the instrumentation. These are shown in Fig. 4.13, where the almost complete coverage of the detector is also apparent. The arrangement of these gaps, and the thickness of each of the layers was carefully chosen after dedicated MC studies to optimize the physics capabilities.

In these gaps, resistive plate chambers were installed. Two cylindrical RPCs were also placed between the EMC and the magnet to detect particles leaving the EMC and link any EMC clusters to IFR energy deposits.

The resistive plate chambers (see Fig. 4.14) consist of two graphite electrodes separated by two $2\,\mathrm{mm}$ thick sheets of bakelite, and in between these, another $2\,\mathrm{mm}$ gap filled with

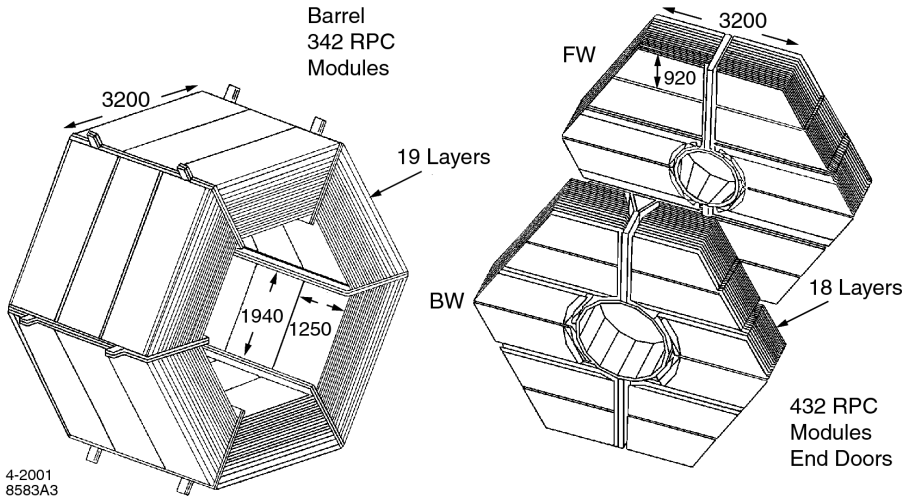

Figure 4.13: Schematic view of the IFR, with the barrel on the left and the forward (FW) and backward (BW) endcaps on the right.

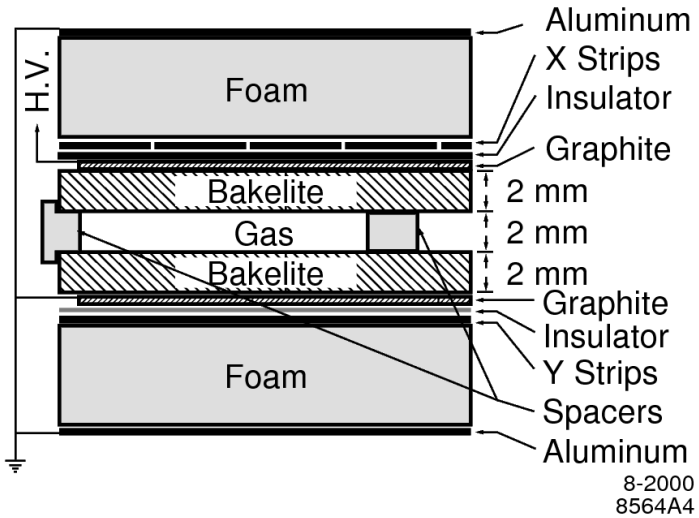

Figure 4.14: Resistive plate chamber design.

a mixture of gases: argon, freon and isobutane in the proportions 57:39:4. Readout strips are located next to the graphite, separated from it only by a film of insulator. They are placed orthogonally (hence the labels "X strip" and "Y strip" in the figure), providing three-dimensional positional information when combined with the distance of the RPC to the interaction point. The apparatus works as a capacitor, with one of the graphite electrodes grounded and the other one set to an 8 kV voltage. The passage of a charged particle or a hadronic shower do not cause a discharge, but induce temporary changes in the charge accumulated at each electrode, that are capacitatively read by the readout strips.

4.8.3 Performance

During *BABAR*'s first year of running, an 8% pion misidentification probability was found for a 90 $\%$ muon efficiency.
The calibration of the angular resolution and efficiency of the detection of neutral hadrons was studied through the process $\mathrm{e^+e^-} \to \phi\gamma \to \mathrm{K^0_S K^0_L}\gamma$, and yielded efficiencies between 20 and 40%, and angular resolutions around 60 mrad for $\mathrm{K^0_L}$ that did not interact in the EMC. When the latter also provided information, the resolution was twice as good.
However, shortly after installation, the performance of the RPC was observed to degrade quickly, with the muon efficiency dropping at an average rate of 1.2% per month and growing numbers of plates being declared "dead" (efficiencies less than 10%). The RPCs in the endcaps were replaced by new RPCs built with more stringent quality constraints, except for the first five, in whose place brass was placed to improve pion rejection. A different solution was adopted for the barrel RPCs. These were substituted by limited streamer tubes.

4.8.4 Limited streamer tubes

The principle of operation of limited streamer tubes is similar to that of the RPCs. In the case of *BABAR*, a conducting wire with a 100 $\mu\mathrm{m}$ diameter is placed in a long resistive cell (the "tube"), with a section of $15 \times 17\,\mathrm{mm}^2$, the wire playing the role of the anode, and the tube, of the cathode. The volume between them is filled with a gas that is ionized upon the passage of a charged particle or the spread of a hadronic shower, altering the charge distribution in the cylindrical capacitor. The signal can then be read either by external strips attached to both sides, or from the wires directly. In *BABAR*, the latter method is used to measure the ϕ coordinate, and the former, to read the z coordinate.
Their efficiency is monitored by using di-muon events and cosmic rays, finding an average of 90%, without any noticeable degradation trend over time.

4.9 Trigger

The aim of the trigger is to reduce the potential number of events per second reconstructed by the detector, which is essentially determined by the frequency of bunch crossing, to a manageable level of events that can be recorded. Of course, the goal of the trigger is to reject badly reconstructed events and background while retaining as much signal as possible.

In *BABAR*, that is achieved through a two-stage trigger, composed of the level-1 trigger (L1T), implemented in hardware, and the level-3 trigger, which is carried out by software, and after which all surviving events are recorded.

4.9.1 Level-1 trigger

The level-1 trigger consists of a global trigger (GLT) that combines the input from several individual triggers linked to the different subsystems of the detector, and accepts events at rates around 1 kHz, its limit being 2 kHz. The individual triggers feeding the global one are the DCH trigger (DCT), the EMC trigger (EMT) and the IFR trigger (IFT). These are continuously producing abstract data (*primitives*) describing the objects found by the subdetectors they are associated to, and are passed to the GLT. The global trigger then tries to match them to any of 24 *trigger lines* that represent events of interest, and if the timing of the trigger signal coincides with one bunch crossing, the fast control and timing system issues an *accept* signal. It is at this point that some classes of physics events, such as typical QED processes that are used only in calibration, are scaled down, making their acceptance less likely.
The DCT produces its primitives by looking for sequential DCH hits in neighboring cells. These are then joined if possible to construct either short tracks, that traverse only a few superlayers, and long ones, that reach the end of the chamber. Axial superlayers are also examined looking for segments consistent with tracks with transverse momenta greater than $800\,\mathrm{MeV/c}$.
The EMT sums the energy deposited on 40 strips along the ϕ polar angle, and finds a peak whose energy is compared to thresholds for different physics processes: minimum ionizing particle cluster ($\mathrm{E} > 120\,\mathrm{MeV}$), intermediate energy cluster ($\mathrm{E} > 307\,\mathrm{MeV}$), high energy electron or photon ($\mathrm{E} > 768\,\mathrm{MeV}$), minimum ionizing particle in forward endcap ($E > 100\,\mathrm{MeV}$) and backward high energy cluster ($\mathrm{E} > 922\,\mathrm{MeV}$).
The IFT primitives are just single clusters or back-to-back coincidences. These select cosmic ray events for calibration purposes, and $\mu^+\mu^-$ events.
The different trigger subsystems are optimized to select high multiplicity, multi-hadronic events, resulting in efficiencies over 99% for $\mathrm{B\overline{B}}$ events for both the DCT and the EMT individually, and over 99.9% when combined.

4.9.2 Level-3 trigger

The level-3 trigger must reduce by $\gtrsim 10$ the number of events accepted by the L1T. It is implemented in software and run in computing farms, which allow the use of information from all the subdetectors. Examples are the rejection events with tracks not originating from the interaction point, as these are likely to be machine background, or events whose timing does not match a bunch crossing.
Level-3 trigger lines may also be prescaled to reduce the rate of less interesting physics events, such as Bhabha scatterings. Calculation of efficiencies requires accepting events that do not satisfy any of the level-3 criteria. These are known as *L1 passthrough* events.

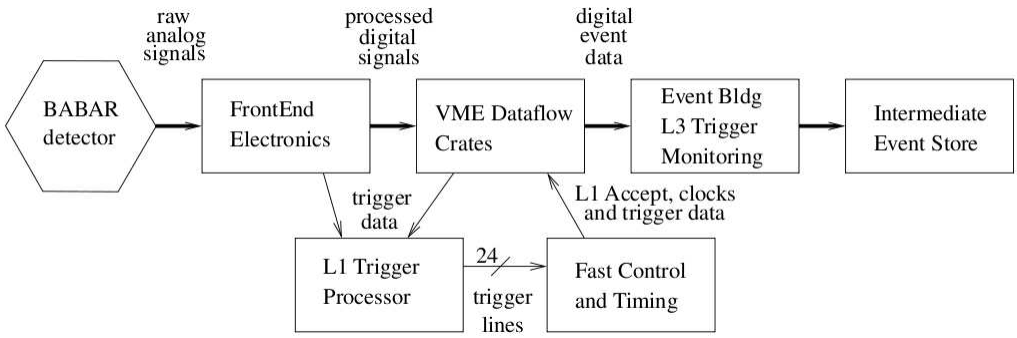

Figure 4.15: Schematic explanation of the interplay between the detector, the triggers and the first stages of the reconstruction process, known globally as the data acquisition system.

4.10 Data Aqcuisition

By data acquisition (DAQ) system we refer to the overall architecture by which the detector, the triggers and the computing structure are governed. The diagram in Fig. 4.15 schematically depicts it. The front end electronics process and digitize the signals coming from the detector and passes them to the the level-1 trigger and the data flow buffers. If an accept signal is issued by the fast control and timing, the event is passed to the level-3 trigger, which also performs some basic data quality monitoring. Finally, if the event is accepted by the L3T, it is written to disk, where it will be passed to the online prompt reconstruction software in a matter of days. The DAQ is also responsible for recording the detector conditions, that will be used in the production of simulated data to better reproduce the running conditions (see Sec. 7.2.2).

4.11 Online Prompt Reconstruction

After a data sample, typically consisting of around an hour of experiment running, has been logged on to disk, it goes through a prompt calibration processing, during which some of the calibration methods mentioned earlier in the chapter are run, and part of the data quality monitoring is performed. Following that, the data continue to event reconstruction, where tracks and clusters are found, and particle identification information (PID) is calculated. An event, by then essentially a collection of tracks, EMC clusters and IFR clusters, is stored in a database that will be accessed by the analysts reconstruction code to form *candidates* for events of a given decay channel (see Sec. 7.3). Once all these quantities have been calculated, a more detailed data quality check is made.

5 Radiation damage study of the SVT

5.1 Introduction

The SVT sub-detector is one of the most crucial parts of the *BABAR* experiment, as it provides the vertex position measurement that is necessary for time dependent analysis. In the $\mathrm{B}^0 \rightarrow \mathrm{K}^0_\mathrm{s}\mathrm{K}^0_\mathrm{s}\mathrm{K}^0_\mathrm{s}$ analysis it plays an important role, as it is the sub-detector that has the most impact on the reconstruction efficiency. To obtain a precise vertex measurement, the sub-detector is very close to the IP and hence the beam, and is exposed to a large radiation dose. The result is radiation damage that can be critical for the performance. The quality of the data is ensured by on-line and off-line data quality control which allows only the usage of data collected by parts of the SVT that have sustained non-critical radiation damage. The purpose of the present study is to determine how much radiation the most exposed parts of the SVT have absorbed and how severe the radiation damage is. This can be particularly interesting for future experiment with comparable radiation conditions to estimate the lifetime of their detector. The dominant source of radiation is the beam bending just before the IP. As a result the most irradiated parts of the SVT are the midplane modules that are situated along the x-axis, as the "bending axis" (parallel to the y-axis) is perpendicular to this plane. The modules used for the study are shown in Fig. 5.1. We cannot use all midplane modules, as half of them, the forward modules, have already sustained more than the critical radiation damage and our method uses data that can only be collected from working modules.

5.2 Theoretical aspects of radiation damage in silicon detectors

5.2.1 Selection of basic features of silicon detectors

Detectors in HEP work as follows: some particle interacts with the detector material while passing through, deposes energy, and we measure this energy. A common approach is to use such kind of detector materials that the energy loss is mainly through ionization, this way, if the charges can be separated and collected, a measurement of the current gives a measurement of the deposed energy. Silicon (or semi-conductor in general) detectors are particularly adapted for this task, as they have an internal electric field that can separate the charges created by passing-through charged particles. This electric field is created by the connection of n-type and p-type material which creates a n-p junction. n-type material is silicon that has been doped with a an element that has more valence electrons than silicon (the donor, e.g. As), p-type material is silicon that has been doped with an element that has one valence electron less than silicon (the acceptor, e.g. B). While in n-type silicon this adds

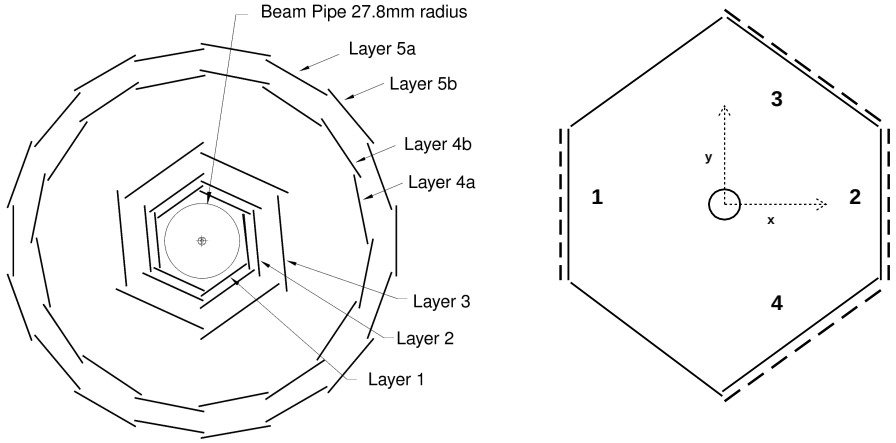

Figure 5.1: On the left is shown a reminder of the SVT layout, while on the right is shown a schematic of layer 1 that is subject to the radiation damage study. The orientation is chosen in the way that the electrons come out of the schematic and move along the positive direction of the z-axis. The modules used for the study are the midplane modules number 1 (L1M4B) and number 2 (L1M1B) and non-midplane modules number 3 (2 modules, L1M2F and L1M2B) and number 4 (2 modules, L1M6F and L1M6B). The nomenclature for the modules is L(ayer)[#]M(odule)[#]F(orward)/B(ackward). The individual chips are indicated by the short broad lines parallel to the modules. The orientations with respect to the beams, i.e. the forward and backward directions, are shown in the detector chapter (Fig. 4.6).

electrons that can move into the valence band and are highly mobile, in p-type silicon there are "missing" electrons, so-called holes. When the n-type and p-type silicon is connected, thermal equilibrium is established when electrons and holes recombine. This builds up a space charge due to the flow of charged particles in a before locally neutral[1] medium, until the potential difference Φ created by this space charge prevents further charge flow. In the stable system (part of) the donor and acceptor atoms are ionized and the electric field between them depletes this regions, the potential difference is called built-in voltage $\mathrm{V_{bi}}$. A larger depleted area can be obtained by doping one side more heavily than the other and creating a so-called $\mathrm{p^+n}$ abrupt junction where, due to overall charge neutrality, the depleted region of thickness W extends much further into the less heavily doped region as displayed schematically for a reversed biased abrupt $\mathrm{p^+n}$ diode in Fig. 5.2 (top plot on the left hand side) where it has been assumed a homogeneous distribution of dopant atoms and that the depletion approximation is valid. This approximation assumes that the space charge is constant in the region 0<x<W. In silicon detectors, the region W is increased by applying an additional external voltage, the so-called reverse bias voltage V that leads to a fully depleted silicon and W being a function of this voltage we write W(V) from now on. The system is described by the Poisson equation for the potential $\Phi(\mathrm{x})$:

$$-\frac{\mathrm{d}^2\Phi(\mathrm{x})}{\mathrm{dx}^2} = \frac{\rho_{\mathrm{el}}}{\epsilon\epsilon_0} = \frac{\mathrm{e}\cdot\mathrm{N_{eff}}}{\epsilon\epsilon_0}\ , \tag{5.1}$$

where $\mathrm{N_{eff}}$ is the effective doping concentration which is given by the difference between the concentration of ionized donors and acceptors in the space charge region and $\epsilon = 11.9$ is the permittivity of silicon. Integration of Eq. 5.1 using the boundary conditions $\mathrm{E(x = W)} = -\frac{\mathrm{d}}{\mathrm{dx}}\Phi(\mathrm{x = W}) = 0$ yields an expression for the electrical field strength that depends linearly on x (central plot on the left hand side of Fig. 5.2). The maximum field strength at the $\mathrm{p^+ - n}$ interface (x=0) is given by

$$\mathrm{E_m(V)} = -\frac{\mathrm{e}\cdot\mathrm{N_{eff}}}{\epsilon\epsilon_0}\mathrm{W(V)}\ . \tag{5.2}$$

A further integration using the boundary condition $\Phi(\mathrm{x = W}) = 0$ yields a parabolic function for the potential:

$$\begin{cases} \Phi(\mathrm{x}) = -1\frac{1}{2}\frac{\mathrm{e}\cdot\mathrm{N_{eff}}}{\epsilon\epsilon_0}(\mathrm{x}-\mathrm{W})^2 \\ 0 \le x \le W \wedge W \le d\ , \end{cases} \tag{5.3}$$

where d is the thickness of the silicon. The corresponding electron potential energy ($-\mathrm{e}\cdot\Phi \equiv \mathrm{q_0}\cdot\Phi$) is shown in Fig. 5.2 (bottom left). Using the condition $\Phi(\mathrm{x} = 0) = -\mathrm{V_{bi}} - \mathrm{V}$ the depletion depth can be expressed as function of the bias voltage:

$$\begin{cases} \mathrm{W(V)} = \sqrt{\frac{2\epsilon\epsilon_0}{\mathrm{e}\cdot\mathrm{N_{eff}}}(\mathrm{V}+\mathrm{V_{bi}})} \\ W \le d\ . \end{cases} \tag{5.4}$$

When the bias voltage is increased until $\mathrm{W} = \mathrm{d}$, the diode is fully depleted and the corresponding voltage is called *depletion voltage* $\mathrm{V_{dep}}$:

$$\mathrm{V_{dep}} + \mathrm{V_{bi}} = \frac{\mathrm{e}}{2\epsilon\epsilon_0}|\mathrm{N_{eff}}|\mathrm{d}^2\ . \tag{5.5}$$

[1] Is is still globally neutral after recombination and has been globally and locally neutral before creation of the junction.

In many cases (and in this work) the build-in voltage V_{bi} is neglected as it is much smaller than the bias voltage. The right hand side of Fig. 5.2 shows a schematic of the working principle of a silicon detector, for shortness we do not further go into detail.

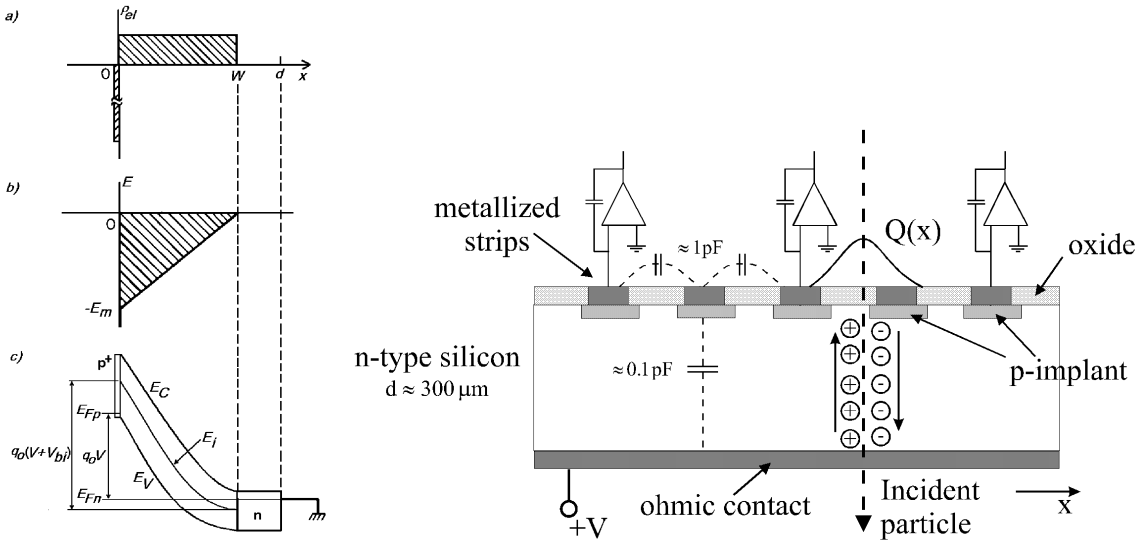

Figure 5.2: On the left: Schematic figure of a $p^+ - n$ abrupt junction with a) electrical charge desity, b) electric field strenth and c) eletron potential energy.
On the right: Schematic cross section of silicon microstrip detector.
Both figures are taken from [42].

5.2.2 Damage mechanism

Radiation damage can be roughly separated into surface and bulk damage. We consider only bulk damage as it is the limiting factor for silicon detectors in HEP experiments [42].
The bulk damage produced in silicon particle detectors by hadrons (neutrons, protons, pions and others) or higher energetic leptons is caused primarily by the displacement of an atom out of it's lattice site resulting in a silicon interstitial and a left over vacancy (Frenkel pair). Both can migrate through the lattice and may finally form point defects with impurity atoms being resident in the silicon. For detail on the damage mechanism see [42].

Ionizing and non-ionizing radiation

The radiation is composed of both charged and neutral particles. Charged particles interact mainly through Coulomb interaction at lower energies. Thus, most of the energy of the particle is lost due to ionization of lattice atoms which is a fully reversible process and does not need to to be considered for this study. On the other hand some of the deposed energy, both from charged and neutral particles, introduces permanent damage and are relevant for this study. To describe the permanent part, it is convenient to normalize all interactions, of

both charged and neutral particles, to the neutron, as it is interacting in a non-ionizing way only. The main reactions are elastic scattering and above 1.8 MeV also nuclear reactions. The equivalent fluence Φ_{eq} defined as the fluence of 1 MeV neutrons that would have had the same effect on the material. The fluence of a radiation is the number of particles that passed through a given surface. The connection between the actual fluence Φ and Φ_{eq} is done by so-called hardness factors κ that describe the radiation source.

$$\Phi_{\mathrm{eq}} = \kappa\Phi = \kappa \int \phi(\mathrm{E})\mathrm{dE} \,, \tag{5.6}$$

where ϕ is the energy spectrum of the source. In this study, the radiation sources are mainly beam backgrounds which originate from the beam bending and/or are the result of showers created when a beam electron or positron interacts with material, such as the beam pipe or the supporting structures. The particle composition and energy spectra of the radiation is unknown, and therefore the average effective value of κ has to be measured.

The NIEL scaling hypothesis

The radiation damage is produced by different particles at different ranges of energy by various kinds of interactions. The so-called Non Ionizing Energy Loss (NIEL) hypothesis leads to an effective model of radiation damage that describes well the radiation-induced changes observed in the material. The assumption is, for a given type of an incoming particle, that any displacement-induced change in the material scales linearly with the amount of energy imparted in displacing collisions, no matter what the actual displacement mechanism is.
In this study, we examine the consequences of the radiation-induced displacements on the doping concentration, as the doping determines the depletion voltage.

Dependence of the effective doping on the fluence

The change observed in the absolute value of the effective doping concentration $|\mathrm{N_{eff}}|$ of bulk material as a function of the exposition to a given fluence is shown in Fig. 5.3. In initially n-type silicon, at lower fluences, $\mathrm{N_{eff}}$ is reduced by donor-removal and acceptor like states are generated. At higher fluences this leads to an effective inversion of the bulk type in the material. Due to annealing effects, $|\mathrm{N_{eff}}|$ is in principle time-dependent. The lifetime of the annealing effect is of the order of tens of minutes. As the measurements that are used for this study have been done during shut down periods, we only need to consider the stable part, which is given by:

$$|\mathrm{N_{eff}}| = \mathrm{N_{C_0}}(1 - \exp(-\mathrm{c}\Phi_{\mathrm{eq}})) + \mathrm{g_c}\Phi_{\mathrm{eq}} \tag{5.7}$$

N_{C_0} is the stable damage parameter. c is the removal constant and describes how easily lattice atoms can be removed; g_c is the introduction rate of stable acceptors and describes how many of stable damage induced acceptors are created. Both c and g_c are material constants and have to be found experimentally.

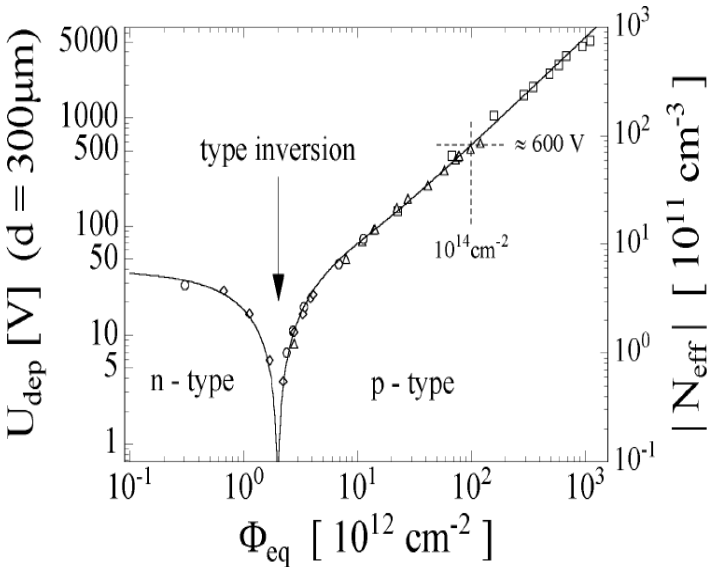

Figure 5.3: Depletion voltage $\mathrm{V_{dep}}$ and effective doping concentration $\mathrm{N_{eff}}$ as function of $1\,\mathrm{MeV}$ neutron equivalent fluence measured directly after irradiation. Plot taken from [42].

Dependence of the depletion voltage on the absorbed dose

Experimentally we measure V_{dep} in volts and we want to express it as a function of the absorbed dose D in [rad] ($[\equiv 0.01\mathrm{J/kg}]$). We use the relation between $\mathrm{V_{dep}}$ and $\mathrm{N_{eff}}$, Eq. (5.5), and between the dose and the fluence[2]

$$\Phi[\frac{1}{m^2}] = \frac{D[rad]}{1.6 \cdot 10^{-8} dE/dx[\,\mathrm{MeV}cm^2/g]} \tag{5.8}$$

where the thickness d=0.03cm and the energy loss dE/dx=$1.861\,\mathrm{MeV}cm^2/g$ (at the ionization minimum) are material properties of the silicon wafers. We express the hardness factor κ by means of a new hardness factor a that has the value 1 for a pure irradiation by $900\,\mathrm{MeV}$ electrons[3]. To compute the conversion factor between κ and a between the electron and neutron NIEL we take the value from [44]:

$$\frac{\mathrm{NIEL}(900\,\mathrm{MeVe^-})}{\mathrm{NIEL}(1\,\mathrm{MeVn})} = 8.106 \cdot 10^{-2} \tag{5.9}$$

Also, due to different interaction mechanisms the same amount of NIEL does not produce the same damage for neutrons and electrons. It has been estimated in Ref. [45] that electrons produce approximately only one third of the damage with the same amount of NIEL as neutrons. This results in

$$\kappa = \mathrm{a} \cdot 2.7 \cdot 10^{-2}\,. \tag{5.10}$$

[2]Dose equals fluence times energy loss.

[3]This redefinition is for "historical" reasons. A test-bench measurement [43] of $\mathrm{V_{dep}(D)}$ has been performed with a 900 MeV electron beam and the new hardness a is defined relative to this measurement

Putting together Eq. (5.5), Eq. (5.8) and Eq. (5.10) with Eq. (5.7) we have the relation between $\mathrm{V_{dep}}$ and the absorbed dose D:

$$\mathrm{V_{dep}(D)} = \frac{\mathrm{e}\cdot\mathrm{d}^2}{2\cdot\epsilon_0\epsilon_\mathrm{r}}\mathrm{N_{C_0}}(1-\exp(-\mathrm{c}\cdot\frac{2.710^{-2}\mathrm{a}\cdot\mathrm{D}}{1.6\cdot10^{-8}\cdot(\mathrm{dE/dx})})) + \mathrm{g_c}\cdot\frac{2.710^{-2}\mathrm{a}\cdot\mathrm{D}}{1.6\cdot10^{-8}\cdot(\mathrm{dE/dx})} \tag{5.11}$$

The material dependent parameters $\mathrm{g_c}$, c and $\mathrm{N_{c0}}$ are taken from Ref. [42], their values are shown in Tab. 5.1. As can be seen in Tab. 5.1 the c and $\mathrm{N_{c0}}$ parameters depend on the

Parameter	Value
$\mathrm{g_c}$	$1.5\cdot10^{-2}\mathrm{cm}^{-1}$
$\mathrm{c}\times\mathrm{N_{eff0}}$	$11\cdot10^{-2}\mathrm{cm}^{-1}$
$\mathrm{N_{c0}}\times\mathrm{c}$	$7.5\cdot10^{-2}\mathrm{cm}^{-1}$

Table 5.1: Material dependent parameters taken from [42], $\mathrm{N_{eff0}}$ is the initial effective doping that is calculated from the initial depletion voltage.

initial doping concentration and with it on the initial depletion voltage $\mathrm{V_{dep}}(0)$. The values of $\mathrm{V_{dep}}(0)$ have been measured for each wafer by the SVT group before installing them. Each module is made of several silicon wafers that are bonded to form a module [46]. For technical reasons, for each module, these wafers come from two different productions and may have different effective doping. We assign the higher $V_{\mathrm{dep}}(0)$ for the module, as this is the one that dominates the noise. Once the a parameter is determined, we can access the dose corresponding to inversion by solving the null problem $\mathrm{V(D)} = 0$ numerically. This corresponds to solving the equation

$$0 = \mathrm{A}(1-\exp(-\mathrm{Bx})) + \mathrm{Dx} \tag{5.12}$$

for x. There are several solutions $\mathrm{x_i}$:

$$\mathrm{x_i} = -\frac{\mathit{RootOf}\left(-\_Z\ (\mathrm{D}) + \mathrm{A}\left(1-\mathrm{e}^{-Z}\right)\mathrm{B}\right)}{\mathrm{B}}\ , \tag{5.13}$$

where RootOf stands for all the roots in some variable $\_Z$. We solve this equation numerically using Maple [47] and choose the correct solution (positive and non-zero).

5.3 Measurement and analysis

5.3.1 Overview and analysis strategy

To ensure a completely depleted detector when taking data, the bias voltage V_{bias} is chosen to be approximately 10 V higher than the depletion voltage V_{dep}. The bias voltage can be adapted on-line individually for each module in case the data quality monitoring shows that a module is not completely depleted. The actual depletion voltage remains unknown. During shutdown periods, the SVT does not need to be depleted. This offers the possibility to

measure the actual depletion voltage of the individual modules indirectly by measuring the electronic noise as a function of the applied bias voltage. When decreasing the bias voltage in steps of 1 or 2 V, the noise suddenly increases when the bias voltage falls below the depletion voltage.
As shown in Fig. 5.3, the depletion voltage is a function of the absorbed dose. By measuring the depletion voltage we have (in principle) access to the absorbed dose, as we know the initial depletion voltage of the modules from measurements that have been done before installing the modules. There are three main complications that constrain the study:

1. **Ambiguity of $\mathrm{V_{dep}}$ Eq. 5.11:** As can be seen in Fig. 5.3 we cannot read unambiguously the dose that is connected with a given V_{dep}.

2. **The composition of the radiation is unknown:** As the hardness a of the radiation is unknown, it has to be extracted from data.

3. **The embedded radiation measurement in the midplane modules is not reliable**

These three complications are interconnected; we can, in principle, resolve the first two by the direct dose measurement that is provided by the diodes/diamonds that are embedded in the support structure of the SVT (see detector chapter, Fig. 4.6). The raw dose measurement for the midplane modules is shown in Fig. 5.4. Unfortunately, this measurement is, at least for the midplane modules, not very reliable for two reasons. Firstly, for the midplane modules, the radiation profile varies strongly from chip to chip. We correct for that by using occupancy measurements (detailed in Sec. 5.3.3). Secondly, the diodes/diamonds are located at some distance to the modules. This can be taken care of by a correction factor, assuming the knowledge of the hardness factor a, as the shape of the curve (we can assume the dose measurement of a given module are relatively correct) and the initial $\mathrm{V_{dep}}$ at zero absorbed dose are known. The problem is that we do not know the hardness factor a and have to measure it. Clearly we cannot use the same dose measurement (the one from the diode/diamonds for the midplane modules) twice, i.e. we need to add more information to get an independent measurement for a. The solution is to use two non-midplane modules for the measurement of a. The advantage is that these modules have absorbed less radiation. We have tested that the radiation profile is approximately uniform and estimate that the embedded dose measurement is reasonably reliable. A disadvantage is that the assumption has to be made that the radiation hardness does not depend on the position, i.e. the hardness factor a is the same for midplane and non-midplane modules. As SVT experts estimate the uncertainty of the absolute embedded dose measurement to be up to 30%, we decide to assign a conservative 30% error for the dose measurements. In summary: we have to make a number of assumptions in order to do this study with the given data. As result we do not feel comfortable to give an actual dose measurement. On the other hand we have determined whether or not the midplane modules L1M1 and L1M4 have undergone type inversion or not.

5.3.2 Extraction of V_{dep} from noise measurements

The electronic noise is measured internally in the ATOM [48] chips. Each layer-1 module has 7 chips (0-6), i.e. we have 7 measurements for each module (in reality some chips are

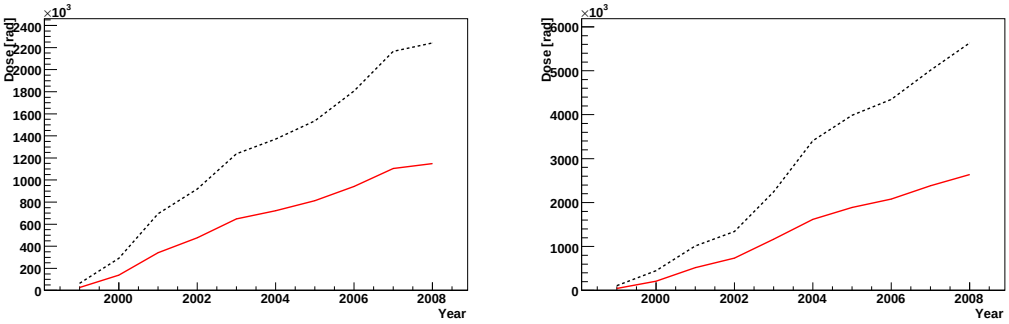

Figure 5.4: On the left is shown the accumulated dose measurements of the diode/diamond closest backward module of L1M1. The raw dose measurement (black dashed) is shown along with a distance-corrected dose measurement (red solid), where the distance-corrected dose, that is expected to have been absorbed by the module, is evaluated by an algorithm that takes into account the distance between module and diode/diamond and also information from other diodes/diamonds besides the closest one. On the right is shown the same for L1M4. As we show in Sec. 5.3.3 this correction overestimates the absorbed dose by $\sim 20\%$.

not operational and we have less measurements). The noise is scanned as function of V_{bias} by applying bias voltages in steps of 1 or 2 V from zero to 60 V.
In order to look for a sudden increase of noise as function of $\mathrm{V_{bias}}$, we use an algorithm that compares the noise in neighboring voltage steps to decide on whether V_{dep} has been reached. The algorithm moves from high voltage, where the noise is small and constant, to low voltage. When the change in noise passes a certain level, we take the voltage of the previous bin as an the estimation of V_{dep}. This level is defined using the absolute minimum and maximum noise of the individual chip. To estimate the error of the V_{dep} values, we perform iterative fits with a straight line where we include each time one more bin going from high to low voltage. When the probability of the fits gets lower than 68%, we stop the fits and assign the difference between the last added bin and the estimated V_{dep} as an error. This procedure has been checked on modules that are not used for the study. The result for a particular chip is shown in Fig. 5.5.

5.3.3 Data analysis

Fit to non-midplane modules

We use the dose and V_{dep} measurements from the two non-midplane modules L1M2 and L1M6. As each module has forward and backward sides, this gives us 4 effective modules.
We use a χ^2 fit of Eq. 5.11 to the data to estimate a. Each data point has errors in both voltage and dose. These are taken into account by the *effective variance method* [49], where, for the fit, an effective uncertainty on the voltage is calculated that takes into account the uncertainties in the dose measurements. The different $\mathrm{V_{dep}}(0)$ of each module is taken into account

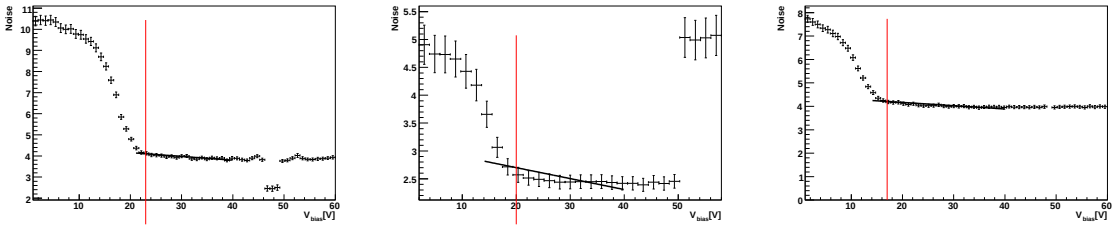

Figure 5.5: Noise scan for one particular chip (L1M4B, Chip 6) for the three series of measurements that are included in this study. The red dotted line marks the estimated depletion voltage, the black line is used to determine the uncertainty of this estimation. The plots are ordered from left to right according to increasing absorbed radiation. The corresponding decrease of $\mathrm{V_{dep}}$ can be observed by eye.

by an additional dimension in the fit. This way we can fit simultaneously the parameter a for all the modules. We find:

$$\mathrm{a} = 6.07 \pm 0.57 \tag{5.14}$$

This means that the radiation is $\sim$6 times harder than a pure 900 MeV electron beam. Projections of the fit result on each module are shown in Fig. 5.6.

Adding the midplane modules

With the hardness a measured, we fully determine the function Eq. 5.11. We could now, for each V_{dep} measurement done in the midplane, give two possible values for the absorbed dose. The problem is that, especially for the latest measurement, corresponding to the highest dose, it is not at all clear if the data point is before or after type inversion. Therefore we decide to use additional information from the embedded dose measurement. We then have data points (V_{dep},D) that we can superimpose to Eq. 5.11. As we then have the relative position of the data points in the midplane, we can determine how likely it is that the last point is before or after type inversion.
We know that the radiation profile is very non-uniform in the midplane. We use the occupancy profile of the SVT chips to do a relative correction, assuming that the occupancy profile is proportional to the absorbed dose. We take chip three, which is the most irradiated one as a reference, given that it is the closest to the diode/diamond. The occupancy profiles of the modules that are subject to this study are shown in Fig. 5.7 Additionally the diode/diamond is at some distance to chip 3 (orthogonal to the "chip axis"). As a result the dose measurement is not exact, but scaled by a multiplicative factor that is the same for all the chips. To summarize, each chip of the same module is corrected by a global factor (to account for the distance between the module and the diode/diamond) and a relative factor (to account for the non-uniformity of the radiation).
The global factors are found by two fits, one for each midplane module. As input of the fit are used the occupancy-corrected doses for each chip and V_{dep}. We define a common factor for all the chips in a module. This factor is being varied to minimize the distance between

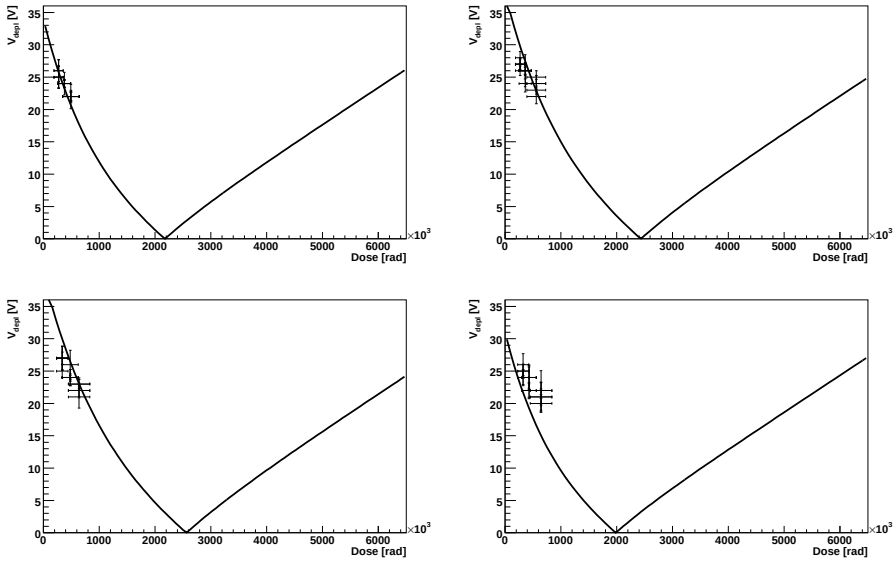

Figure 5.6: Projections on forward and backward parts of the used non-midplane modules: L1M2F (top left), L1M2B (top right), L1M6F (bottom left) and L1M6B (bottom right). The fit is done simultaneously for all modules. Each chip corresponds to a point with error bars. We include only working chips with reliable measurement of V_{dep}.

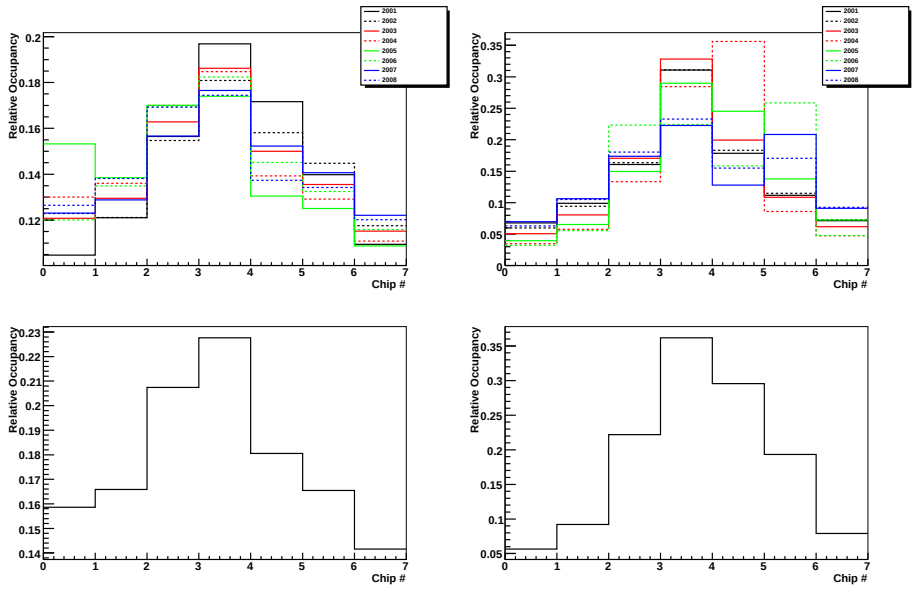

Figure 5.7: Occupancy profiles shown year by year (top) and integrated (bottom). The distributions on the left correspond to L1M1B and the ones on the right to L1M4B.

the data points and the function of Eq. 5.11. We find a scale factor of 0.788 for L1M1 and 0.698 for L1M4.
The result when applying both corrections is shown in Fig. 5.8.

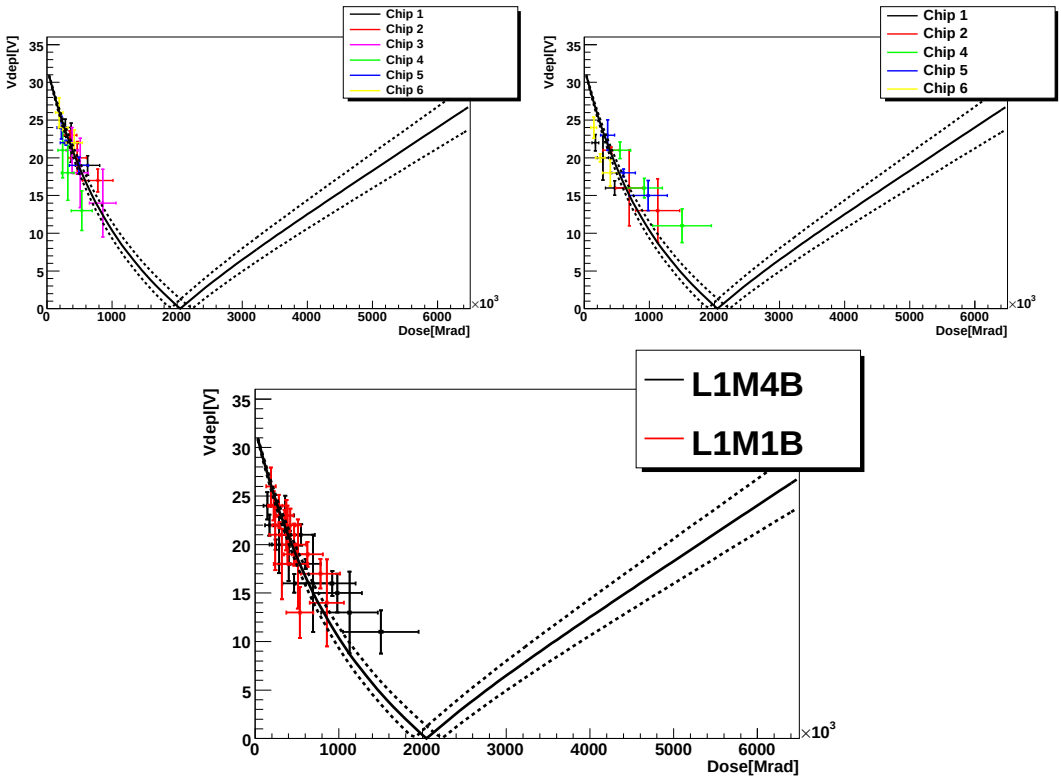

Figure 5.8: Occupancy and global scale corrected chips from L1M1 (upper left) L1M4 (upper right) and both modules (lower plot) superimposed. They are compared to the theoretical model with the hardness-factor fitted on non-midplane modules (solid line) where the uncertainties of the fit have been propagated (dashed line). Each chip corresponds to a point with error bars.

5.4 Results

To determine the probability that the midplane-modules have already passed the minimum of the curve, i.e. that inversion already took place, we scan[4] the χ^2 for different values of the fitted parameter a around the nominal value. This corresponds to shifting the dose scale or, what is equivalent, shifting the hardness a. We say that the module has already undergone inversion if at least one data point is beyond the minimum of the curve. We then can use the difference in the χ^2 to express the probability for that, i.e. we compare two hypothesis:

[4] See likelihood scan technique in Sec. 7.6.2

- The first is the configuration at the minimum of the χ^2 scan that corresponds to the point $\mathrm{a} = 6.070$ found by scale-correction and yields a χ^2 of 27.8. Here the silicon has not undergone inversion as can be seen in Fig. 5.8.
- The second is the configuration where the point with the highest dose has passed the minimum, this corresponds to a value of $\mathrm{a} = 8.271$.

As can be seen in figure 5.9, the difference for both hypothesis in terms of χ^2 is 19.5 units. We can compare the corresponding probabilities[5] $\mathrm{P}_{\chi^2}(27.8) = 0.723$ and $\mathrm{P}_{\chi^2}(27.8+19.5) = 0.056$ and conclude that the first hypothesis is much more likely than the second one. In summary is it much more likely that backward modules of L1M1 and L1M4 have not passed the point of inversion at 2.048 ± 0.165 Mrad, than the hypothesis that either passed this point. The forward modules on the other hand were not subject to this study, and it is very likely that they have undergone inversion (some chips in these modules are no longer working).

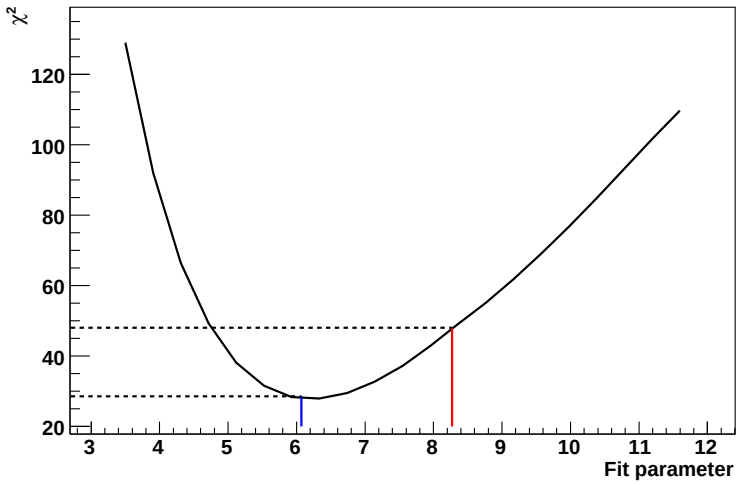

Figure 5.9: Scan of the χ^2 for the fit parameter for 2 scale-corrected midplane modules. The blue line is the value for the scale-corrected midplane-module data points wrt the model fitted to non-midplane modules. The red line is the value of the fit parameter so that the minimum of the curve would correspond to the highest dose-value for the scale-corrected points.

[5] In the scan there are 33 degrees of freedom corresponding to the number of data points

6 Study of the π^0 reconstruction efficiency

Primer: For shortness and to keep this chapter in the detector context, some knowledge of reconstruction and likelihood fitting techniques is assumed. These subjects are introduced later in this document, in the context of the core analyses. Also we use some *BABAR* "jargon", in particular particle list, that are defined in the appendix.

6.1 Introduction

6.1.1 Motivation for the study

The correct simulation of neutral particles with non-zero lifetime is a crucial point for many *BABAR* analyses. As neutral particles have no tracks, they have to be reconstructed indirectly from their decay products. The reconstruction and simulation of π^0s is particularly difficult, as even the decay products are neutral photons. The photons are detected as clusters in the EMC, and in the absence of any track, the uncertainty of the momentum measurement is large. The only information on the direction of the photons comes from the cluster shape. It is known in *BABAR* that there is some disagreement between fully reconstructed MC and data in kinematical observables that leads to a bias in the reconstruction efficiency estimated from MC. As a result the collaboration assigns a systematic error of 3% on the π^0 reconstruction efficiency. This systematic uncertainty has been estimated using τ-decays, that provide a clean environement (low backgrounds and low multiplicity) and allow for a precise measurement of the double ratio $\mathrm{R}(\mathrm{p}(\pi^0))$

$$\mathrm{R}(\mathrm{p}(\pi^0)) = \frac{\mathrm{R}(\mathrm{p}(\pi^0))_{\mathrm{data}}}{\mathrm{R}(\mathrm{p}(\pi^0))_{\mathrm{MC}}} \, . \tag{6.1}$$

The individual ratios are defined as

$$\mathrm{R}(\mathrm{p}(\pi^0))_{\mathrm{MC/data}} = \frac{\frac{\mathrm{dN}(\tau \to \mathrm{X}\pi^0)_{\mathrm{MC/data}}}{\mathrm{d}(\mathrm{p}(\pi^0))}}{\mathrm{N}(\tau \to \mathrm{X})_{\mathrm{MC/data}}} \, , \tag{6.2}$$

where N are the signal yields found in data and MC and X are particles other than the π^0 of the tau decay, for instance $\mathrm{K}/\pi\ \nu$ or $\mathrm{e}/\mu\ \nu\nu$. As $\mathrm{R}(\mathrm{p}(\pi^0))$ is expected to be dependent on the π^0 momentum, this dependence is taken into account.

The interest of using a double ratio is to get an estimate of the bias due to π^0 simulation

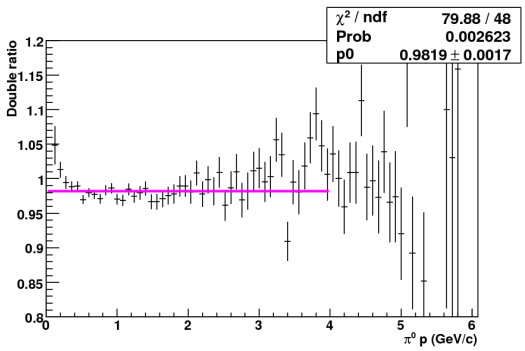

Figure 6.1: Double ratio from τ decays as a function of the π^0 momentum. The magenta solid line is the result of a fit using a flat line.

only; any other simulation defects are expected to cancel out. The τ analysis has been done with several channels and the combined result is shown in Fig. 6.1. The τ decays used for this study were low multiplicity events that provide a clean environment and it cannot be assumed that the same difference between MC and data exist in high multiplicity hadronic events. Hence a crosscheck is needed to confirm this hypothesis. The present study aims to determine the double ratio with $\mathrm{D}^0 \to \mathrm{K}^\pm\pi^\pm\pi^0$ and $\mathrm{D}^0 \to \mathrm{K}^\pm\pi^\pm$ decays

$$\mathrm{R}(\mathrm{p}_{\pi^0}) = \frac{\frac{\mathrm{N}_{\mathrm{K}\pi\pi^0}(\mathrm{p}_{\pi^0})}{\mathrm{N}_{\mathrm{K}\pi}} \cdot \frac{\mathrm{Br}(\mathrm{K}\pi)}{\mathrm{Br}(\mathrm{K}\pi\pi^0)}\big|_{\mathrm{data}}}{\frac{\mathrm{N}_{\mathrm{K}\pi\pi^0}(\mathrm{p}_{\pi^0})}{\mathrm{N}_{\mathrm{K}\pi}} \cdot \frac{\mathrm{Br}(\mathrm{K}\pi)}{\mathrm{Br}(\mathrm{K}\pi\pi^0)}\big|_{\mathrm{MC}}} \,. \tag{6.3}$$

6.1.2 Analysis strategy

We reconstruct $\mathrm{D}^0 \to \mathrm{K}^\pm\pi^\pm\pi^0$ and $\mathrm{D}^0 \to \mathrm{K}^\pm\pi^\pm$ decays from D^* that decay to D^0 and a slow $\pi^\pm$ (π_s in the following). We compare data and MC by extracting the signal yields in bins of π^0-momentum $\mathrm{p}(\pi^0)$ using 2-dimensional binned fits to the reconstructed mass of the D^0, $\mathrm{m}_{\mathrm{D}^0}$, and the difference between $\mathrm{m}_{\mathrm{D}^0}$ and the mass of the D^*, $\Delta\mathrm{m}$. We divide the MC and data samples in 20 bins of $\mathrm{p}(\pi^0)$, which contain approximately the same number of signal events. This way we expect comparable errors for all bins. The momentum ranges for the different bins are given in Tab. 6.2.

We use the PDF parameterizations that have been used in the *BABAR* mixing analyses of $\mathrm{D}^0 \to \mathrm{K}^\pm\pi^\pm\pi^0$ [50] and $\mathrm{D}^0 \to \mathrm{K}^\pm\pi^\pm$ [51]. We also adapt the selection criteria of the $\mathrm{D}^0 \to \mathrm{K}^\pm\pi^\pm\pi^0$ mixing analysis, as far as no π^0 properties are used, i.e. we do not use any information coming from the π^0 in the selection.

6.2 Reconstruction

6.2.1 Data samples

On-peak and off-peak data samples

We use the complete *BABAR* $\Upsilon(4S)$ data sample and the off-peak data taken 40 MeV below the $\Upsilon(4S)$. Details on the luminosity can be found in Tab. 6.1.

run	$\mathcal{L}_{\mathrm{on-peak}}$ $[pb^{-1}]$	$\mathcal{L}_{\mathrm{off-peak}}$ $[pb^{-1}]$
1	20590.263	2621.575
2	62061.168	7029.485
3	32632.993	2493.003
4	100782.897	10225.460
5	133753.256	14540.778
6	79013.588	7884.674

Table 6.1: Luminosity for the onpeak and offpeak data samples

Monte Carlo (MC) samples

We use the following simulated data samples:

- 708762k generic B^+B^- events (SP-1235)
- 717995k generic $B^0\bar{B}^0$ events (SP-1237)
- 1128544k generic $\mathrm{c\bar{c}}$ (SP-1005)
- 911218k generic uds events (SP-998)

To take into account the different luminosities of the different MC samples, we arbitrarily reject events in the generic $\mathrm{b\bar{b}}$ and $\mathrm{c\bar{c}}$ samples to obtain a complete generic MC sample with the correct proportions of events.

6.2.2 Reconstruction

We reconstruct $\mathrm{D}^0 \to \mathrm{K}\pi^{\pm}$ and $\mathrm{D}^0 \to \mathrm{K}\pi^{\pm}\pi^0$ simultaneously from the `AllEventsSkim`[1] (Run 1-6). We require:

- For the kaon: `GoodTracksVeryLoose`[2] and `KLHLoose`[2]
- For the pion: `GoodTracksVeryLoose` and `piLHLoose`[2]

[1] Defined in "techniques" section for the core analysis, Sec. 7.3
[2] Defined in appendix A

- For the π^0: `pi0VeryLoose`[2]

We then combine the D^0 with a π_s to a $\mathrm{D}^{*\pm}$ using the beamspot-constraint and require for the π_s:

- `GoodTracksVeryLoose`
- At least 6 hits in DCH and 6 hits SVT
- $\mathrm{p_T} > 0.05$ GeV

6.3 Selection and backgrounds

We use the same selection criteria as in Ref. [50] as far as the selection is applicable for the K and the π for both $\mathrm{D}^0 \to \mathrm{K}\pi$ and $\mathrm{D}^0 \to \mathrm{K}\pi\pi^0$.

6.3.1 Selection for $\mathrm{D}^0 \to \mathrm{K}\pi$

We require

- $\mathrm{K}^\pm$ that pass `KLHVeryTight`[2]
- $\pi^\pm$ that pass `piLHVeryTight`[2]

Additionally we apply the following selection criteria:

- $1.74 < \mathrm{m_{D^0}} < 1.98\ \mathrm{GeV/c^2}$
- $0.139 < \Delta\mathrm{m} < 0.155\ \mathrm{GeV/c^2}$
- $\mathrm{p(D^*)} > 2.5\ \mathrm{GeV/c}$ (only continuum events)
- $\mathrm{P}(\chi^2)_{\mathrm{K}\pi^\pm} > 0.01$
- At least 6 slow-π hits in the DCH
- Use $\frac{\mathrm{dE}}{\mathrm{dx}}$ information from SVT and DCH to reject slow electrons (|"Pull"|<2.58)

6.3.2 Additional selection for $D^0 \to K\pi\pi^0$

We require the π^0-candidate to pass the `Pi0VeryLoose` list and apply the following additional selection on the π^0-candidate:

- $\mathrm{LAT} < 0.8$
- $\mathrm{E}_\gamma > 0.1$ GeV
- $0.42 < \Theta(\gamma) < 2.4$

- $\mathrm{p}(\pi^0) > 0.25\ \mathrm{GeV/c}$

LAT is the lateral moment of the cluster that is reconstructed as a photon of the π^0 decay. It is defined as the ratio of two quantities:

1. The sum of energies of all but the 2 most energetic crystals, weighted by the square of the distance to the cluster center.

2. The Sum of all energies including the 2 most energetic crystals, weighted by r^2 where r is the length scale of a crystal (5 cm).

E_γ is the reconstructed energy of the photons of the π^0 decay. The selection on $\Theta(\gamma)$ is a geometrical constraint to only accept π^0 that are reconstructed in the barrel region of the EMC. Finally, we take only events into account where the momentum of the π^0 is larger than $250\,\mathrm{MeV/c^2}$ to avoid the SCF dominated low-momentum region.

6.3.3 Candidate selection

In case there are several candidates after the selection cuts, we keep one candidate per event and per decay mode. The distribution of the number of candidates after selection can be found in Fig. 6.2. Among the candidates that pass the selection, we choose the one with the highest $\mathrm{D}^0_{\mathrm{K}\pi}$-vertex-fit probability. In case there are several candidates with the same probability, they share the π_s-track. We then choose the candidate with the highest probability of the $\mathrm{D}^0_{\mathrm{K}\pi\pi_\mathrm{s}}$ vertex fit.
In the $\mathrm{D}^0 \rightarrow \mathrm{K}^\pm\pi^\pm\pi^0$-channel there may also be several candidates due to γ-combinatorics in the π^0 reconstruction. To avoid any bias the in the π^0 selection concerning, we apply an arbitrary selection which is based on the event timestamp. This arbitrary choice introduces

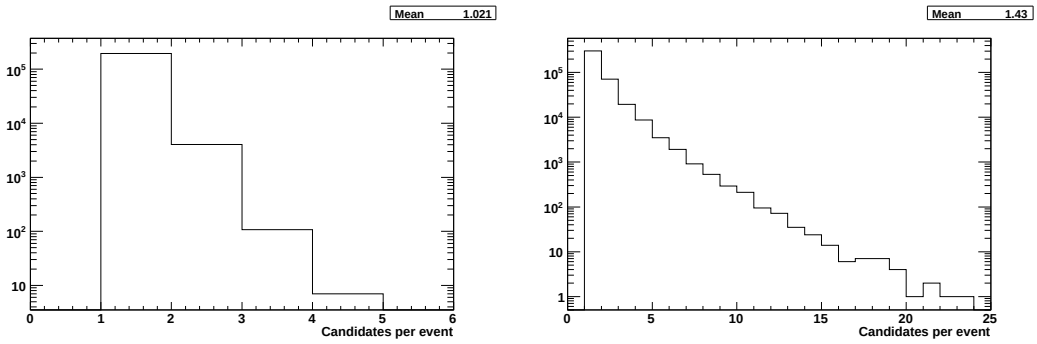

Figure 6.2: Number of $\mathrm{K}\pi^\pm$ (left) and $K\pi^\pm\pi^0$ (right) candidates after selection in signal MC.

a difference between data and MC due to different numbers of photons: there are more photons in data than in MC and this results in more combinatorial π^0 in data. It is therefore more likely to choose the "wrong" candidate[3] in data and real signal events can migrate to another

[3]It is of course possible that the "correct" candidate is not reconstructed at all, and that we choose only between "wrong" candidates.

species than signal, i.e. in one of the background categories (defined below, Sec. 6.3.4). We quantify the different probabilities to choose the "correct" candidate in data and MC, by looking at background subtracted data and signal MC for the chosen candidates and for all the candidates. For each bin of π^0 momentum we can then quantify the fraction of "wrong" candidates in data and MC. To subtract background we scale the generic MC samples to the data luminosity and subtract everything that is not signal. For the chosen candidates, the total event yields for background subtracted data and signal MC agree very well (0.368% difference). The chosen candidates in comparison with all candidates for data and MC are shown in the top of Fig. 6.3. We obtain the probability to choose the "correct" candidate by dividing the number of the chosen candidates by the number of all candidates for a given $\mathrm{p}(\pi^0)$ bin. We divide the probability for data by the probability for MC to obtain correction factors that we multiply with the MC event yield when calculating the double ratio. The corresponding distributions are shown in the bottom of figure Fig. 6.3.

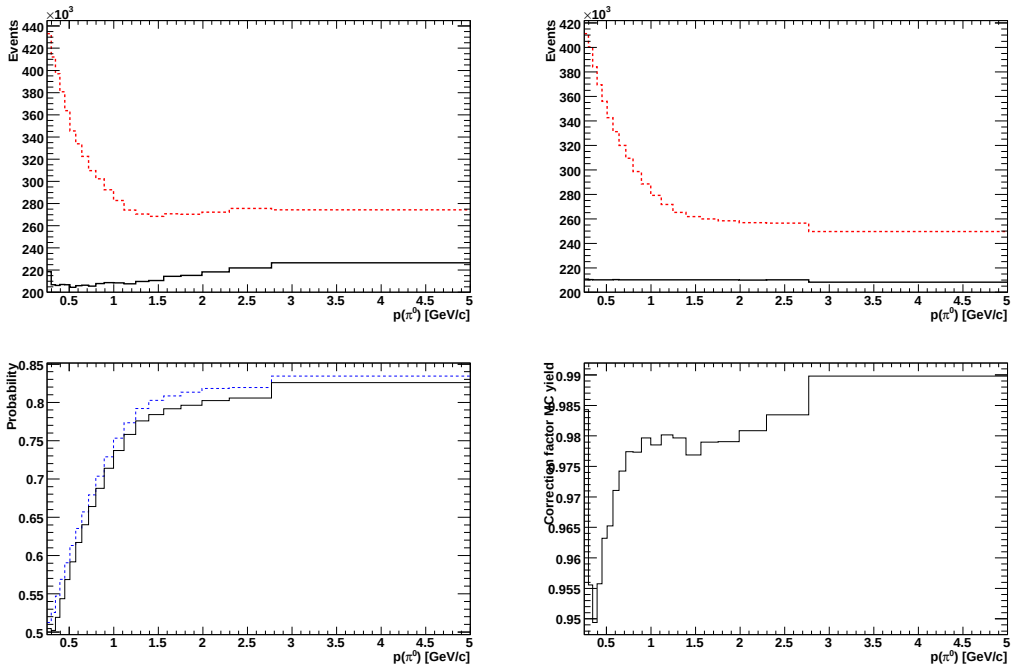

Figure 6.3: Number of chosen candidates (black solid) and of all candidates (red dashed) for background-subtracted data (top left) and MC (top right).
The probability to choose the "correct" candidate (bottom left) for data (black solid) and MC (blue dashed) and the MC-yield correction factor (bottom right).

6.3.4 Signal and background categories

The signal and 3 background categories are defined in the same way for the modes $\mathrm{D}^0 \to \mathrm{K}^{\pm}\pi^{\pm}\pi^0$ and $\mathrm{D}^0 \to \mathrm{K}^{\pm}\pi^{\pm}$. We use generator level ("true") information to separate the categories from the generic MC sample:

- **Signal:** We obtain our signal MC samples by filtering $\mathrm{c\bar{c}}$ generic MC, requiring signal decays in the generated level. We tolerate additional photons in the decay tree to avoid rejecting radiative events with photons generated by the PHOTOS module. This filtering procedure has been checked using exclusive MC signal samples. Distributions of $\mathrm{m_{D^0}}$ and Δm for signal events ($\mathrm{D^0 \to K^{\pm}\pi^{\pm}\pi^0}$ and $\mathrm{D^0 \to K^{\pm}\pi^{\pm}}$) are shown in Fig. 6.4. In the channel with π^0, there is a substantial amount of wrongly reconstructed events (SCF), particularly at low π^0-momentum. We therefore split the signal into truth-matched (TM) and SCF for the $\mathrm{p}(\pi^0)$ bins below a π^0 momentum of 0.9959 $\mathrm{GeV/c}$ (up to bin number 10). Distributions of TM and SCF events are shown in Fig. 6.5 . Starting from $\mathrm{p}(\pi^0)$ bin number 11, the SCF signal is absorbed in the TM component; separating the two worsens the fit result due to the limited statistics available to model the SCF.

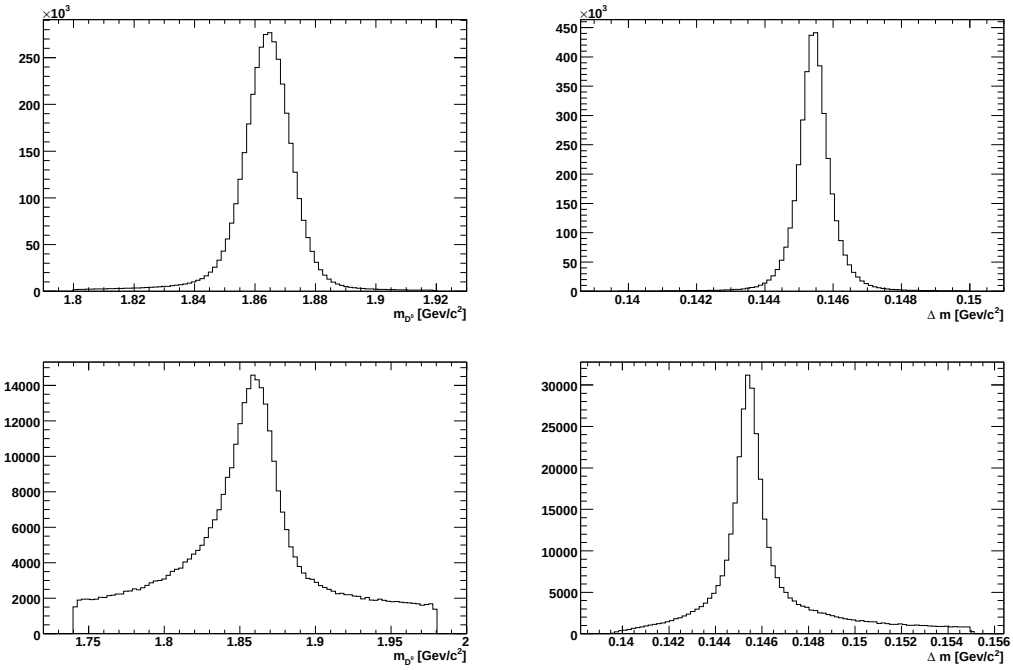

Figure 6.4: Distributions of $\mathrm{m_{D^0}}$ (left) and $\Delta\mathrm{m}$ (right) for $\mathrm{D^0 \to K^{\pm}\pi^{\pm}}$ (top) and $\mathrm{D^0 \to K^{\pm}\pi^{\pm}\pi^0}$ (bottom) in signal MC events.

- **Peaking background category 1:** We use the generic $\mathrm{c\bar{c}}$ and $\mathrm{b\bar{b}}$ MC samples to isolate events where the $\mathrm{D^{*\pm}}$ is reconstructed using a true $\mathrm{D^0}$ but a random π_s. This background is peaking in $\mathrm{m_{D^0}}$ but not in $\Delta\mathrm{m}$. The corresponding distribution of $\mathrm{m_{D^0}}$ and $\Delta\mathrm{m}$ are shown in Fig. 6.6.

- **Peaking background category 2:** We use the generic $\mathrm{c\bar{c}}$ and $\mathrm{b\bar{b}}$ MC samples to isolate events where the $\mathrm{D^0}$ is wrongly reconstructed. This may be caused, for instance, by a lepton or a kaon that is wrongly identified as pion daughter of the $\mathrm{D^0}$. Another

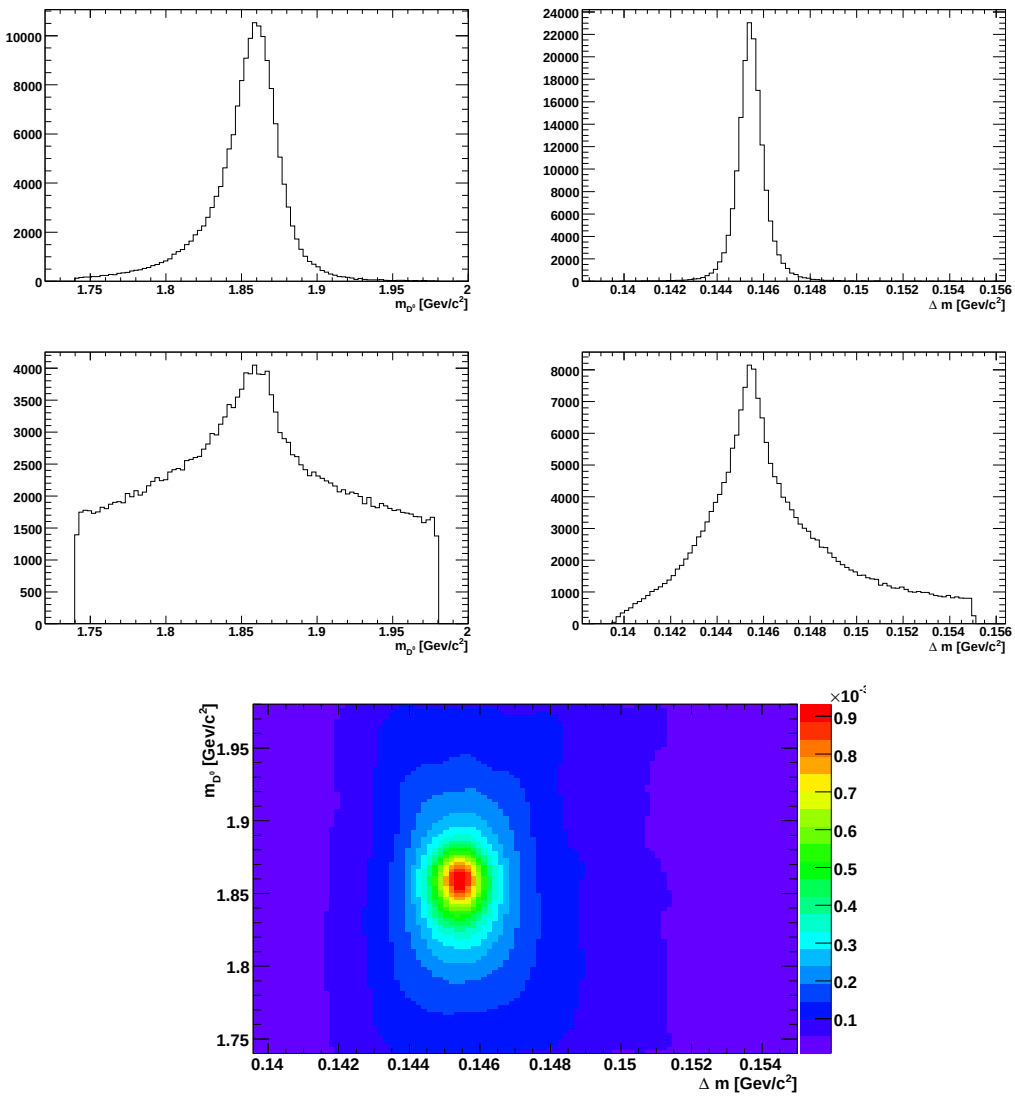

Figure 6.5: TM (top) and SCF (middle) for $\mathrm{m_{D^0}}$ (left) and $\Delta\mathrm{m}$ (right) in the region $(0.449215 < \mathrm{p}(\pi^0) < 0.5084)\,\mathrm{GeV/c}$. The bottom plot shows the smoothed 2-dimensional histogram of the SCF component.

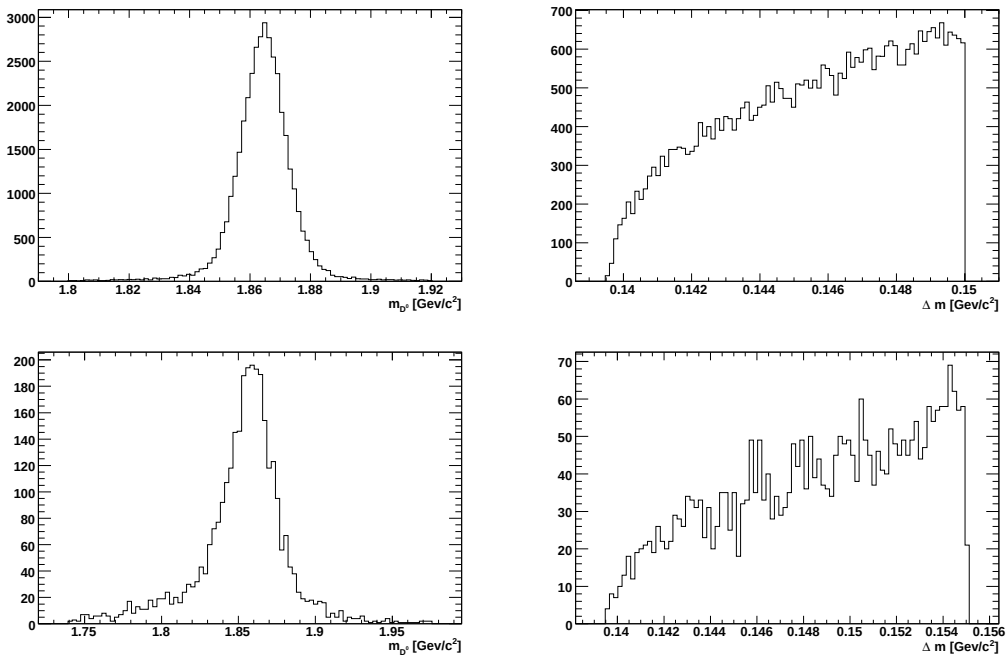

Figure 6.6: Distributions of $\mathrm{m_{D^0}}$ (left) and $\Delta\mathrm{m}$ (right) for $\mathrm{D^0} \rightarrow \mathrm{K^{\pm}\pi^{\pm}}$ (top) and $\mathrm{D^0} \rightarrow \mathrm{K^{\pm}\pi^{\pm}\pi^0}$ (bottom) in peaking background category 1.

possible source is feed-down from non-signal channels where one daughter of a real $\mathrm{D^0}$ is not reconstructed. As these events may contain a correctly reconstructed $\mathrm{D^{*\pm}}$, this background peaks in $\Delta\mathrm{m}$. The corresponding distribution of $\mathrm{m_{D^0}}$ and $\Delta\mathrm{m}$ are shown in Fig. 6.7.

- **Combinatorial background:** This background consists of candidates that have been reconstructed from uncorrelated tracks and clusters. The corresponding distributions of $\mathrm{m_{D^0}}$ and Δm are shown in Fig. 6.8. We use the generic MC samples to extract this component. In the $\mathrm{c\bar{c}}$ and $\mathrm{b\bar{b}}$ samples, we absorb all the events that are left after removing signal and peaking background categories 1 and 2 into the combinatorial component. The uds generic MC sample is purely combinatorial.

6.4 The likelihood fits

We use a binned extended χ^2 fit to extract the signal and background yields. The function that is minimized is given by

$$\mathrm{F(m_{D^0}, \Delta m)} = \exp(\sum_{\mathrm{i}} \mathrm{N_i}) \sum_{\mathrm{i}} \mathrm{N_i} \cdot \mathcal{P}_{\mathrm{i}}(\mathrm{m_{D^0}}, \Delta\mathrm{m}) \,, \tag{6.4}$$

where the parameters i runs over the different species, i.e. signal, continuum background, peaking background category 1 and peaking background category 2. $\mathrm{N_i}$ is the event yield for

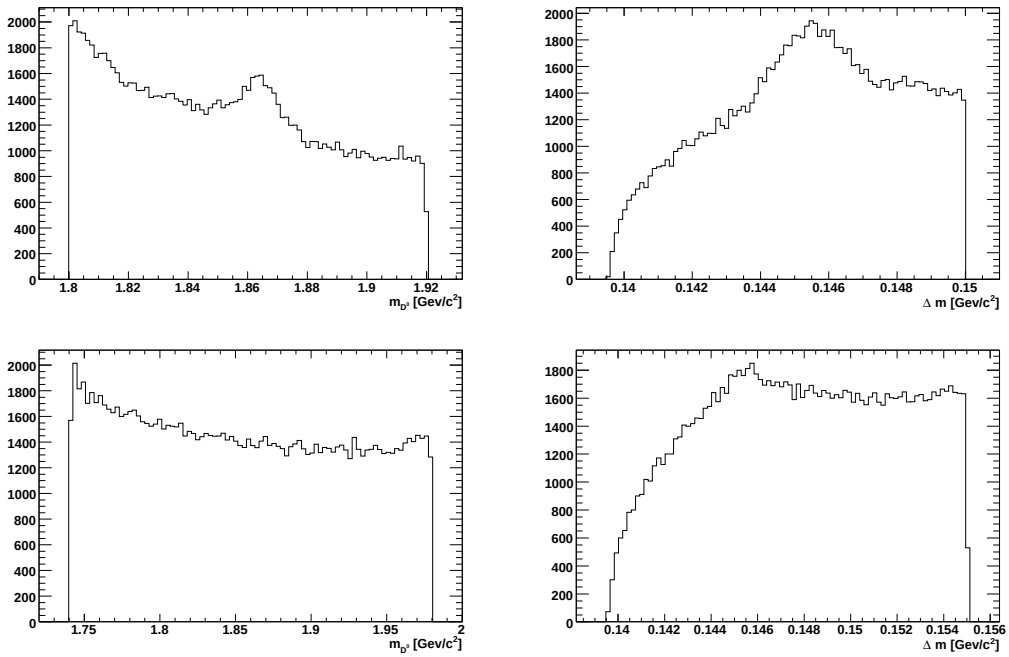

Figure 6.7: Distributions of $\mathrm{m_{D^0}}$ (left) and $\Delta\mathrm{m}$ (right) for $\mathrm{D^0 \to K^{\pm}\pi^{\pm}}$ (top) and $\mathrm{D^0 \to K^{\pm}\pi^{\pm}\pi^0}$ (bottom) in peaking background category 2.

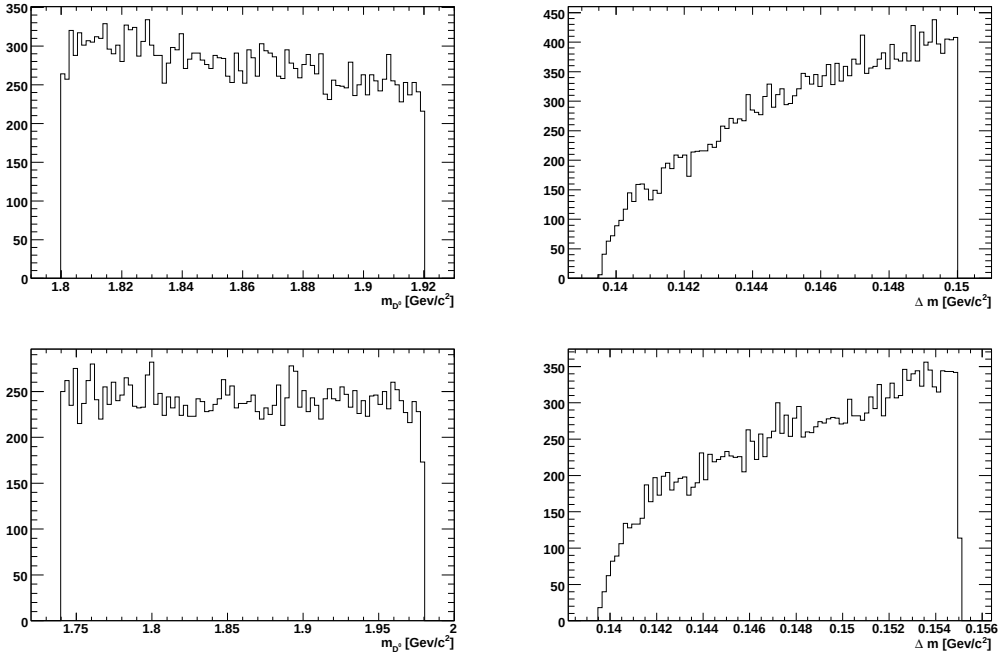

Figure 6.8: Distributions of combinatorial background events for $\mathrm{m_{D^0}}$ (left) and $\Delta\mathrm{m}$ (right) for $\mathrm{D^0 \to K^{\pm}\pi^{\pm}}$ (top) and $\mathrm{D^0 \to K^{\pm}\pi^{\pm}\pi^0}$ (bottom)

the of the species i and $\mathcal{P}_{\rm i}$ is the corresponding 2-dimensional PDF, which may differ in the signal description (see below) between $\rm p(\pi^0)$ bins. For the binned χ^2 fits we use different binnings to account for the different topologies in $\rm m_{D^0}$ and Δm for low- and high-momentum π^0s. For the first 10 $\rm p(\pi^0)$ bins we use 50×50 bins, while for higher π^0 momentum, to avoid bins with no or a small number of entries, we use 46×46 bins histograms with an adaptive binning that has larger bins towards the borders. The parameterizations for the different species are:

- **Signal $D^0 \to K^\pm\pi^\pm\pi^0$:**
  The signal PDF for $\rm D^0 \to K^\pm\pi^\pm\pi^0$ is separated into wrongly reconstructed events (SCF) and correctly reconstructed events (TM):

$$\mathcal{P}_{\rm sig} = (1 - \rm f_{SCF})\mathcal{P}_{\rm SCF} + \rm f_{SCF}\mathcal{P}_{\rm TM} \tag{6.5}$$

  where $\rm f_{SCF}$ is the fraction of wrongly reconstructed events that is taken from signal MC and fixed in the fit. For the $\rm p(\pi^0)$ bins 11-20 the SCF component is small and absorbed in the TM component ($\rm f_{SCF} = 0$). For TM signal, we use the two-dimensional PDF, including correlations between $\rm m_{D^0}$ and Δm, from Ref. [50]:

$$\mathcal{P}_{\rm TM}(\rm m_{D^0}, \Delta m) = f_{s1} \cdot s_1 + (1 - f_{s1})\{f_{s2} \cdot s_2 + (1 - f_{s2})[f_{s3} \cdot s_3 + (1 - f_{s3}) \cdot s_4]\} \ , \tag{6.6}$$

  where

$$\begin{aligned} \rm s_1 &= s(m_{D^0}, \Delta m; \overline{m}_1, \sigma_{m1}, \overline{\Delta m}_1, \sigma_{\Delta m1}, c_1) \\ \rm s_2 &= s(m_{D^0}, \Delta m; \overline{m}_2, \sigma_{m2}, \overline{\Delta m}_2, \sigma_{\Delta m2}, c_2) \\ \rm s_3 &= s(m_{D^0}, \Delta m; \overline{m}_3, \sigma_{m3}, \overline{\Delta m}_3, \sigma_{\Delta m3}, c_3) \\ \rm s_4 &= g(m_{D^0}; \overline{m}_4, \sigma_{m4}) \times cb_s(\Delta m; \overline{\Delta m}_4, \sigma_{\Delta m4}, \alpha_4) \ , \end{aligned} \tag{6.7}$$

  with

$$\rm s(x, y; \overline{x}, \sigma_x, \overline{y}, \sigma_y, c) = \exp(-\frac{(x - \overline{x})^2}{2\sigma_x^2}) \exp(-\frac{(y - \overline{y})^2}{2(\sigma_y + c((x - \overline{x})/\sigma_x)^2)^2}) \tag{6.8}$$

  and

$$\rm g(x; \overline{x}, \sigma) = \exp\left(-\frac{(x - \overline{x})^2}{2\sigma^2}\right) \tag{6.9}$$

  and

$$\rm cb_s(x; \overline{x}, \sigma, \alpha) = \begin{cases} \exp\left(-\frac{(x-\overline{x})^2}{2\sigma^2}\right) & \text{if } \frac{(x-\overline{x})}{\sigma} < \alpha \\ a\left(b + \frac{(x-\overline{x})}{\sigma}\right)^{-2} & \text{if } \frac{(x-\overline{x})}{\sigma} \geq \alpha \end{cases} \tag{6.10}$$

$$\alpha > 0, \quad a = (2/\alpha)^2 \exp(\alpha^2/2), \quad b = (2/\alpha) - \alpha$$

  The fractions $\rm f_{s1}$, $\rm f_{s2}$ and $\rm f_{s3}$ are fitted on signal MC and fixed in the nominal fit. All the other parameters are free to vary. For the SCF component we use a two-dimensional histogram that has been smoothed using ROO2DKEYSPDF (see Fig. 6.5).

- **Signal** $\mathrm{D}^0 \to \mathrm{K}^\pm\pi^\pm$**:**
  For $\mathrm{D}^0 \to \mathrm{K}^\pm\pi^\pm$ signal, we use the two-dimensional and correlated PDF, including correlations between $\mathrm{m_{D^0}}$ and $\Delta\mathrm{m}$, from Ref. [51]:

$$\mathcal{P}_{\mathrm{sig}}(\mathrm{m_{D^0}}, \Delta\mathrm{m}) = \mathrm{f_{wide}}\mathrm{S_{wide}} + (1 - \mathrm{f_{wide}})\left[\mathrm{f_{JSU}}\mathrm{S_{Jsu}} + (1 - \mathrm{f_{JSU}})\mathrm{S_{core}}\right] , \tag{6.11}$$

with

$$\begin{aligned}&\mathrm{S_{wide}}(\mathrm{m_{D^0}}, \Delta\mathrm{M}) = \\ &\mathrm{G_{corr}}(\mathrm{m_{D^0}}, \Delta\mathrm{M}; \mathrm{m_{CG}}, \sigma_{\mathrm{CG}}, \Delta\mathrm{M_{CG}}, \sigma\Delta\mathrm{MCG}, \mathrm{k_{corr}}) ,\end{aligned} \tag{6.12}$$

$$\begin{aligned}&\mathrm{S_{JSU}}(\mathrm{m_{D^0}}, \Delta\mathrm{M}) = \mathrm{JSU}(\Delta\mathrm{M}; \Delta\mathrm{M_{JSU}}, \sigma_{\Delta\mathrm{M_{JSU}}}, \delta, \gamma) \\ &\cdot[\mathrm{f_{core}}\mathrm{g}(\mathrm{m_{D^0}}; \bar{\mathrm{m}}_1, \sigma_1) + (1 - \mathrm{f_{core}})\mathrm{g}(\mathrm{m_{D^0}}, \bar{\mathrm{m}}_2, \sigma_2)]\end{aligned} \tag{6.13}$$

and

$$\begin{aligned}&\mathrm{S_{core}}(\mathrm{m_{D^0}}, \Delta\mathrm{M}) = \\ &\mathrm{f_{core}}\mathrm{g}(\mathrm{m_{D^0}}; \bar{\mathrm{m}}_1, \sigma_1)\mathrm{g}(\Delta\mathrm{M}; \Delta\mathrm{M}_1, \sigma_{\Delta\mathrm{M}_1}) \\ &+(1 - \mathrm{f_{core}})\mathrm{g}(\mathrm{m_{D^0}}; \bar{\mathrm{m}}_2, \sigma_2)\mathrm{g}(\Delta\mathrm{M}; \Delta\mathrm{M}_2, \sigma_{\Delta\mathrm{M}_2}) ,\end{aligned} \tag{6.14}$$

where

$$\begin{aligned}&\mathrm{G_{corr}}(\mathrm{x}, \mathrm{y}; \bar{\mathrm{x}}, \sigma_{\mathrm{x}}, \bar{\mathrm{y}}, \sigma_{\mathrm{y}}, \mathrm{k_{corr}}) \equiv \\ &\exp\left(-\frac{(\mathrm{x} - \bar{\mathrm{x}})^2}{2\sigma_{\mathrm{x}}^2}\right)\exp\left(-\frac{(\mathrm{y} - \bar{\mathrm{y}})^2}{2\left(\sigma_{\mathrm{y}} + \mathrm{k_{corr}}((\mathrm{x} - \bar{\mathrm{x}})/\sigma_{\mathrm{x}})^2\right)^2}\right) ,\end{aligned} \tag{6.15}$$

$$\begin{aligned}&\mathrm{JSU}(\mathrm{x}; \bar{\mathrm{x}}, \sigma, \delta, \gamma) \equiv \mathrm{C_{JSU}} \\ &\frac{\delta}{\sigma\sqrt{2\pi}\sqrt{1 + \left(\frac{\mathrm{x}-\bar{\mathrm{x}}}{\sigma}\right)^2}}\exp\left\{-\frac{1}{2}\left[\gamma + \delta\sinh^{-1}\left(\frac{\mathrm{x} - \bar{\mathrm{x}}}{\sigma}\right)\right]^2\right\}\end{aligned} \tag{6.16}$$

and

$$\sinh^{-1}(\mathrm{x}) = \log\left(\mathrm{x} + \sqrt{1 + \mathrm{x}^2}\right) . \tag{6.17}$$

The δ and σ parameters are fitted on signal MC and fixed in the nominal fits. When they are allowed to vary the bias increases significantly, as indicated by validation tests on the MC sample. All other parameters are free to vary.

- **Combinatorial background:**
  We use the same parameterization for $\mathrm{D}^0 \to \mathrm{K}^\pm\pi^\pm\pi^0$ and $\mathrm{D}^0 \to \mathrm{K}^\pm\pi^\pm$ where $\mathrm{m_{D^0}}$ and $\Delta\mathrm{m}$ are taken as uncorrelated:

$$\mathcal{P}_{\mathrm{comb}}(\mathrm{m_{D^0}}, \Delta\mathrm{m}) = \mathcal{P}_{\mathrm{comb}}(\mathrm{m_{D^0}}) \cdot \mathcal{P}_{\mathrm{comb}}(\Delta\mathrm{m}) , \tag{6.18}$$

with

$$\mathcal{P}_{\mathrm{comb}}(\mathrm{m_{D^0}}) = 1 + \mathrm{b_1} \cdot (\mathrm{m_{D^0}} - 1.865) \tag{6.19}$$

and

$$\mathcal{P}_{\mathrm{comb}}(\Delta\mathrm{m}) = \sqrt{(\Delta\mathrm{m}/\Delta\mathrm{m_0})^2} \cdot \exp(-\mathrm{c} \cdot (\Delta\mathrm{m}/\Delta\mathrm{m_0})^2 - 1) \,, \tag{6.20}$$

where $\Delta\mathrm{m_0} = 0.13957\,\mathrm{GeV/c^2}$ [1] corresponds to the charged pion mass. The parameters c and $\mathrm{b_1}$ are free to vary in the fits.

- **Peaking background category 1:**
  For $\mathrm{D^0} \to \mathrm{K^\pm\pi^\pm\pi^0}$ and $\mathrm{D^0} \to \mathrm{K^\pm\pi^\pm}$ we take the product of the PDFs for $\mathrm{m_{D^0}}$ and $\Delta\mathrm{m}$, assuming no correlations:

  $$\mathcal{P}_{\mathrm{Cat1}}(\mathrm{m_{D^0}}, \Delta\mathrm{m}) = \mathcal{P}_{\mathrm{Cat1}}(\mathrm{m_{D^0}}) \cdot \mathcal{P}_{\mathrm{Cat1}}(\Delta\mathrm{m}) \,. \tag{6.21}$$

  For $\mathrm{D^0} \to \mathrm{K^\pm\pi^\pm\pi^0}$ we use the same parameterization for $\Delta\mathrm{m}$ as for the combinatorial background

  $$\mathcal{P}_{\mathrm{Cat1}}(\Delta\mathrm{m}) = \mathcal{P}_{\mathrm{comb}}(\Delta\mathrm{m}) \,, \tag{6.22}$$

  while for $\mathrm{m_{D^0}}$ we take the projection of the signal parameterization:

  $$\mathcal{P}_{\mathrm{Cat1}}(\mathrm{m_{D^0}}) = \int \mathcal{P}_{\mathrm{sig}}(\mathrm{m_{D^0}}, \Delta\mathrm{m})\, \mathrm{d}\Delta\mathrm{m} \,. \tag{6.23}$$

  For $\mathrm{D^0} \to \mathrm{K^\pm\pi^\pm}$ we use smoothed histograms for $\mathcal{P}_{\mathrm{Cat1}}(\Delta\mathrm{m})$ and $\mathcal{P}_{\mathrm{Cat1}}(\mathrm{m_{D^0}})$ that are taken from simulation.

- **Peaking background category 2:**
  For $\mathrm{D^0} \to \mathrm{K^\pm\pi^\pm\pi^0}$ and $\mathrm{D^0} \to \mathrm{K^\pm\pi^\pm}$ we take the uncorrelated product of the PDFs for $\mathrm{m_{D^0}}$ and $\Delta\mathrm{m}$:

  $$\mathcal{P}_{\mathrm{Cat2}}(\mathrm{m_{D^0}}, \Delta\mathrm{m}) = \mathcal{P}_{\mathrm{Cat2}}(\mathrm{m_{D^0}}) \cdot \mathcal{P}_{\mathrm{Cat2}}(\Delta\mathrm{m}) \,. \tag{6.24}$$

  For both decay modes we use smoothed histograms for $\mathcal{P}_{\mathrm{Cat2}}(\Delta\mathrm{m})$ and $\mathcal{P}_{\mathrm{Cat2}}(\mathrm{m_{D^0}})$ that are taken from simulation.

6.5 Fit validation

We use fits to the MC samples to validate the fitting tool. As we know how many signal events there are in these sample, we can use them to estimate the bias introduced by the fitting procedure. We vary the initial values of all fit parameters and take into account only properly converged fits with a positive definite covariance matrix. In Fig. 6.9 we show the difference between the true and the fitted signal yields in units of the statistical error for fits to $\mathrm{D^0} \to \mathrm{K^\pm\pi^\pm\pi^0}$ MC. Some of the biases seem sizable, but one should keep in mind that we fit high statistics samples, and even the largest bias corresponds to only $\sim$1.5% of the signal yield. Additionally, as we are looking at ratios, biases should cancel out as we can assume them to be comparable for MC and data. As we will see below, this assumption is reasonable given that the residuals of the fit projections for data and MC are similar. The fit to $\mathrm{D^0} \to \mathrm{K^\pm\pi^\pm}$ MC yields a bias of 5.853 units of the statistical error, which corresponds to a bias of 0.447%.

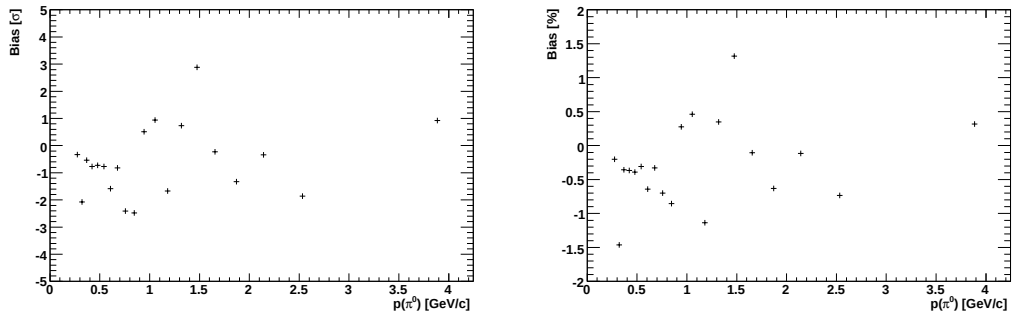

Figure 6.9: Bias between true and fitted yields in fits to MC samples in units of the statistical error (left) and in units of percent of the the fitted yield (right).

6.6 Systematic uncertainties

We assign the bias observed in the fits to MC as a systematic uncertainty. Given that these biases are expected to cancel out in the double ratio, this is a conservative approach. When comparing the residual distributions of the fit projections on $\mathrm{m_{D^0}}$ and $\Delta\mathrm{m}$, shown in Fig. 6.11 and in appendix A, the shapes and sizes are comparable which justifies the cancel-out assumption. We therefore do not assign an additional systematic error for parameters that are fixed in the fits. The largest systematic uncertainty is from the branching fraction measurements of the decays $\mathrm{D^0} \to \mathrm{K^\pm}\pi^\pm\pi^0$ and $\mathrm{D^0} \to \mathrm{K^\pm}\pi^\pm$, taken from Ref. [1]:

$$\delta_{PDG} = \sqrt{[\frac{\sigma(\mathcal{B}(D^0 \to K^\pm\pi^\pm))}{\mathcal{B}(D^0 \to K^\pm\pi^\pm)}]^2 + [\frac{\sigma(\mathcal{B}(D^0 \to K^\pm\pi^\pm\pi^0))}{\mathcal{B}(D^0 \to K^\pm\pi^\pm\pi^0)}]^2} = 0.0379\,. \qquad (6.25)$$

As this uncertainty is common to all $\mathrm{p}(\pi^0)$ bins, we do not include it in the error bars of the individual double-ratios in the result plot below, but we show instead dashed lines that indicate the one standard deviation region.

6.7 Results

The double ratio $\mathrm{R}(\mathrm{p}(\pi^0))$ is shown in Fig. 6.10 and the fit results are summarized in Tab. 6.2. For shortness we do not show all the corresponding projection plots for the $\mathrm{D^0} \to \mathrm{K^\pm}\pi^\pm\pi^0$ fits here, but show as example bin number 5 in Fig. 6.11. All projection plots for the other $p(\pi^0)$ bins are shown in appendix A. The fit projections for the $\mathrm{D^0} \to \mathrm{K^\pm}\pi^\pm$ data and MC fits are shown in Fig. 6.12. We find $(2.131 \pm 0.001) \times 10^6$ signal events in the fit to data and $(2.145 \pm 0.001) \times 10^6$ signal events in the fit to MC. We fit the distribution shown in Fig. 6.10 with a horizontal line to estimate the average[4] double ratio:

[4]The previous study used a straight line to fit the distribution, but as we clearly observe a non-linear distribution, we just evaluate the average.

	average
"raw" double ratio	1.032 ± 0.002
corrected double ratio	1.060 ± 0.002
single ratio	1.021 ± 0.002

Keeping in mind the $\sim 3.8\%$ uncertainty, all averages are compatible with a 3% uncertainty in the reconstruction efficiency. In particular, the corrected ratio has as similar dependence on the the π^0 momentum compared to the previous study [52], but is globally shifted to higher values. A difference between the two analyses is not unexpected, as the present study uses a two-dimensional fit that includes peaking components, while the previous study combined two independent 1-dimensional fits and substracted peaking background using MC. Also the correction shifts the double ratio to higher values, as there are more candidates in data than in MC over the whole π^0 range.

In conclusion, due to the systematic effects from the branching fraction measurements and the differences between data and simulation that are not due to the π^0 simulation and do not cancelled out in the double ratio, namely the different number of photons, the study does not provide a satisfactory cross-check to the τ-derived results.

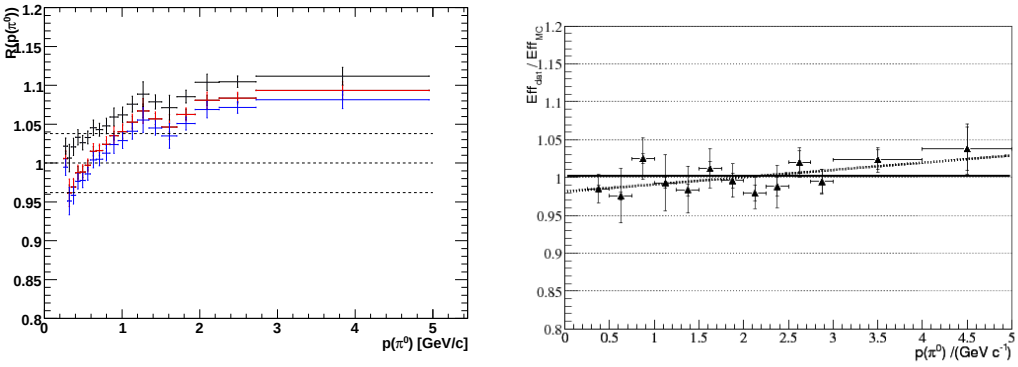

Figure 6.10: Double ratio as obtained in the present study (left) and in the previous study (right). The red points indicate the "raw" double ration, the black ones are corrected for the difference of the number of candidates between data and MC. The blue points give the simple ratio $\frac{N_{K\pi\pi^0}(p_{\pi^0})|_{data}}{N_{K\pi\pi^0}(p_{\pi^0})|_{MC}}$, where the MC yield has been scaled to luminosity. The dashed lines indicate the uncertainty from the branching fraction measurements.

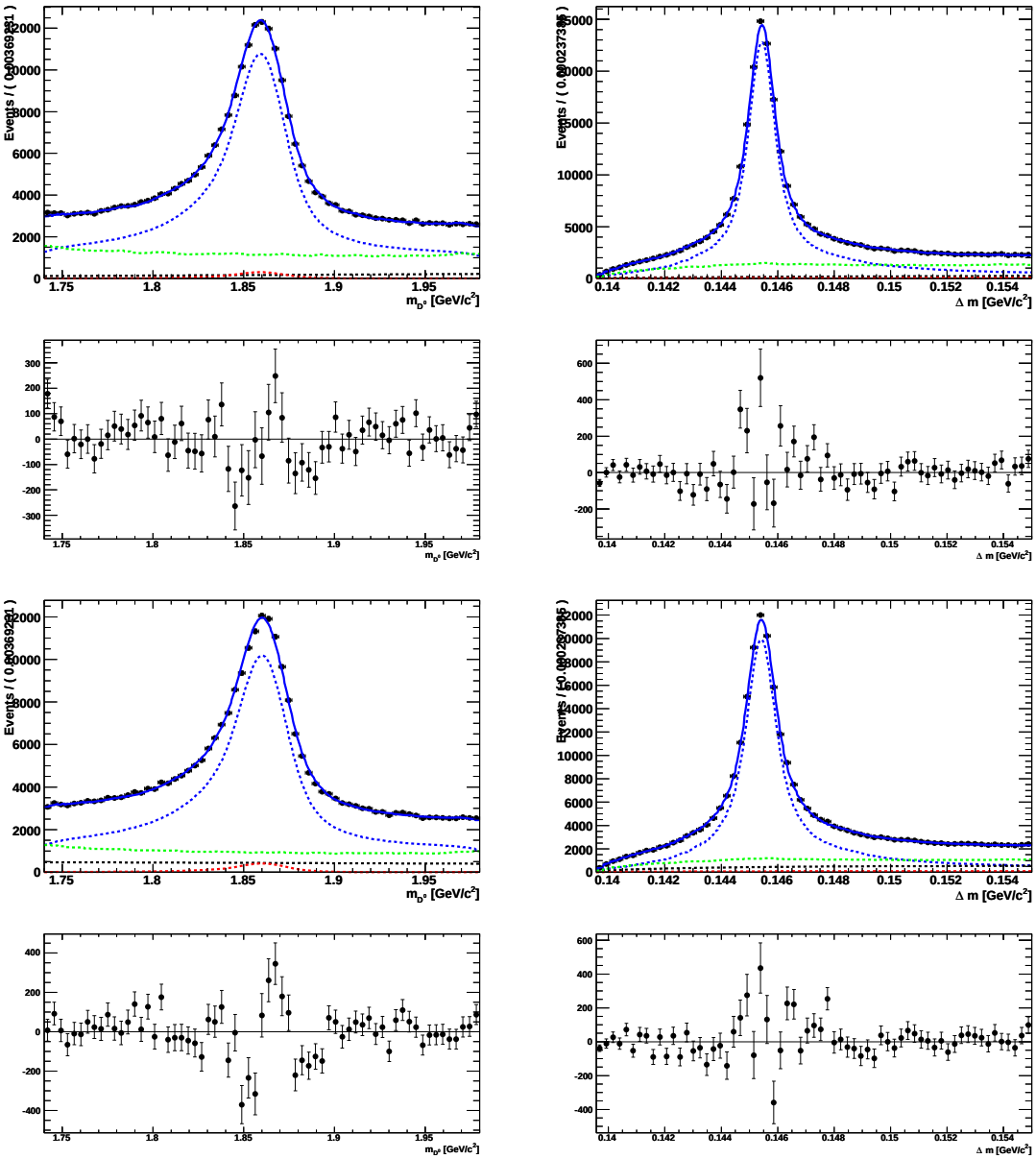

Figure 6.11: Fit projections for $\mathrm{p}(\pi^0)$-slice 5. The top plot are fits to MC, the bottom plots fits to data. The residuals show the bias in absolute numbers and are comparable in shape and size.

Slice	$p(\pi^0)$[GeV/c]	N_{Data}	N_{MC}	$R \pm stat \pm sys$
1	0.250-0.297	207157 ± 1390	210201 ± 1261	$1.006 \pm 0.009 \pm 0.005$
2	0.297-0.344	194916 ± 1467	206818 ± 1456	$0.962 \pm 0.010 \pm 0.009$
3	0.344-0.394	198985 ± 1463	209515 ± 1388	$0.969 \pm 0.010 \pm 0.005$
4	0.394-0.449	202111 ± 1356	208880 ± 990	$0.987 \pm 0.008 \pm 0.006$
5	0.449-0.508	202913 ± 1019	209489 ± 1123	$0.988 \pm 0.007 \pm 0.006$
6	0.508-0.572	204064 ± 966	208864 ± 834	$0.997 \pm 0.006 \pm 0.006$
7	0.572-0.641	207909 ± 891	209006 ± 845	$1.015 \pm 0.006 \pm 0.008$
8	0.641-0.716	209047 ± 900	209942 ± 836	$1.016 \pm 0.006 \pm 0.006$
9	0.716-0.798	209323 ± 820	208597 ± 607	$1.024 \pm 0.005 \pm 0.011$
10	0.798-0.891	211229 ± 889	208204 ± 718	$1.035 \pm 0.006 \pm 0.011$
11	0.891-0.996	214960 ± 1308	210841 ± 1130	$1.040 \pm 0.009 \pm 0.005$
12	0.996-1.113	217460 ± 1169	210820 ± 1039	$1.053 \pm 0.008 \pm 0.006$
13	1.113-1.245	216696 ± 1071	207235 ± 1413	$1.067 \pm 0.009 \pm 0.008$
14	1.245-1.392	217849 ± 971	210370 ± 1002	$1.057 \pm 0.007 \pm 0.006$
15	1.392-1.559	217958 ± 892	212554 ± 971	$1.046 \pm 0.007 \pm 0.012$
16	1.559-1.753	218800 ± 923	210124 ± 960	$1.063 \pm 0.007 \pm 0.005$
17	1.753-1.988	220384 ± 849	208100 ± 987	$1.081 \pm 0.007 \pm 0.007$
18	1.988-2.296	222929 ± 799	209961 ± 724	$1.084 \pm 0.006 \pm 0.005$
19	2.296-2.770	223363 ± 858	208446 ± 823	$1.094 \pm 0.006 \pm 0.009$
20	2.770-5.000	227595 ± 818	208525 ± 720	$1.114 \pm 0.006 \pm 0.006$

Table 6.2: Fit Results for the yields and the double ratio R in the different $p(\pi^0)$ bins.

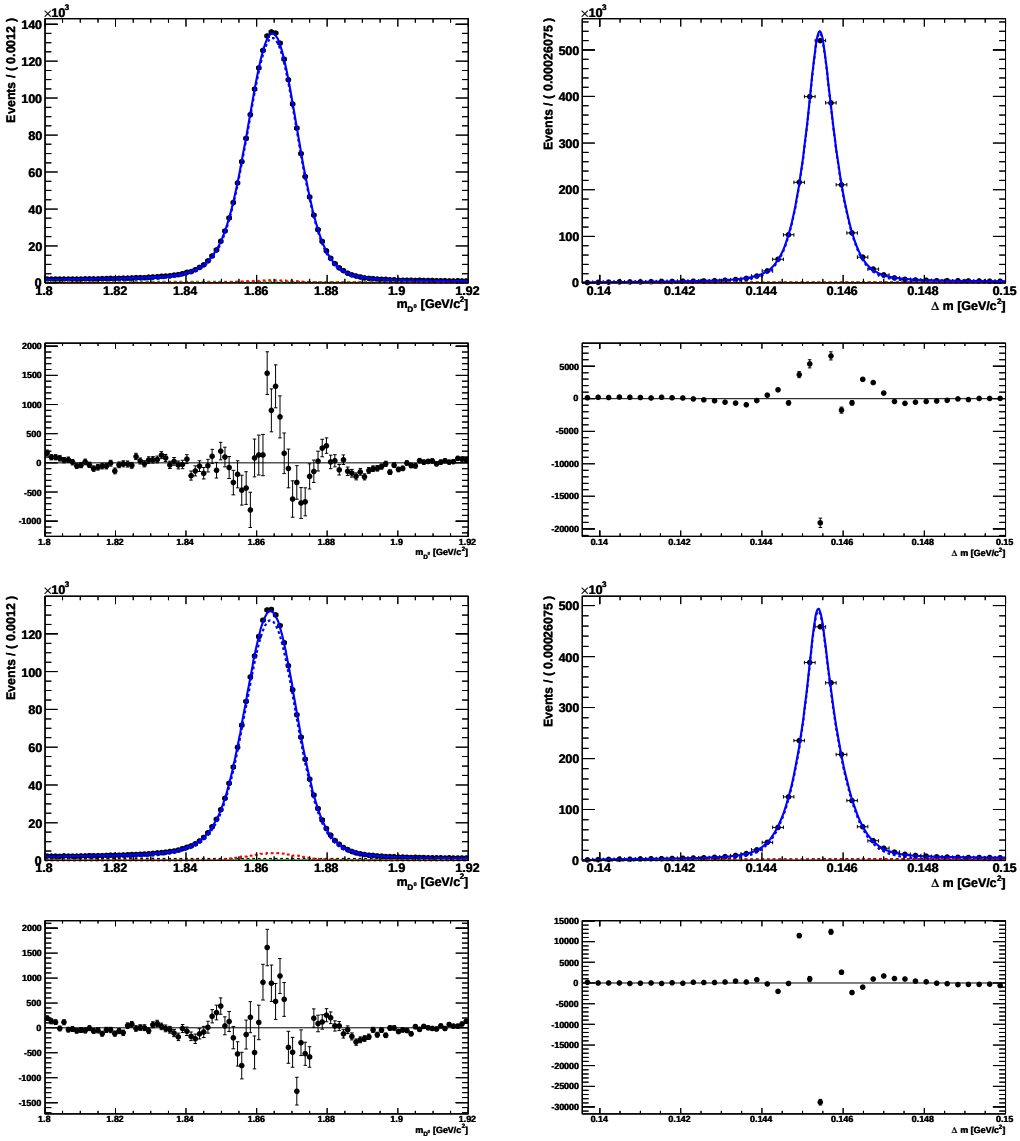

Figure 6.12: Fit Projections of fits to MC (top) and data (bottom) for $\mathrm{D}^0 \rightarrow \mathrm{K}^{\pm}\pi^{\pm}$. The residuals show the bias in absolute numbers and are comparable in shape and size.

Part III

Analysis of $B^0 \to K^0_S K^0_S K^0_S$

7 Reconstruction and analysis techniques

7.1 Introduction

In this work we present two analysis of the decay channel $\mathrm{B}^0 \to \mathrm{K}^0_\mathrm{s}\mathrm{K}^0_\mathrm{s}\mathrm{K}^0_\mathrm{s}$: the first one is time-dependent and extracts the TDCPV parameters of the decay and the second one is a time-integrated amplitude analysis that measures the structure of the resonant contributions to the decay. Both analyses are based on the same reconstructed and simulated data samples and in this part of the work we present their common aspects[1] which concern reconstruction and analysis techniques. The event selection differs between the analyses and is detailed in the dedicated chapters (Chap. 8 for the TD analysis and Chap. 9 for the DP analysis).

7.2 Data Samples

7.2.1 On-peak and off-peak data samples

We use the complete *BABAR* $\Upsilon(4S)$ data sample and the off-peak data taken 40 MeV below the $\Upsilon(4S)$. Details on the luminosity can be found in Tab. 7.1.

run	$\mathcal{L}_{\mathrm{on-peak}}$ [pb^{-1}]	$\mathrm{N}_{\mathrm{B\bar{B}}}$	$\mathcal{L}_{\mathrm{off-peak}}$ [pb^{-1}]
1	20397.1	22389980.4	2615.4
2	61075.7	67394307.5	6922.8
3	32278.2	35569248.8	2468.0
4	100282.0	110449802.7	10121.2
5	133262.5	147190396.5	14485.4
6	78750.7	84767412.6	7884.2
total	426046.4	467761148.5	44497.2

Table 7.1: Luminosity for the on-peak and off-peak data samples

[1] This in not entirely true. We do not use tagging information for the DP analysis, but yet the *BABAR* tagging algorithm is presented in this chapter. This choice allows for a more consistent presentation of the tagging procedure as a part of the $\Delta\mathrm{t}$ measurement, and we do use a selection requirement on $\Delta\mathrm{t}$ in the DP analysis to remove pathological events.

7.2.2 Simulation (Monte Carlo) data samples

For statistical data analysis it is crucial to use fully simulated data , aka Monte Carlo (MC), that reproduces the actual data as well as possible. It is particularly important for any blind analysis, as it is completely validated on simulated events before looking at the variables of interest in real data. Some properties of the data sample can only be studied using MC[2]:

- Reconstruction effects, such as mis-reconstructed events and reconstruction efficiencies.
- Properties of the signal that, at least for low statistics, cannot be studied directly on data, such as correlations between variables.
- The training of the neural network (NN) (see Sec. 7.5) can be done with a pure signal sample taken from simulation.
- The background composition, in particular peaking background from B decays. A generic MC sample is used to identify modes that have been wrongly reconstructed. Generic MC is aimed to be a reproduction, as accurate as possible, of the actual B-meson decays in data. It contains the main decay channels and most of the minor contributions. As sometimes the BF of a given decay channel has not been measured yet (at the time of production), this has to be corrected for when calculating the expected yield in data if there has been a measurement since, or a systematic uncertainty has to be assigned for an estimate. For more detailed studies and appropriate modeling of certain background decay modes, exclusive MC can be produced.

The *BABAR* collaboration uses different software packages for the full simulation, which are used to generate the decay and simulate the reaction of the detector:

- EvtGen: The `EvtGen` package [53] provides a framework in which decays can be added as modules, the so-called models, that are used to generate events. It has implemented detailed models to describe the physics of B mesons: in particular it has detailed models for semi-leptonic decays and CP-violating decays. It produces correct results for the angular distributions in sequential decays, including all correlations. One of the novel features of `EvtGen` is that it uses amplitudes, instead of probabilities, for the simulation of the decays. A good example is the `PTo3P` model that is adapted for 3-body decays and that we use as part of the signal generation in this work. What we provide to the framework are the isobar magnitudes and phases, spins, Blatt-Weisskopf parameters and line-shape parameters. The framework then builds the PDF for the decay from the isobar amplitudes.
- JETSET: The `EvtGen` package has an interface to the `JETSET` [54] package that is used to generate continuum events ($\mathrm{e^+e^-} \to \mathrm{q\bar{q}}, \mathrm{q} = \mathrm{u, d, s, c}$) and B decays for which

[2] Actually a data control sample could also be used for some of these studies. Using MC on the other hand is much easier and there is never a guarantee that a control sample, that is necessarily different than the actual data sample (even when the event topology is very similar), behaves in the same way as the actual data sample.

there is no specific model implemented. This is the case for a minority of B decays in the generic MC.

- GEANT4: The GEANT4 package [55] is used to simulate the passage and interaction of the particles in the generated events with the detector material. To this end a detailed model of the detector, both in geometry and material, is implemented. Among the simulated processes are energy loss in the different detector parts, re-scattering and photon conversions. Each interaction with the detector is recorded as a "gHit". In the end the simulation is supposed to generate the actual readout that is stocked on tape as real data. To this end, the "gHits" are further processed to simulate the readouts of the electronics, the data acquisition system and the trigger. To obtain a realistic signal, electronic noise and machine backgrounds are added. The noise and backgrounds change over time and are recorded regularly ($\sim$1Hz) during detector operations. As this recording frequency is not correlated with the trigger, it is an almost pure background sample.

Simulated data are used in several places in both analyses. It is mandatory to control MC inaccuracies by means of a data control sample. In case of biases, corrections should be applied or if the difference is small a systematic uncertainty can be assigned without correcting. In this analysis the vertex measurement is the most crucial part, and we use the control sample $\mathrm{B}^0 \to \mathrm{J}/\psi\,\mathrm{K}^0_\mathrm{s}$ to assign a systematic uncertainty for MC-data differences. Many *BABAR* analyses have K^0_s in the final state and it is known that the K^0_s reconstruction efficiency is not the same in data and MC. For efficiency correction we use a standard recipe that is provided by the tracking group that has been obtained from inclusive K^0_s decays and is presented in more detail in the amplitude analysis chapter (Sec. 9.7.4). We use the following MC samples[3]:

- 702558k generic $\mathrm{B}^0\bar{\mathrm{B}}^0$ events (SP-1235);
- 685320k generic $\mathrm{B}^+\mathrm{B}^-$ events (SP-1237);
- 350k pseudo-non-resonant signal events, generated with a broadened $\mathrm{f}_0(980)$ resonance (SP-6994);
- 963k non-resonant signal events (SP-8996);
- 1846k resonant signal events including $\mathrm{f}_0(980)\mathrm{K}^0_\mathrm{s}$, $\mathrm{f}_\mathrm{X}(1500)\mathrm{K}^0_\mathrm{s}$, non-resonant(NR)$\mathrm{K}^0_\mathrm{s}$ (SP-9855);
- 754k resonant signal events including $\mathrm{f}_0(980)\mathrm{K}^0_\mathrm{s}$, $\mathrm{f}_\mathrm{X}(1500)\mathrm{K}^0_\mathrm{s}$, $\mathrm{NRK}^0_\mathrm{s}$, $\chi_{\mathrm{c}0}\mathrm{K}^0_\mathrm{s}$ (SP-9880);
- 1747k resonant signal events generated using the amplitude analysis outcome, including $\mathrm{f}_0(980)\mathrm{K}^0_\mathrm{s}$, $\mathrm{f}_0(1710)\mathrm{K}^0_\mathrm{s}$, $\mathrm{NRK}^0_\mathrm{s}$, $\chi_{\mathrm{c}0}\mathrm{K}^0_\mathrm{s}$, $\mathrm{f}_2(2010)\mathrm{K}^0_\mathrm{s}$ (SP-10045);
- 175k $\mathrm{K}^0_\mathrm{s}\mathrm{K}^0_\mathrm{s}\mathrm{K}^0_\mathrm{L}$ non-resonant events (SP-4494);

[3]The MC sample reference number in *BABAR* is indicated as SP-XXXX

- 350k $\mathrm{K^0_S K^0_S K^0_L}$ non-resonant events (SP-8997);
- 175k $\mathrm{K^{*0} K^0_S K^0_S}$ events (SP-8998);
- 7027k $\mathrm{B^+ \to K^+ K^0_S K^0_S}$ and $\mathrm{B^- \to K^- K^0_S K^0_S}$ events (SP-3915);
- 441k $\mathrm{B^+ \to K^+ K^0_S K^0_S}$ and $\mathrm{B^- \to K^- K^0_S K^0_S}$ events (SP-9000);
- 175k $\mathrm{B^+ \to K^{*+} K^0_S K^0_S}$ and $\mathrm{B^- \to K^{*-} K^0_S K^0_S}$ events (SP-9001).

When we refer to resonant MC in the following, this corresponds to SP-10045 that is our nominal signal MC and has been generated using the fit result to data of the amplitude analysis.

7.3 Reconstruction

As we have described in Sec. 4.11, data is available for the analyst after "Online Prompt Reconstruction" and is common to all analyses. In a second stage, this "raw" data is further processed individually for each analysis[4] with the reconstruction of *composites*: objects that are not directly observed in the detector. For instance, we do not observe a $\mathrm{K^0_S}$ directly in the detector, but the tracks of the charged pions that it decays to (see Sec. 7.3.1). We do not know a priori if a given track corresponds to a pion, and we have to make assumptions (particle hypothesis) on the so-called "candidate", such as mass and charge. Particle identification (PID) tells us how likely it is that assumptions about tracks are correct and several standard list are available for the analyst. We can then use these pion candidates to reconstruct $\mathrm{K^0_S}$ candidates, and the $\mathrm{K^0_S}$ candidates are then used to form $\mathrm{B^0}$ candidates. At each step where candidates are formed, particle hypothesis are made. After the $\mathrm{B^0}$ candidate is formed, the decay vertex of the $\mathrm{B^0}$ candidate can be fitted (see Sec. 7.3.5) which is necessary for the $\Delta\mathrm{t}$ measurement. The $\Delta\mathrm{t}$ measurement is only meaningful if the other side of the event has been at least partly reconstructed, the vertex of the other B has been measured and the flavor of the other B has been tagged (see Sec. 7.3.4).

7.3.1 Tracking

The inner parts of the detector are in the solenoid field and charged particles follow a trajectory along helices that can be described by five parameters that are defined at the point of closest approach (`POCA`) to the z-axis:

- $\mathrm{d_0}$: the $\mathrm{x-y}$ distance to the z-axis;
- $\mathrm{z_0}$: the z-axis coordinate;
- ϕ_0: the azimutal angle of the `POCA`;

[4] There are so-called *skims* that are data samples that have passed certain pre-selections, but in the case of the present analysis we use the so-called AllEventsSkim that has no pre-selection.

- λ: the dip angle of the track at the POCA with respect to the $\mathrm{x} - \mathrm{y}$ plane. The relation with the cylindrical polar angle θ is given by $\theta = \pi/2 - \lambda$;

- ω: the curvature of the track. The sign of ω is given by the charge of the particle, its magnitude by the transverse momentum $\mathrm{p_t}$ of the track ($\omega \propto 1/\mathrm{p_t}$).

The tracks are fitted by using a Kalman filter technique [56]. In a boot-strapping procedure, each vertex is essentially fitted independently; the results of the fits are propagated iteratively and recursively to the neighboring vertices. The result is a global fit of all the tracks. Local information is used to make corrections, for instance for the material distribution, dead parts of the detector, inhomogeneities in the solenoid field and energy loss of low momentum tracks. The algorithm starts with the hits found in the DCH by the Level 3 Trigger. The hits are used to form a track that starts from the beamspot and further hits are added to that track if they are consistent. The beamspot in *BABAR* is a region that is calculated as an average from all the events of the previous ten minutes. In a second step, the remaining hits in the DCH are analyzed to check if they are consistent with tracks that do not originate at the beamspot or with particles that are stopped in the DCH due to their low momentum. $\mathrm{K_s^0}$ are one example of tracks that do not originate from the beamspot, as they are long-lived enough for some of them to decay outside the SVT. In a third step, the SVT hits are analyzed and added to the DCH tracks if they are consistent. Hits in the SVT that are not matched with any DCH tracks are used to look for low momentum tracks that come from particles that have been stopped in the SVT. The reconstructed tracks are then stored in lists, according to different selection criteria. In this analysis we use the `ChargedTracks` list, that contains all charged tracks and assigns the pion mass hypothesis to all of them. In the case of $\mathrm{K_s^0}$ the reconstruction is done using a geometrically constrained fit. Due to the constraints in this fit the combinatorial background is very low and no tight selection on the track quality is necessary.

7.3.2 Calorimeter algorithms

The interaction of photons and $e^{\pm}$ in the EMC typically results in electromagnetic showers[5]. These showers depose energy over several neighboring crystals that form a cluster. A cluster can contain energy deposits coming from several particles, in which case the cluster usually has several maxima (bumps) of deposed energy. The calorimeter algorithm aims to separate these contributions, and assigns the relevant part of the total cluster energy to the different maxima. To this end the correct shape of the cluster has to be found. The algorithm starts by looking for crystals with deposed energy larger than $10\,\mathrm{MeV}$, that are used as seeds for the cluster formation. From the seeds, the algorithm adds neighboring crystals to the cluster: it adds crystals with more than $1\,\mathrm{MeV}$ of deposed energy and christals with less than $1\,\mathrm{MeV}$ if they are neighbors to a crystal that has $3\,\mathrm{MeV}$ or more of deposed energy. Local maxima are identified by standard methods and get assigned fractions of the energy in the different crystals in the cluster. The fractions depend on the ratio of the distance between the crystal and the maximum and the Moliere radius of the crystals. In a last step, the bumps

[5] Hadrons and muons are seen a non-showering particles in the EMC.

are matched with tracks. In case of a match, the track is linked to the bump and the new object is considered as a single particle. The remaining bumps with no matched track are considered as neutral objects and are classified in the neutral lists. The list we require for bumps from which we reconstruct π^0 candidates is called `CalorClusterNeutral` and has no requirements except that there is no match with any track.

7.3.3 Particle identification (PID)

Particle identification of charged particles is one of the crucial points in the *BABAR* experiment, as the flavor of the $\mathrm{B_{tag}}$ is identified by its daughter particles (see Sec. 7.3.4). There are five long-lived particles that can be tracked in the detector: electrons, muons, pions, kaons and protons. All sub-detectors (SVT, DCH, EMC, DIRC and IFR) contribute to the PID and the contributions of the sub-detectors are combined in PDF's, one for each of the five species. The PDF of a species gives the probability, as a function of the output of the detector, that a particle belongs to that species. While electrons and muons can be separated rather easily, for instance by their EMC shower shape and the IFR response, kaons and pions are much harder to distinguish. Protons are rather rare and we do not consider them here. The PDFs of kaons and pions are constructed as the product of the individual PDFs from the SVT, the DCH and the DIRC. For the SVT and the DCH, the energy loss $\mathrm{dE/dx}$ is measured and compared to the Bethe-Bloch expectation for a given particle hypothesis. For the DIRC, a MC based binned likelihood function is used, which depends on the angle between tracks and Cerenkov photons and on the number of photons. Likelihood ratios are used to assign a given track to a list. In the present analysis we do not use PID as requirement for the signal $\mathrm{B^0}$, on the other hand it is implicitly used for the tagging procedure that is necessary for the measurement of CP asymmetries and is described in the next sub-section.

7.3.4 Flavor tagging

As mentioned earlier (compare Fig. 2.4 in chapter 2), flavor specific neutral B decays can be used to tag $\mathrm{B\bar{B}}$ events. For instance in semi-leptonic neutral B decays, due to charge conservation, the charge of the lepton in the final state identifies the flavor of the b valence quark. If the lepton is negatively charged, the valence quark is a b and the $\mathrm{B_{tag}}$ meson[6] is tagged as $\mathrm{\bar{B}^0}$ and the other B, $\mathrm{B_{CP}}$[7], is a $\mathrm{B^0}$ at the same instant; if the lepton is positively charged, the $\mathrm{B_{tag}}$ is tagged as $\mathrm{B^0}$ and the $\mathrm{B_{CP}}$ is a $\mathrm{\bar{B}^0}$ at the same instant. As we have mentioned in the previous section, particles can only be identified with a certain probability, and this probability has to be propagated to the uncertainty of the measurement (in this analysis the statistical uncertainty σ in the $\mathcal{S}$ and $\mathcal{C}$ parameters). In *BABAR* the probability of wrongly identifying the flavor of the $\mathrm{B_{tag}}$ is called the mis-tag rate ω, which is different for misidentifying a $\mathrm{B^0}$ and a $\mathrm{\bar{B}^0}$. ω describes the probability that a true $\mathrm{B_{tag}} = \mathrm{B^0}$ is identified as $\mathrm{\bar{B}^0}$, and $\bar{\omega}$ describes the probability that a true $B_{tag} = \bar{B}^0$ is identified as $\mathrm{B^0}$. Not all events are actually tagged, the tagging efficiency ϵ_{tag} denotes the fraction of neutral

[6] To be unambigous: This is the flavor of the tag-side B, we cannot make any definite statement on the signal-side B at decay time

[7] Flavor tagging works of course as well when the signal-side B does not decay to a *CP* eigenstate.

B decays that are assigned a tag. With these definitions, the "effective tagging efficiency" Q can be defined[8]:

$$\mathrm{Q} = \epsilon_{\mathrm{tag}}(1 - 2\langle\omega\rangle)^2 \quad , \quad \sigma \propto \frac{1}{\sqrt{Q}} \tag{7.1}$$

The statistical σ uncertainty of tagging dependent variables is inversely proportional to the square root of Q. ϵ_{tag} and ω are found in a fit to data (see Tab. 7.3) and the former corresponds to the fraction of B decays where at least one candidate is fully reconstructed and the tag-side B has been vertexed and tagged. Experimentally the following definitions are more convenient:

$$\langle\omega\rangle = \frac{1}{2}(\omega + \bar{\omega}) \quad , \quad \Delta\omega = (\omega - \bar{\omega}) \tag{7.2}$$

$$\mathcal{D} = 1 - 2\omega \quad , \quad \bar{\mathcal{D}} = 1 - 2\bar{\omega} \tag{7.3}$$

$$\langle\mathcal{D}\rangle = \frac{1}{2}(\mathcal{D} + \bar{\mathcal{D}}) \quad , \quad \Delta\mathcal{D} = \mathcal{D} - \bar{\mathcal{D}} \tag{7.4}$$

where $\mathcal{D}$ is the tagging dilution, and $\Delta\mathcal{D}$ and $\Delta\omega$ describe differences in performance of the tagging procedure between B^0 and $\bar{\mathrm{B}}^0$.

The flavor tagging algorithm

In a first step the tagging algorithm removes all tracks and neutral objects that belong to the fully reconstructed signal B. The left over tracks and neutral object are then used to form $\mathrm{B}_{\mathrm{tag}}$ daughter candidates. In a geometrical fit, the candidates are fitted to a common decay vertex: the decay vertex of the $\mathrm{B}_{\mathrm{tag}}$. The fit takes into account the beam energies, the beam spot position and the flight direction of the fully reconstructed signal B. The flavor of the $\mathrm{B}_{\mathrm{tag}}$ is assigned with a NN, the `TAG04` NN [57]. The output of the NN is a signed probability [-1,1], where the magnitude represents the confidence of the assignment, and the sign corresponds to the flavor of the $\mathrm{B}_{\mathrm{tag}}$. A negative sign stands for $\mathrm{B}_{\mathrm{tag}} = \bar{\mathrm{B}}^0 (\Rightarrow \mathrm{q}_{\mathrm{tag}} = -1)$ and a positive sign for $\mathrm{B}_{\mathrm{tag}} = \mathrm{B}^0 (\Rightarrow \mathrm{q}_{\mathrm{tag}} = +1)$. The NN itself has as input variables the output of other NNs that are optimized to find any of the distinct nine processes, the "sub-taggers", which would identify the b valence quark of the B parent particle. The algorithm classifies an event into one of seven mutually exclusive and hierarchical tagging categories c, not the same as the sub-taggers, and the Q is the sum of their contributions and yields $\mathrm{Q} = \sum_{\mathrm{c}} \epsilon^{\mathrm{c}}_{\mathrm{tag}}(1 - 2\omega_{\mathrm{c}})^2 = 31.2 \pm 0.3$. In order of increasing tagging dilution, these categories are: `Lepton`, `KaonI`, `KaonII`, `Kaon-Pion`, `Pion`, `Other` and `Notag`. The tagging categories are defined for intervals of the NN output, but their names are related to the sub-taggers that contribute the most. In the case of the `Lepton` and `KaonI` tagging categories, the PID information is used additionally for the category definition. The nine sub-taggers are `Lepton` (3 sub-taggers: `Electron`, `Muon`, `KinLep`), `Kaon`, `SlowPion`, `KPi`, `MaxPstar`, `FSC` and `Lambda`. We summarize the structure of the sub tagger NN in Tab. 7.2. The motivation for the different sub-taggers and the definitions of the NN input variable definitions from each one of them are:

[8] We use here the average mistag rate $\langle\omega\rangle$ that will be introduced below

- The `Lepton` sub-taggers exploit the semi-leptonic decays of the B meson ($\mathcal{B}$ $\sim$10.4%), where the $\mathrm{b}(\bar{\mathrm{b}})$ emits a virtual $\mathrm{W}^{-}(\mathrm{W}^{+})$ that decays to a lepton (the "direct" lepton) and (anti)neutrino. p^{*} is the CM momentum of all $\mathrm{B}_{\mathrm{tag}}$ daughter particles. $\mathrm{E}_{90}^{\mathrm{W}}$ is the energy contained in the hemisphere defined by the direction of the virtual $\mathrm{W}^{\pm}$. $cos(\theta_{miss})$ is the cosine of the missing momentum (due to the neutrino) and the leptons momentum. q is the electric charge of the particles.

- The `Kaon` sub-tagger is the highest contributor to *BABAR*'s Q value due to the high branching fraction of inclusive $\mathrm{B}^{0} \rightarrow \mathrm{K}^{\pm}\mathrm{X}$ decays ($\sim$78%). The charge of the kaon gives information on the flavour of the B meson, via the process $\mathrm{b} \rightarrow \mathrm{c} \rightarrow \mathrm{s}$ that produces so-called *right-sign* kaons. *Wrong-sign* kaons can be produced, for instance, in the process $\mathrm{b} \rightarrow \mathrm{W}^{-}\mathrm{c}$, where $\mathrm{c} \rightarrow \mathrm{s}$ gives a *right-sign* kaon, but the decay $\mathrm{W}^{-} \rightarrow \bar{\mathrm{c}}\mathrm{s}$ and $\bar{\mathrm{c}} \rightarrow \bar{\mathrm{s}}$ gives a *wrong-sign* kaon. The K1, K2 and K3 variables are the PID likelihood of the best three kaons in the event, nK_s^0 is the number of $\mathrm{K}_{\mathrm{s}}^{0}$ and $\sum \mathrm{p}_{\mathrm{t}}^{2}$ is the sum of the squares of the transverse momenta. $\sum \mathrm{p}_{\mathrm{t}}^{2}$ help to distinuish between kaons that come from $\mathrm{W}^{\pm}$ or from charmed objects.

- The `SlowPion` sub-tagger adds information by identifying slow pions from $B^0 \rightarrow D^{*+}X$ decays that are followed by a $\mathrm{D}^{*+} \rightarrow \mathrm{D}^{0}\pi^{+}$ decay $\sim \frac{2}{3}$ of the time. For $\cos(\theta_{\mathrm{thr}})$ see Sec. 7.5, $\mathcal{L}_{\mathrm{K}}$ is the kaon PID that is used to reject slow kaons from the D^0 decay.

- The `MaxPstar` sub-tagger identifies fast particles that come form an energetic virtual $\mathrm{W}^{\pm}$. Their charge contains flavor information, they can either be mis-identified leptons or hadrons, for instance from $\mathrm{B}^{0} \rightarrow \mathrm{D}^{*}\pi$. $\cos(\theta)$ is the angle between the the thrust axis of the $\mathrm{B}_{\mathrm{tag}}$ and the fast particle.

- The `KPi` sub-tagger adds information to tags from D^* decays, as the subsequent decay proceeds in $\sim$53% of the times via $\mathrm{D}^{0} \rightarrow \mathrm{K}^{-}\mathrm{X}$, where the kaons flies in the same direction as the slow pion. $\cos(\theta_{\mathrm{K},\pi})$ is the angle between kaon and pion.

- The `FSC` (for fast-slow) sub-tagger exploits that in $\mathrm{b} \rightarrow \mathrm{cW}^{-}$ decays the slow pions flies approximately back-to-back with the fast decay products of the W^{-} decay. The $\cos(\theta_{\mathrm{SlowFast}})$, $\cos(\theta_{\mathrm{SlowThrust}})$, $\cos(\theta_{\mathrm{FastThrust}})$ variables are the angles between the slowest and fastest track, between the slowest track and the thrust axis of the $\mathrm{B}_{\mathrm{tag}}$ and the fastest track and the thrust axis respectively. $\mathrm{p}_{\mathrm{Slow}}^{*}$, p_{Fast}^{*} are the momenta in the CM of the slowest and fastest track respectively.

- The `Lambda` sub-tagger identifies the rare but clean signature of decays where the strange quark in $\mathrm{b} \rightarrow \mathrm{c} \rightarrow \mathrm{s}$ forms a Λ baryon. M_{Λ}, χ^2, $\cos(\theta)$, p_{Λ} and p_{p} are the mass, the χ^2 of the decay vertex fit from $\Lambda \rightarrow \mathrm{p}\pi$, the angle between it's momentum ans it's flight direction and the momentum of the proton daughter particle respectively.

sub-tagger	NN	Discriminating variables	Training target
Electron	4:12:1	p^*, E^W_{90}, $\cos(\theta_{\rm miss})$, q	Classify B^0 vs. $\bar{B}^0$
Muon	4:12:1	p^*, E^W_{90}, $\cos(\theta_{\rm miss})$, q	Classify B^0 vs. $\bar{B}^0$
KinLep	3:3:1	p^*, E^W_{90}, $\cos(\theta_{\rm miss})$	Recognize leptons from "direct" decays
Kaon	5:10:1	K1, K2, K3, nK^0_s ,$\sum p^2_t$	Classify B^0 vs. B^0
SlowPion	3:10:1	p^*, $\cos(\theta_{\rm thr})$, $\mathcal{L}_{\mathcal{K}}$	Recognize true slow pions
MaxPstar	3:6:1	p^*, $DOCA_{xy}$, $\cos(\theta)$	Recognize fast tracks
KPi	3:10:1	Kaon tag, SlowPion tag, $cos(\theta_{K,\pi})$	Recognize pairs of true kaons and slow pions
FSC	6:12:1	$\cos(\theta_{\rm SlowFast})$, $p^*_{\rm Slow}$, $p^*_{\rm Fats}$, $\cos(\theta_{\rm SlowThrust})$, $\cos(\theta_{\rm FastThrust})$ $\mathcal{L}_{\rm K\ Slow}$	
Lambda	6:14:1	M_Λ, χ^2, $\cos(\theta)$ flight length, p_Λ, p_p	Recognize Λ decays
Tag04	9:20:1	All of the above tags	Classify B^0 vs. $\bar{B}^0$

Table 7.2: Summary of the different sub-taggers. The second row indicates the number of input layers, hidden layers and output layer respectively for the NNs. The third row gives the input variables that are defined in the text, the last row details the target of the training

Category	$\varepsilon_{\rm tag}(\%)$	$\Delta\varepsilon_{\rm tag}(\%)$	$\omega(\%)$	$\Delta\omega(\%)$	$Q(\%)$	$\Delta Q(\%)$
Lepton	8.96 ± 0.07	-0.1 ± 0.2	2.9 ± 0.3	0.2 ± 0.5	7.95 ± 0.11	-0.12 ± 0.37
KaonI	10.81 ± 0.07	-0.0 ± 0.2	5.3 ± 0.3	0.0 ± 0.6	8.64 ± 0.14	-0.00 ± 0.45
KaonII	17.18 ± 0.09	0.2 ± 0.3	14.5 ± 0.3	0.4 ± 0.6	8.64 ± 0.17	0.08 ± 0.50
Kaon-Pion	13.67 ± 0.08	0.1 ± 0.2	23.3 ± 0.4	-0.6 ± 0.7	3.91 ± 0.12	0.20 ± 0.34
Pion	14.19 ± 0.08	-0.7 ± 0.3	32.6 ± 0.4	5.1 ± 0.7	1.73 ± 0.09	-1.10 ± 0.23
Other	9.55 ± 0.07	0.3 ± 0.2	41.5 ± 0.5	3.8 ± 0.8	0.28 ± 0.04	-0.24 ± 0.09
Total	74.36 ± 0.10	-0.2 ± 0.6			31.1 ± 0.30	-1.3 ± 0.9

Table 7.3: Performance of the tagging algorithm on data. The results are a fit to a data sample of over 133000 fully reconstructed $B_{\rm flav}$ decays. Here $\Delta\varepsilon = \varepsilon_{B^0} - \varepsilon_{\bar{B}^0}$, $\Delta\omega = \omega_{B^0} - \omega_{\bar{B}^0}$ and $\Delta Q = Q_{B^0} - Q_{\bar{B}^0}$ refer to differences between B^0 and $\bar{B}^0$ tags in tagging efficiency, mis-tag fraction and effective tagging efficiency, respectively.

7.3.5 Vertexing

In the vertexing procedure the TreeFitter [58] algorithm plays the central role. The algorithm has been developed in *BABAR* and is particularly adapted for decay chains that contains non-zero lifetime particles, such as K^0_s . It performs a global fit using a Kalman filter technique [56] to the whole decay chain. Momentum and geometric constraints are automatically applied. In a first step, the K^0_s composite candidates are formed. For a $K^0_s \to \pi^+\pi^-$ we require that a candidate satisfies the KsDefault list:

- All charged tracks are assigned the pion mass hypothesis.
- If the invariant mass of two "pions" measured at their DOCA is between 0.45 GeV/c^2 and 0.55 GeV/c^2, the candidate is further processed.
- TreeFitter is used to perform a geometrical fit a particle that decayed to the "pions", this fit uses the constraint that the two "pions" originate from the same decay vertex.

- If the reconstructed mass is between 0.47267 GeV/c^2 and 0.52267 GeV/c^2, the candidate passes the selection.

For a $K_s^0 \to \pi^0\ \pi^0$ we require that a candidate satisfies the `KsToPi0Pi0Default` GeV/c^2 list[9] :

- Any bump or multi-bump in the calorimeter that is not matched with a charged track is considered as "photon".
- π^0 candidates are formed from pairs of bumps by adding their four-momenta, "photons" with less than 30 MeV are rejected. The energy of the π^0 has to be larger than 0.2GeVand the mass is required to be between 0.1 and 0.155 GeV/c^2.
- Pairs of π^0 candidates are used to form $\mathrm{K_s^0}$ candidates. If the invariant mass is between 0.34 GeV/c^2 and 0.62 GeV/c^2 the candidate is further processed. `TreeFitter` is used to fit the $\mathrm{K_s^0}$ candidates, in the fit procedure the primary vertex of the decay is used and the probability of the χ^2 of the fit has to exceed 10^{-5}. If the fitted mass is between 0.446 GeV/c^2 and 0.540 GeV/c^2, the candidate passed the list requirements

We reconstruct the two sub-channels $\mathrm{B^0} \to 3\mathrm{K_s^0}(\pi^+\pi^-)$ and $\mathrm{B^0} \to 2\mathrm{K_s^0}(\pi^+\pi^-)\mathrm{K_s^0}(\pi^0\pi^0)$ simultaneously[10], by merging the two composites `KsDefault` and `KsToPi0Pi0Default` in a way that the composite can either be a $\mathrm{K_s^0}(\pi^+\pi^-)$ or a $\mathrm{K_s^0}(\pi^0\pi^0)$. We then form $\mathrm{B^0}$ candidates that contain three $\mathrm{K_s^0}$ candidates, one from the merged list and two from the `KsDefault` list. A global fit using `TreeFitter` is then performed to find the decay vertex of the $\mathrm{B^0}$ candidate and the event-shape variables (see Sec. 7.5.3). In this fit the $\mathrm{K_s^0}$ masses and the $\mathrm{B^0}$ mass are constrained to the world average [1]. In a second fit the masses are free to vary to obtain the $\mathrm{K_s^0}$ kinematical variables (see Sec. 7.5.2) and the $\mathrm{B^0}$ kinematical variables $\mathrm{m_{ES}}$ and $\Delta\mathrm{E}$ (see Sec. 7.5) . Further requirements are applied on the reconstructed candidates in the event selection, see Sec. 8.2 for the TD analysis, and Sec. 9.2 for the amplitude analysis.

7.4 The $\Delta\mathrm{t}$ measurement

7.4.1 The $\Delta\mathrm{z}$ measurement

The time between the decay of the two B mesons is determined by measuring the separation along the z-axis of the two decay vertices. The average separation between the two vertices due to the boosted $\Upsilon(4S)$ rest frame is given by

$$\beta\gamma\mathrm{c}\tau_{\mathrm{B^0}} = 257\mu\mathrm{m}\ . \tag{7.5}$$

For an average event to contribute to the measurement, its uncertainty on $\Delta\mathrm{z}$ has to be smaller than this value. The SVT is able to provide a measurement of the position in z with a precision of 70 $\mu\mathrm{m}$ (see Sec. 4.4.3) for a single track. The uncertainty of $\Delta\mathrm{z}$ measurement

[9] There are further standard requirements that are not mentioned explicitly here. For shortness we concentrate on the main properties.

[10] In the DP analysis, we only use $\mathrm{B^0} \to 3\mathrm{K_s^0}(\pi^+\pi^-)$

depends on the uncertainties of both z-measurements, for the signal B and the tag-side B. The vertex of the fully reconstructed signal B is usually reconstructed from several tracks, the daughter particles of the signal B. This gives a resolution on the z-position of $\sim$65 μm for more than 99% of the candidates on the signal side (and even $\sim$45 μm for more than 80%). The resolution is evalutated by substracting the true value from the reconstructed one, and the uncertainty corresponds to the RMS of this residual distribution. Unfortunately the z-measurement of the tag-side B is much poorer and as a result the resolution on the Δz measurement is dominated by the tag-side z-position measurement. The poor z-measurement is due to the inclusive reconstruction of $\mathrm{B_{tag}}$ that is necessary to keep reconstruction efficiencies at a reasonable level. As a result most of the tag-side events are only partly reconstructed and that leads to a total uncertainty on the Δz measurement of $\sim$190 μm ($\sim$150 μm for 99% of the events). These numbers are smaller than the one given in Eq. 7.5 and allow a reasonable Δz measurement. Some of the events ($\sim$1%, "outliers") do not have correctly-determined vertex positions, and engender in verly long tails that result in a misleading value for the RMS in the residual distribution. We remove events with failed fits by requirements on the error of the Δt measurment (see Sec. 8.2 and Sec. 9.2). The algorithm that reconstructs the $\mathrm{B_{tag}}$ vertex uses only tracks that are not matched with the signal B. Due to the inclusive reconstruction, a global vertex fit is not always possible. In case tracks are reconstructed to give long-lived particles such as $\mathrm{K^0_s}$ or Λ, the trajectories of these composite particles is used to avoid biases due to the displaced secondary vertex. Track that are consistent with photon conversions are not taken into account for the vertexing. Another source of bias are decays of charmed mesons. Even though their lifetime is comparable to the one of the B mesons and much shorter than the lifetime of $\mathrm{K^0_s}$ or Λ, biases can be introduced. These biases are unavoidable, but an iterative procedure is used to reduce them. The track that contributes the most to the χ^2 is removed from the fit of the $\mathrm{B_{tag}}$ vertex. If the increase in χ^2 is larger than six, the fit is repeated without this track and the procedure is repeated until the increase is smaller than six. The leftover bias in the Δz measurement is taken into account in the Δt resolution function, see Sec. 7.4.3.

7.4.2 The Δt determination

To determine Δt from the Δz measurement, the *BABAR* reconstruction code uses the boost $\beta\gamma$ of the $\Upsilon(4S)$ in the laboratory frame

$$\Delta \mathrm{t} = \frac{\Delta \mathrm{z}}{\beta\gamma \mathrm{c}} \, . \tag{7.6}$$

The value of $\beta\gamma$ is known to high precision from the beam energies that are monitored continuously. For $\Upsilon(4\mathrm{S})$ running this value is $\beta\gamma = 0.56$. Eq. 7.6 is a good approximation obtained assuming that the B mesons are produced at rest in the $\Upsilon(4\mathrm{S})$ rest frame and hence have negligible momenta. It is possible to take into account the non-zero momentum of the B mesons $\mathrm{p^*_B} = 340\,\mathrm{MeV/c}$ in the $\Upsilon(4S)$ rest frame to get a more accurate determination of Δt. In the case of a fully reconstructed B meson, as the signal B of the present analysis, $\mathrm{p^*_B}$ can be measured and used to correct Eq. 7.6:

$$\Delta z = \beta\gamma\gamma^*_{rec} c(t_{rec} - t_{tag}) + \gamma\beta^*_{rec}\gamma^*_{rec}\cos(\theta^*_{rec}) c(t_{rec} + t_{tag}) \, , \tag{7.7}$$

with the boost factor in the CM frame of the reconstructed B meson $\gamma^*_{\mathrm{rec}} = 1.002$, its speed $\beta^*_{\mathrm{rec}} = 0.064$ and its angle with respect to the z axis θ^*_{rec}. The value of $\mathrm{t_{rec}} + \mathrm{t_{tag}}$ is not directly measured but can be expressed as function of the distance in x-y of the two B mesons. This distance is small ($\sim$35-40 $\mu\mathrm{m}$) when compared to the $\mathrm{B_{tag}}$ vertex measurement, and the estimate $\mathrm{t_{rec}} + \mathrm{t_{tag}} = \tau_{\mathrm{B}} + |\Delta \mathrm{t}|$ is used instead. To determine the corrected value of $\Delta \mathrm{t}$, the equation

$$\Delta \mathrm{z} = \beta\gamma\gamma^*_{\mathrm{rec}}\mathrm{c}(\mathrm{t_{rec}} - \mathrm{t_{tag}}) + \gamma\beta^*_{\mathrm{rec}}\gamma^*_{\mathrm{rec}}\cos(\theta^*_{\mathrm{rec}})\mathrm{c}(\tau_{\mathrm{B}} + |\Delta \mathrm{t}|) \tag{7.8}$$

has to be solved for $\Delta \mathrm{t}$. In the end the difference between Eq. 7.6 and Eq. 7.8 is very small and the correction in $\Delta \mathrm{t}$ is only $\sim$0.02 ps. The use of Eq. 7.8 improves the resolution by about 5%. As we take the resolution function in this work from MC (see Sec. 7.4.3) and as we are biased on the signal side due to the indirect reconstruction from the long-lived $\mathrm{K^0_s}$, we use the non-corrected average determination of Eq. 7.6 for the analysis. Another advantage of this approach is that, contrarily to the approach using Eq. 7.8, no correlations are introduced in the less-understood continuum background.

7.4.3 The $\Delta \mathrm{t}$ resolution model

The $\Delta \mathrm{t}$ measurment has an experimental resolution that is described in *BABAR* analyses as a sum of three Gaussians, the core, tail and outlier Gaussians:

$$\begin{aligned} \mathcal{R}(\delta_{\mathrm{t}}; \sigma_{\Delta \mathrm{t}}) \;=\; & (1 - \mathrm{f_{tail}} - \mathrm{f_{out}})\mathrm{G}\left(\delta_{\mathrm{t}}, \mathrm{s^b_{core}}\sigma_{\Delta \mathrm{t}}, \mathrm{s^\sigma_{core}}\sigma_{\Delta \mathrm{t}}\right) \\ & + \mathrm{f_{tail}}\mathrm{G}\left(\delta_{\mathrm{t}}, \mathrm{s^b_{tail}}\sigma_{\Delta \mathrm{t}}, \mathrm{s^\sigma_{tail}}\sigma_{\Delta \mathrm{t}}\right) + \mathrm{f_{out}}\mathrm{G}\left(\delta_{\mathrm{t}}, \mathrm{s^b_{out}}, \mathrm{s^\sigma_{out}}\right) \;, \end{aligned} \tag{7.9}$$

where the G functions are normalized Gaussians:

$$\mathrm{G}(\delta \mathrm{t}, \mu, \sigma) = \frac{1}{\sigma\sqrt{2\pi}} \exp(-\frac{(\delta \mathrm{t} - \mu)^2}{2\sigma^2}). \tag{7.10}$$

$\delta \mathrm{t} = \Delta \mathrm{t} - \Delta \mathrm{t_{true}}$ is the difference between reconstructed and true value of Δt and $\sigma_{\Delta t}$ is the per event resolution that is estimated by the fit. The means and widths of the core and tail Gaussians depend on the error of the measurement. This dependence takes into account the experimentally observed correlation between these variables, that is due to the vertex reconstruction from non-zero lifetime particles, such as D mesons. In analyses that reconstruct the signal decay vertex from charged tracks that come directly from the signal B, the resolution function is dominated by the tag-side B meson. This allows the use of the same resolution function that has been fitted on data in $\mathrm{B} \to \mathrm{c\bar{c}K^{(*)}}$ analyses. In the case of the present analyses, the signal B is reconstructed from non-zero lifetime $\mathrm{K^0_s}$, and the resolution function, in particular the correlation with $\sigma_{\Delta \mathrm{t}}$, is not the same as in $\mathrm{B} \to \mathrm{c\bar{c}K^{(*)}}$ analyses. We therefore fit the resolution function on signal MC (see Tab. 8.10 in Sec. 8.4.1).

7.5 Discriminating variables

7.5.1 B meson kinematic variables

The kinematic variables are chosen in a way that takes full advantage of the known initial state at a $\mathrm{e^+e^-}$ collider. Two almost uncorrelated variables are defined [59]: the energy-

substituted mass m_{ES} and the energy difference ΔE, defined as

$$m_{ES} = \sqrt{(\frac{s}{2} + \vec{p_i} \cdot \vec{p_B})^2/E_i^2 - \vec{p_B}^2}\ , \quad \Delta E = E_B^* - \sqrt{s}/2\ . \tag{7.11}$$

$(\mathrm{E_i}, \vec{\mathrm{p_i}})$ is the four-momentum of the initial state, $\vec{\mathrm{p_B}}$ is the momentum of the B candidate, both in the laboratory frame and $\sqrt{\mathrm{s}}$ is the center-of-mass energy. $\mathrm{m_{ES}}$ has the advantage that it does not depend on a mass hypothesis of the particles in the final state, but only on the reconstructed momentum of the B candidate and the well known initial state conditions precisely measured by PEP-II . The result is a better mass resolution compared to a measurement that includes the energy of the B candidate. For signal events $\mathrm{m_{ES}}$ peaks at the B meson mass while continuum events show no peaking structure due to their combinatorial nature. ΔE on the other hand depends on the energy of the B meson in the CM frame of the electron-positron system, and also on the mass hypothesis made for the particles in the final state. For signal it peaks at zero, for continuum events it is flatly distributed. Moreover this variable is useful to discriminate wrongly reconstructed events from B decays, as wrongly identified particles in the final state give a shift in the peak, due to the wrong mass hypothesis. Signal and continuum distributions of $\mathrm{m_{ES}}$ and ΔE are shown in Sec. 8.2 and Sec. 9.2.

7.5.2 K_s^0 kinematic variables

$\mathrm{K_s^0}$ variables are not used in the fit, but for event selection (see Sec. 8.2). For the vertex fit the masses of the $\mathrm{K_s^0}$ are constrained to the world average [1]. The invariant mass of a $\mathrm{K_s^0}$, m($\mathrm{K_s^0}$), is calculated independently from the 4-momenta of the pion daughters. The decay length $\mathrm{r_{dec}}$ is defined as the 2D decay distance between the decay vertex of the $\mathrm{K_s^0}$ and the center of the beamspot,

$$\mathrm{r_{dec}} = \sqrt{(\mathrm{x_{vtx}} - \mathrm{x_{bs}})^2 + (\mathrm{y_{vtx}} - \mathrm{y_{bs}})^2}. \tag{7.12}$$

The pointing angle α is the two-dimensional angle between the momentum vector and the vector connecting the center of the beam-spot to the decay vertex of the $\mathrm{K_s^0}$,

$$\cos\alpha = \hat{\mathrm{r}}_{\mathrm{dec}} \cdot \hat{\mathrm{P}}_{\mathrm{xy}}\ , \tag{7.13}$$

where $\hat{r}_{\mathrm{dec}}$ and $\hat{P}_{\mathrm{xy}}$ are unit vectors.

7.5.3 Event-shape variables and Neural Network (NN)

Event shape variables are used to exploit the different topologies in the $\Upsilon(4\mathrm{S})$ rest frame of $\mathrm{e^+e^-} \to \Upsilon(4\mathrm{s}) \to \mathrm{B\bar{B}}$ events and continuum events that are produced via $\mathrm{e^+e^-} \to \mathrm{q\bar{q}}$, $(\mathrm{q} = \mathrm{u, d, s, c})$. In signal events the $\Upsilon(4\mathrm{s})$ ($\mathrm{m_{\Upsilon(4s)}} = 10.579$ GeV) that decays to $\mathrm{B\bar{B}}$ pairs has just enough mass to produce a pair of B mesons ($\mathrm{m_B} = 5.279$ GeV), which means the B mesons are produced almost at rest in the $\Upsilon(4\mathrm{S})$ rest frame. As the momenta of the daughters of the B meson are much bigger than the B momentum, their decay is almost isotropical. We use the following variables to describe the event topology:

- $\cos(\theta_{\mathrm{B_{mom}}})$ is defined as the angle between the B momentum and the beam axis. For $\mathrm{B\bar{B}}$ events $\theta_{\mathrm{B_{mom}}}$ is distributed as $\sin^2(\theta)$, due to the decay of the spin-1 $\Upsilon(4\mathrm{S})$ resonance to two spin-0 particles. For continuum events the $\theta_{\mathrm{B_{mom}}}$ distribution is flat as the B candidate is reconstructed from random combinations of tracks.

- $\cos(\theta_{\mathrm{B_{thr}}})$ is defined as the angle between the thrust axis of the B candidate and the z axis. The thrust axis $\hat{\mathrm{T}}$ of an ensemble of particles, in this case the particles the B candidate is reconstructed from, is defined as the axis on which the sum of the projections of the momenta of the particles, the thrust $\hat{\mathrm{T}}$ is maximal:

$$\hat{\mathrm{T}} = \max\left(\frac{\sum_{\mathrm{i}} |\hat{\mathrm{T}}_{\mathrm{i}} \cdot \mathrm{p}_{\mathrm{i}}^*|}{\sum_{\mathrm{i}} |\mathrm{p}_{\mathrm{i}}^*|}\right) . \tag{7.14}$$

  For $\mathrm{B\bar{B}}$ $\hat{\mathrm{T}}$ takes almost random values, as the events are mostly isotropical. For $\mathrm{q\bar{q}}$ events on the other hand, $\hat{\mathrm{T}}$ follows the direction of the jets of the events, that are strongly directional.

- L_0 and L_2 are defined using information of the rest of the event (ROE), i.e. the decay of the other B meson. We cannot use any angular distribution information of the decay of the signal B, as it contains information of the 3-body decay we want to study in the amplitude analysis[11]. On the other hand there is no problem looking at the angular distribution of the ROE that is as discriminant as the signal B, at least if it is partly or completely reconstructed, as it is the case in $\sim$80% of the events. The reconstructed momenta of the ROE can be used to construct the following polynomials:

$$\mathrm{L}_0 = \sum_{\mathrm{i}}^{\mathrm{ROE}} \mathrm{p}_{\mathrm{i}} , \tag{7.15}$$

$$\mathrm{L}_1 = \sum_{\mathrm{i}}^{\mathrm{ROE}} \mathrm{p}_{\mathrm{i}} |\cos\theta_{\mathrm{i}}| , \tag{7.16}$$

$$\mathrm{L}_2 = \sum_{\mathrm{i}}^{\mathrm{ROE}} \mathrm{p}_{\mathrm{i}} |\cos\theta_{\mathrm{i}}|^2 . \tag{7.17}$$

  p_{i} and θ_i are the momenta and the angles with respect to the beam axis of the objects in the ROE, i.e., in case the event has been correctly reconstructed, the decay products of the other B. L_1 turns out to have no-significant discriminating power, its expectation value is zero for signal and continuum events. We only use L_0 and L_2 to train the NN.

- The worst of the reconstructed $\mathrm{K_s^0}$ masses $\mathrm{m}^{\mathrm{W}}_{\mathrm{K_s^0}}$ is defined as the mass of the $\mathrm{K_s^0}$ that is the farest from the world average [1]. This variable is not an event-shape one, but as the mass of the $\mathrm{K_s^0}$ is constrained when reconstructing it from pions, adding this information to the NN does not introduce any significant correlations between the fit variables.

All variables that are used to train the NN (and L_1) are shown in Fig. 7.1

[11] We actually construct the Square Dalitz Plot from this information, see Sec. 3.3.7.

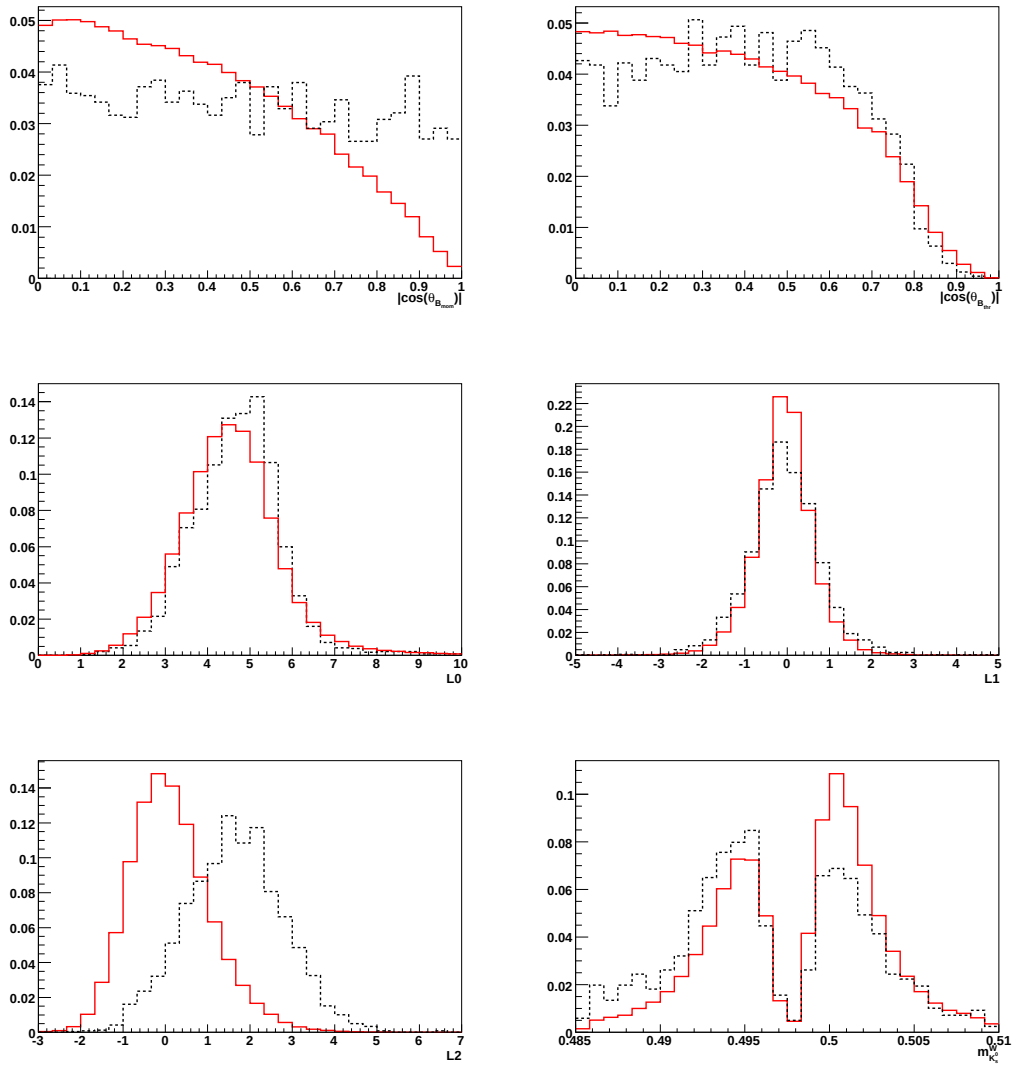

Figure 7.1: Distributions of the event shape variables from side-band (solid red line) and signal MC (dashed black line). Only B mesons decaying to K_s^0 reconstructed from charged pions are included for the plots.

The Neural Network

All of the above event shape variables have discriminating power, but as they are all functions of the same information, namely the flight direction of the particles in the $\Upsilon(4s)$ rest frame, they are all correlated. We use a NN to combine the discriminating power of these variables into a single variable. We choose the Clermont-Ferrand ANN (CFMlpANN) [60] implementation of TMVA [61], as it shows the best discrimination power what can be seen in Fig. 7.2. As training samples we use non-resonant MC as signal and off-peak and side-band data as continuum background. The NN has 4 layes, with 5 nodes in the first layer and 2 nodes in the last. We transform the raw output of the NN to a variable that is limited to the

interval [0,1]. The distribution of the transformed NN is fittable using an analytical formula for continuum events[12],

$$NN = \cos^{-1}(NN_{raw}) \tag{7.18}$$

and project onto the interval [0,1]. The transformed output of the NN is shown in Fig. 7.3.

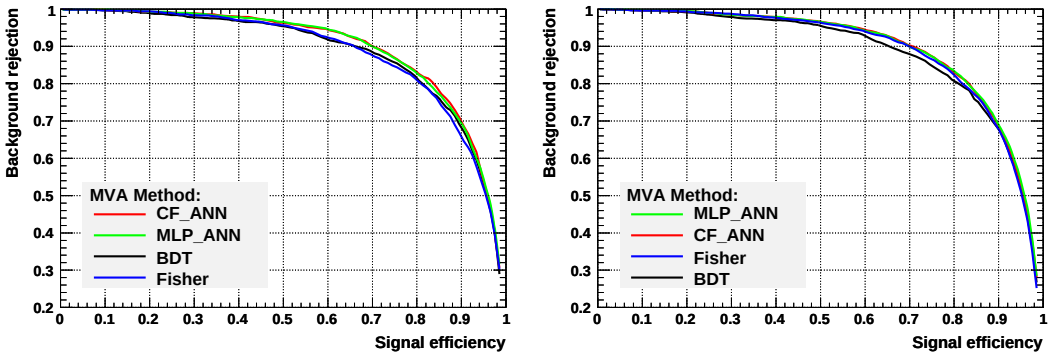

Figure 7.2: The background rejection over signal efficiency curves for $B^0 \to K^0_s(\pi^+\pi^-)K^0_s(\pi^+\pi^-)K^0_s(\pi^+\pi^-)$ (left) and $B^0 \to K^0_s(\pi^+\pi^-)K^0_s(\pi^+\pi^-)K^0_s(\pi^0\pi^0)$ (right) show that the CFMlpANN has the best discriminating power or is at least equally discriminating when comparing to other standard classifiers.

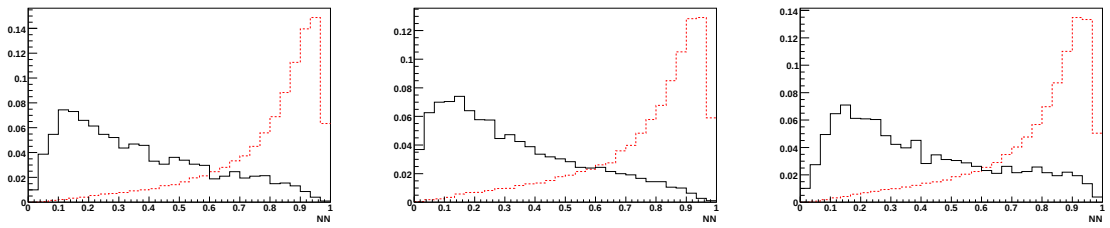

Figure 7.3: Transformed NN output for the TD analysis: on the left ($B^0 \to K^0_s(\pi^+\pi^-)K^0_s(\pi^+\pi^-)K^0_s(\pi^+\pi^-)$) and in the middle ($B^0 \to K^0_s(\pi^+\pi^-)K^0_s(\pi^+\pi^-)K^0_s(\pi^0\pi^0)$). The transformed NN output for the amplitude analysis is shown on the right. The NN is the same for both analysis, i.e. we do not retrain it for the amplitude analysis. The output distributions look slightly different, as the selection is tighter in the DP analysis.

[12]Signal events are parameterized using non-parametric PDFs.

7.6 Maximum likelihood fits

7.6.1 General aspects of likelihood fitting

Maximum likelihood fitting is a standard procedure used in HEP experiments to extract parameters of interest from data. When we want to measure, for instance, the physical TDCPV parameters S and C, we assume that the underlying tag-dependent proper time distribution has been sampled from a function, its probability density function (PDF) $\mathcal{P}$, which is normalized and depends on these physical parameters. We then use a model to parameterize this PDF that usually also includes parameters that we are not directly interested in, such as parameters to describe reconstruction effects, e.g. the $\Delta\mathrm{t}$ resolution function. PDFs are not necessarily parameterized using a model: in particular for the discriminating variables that we are not interested in, we use effective descriptions of distributions, taken from simulation. Using the PDFs we can then define the likelihood function:

$$\mathcal{L} = \prod_{\mathrm{i}=1}^{\mathrm{N}} \mathcal{P}(\vec{\mathrm{x}}_\mathrm{i}, \vec{\mathrm{a}}) \ , \tag{7.19}$$

where the index i runs over the events in the data sample, the fit variables are contained in the vector $\vec{\mathrm{x}}$ (e.g. $\Delta\mathrm{t}$), and the fit parameters (e.g. S) are contained $\vec{\mathrm{a}}$. The PDFs can be rather complicated: they have to account for several species of events, for instance signal and different background categories:

$$\mathcal{P}^i \equiv \mathcal{P}(\vec{\mathrm{x}}_\mathrm{i}, \vec{\mathrm{a}}) = \sum_{\mathrm{j}} \mathcal{P}_\mathrm{j}(\vec{\mathrm{x}}_\mathrm{i}, \vec{\mathrm{a}}) \ , \tag{7.20}$$

where the index j runs over the different species. If the variables are not correlated, the likelihood function can be expressed as a product of the individual dimensions:

$$\mathcal{P}_\mathrm{j}(\vec{\mathrm{x}}_\mathrm{i}, \vec{\mathrm{a}}) = \prod_{\mathrm{k}} \mathcal{P}_{\mathrm{j,k}}(\vec{x}_{\mathrm{i,k}}, \vec{a}_\mathrm{k}) \ , \tag{7.21}$$

where $\vec{\mathrm{a}}_\mathrm{k}$ is the associated subset of $\vec{\mathrm{a}}$, and $\vec{x}_{\mathrm{i,k}}$ the fit variable of the dimension k for the event i. To extract the parameters $\vec{\mathrm{a}}$, we vary them to obtain the set of parameters that maximizes the likelihood function, i.e. we obtain the set of parameters that is most likely to describe the sampling function of the data sample. From a technical point of view this maximization is done via a minimization of the negative logarithmic likelihood function (Nll)

$$\mathrm{Nll} = -\log(\mathcal{L}) = \sum_{\mathrm{i}=1}^{\mathrm{N}} \log(\mathcal{P}(\vec{\mathrm{x}}_\mathrm{i}, \vec{\mathrm{a}})) \ , \tag{7.22}$$

using the MIGRAD routine from the Minuit class [62] of RooFit [63]. It calculates numerically the first derivatives of the parameters and iterates to find the global minimum. As this is a local procedure, depending of the initial values of the parameters, the algorithm might converge to a secondary minimum. To ensure convergence to the global minimum, for the amplitude analysis, we perform several fits where we randomize the initial values.

To estimate the statistical uncertainties we run the HESSE routine that calculates the matrix of second derivatives and inverts it to obtain the error matrix. These errors are calculated under the assumption of a parabolic Nll, i.e. they are Gaussian and are only correct for a statistically unlimited data sample. As this work analyzes a statistically limited data sample, we run the MINOS routine to estimate the asymmetric errors of the S and C parameters. This routine assigns the one standard deviation errors using the variation of the likelihood as function of the parameter values.

7.6.2 The likelihood scan technique

To better understand the structure of the likelihood function, we can perform scans of the likelihood for a parameter: in each step we fix the parameter in question to a given value and perform a fit to obtain the corresponding value of the likelihood. All other parameters that are free to vary in the nominal fit are also free to vary in the scans. We repeat this procedure for other values of the parameter and the result of the scan is the Nll as function of the value of the scanned parameter. We use this technique quite extensively. In the TD analysis it allows us to look at the likelihood structure of the correlated variables S and C and to check the compatibility of the results of the sub-channels (see Sec. 8.5). In the amplitude analysis, scans are used to detect multiple solutions in the isobar model (see Sec. 9.6) and to search for possible resonant contributions (see Sec. 9.4). We translate the Nll to the $\Delta 2\mathrm{Nll}$ variable that is defined as twice the difference between a given likelihood value and the likelihood value at the global minimum, and corresponds to the χ^2 distribution. The statistical significance of a fit result can be obtained by $\mathrm{Significance} = \sqrt{\Delta 2\mathrm{Nll}}$ that is equivalent, for the 1 standard deviation error, to the error from MINOS.

7.6.3 Analysis tool validation using toy studies

Toy studies are used to validate the statistical robustness of the fit procedure. A toy sample is a MC data sample that has the same statistical properties as the real data sample, in the sense that the signal and background yields and characteristics correspond to the ones expected in data. The advantage is that a big number of toy data samples, usually more than 500, can be generated and fitted, which allows for a reliable estimation of the statistical significance of a fit result. An estimation of the biases is given by the "pull" distribution, defined by the difference between the generated and the fitted values divided by the error of a given parameter α

$$\mathrm{Pull} = \frac{\alpha_{\mathrm{Fit}} - \alpha_{\mathrm{Gen}}}{\sigma(\alpha_{\mathrm{Fit}})} \,. \tag{7.23}$$

If the likelihood function is correctly implemented in the fitting tool and in the limit of high statistics, there should be no observable bias in the pull distribution, i.e. it should have Gaussian shape, be centered around zero and have unit width. If this is not the case the pull distribution gives the bias in units of the statistical error.
There are two different types of toy studies that are used in this work:

- **Pure toy studies** are based on MC samples that have been generated using the fitting tool itself. The events are sampled from the same PDF as in the fit. This allows to

detect intrinsic biases that could arise e.g. from numerical calculations of normalizations that are not done with a high-enough precision. Pure toy studies are also useful to determine if certain parameters can be freed to vary in a fit procedure or if they have to be fixed to obtain a reliable convergence of the fit. This is usually the case for species that have very low statistics.

- **Embedded toy studies** use fully reconstructed MC for signal events. These events are arbitrarily shuffled from the signal MC, making sure that the same event is not used twice. This procedure ensures that the toy datasets represent the whole Run 1-6 dataset, and not just part a of it. The MC generation is adapted to the changes and shifts that occurred during and between runs, and is different for each run. Contrarily to pure toys, embedded toys are sensitive to reconstruction effects, such as wrongly reconstructed events (SCF) and correlations between variables. We use embedded toys to evaluate the fit bias. If it is small we fit the pull distribution with a Gaussian and assign the sum in quadrature of the bias of the mean and its error as systematic error, this is done in the TD analysis. If it is larger, we shift the parameter values from the fit to data by the bias and assign the sum in quadrature of half the shift and the uncertainty of the shift as systematic error, This is the case in the amplitude analysis, where the low statistics and the many free isobar parameters induce shifts due the non-parabolic shape of the likelihood.

8 Time Dependent $\mathrm{B}^0 \to \mathrm{K}^0_\mathrm{S}\mathrm{K}^0_\mathrm{S}\mathrm{K}^0_\mathrm{S}$ Analysis

8.1 Introduction

As mentioned earlier, we analyze the two submodes $\mathrm{B}^0 \to 2\mathrm{K}^0_\mathrm{s}(\pi^+\pi^-)\mathrm{K}^0_\mathrm{s}(\pi^0\pi^0)$ and $\mathrm{B}^0 \to 3\mathrm{K}^0_\mathrm{s}(\pi^+\pi^-)$ simultaneously to extract the common $\mathcal{S}$ and $\mathcal{C}$ parameters. The event selection for both sub-modes is partly common (Sec. 8.2) and partly different (Sec. 8.2.2 for $\mathrm{B}^0 \to 3\mathrm{K}^0_\mathrm{s}(\pi^+\pi^-)$ and Sec. 8.2.3 for $\mathrm{B}^0 \to 2\mathrm{K}^0_\mathrm{s}(\pi^+\pi^-)\mathrm{K}^0_\mathrm{s}(\pi^0\pi^0)$) to take into account the reconstruction from photons of one of the K^0_s in the second sub-mode. One of the particularities of our decay mode is that there are no direct tracks coming from the decay vertex of the signal B meson. As a consequence we need to ensure a good vertex quality by requiring certain hit patterns in the SVT (Sec. 8.2.4). The background composition is studied for continuum (Sec. 8.2.5) and reconstructed events from B decays (Sec. 8.2.6), and we remove background involving intermediate charmonium resonances (Sec. 8.2.7). The likelihood function is presented in Sec. 8.3.1 where we detail how the PDF has been split to allow for a common fit to both sub-modes. The analysis has been done blindly, i.e. the fitting tool has been completely validated using MC simulation (Sec. 8.4), before performing CP-blind fits. The nominal fit to extract the CPV parameters (Sec. 8.5) has been performed after obtaining satisfactory results from all the validation studies. Systematic uncertainties have been evaluated from data or from the MC-data differences that have been estimated using different versions of the control sample $\mathrm{B}^0 \to \mathrm{J}/\psi\,\mathrm{K}^0_\mathrm{s}$ (Sec. 8.6).

8.2 Selection and backgrounds

8.2.1 Common selection criteria in the two submodes

The selection criteria on the B^0 meson are the same for both sub-channels. To remove pathological events we require several very loose criteria:

- The total energy of the event has to be smaller than 20 GeV.
- The absolute value of the event shape variables L_0 and L_2 has to be inferior to 10.
- The proper time $\Delta\mathrm{t}$ measurement has to be within reasonable limits. We require that the absolute value of the $\Delta\mathrm{t}$ is inferior to 20 ps and its error is inferior to 2.5 ps.
- The cosine of the angle between the thrust of the rest of the event and the B momentum ($\cos\theta^{\mathrm{roe}}_\mathrm{T}$) has to be inferior to 0.99.

- The probability of the decay vertex fit of the B candidate has to be non-zero.

- The values of $\mathrm{m_{ES}}$ and $\Delta\mathrm{E}$ have to be inside the fit region: $5.22\mathrm{GeV} < \mathrm{m_{ES}} < 5.29\mathrm{GeV}$ and $-0.18\mathrm{GeV} < \Delta\mathrm{E} < 0.12\mathrm{GeV}$.

In the case of multiple B candidates passing the selection cuts for a single event, we select the candidate with the smallest value of a parameter based on the mass of three K^0_s mesons, defined as

$$\chi^2 = \sum_{\mathrm{i}=1}^{3} \left(\frac{\mathrm{M_{K_S,i}} - \mathrm{M}^{\mathrm{PDG}}_{\mathrm{K_S}}}{\sigma_{\mathrm{M_{K_S,i}}}} \right)^2 ,$$

where $\mathrm{M_{K_S}}$ is the mass of the reconstructed meson, $\sigma_{\mathrm{M_{K_S}}}$ is the measured errors, and $\mathrm{M}^{\mathrm{PDG}}_{\mathrm{K_S}}$ is the value from Ref. [1]. In case one event has candidates in both $\mathrm{B}^0 \to 3\mathrm{K}^0_\mathrm{s}(\pi^+\pi^+)$ and $\mathrm{B}^0 \to 2\mathrm{K}^0_\mathrm{s}(\pi^+\pi^-)\mathrm{K}^0_\mathrm{s}(\pi^0\pi^0)$, we choose the events in $\mathrm{B}^0 \to 3\mathrm{K}^0_\mathrm{s}(\pi^+\pi^+)$. A priori, as there are two B mesons, it is possible that the two decays happen in one event, but the probability is small enough to be neglected for the purpose of the present analysis.

8.2.2 Event selection for the $B^0 \to 3K^0_s(\pi^+\pi^+)$ submode

We apply the following selection on each of the three K^0_s candidates:

- The α angle (see Sec. 7.5.2) has to be smaller than 0.2 rad.

- The two-dimensional decay-length has to be between 0.2 cm and 40 cm.

- The reconstructed mass fo the K^0_s has to be within a 12 MeV/c^2 mass window from the world average [1].

These cuts have been optimized for an earlier *BABAR* analysis [64].

The average number of B candidates after selection in reconstructed signal MC events is 1.005. We use the MC matching algorithm to estimate the fraction of mis-reconstructed events, also referred to as self cross feed (SCF). To define a candidate as truth matched (TM) we require that at least two out of four (B^0 meson and three K^0_s) are matched. In addition to this, the identity and the mother of the matched particles must be correct. With this criterion we estimate the SCF rate to be 1.59%. Considering the low SCF rate, we do not treat this component separately from TM events in the present analysis. Any bias introduced by not splitting SCF is quantified in the embedded-toy studies and assigned as systematic uncertainty. Fig. 8.1 shows the $\mathrm{m_{ES}}$ and $\Delta\mathrm{E}$ distributions for MC (TM and SCF) and off-peak data. The reconstruction efficiencies for each selection requirement obtained in signal MC are given in Tab. 8.1. We find a signal reconstruction efficiency of 13.5% before selection, which is due to the strongly constrained vertex fits for all three K^0_s, and 6.7% after selection. The selection criteria are summarized in Tab. 8.2.

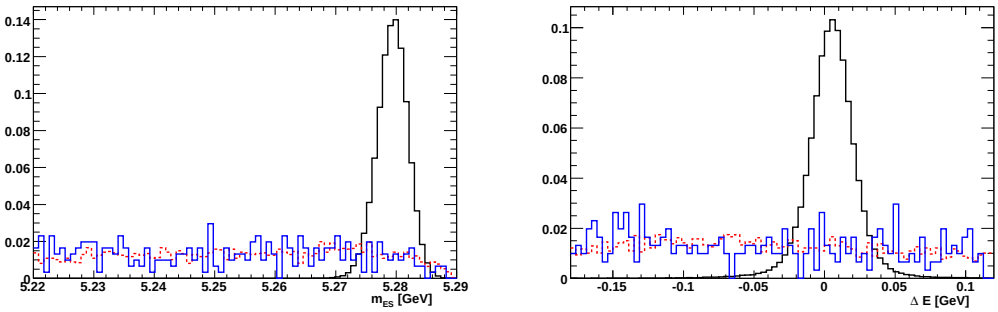

Figure 8.1: m_{ES} (left) and ΔE (right) distributions for the TM (black solid) and SCF (red dashed) components in $B^0 \to 3K^0_s(\pi^+\pi^-)$. The comparison with off-peak data (blue) shows the combinatorial nature of SCF events.

8.2.3 Event selection for the $B^0 \to 2K^0_s(\pi^+\pi^-)K^0_s(\pi^0\pi^0)$ submode

In this submode we use different selection requirements for $\mathrm{K^0_s}$ that decay to charged and neutral pions. For $\mathrm{K^0_s}$ decaying to charged pions we require:

- The alpha angle (see Sec. 7.5.2) has to be smaller than 0.2 rad.
- The decay length has to be between 0.2 cm and 60 cm.
- The reconstructed mass of the $\mathrm{K^0_s}$ has to be within a 12 MeV/c^2 mass window from the world average [1].
- The lifetime significance $\frac{\tau}{\sigma(\tau)}$ has to be superior to 5.

For $\mathrm{K^0_s}$ decaying to neutral pions we require

- The reconstructed mass of the $\mathrm{K^0_s}$ has to be between 0.48 and 0.52 GeV/c^2.
- The energy of the photons that the neutral pions are reconstructed from has to be superior to 50 MeV.
- The lateral moment[1] of the photon bumps have to be smaller than 0.55.
- The invariant mass of the π^0 has to be smaller than 0.141 GeV/c^2. There is also implicitly a lower bound on the mass due the the `KsToPi0Pi0Default` list (see chapter 7, Sec. 7.3).

The average number of candidates after selection in reconstructed signal MC events is 1.123. Fig. 8.2 shows the $\mathrm{m_{ES}}$ and $\Delta\mathrm{E}$ distributions for MC (TM and SCF) and off-peak data. Details on the reconstruction efficiency is given in Tab. 8.3, we find a reconstruction efficiency of 3.1%. The selection criteria are summarized in Tab. 8.2.

[1] Defined in chapter 6, Sec. 6.3.

selection	$\epsilon_{\rm relative}$	$\epsilon_{\rm absolute}$	events
			1747000
reconstruction		0.135	236324
L0	0.991	0.134	234144
L2	1.000	0.134	234141
Δt & $\sigma(\Delta$t)	0.917	0.123	214775
$E_{\rm tot}$	0.998	0.123	214306
$m_{\rm ES}$	0.961	0.118	205847
ΔE	0.941	0.111	193616
$r_{\rm dec}$	0.862	0.096	166841
$m_{K^0_s}$	0.887	0.085	147926
α	0.988	0.084	146125
$\cos(\theta_{\rm T})$	0.988	0.083	144336
$P(\chi^2(B))$	0.934	0.077	134775
veto χ_{c0}	0.876	0.068	118125
Cat K^0_s	0.993	0.067	117304
Total efficiency		0.067$\pm$ 0.000(2)	

Table 8.1: Efficiencies as estimated from resonant MC (SP-10045) for $B^0 \to 3K^0_s(\pi^+\ \pi^-)$. The χ_{c0} veto and the K^0_s categories are explained in Sec. 8.2.7 and Sec. 8.2.4 respectively.

	$K^0_s \to \pi^+\pi^-$ (in both submodes)	$K^0_s \to \pi^0\pi^0$
α	$\alpha < 0.2$	
$r_{\rm dec}(K_{S,\pi^+\pi^-})$ $m(K_{S,\pi^+\pi^-})$	$(0.2 < r_{\rm dec} < 40)$ cm $\lvert m_{K_S} - m_{\rm PDG}\rvert < 0.012$ GeV/c^2	$0.15 < r_{\rm dec} < 60$ cm $\lvert m_{K_S} - m_{\rm PDG}\rvert < 0.011$ GeV/c^2
$m(K_{S,\pi^0\pi^0})$ LAT $m(\pi^0)$ E_γ		$0.48{\rm GeV} < m_{K_S} < 0.52$ GeV/c^2 LAT < 0.55 $m_{\pi^0} < 0.141$ GeV/c^2 $E_\gamma > 0.05$ GeV

Table 8.2: Summary of selection cuts on K^0_s candidates. In the $B^0 \to 2K^0_s(\pi^+\pi^-)K^0_s(\pi^0\pi^0)$-submode we apply an additional cut on the lifetime significance, $\frac{\tau}{\sigma(\tau)} > 5$ on the $K^0_s \to \pi^+\pi^-$.

selection	$\epsilon_{\mathrm{relative}}$	$\epsilon_{\mathrm{absolute}}$	events
			1747000
reconstruction		0.116	201822
L0	0.992	0.115	200215
L2	1.000	0.115	200211
$\Delta\mathrm{t}$ & $\sigma(\Delta\mathrm{t})$	0.853	0.098	170745
$\mathrm{E_{tot}}$	0.998	0.098	170442
$\mathrm{m_{ES}}$	0.942	0.092	160610
$\Delta\mathrm{E}$	0.853	0.078	137041
$\cos(\theta_{\mathrm{T}})$	0.990	0.078	135641
LAT	0.908	0.071	123224
$\mathrm{m_{K^0_s\to\pi^0\pi^0}}$	0.823	0.058	101403
$\mathrm{m_{\pi^0}}$	0.896	0.052	90811
$\mathrm{E_\gamma}$	0.871	0.045	79065
$\mathrm{m_{K^0_s\to\pi^+\pi^-}}$	0.911	0.041	72054
$\mathrm{tau}/\sigma(\tau_{\mathrm{K^0_s\to\pi^0\pi^0}})$	0.939	0.039	67670
$\mathrm{r_{dec}}$	0.978	0.038	66186
$\mathrm{P}(\chi^2(\mathrm{K^0_s}))$	1.000	0.038	66186
$\mathrm{P}(\chi^2(\mathrm{B^0}))$	0.962	0.036	63703
veto χ_{c0}	0.857	0.031	54602
Cat $\mathrm{K^0_s}$	0.981	0.031	53562
Total efficiency		0.031$\pm$ 0.000(1)	

Table 8.3: Reconstruction efficiencies as estimated from resonant MC (SP-10045) for $\mathrm{B^0}\to 2\mathrm{K^0_s}(\pi^+\pi^-)\mathrm{K^0_s}(\pi^0\pi^0)$

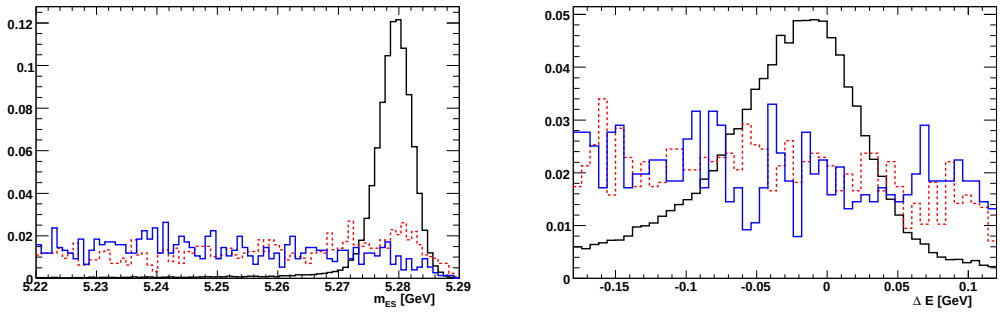

Figure 8.2: m_{ES} (left) and ΔE (right) distributions for the TM (black solid) and SCF (red dashed) components in $B^0 \to 2K^0_S(\pi^+\pi^-)K^0_S(\pi^0\pi^0)$. The comparison with off-peak data (blue) shows the combinatorial nature of SCF events. The small peaking component is due to some imperfection in the truth-matching algorithm.

8.2.4 Vertex requirements

One of the challenges of the present analysis is the fact that there are no charged particles that originate from the B primary vertex. To obtain the position of the B vertex from the K^0_S flight direction and ensure a good Δt reconstruction, it is enough to require that at least one K^0_S decays in the inner part of the SVT. The vertex reconstruction is dominated by the "best" K^0_S, i.e. the K^0_S that decay products have the most impacts in the SVT. We define four K^0_S classes based on SVT hit patterns:

- Class 1: both pions originating from the K^0_S have at least one hit in both sides of the double-sided (Φ and z) silicon modules in the 3 inner layers of the SVT.
- Class 2: both pions have at least one hit in Φ and in z but do not satisfy the requirements of Class 1. These are K^0_S that have hits in the outer layers of the SVT.
- Class 3: either of the two pions has at least one SVT hit in either Φ or z, but the K^0_S does not belong to Class 1 or Class 2. These are K^0_S that decay inside the SVT but have not enough hits to provide a good vertex measurement.
- Class 4: neither pion has any SVT hits.

We require that an event has at least one $K^0_S(\pi^+\pi^-)$ in Class 1 or 2, i.e. is fully contained within the inner SVT. The losses in efficiencies induced by this requirement are small: less than 0.4% for $B^0 \to 3K^0_S(\pi^+\pi^-)$ and less than 2.1% for $B^0 \to 2K^0_S(\pi^+\pi^-)K^0_S(\pi^0\pi^0)$. In Fig. 8.3 are shown the Δt error distributions for events that pass the K^0_S-class requirements for signal MC and on-peak data.

8.2.5 Continuum background

For a good discrimination between signal and continuum background in our fit we use NNs (see Sec. 7.5.3) which differ between the two submodes. To train the NN, we used signal

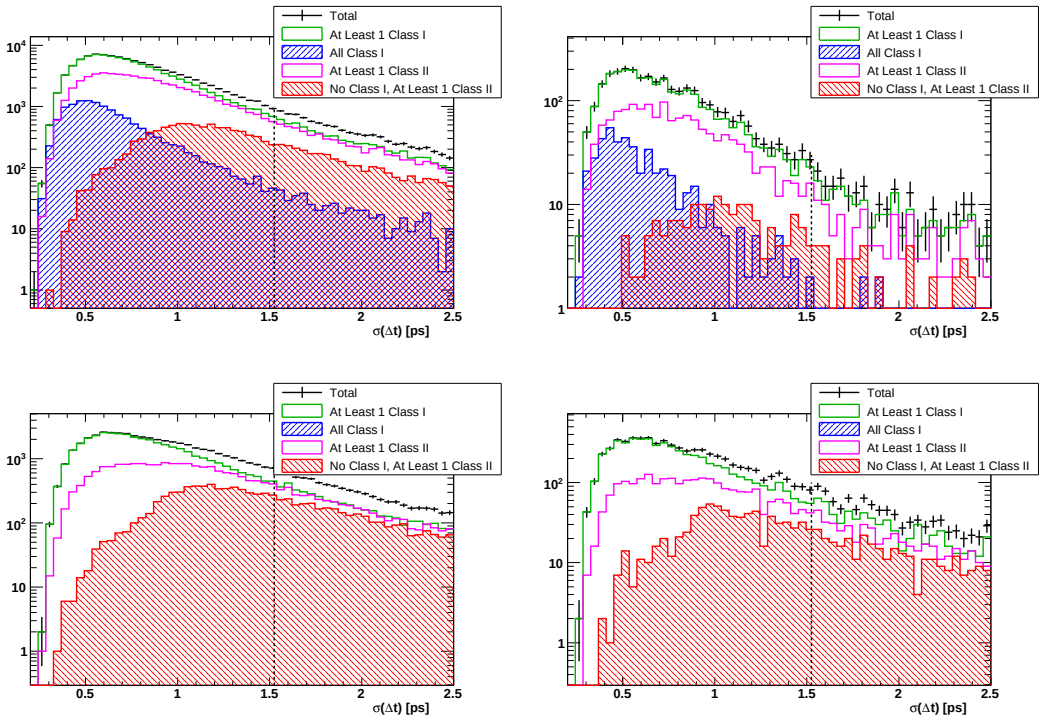

Figure 8.3: On the top is shown the error distribution for the Δt measurement for $B^0 \to 3K^0_S(\pi^+\pi^-)$ in signal MC (left) and on-peak data (right). In 91% of the events there is one K^0_s that is in Class 1. On the bottom is shown the same for $B^0 \to 2K^0_S(\pi^+\pi^-)K^0_S(\pi^0\pi^0)$, 84% of the events have one K^0_s that is in Class 1. Most of the events that have at least one K^0_S in Class 1 or Class 2 have an error on the Δt measurement that smaller than 1.525 ps, that is the average lifetime of the B^0 indicated by the dashed vertical line. If the error is larger that the value itself, no information is added to the fit.

MC (SP-8996) with nominal cuts as a signal sample. The continuum background samples were taken from data, both off-peak and on-peak sidebands, which are defined as:

- For $B^0 \to 3K^0_S(\pi^+\pi^-)$:
  - $5.2\,\mathrm{GeV/c^2} < m_{ES} < 5.27\,\mathrm{GeV/c^2}$
  - $-0.25\mathrm{GeV} < \Delta E < 0.25\mathrm{GeV}$
- For $B^0 \to 2K^0_S(\pi^+\pi^-)K^0_S(\pi^0\pi^0)$:
  - $5.22\,\mathrm{GeV/c^2} < m_{ES} < 5.255\,\mathrm{GeV/c^2}$
  - $-0.25\mathrm{GeV} < \Delta E < 0.25\mathrm{GeV}$

Using these definitions, the rates of signal Monte Carlo events in the sidebands are 2.1% and 3.6%, respectively, where the better part of the signal events in the sidebands are from SCF. The sidebands have loose criteria to provide a sufficient number of events to train the NN.

8.2.6 Background from B Decays

The specific B decay modes that we wrongly reconstruct as our signal have been identified and studied using the high statistics generic MC samples of $B^0\bar{B}^0$ and B^+B^- decays (SP-1237 and SP-1235, respectively). These samples represent roughly 3 times the *BABAR* statistics. For this study, we applied the same reconstruction and selection procedure as on data[2]. As a first step, we identified among the selected events in both generic MC samples the following types of decay channels:

- **Signal events**, both resonant($f_0(980)K^0_S$) and non resonant, in the $B^0\bar{B}^0$ sample.
- **Allowed charmonium modes**, namely $K^0_S\chi_{c0}(K^0_SK^0_S)$ and $K^0_S\chi_{c2}(K^0_SK^0_S)$. Most events of the former are removed from the data sample by the veto (see Sec. 8.2.7).
- **Forbidden charmonium modes**. In spite of the fact that all the other charmonia do not decay to $K^0_sK^0_s$, we found the modes $K^0_S\eta_c(K^0_SK^0_S)$ and $K^0_S\eta_c(2S)(K^0_SK^0_S)$. These modes are not considered in the following.
- **b→s decays** for which we reconstructed 3 events or more in the generic samples (which correspond roughly to an expectation of one event in the data sample). Each of these modes is considered as a specific B background component in the maximum likelihood fit. We obtain the corresponding PDFs from exclusive MC samples.

For this study we consider the MC truth information of the signal-side B and the tag-side B_{tag} of the event. If the signal mode or one of the background types is on either side of the event, the event gets assigned to the associated category.
The number of events from modes of each of these types is detailed in Tab. 8.4 and Tab. 8.5 for the neutral and charged generic MC samples, respectively. After filtering all the modes detailed above from the generic samples, the remaining events consist mainly of B decay modes with D mesons. We define the residual samples as two additional B background components, one per generic sample. We use the filtered samples to obtain the corresponding PDFs for the maximum likelihood fit. The number of events from each submode in the filtered generic samples are detailed in Tab. 8.6. The frequencies of modes reconstructed in the filtered neutral generic MC sample and in the filtered charged generic MC sample are detailed in Tab. 8.7. Modes that appeared less then 3 times are not shown in the tables. The numbers take into account both sides of events. To summarize, each of the individual $b \to s$ B background modes is treated as a separate component in the maximum likelihood fit, in addition to two components from the filtered charged and neutral generic samples. The motivation not to group the different individual modes into classes is that, for most of them, the branching fractions ($\mathcal{B}$) are not measured and had to be estimated. Treating them separately makes easier the estimation of systematic errors related to their fixed yields in the fit. To estimate the systematics we then vary the estimated yields by $\pm$ 100% (see section 8). Table 8.8 details the reconstruction efficiencies of these B-background modes (including the vetoes), the $\mathcal{B}$ used for each one and the resulting yields. These yields are used in the fit

[2]Charmonium vetoes have not been applied previously to the generic samples study. It is applied before creating the PDFs.

and in the different toy validations detailed in Section 8.4. Distributions of $\mathrm{m_{ES}}$, $\Delta\mathrm{E}$ and the transformed NN for each of the B background components are given in Appendix B. The sources of the Branching Fractions used to estimate the yields of the individual components are as follows:

- $\mathrm{K^0_S K^0_S K^0_L}$: The value at the minimum of the likelihood function of the *BABAR* $\mathrm{B^0} \to \mathrm{K^0_S K^0_S K^0_L}$ analysis [65]. In this analysis a limit was set on the $\mathcal{B}$. The number is excluding decays via $\phi\mathrm{K^0_S}$.

- $\mathrm{K^0_S K^0_S K^{*0}}$: assumed as equal to $\mathcal{B}(\mathrm{K^+K^-K^{*0}})$ [15].

- $\mathrm{K^0_S K^0_L K^{*0}}$: as $\mathrm{K^0_S K^0_S K^{*0}}$.

- $\mathrm{K^0_S K^0_S K^+}$: The central value of the *BABAR* $\mathrm{B^+} \to \mathrm{K^0_S K^0_S K^+}$ analysis [66].

- $\mathrm{K^0_S K^0_S K^{*+}}$: as $\mathrm{K^0_S K^0_S K^{*0}}$.

Sub Mode	Event Type	Decay Mode	# Events	SP Mode
$3\mathrm{K^0_S}(\pi^+\pi^-)$	Signal	$\mathrm{K^0_S K^0_S K^0_S}$	601 (596)	—
		$\mathrm{f_0(K^0_S K^0_S)\ K^0_S}$	15 (15)	—
	Allowed charmonium	$\chi_{c0}(\mathrm{K^0_S K^0_S})\mathrm{K^0_S}$	27 (27)	—
		$\chi_{c2}(\mathrm{K^0_S K^0_S})\mathrm{K^0_S}$	1 (1)	—
	Forbidden charmonium	$\eta_c(\mathrm{K^0_S K^0_S})\mathrm{K^0_S}$	34 (27)	—
		$\eta_c(2\mathrm{S})(\mathrm{K^0_S K^0_S})\mathrm{K^0_S}$	16 (15)	—
	$\mathrm{b} \to \mathrm{s}$ B backgrounds	$\mathrm{K^0_S K^0_S K^0_L}$	15 (13)	4494, 8997
		$\mathrm{K^0_S K^0_S K^{*0}}$	23 (8)	8998
$2\mathrm{K^0_S}(\pi^+\pi^-)$ $\mathrm{K^0_S}(\pi^0\pi^0)$	Signal	$\mathrm{K^0_S K^0_S K^0_S}$	299 (202)	—
		$\mathrm{f_0(K^0_S K^0_S)\ K^0_S}$	6 (6)	—
	Allowed charmonium	$\chi_{c0}(\mathrm{K^0_S K^0_S})\mathrm{K^0_S}$	16 (10)	—
		$\chi_{c2}(\mathrm{K^0_S K^0_S})\mathrm{K^0_S}$	1 (0)	—
	Forbidden charmonium	$\eta_c(\mathrm{K^0_S K^0_S})\mathrm{K^0_S}$	17 (11)	—
		$\eta_c(2\mathrm{S})(\mathrm{K^0_S K^0_S})\mathrm{K^0_S}$	5 (3)	—
	$\mathrm{b} \to \mathrm{s}$ B backgrounds	$\mathrm{K^0_S K^0_S K^0_L}$	18 (18)	8997
		$\mathrm{K^0_S K^0_S K^{*0}}$	19 (14)	8998
		$\mathrm{K^0_S K^0_L K^{*0}}$	5 (3)	8999

Table 8.4: Signal events, charmonium modes and main $\mathrm{b} \to \mathrm{s}$ modes found in the neutral generic MC sample. For $\mathrm{b} \to \mathrm{s}$ events, which are considered as specific classes of B background in the maximum likelihood fit, we detail the SP mode used to obtain the PDFs. Yields in parentheses correspond to what was found using the BToPPP skimmed generic MC samples

Sub Mode	Event Type	Decay Mode	# Events	SP Mode
$3K^0_S(\pi^+\pi^-)$	$b \to s$ B backgrounds	$K^0_S K^0_S K^+$	9	3915, 9000
$2K^0_S(\pi^+\pi^-)$ $K^0_S(\pi^0\pi^0)$	$b \to s$ B backgrounds	$K^0_S K^0_S K^+$	11	9000
		$K^0_S K^0_S K^{*+}$	5	9001

Table 8.5: Main $b \to s$ modes found in the charged generic MC sample, considered as specific classes of B background in the maximum likelihood fit. We detail the SP mode used to obtain the PDFs.

# Events	Neutral Generic	Charged Generic
$3K^0_S(\pi^+\pi^-)$	63	47
$2K^0_S(\pi^+\pi^-)K^0_S(\pi^0\pi^0)$	239	223

Table 8.6: Number of events from the two submodes in the filtered generic MC samples (χ_{c0} veto is applied).

8.2.7 Charmonium Vetoes

Due to $\mathcal{P}$, CP and angular momentum conservation, the only charmonia expected to decay to $K^0_S K^0_S$ are χ_{c0} and χ_{c2}. B decays to $K^0_S \chi_{c0/c2}(K^0_S K^0_S)$ need careful modeling, because they have a $\sin(2\beta)$ time dependent structure which can diminish the sensitivity of the present analysis to new physics. A safe approach consists in applying vetoes on the invariant mass of the χ particle to remove these events from the data sample. The previous *BABAR* analysis [64] applied vetoes for χ_{c0} and χ_{c2}. We show in the following that we only need to apply a veto for the $\chi_{c0}K^0_S$ mode, as the $\chi_{c2}K^0_S$ contribution in negligible. We assign a systematic uncertainty for χ events that could contribute to the signal, for instance by an unexpected high event yield due to statistical fluctuation (see Sec. 8.6.6).

The veto on χ_{c0} was studied using the MC sample of the decay mode $K^0_S \chi_{c0}(K^0_S K^0_S)$ (SP-9002). The veto was designed to remove 95% of the events, symmetrically from both sides of the resonance. We use:

- $m(K^0_S(\pi^0\pi^0)K^0_S(\pi^+\pi^-)) \notin (3.365, 3.475)$ GeV/c^2
- $m(K^0_S(\pi^+\pi^-)K^0_S(\pi^+\pi^-)) \notin (3.382, 3.464)$ GeV/c^2.

More precisely, the vetoes remove 94.51% and 95.40% from the $B^0 \to 3K^0_S(\pi^+\pi^-)$ and $B^0 \to 2K^0_S(\pi^+\pi^-)K^0_S(\pi^0\pi^0)$ submodes, respectively, or 95.11% in average.

We expect 0.48 $K^0_S \chi_{c2}(K^0_S K^0_S)$ events in the $B^0 \to 3K^0_S(\pi^+\pi^-)$ submode and 0.23 in the $B^0 \to 2K^0_S(\pi^+\pi^-)K^0_S(\pi^0\pi^0)$ one. The expected number was determined using the 90% CL limit from Ref. [15] and assuming the same efficiency as for the χ_{c0} mode. Only two events of this mode, one per submode, have been reconstructed in the neutral generic MC sample that represents roughly 3 times the size of the *BABAR* data sample. The $\mathcal{B}$ for this mode in the MC is twice the limit from Ref. [15]. Due to small expected number of events, we did not apply a veto on this mode.

Generic $B^0\bar{B}^0$

Sub Mode	Decay Mode	# Events
$3K^0_s(\pi^+\pi^-)$	$D^+\rho^-$	5
	$\eta_c K^0_s$ (allowed)	7
	$D^+\pi^-$	5
	$K^{*+}D^-$	5
	$\nu_e e^+ D^-$	5
	$D^{*+}\mu^-\overline{\nu}_\mu$	4
	$\chi_{c0}K^{*0}$	3
	$\eta_c K^{*0}$	3
	$D^{*+}e^-\overline{\nu}_e$	3
	$K^0\pi^+D^-$	3
	$K^0\pi^0\bar{K}^0\bar{K}^0$	3
	$\bar{K}^0\bar{D}^0$	3
$2K^0_s(\pi^+\pi^-)$ $K^0_s(\pi^0\pi^0)$	ρ^+D^-	65
	$D^+a_1^-$	19
	$D^{*+}\rho^-$	17
	$K^{*+}D^-$	16
	$a_1^+D^{*-}$	14
	$D_2^{*+}\pi^-$	7
	$D^{*+}e^-\overline{\nu}_e$	7
	$D^{*+}D_s^{*-}$	8
	$D_s^+D^{*-}$	6
	$D^+\mu^-\overline{\nu}_\mu$	6
	$D^+\pi^-$	6
	D^0K^0	6
	$D^{*+}\mu^-\overline{\nu}_\mu$	5
	$D^{*+}\pi^-$	5
	$D^{*+}\bar{K}^0D^{*-}$	5
	$D^{*+}D_{s1}^-$	5
	$D^{*+}K^-\bar{D}^{*0}$	4
	$D^+K^{*-}\bar{D}^0$	4
	$\eta_c K^0_s$ (allowed)	4
	$D_1^{'+}\mu^-\overline{\nu}_\mu$	3
	$D_s^*\pi^+\pi^-D^-$	3
	$D_s^*D_1^-$	3
	$D^+\bar{K}^{*0}D^-$	3
	$D^+\pi^0\pi^0\rho^-$	3
	$D^+e^-\overline{\nu}_e$	3
	$D^+e^-\overline{\nu}_e$	3
	$K^+\bar{K}^0D^-$	3
	$\omega\pi^+D^-$	3
	$\nu_e e^+ D_1^{'-}$	3
	$D^+D_s^{*-}$	3
	$\rho^+\pi^0D^{*-}$	3

Generic B^+B^-

Sub Mode	Decay Mode	# Events
$3K^0_s(\pi^+\pi^-)$	$D^+\bar{K}^0$	3
	$K^{*+}\bar{D}^0$	3
	$\rho^+\bar{D}^0$	3
$2K^0_s(\pi^+\pi^-)$ $K^0_s(\pi^0\pi^0)$	$\rho^+\bar{D}^0$	45
	$\nu_e e^+\bar{D}^{*0}$	17
	$D^{*0}\pi^-$	15
	$D^{*0}a_1^-$	15
	$D^{*0}\rho^-$	14
	$D^0\pi^-$	14
	$\nu_\mu\mu^+\bar{D}^{*0}$	13
	$D^{*0}D_s^{*-}$	12
	$D^0a_1^-$	11
	$D^{*0}K^{*-}$	10
	D^0K^{*-}	9
	$\rho^+\pi^0\bar{D}^0$	9
	$D^{*0}\bar{K}^0D^{*-}$	7
	$D^0D_s^-$	6
	$D^0D_s^{*-}$	6
	$D^{*0}D_s^-$	5
	$\bar{D}^0e^-\overline{\nu}_e$	5
	$\nu_\mu\mu^+\bar{D}^0$	5
	$\pi^+\bar{D}_1^{'0}$	4
	$D^{*0}K^{*+}\bar{D}^{*0}$	3
	$D^0K^0K^-$	3
	$D^{*+}K^0\bar{D}^0$	3
	$\pi^+\pi^+\pi^0D^{*-}$	3
	$\pi^+\pi^0\pi^0\bar{D}^0$	3
	$\nu_\mu\mu^+\bar{D}_1^{'0}$	3

Table 8.7: Number of the reconstructed events in the main remaining modes in the neutral generic MC sample and in the charged generic MC sample. Charge conjugation is implicit.

Sub Mode	Decay Mode	SP Mode	Eff.($\times 10^{-4}$)	BF($\times 10^{-6}$)	Exp. Yield
$3K^0_s(\pi^+\pi^-)$	$K^0_s K^0_s K^0_L$	4494, 8997	6.4	2.4	0.7 ± 0.7
	$K^0_s K^0_s K^{*0}$	8998	7.5	27.5	9.6
	$K^0_s K^0_s K^+$	3915, 9000	7.9	11.5	4.3
	$B^0\bar{B}^0$ generic		—	—	21.7 ± 4.7
	B^+B^- generic		—	—	15.5 ± 3.9
$2K^0_s(\pi^+\pi^-)$ $K^0_s(\pi^0\pi^0)$	$K^0_s K^0_s K^0_L$	8997	5.9	2.4	0.7
	$K^0_s K^0_s K^{*0}$	8998	4.2	27.5	5.3
	$K^0_S K^0_L K^{*0}$	8999	0.23	27.5	0.3
	$K^0_s K^0_s K^+$	9000	5.6	11.5	2.9
	$K^0_s K^0_s K^{*+}$	9001	5.7	27.5	7.2
	$B^0\bar{B}^0$		—	—	73.6 ± 8.6
	B^+B^-		—	—	73.8 ± 8.6

Table 8.8: Efficiencies, Branching Fractions and expected yields in data for the different modes of B background that have been taken into account in the fit model.

8.3 Maximum likelihood fit

8.3.1 Likelihood function

We use an unbinned extended maximum likelihood (ML) fit to extract physics parameters of interest, the yields and various variables of the signal and background parameterization. A simultaneous fit to the two datasets of the submodes $B^0 \to 3K^0_s(\pi^+\pi^-)$ and $B^0 \to 2K^0_s(\pi^+\pi^-)K^0_s(\pi^0\pi^0)$, gives in particular access to the corresponding signal yields N_{pm} and N_{00}, and to the *CP* asymmetries $\mathcal{S}$ and $\mathcal{C}$. In the context of the ML fit, the two submodes are also referred to as the physics categories pm and 00. Our fit permits to separate, in addition to the yields, all the parameters in the two physics categories and the seven tagging categories (see Sec. 7.3.4). We are able to fit the individual $calS_{pm}$ and $\mathcal{C}_{pm}$ as well as $\mathcal{S}_{00}$ and $\mathcal{C}_{00}$. In the fit we attempt to keep free to vary as many of the signal and background parameters as possible.
The variables we use in the likelihood function are: m_{ES}, ΔE, Δt, $\sigma_{\Delta t}$ and the transformed NN. Some of the parameterizations are specific for the tagging category c and the physics category p of the event, for details see Sec. 8.3.2.
The likelihood function for the i-th event is defined as:

$$\mathcal{P}^i = \sum_j N_j \mathcal{P}^i_j(m_{ES}, \Delta E, \Delta t, \sigma_{\Delta t}, NN; c, p) \,, \tag{8.1}$$

where j stands for the species (signal, continuum background, one for each B-background category), and N_j is the corresponding yield. $\mathcal{P}_j$ is the PDF for species j, evaluated for the event i. It is given by the product of individual PDFs:

$$\begin{aligned} &\mathcal{P}^i_j(m_{ES}, \Delta E, \Delta t, \sigma_\Delta t, NN; c, p) = \\ &\mathcal{P}^i_j(m_{ES}; p) \cdot \mathcal{P}^i_j(\Delta E; p) \cdot \mathcal{P}^i_j(NN; c, p) \cdot \mathcal{P}^i_j(\Delta t, \sigma_{\Delta t}; c, p) \end{aligned} \tag{8.2}$$

neglecting the correlations between the different individual PDFs. The total extended likelihood is given by:

$$\mathcal{L} = \exp(-\sum_{\mathrm{j}} \mathrm{N_j}) \prod_{\mathrm{i}} \mathcal{P}^{\mathrm{i}} \tag{8.3}$$

8.3.2 The PDF

The PDFs are parameterized as follows:

- $\mathrm{m_{ES}}$:
  - **Signal:** We use the sum of a Cruijff function, defined as:

$$\begin{aligned} &\mathrm{Cr(m, m_0, \sigma_l, \sigma_r, \alpha_l, \alpha_r)} = \\ &exp\left(-\frac{(m-m_0)^2}{2\sigma_i^2 + \alpha_i(m-m_0)^2}\right) \begin{cases} \mathrm{i = l} & \mathrm{(m - m_0) < 0} \\ i = r & (m - m_0) > 0 \end{cases} \end{aligned} \tag{8.4}$$

    and an Argus function, defined below as:

$$\mathrm{A(m, m_0, A_c, A_p) = m \cdot (1 - (m/m_0)^2)^{A_p} \cdot e^{A_c(1-(m/m_0)^2)}} \, . \tag{8.5}$$

    The fraction of the Argus function is very small and corresponds to the SCF fraction. As we use very loose cuts on m_{ES}, we need to parameterize the combinatorial tails introduced by the non-separation of SCF. The Argus shape parameter and the corresponding fraction are fitted on MC and fixed in the fit to data.
  - **Continuum:** We use the Argus function.
  - **B-Background:** non-parametric RooKeysPdf, one for each B-background category.
- ΔE:
  - **Signal:** Cruijff function.
  - **Continuum:** 1st order polynomial.
  - **B-Background:** non-parametric RooKeysPdf, one for each B-background category.
- NN:
  - **Signal:** RooKeysPdf [63], split by tagging category.
  - **Continuum:** "SpecialExponent" function, defined as:

$$\begin{aligned} &\mathrm{E_{sp}(x; c_1, a, b_0, b_1, b_2, b_3, c_2, c_3)} = \\ &\mathrm{\cos^2(c_1) \cdot [\cos^2(a) \cdot \mathcal{N}(b_0, b_1) \cdot x^{b_0} \cdot (1-x)^{b_1}} \\ &+ \sin^2(a) \cdot \mathcal{N}(b_2, b_3) \cdot x^{b_2} \cdot (1-x)^{b_3}] \\ &\mathrm{+ \sin^2(c_1) \cdot \mathcal{N}(c_2, c_3) \cdot x^{c_2} \cdot (1-x)^{c_3}} \end{aligned} \tag{8.6}$$

where $\mathrm{x} = \frac{\mathrm{NN}-\mathrm{NN}_\mathrm{min}}{\mathrm{NN}_\mathrm{max}-\mathrm{NN}_\mathrm{min}}$ and $\mathcal{N}$ are normalization factors, computed analytically using the standard Γ function:

$$\mathcal{N}(\alpha,\beta) = \frac{\Gamma(\beta+2+\alpha)}{\Gamma(\alpha+1)\Gamma(\beta+1)} \tag{8.7}$$

– **B-Background:** non-parametric RooKeysPdf, one for each B-background category.

- Δt
  – **Signal:** Since the PDF needs to describe measured quantities, the physical time-dependence is extended to include tagging imperfection and is convoluted with the per-event $\Delta\mathrm{t}$ resolution $\mathcal{R}_\mathrm{sig}$ (Eq. 7.9). For an event with tag-flavor $\mathrm{q_{tag}}$, one has

$$\begin{aligned} \mathrm{f_{q_{tag}}}(\Delta\mathrm{t},\sigma_{\Delta\mathrm{t}},\mathrm{c}) \;=\; & \frac{\mathrm{e}^{-\left|\Delta\mathrm{t}'\right|/\tau_{\mathrm{B}^0}}}{4\tau_{\mathrm{B}^0}}[1+\mathrm{q_{tag}}\frac{\Delta\mathrm{D_c}}{2} && (8.8)\\ & +\mathrm{q_{tag}}\langle\mathrm{D}\rangle_\mathrm{c}\,\mathcal{S}\sin(\Delta\mathrm{m_d}\Delta\mathrm{t}') - \mathcal{C}\cos(\Delta\mathrm{m_d}\Delta\mathrm{t}')] && (8.9)\\ & \otimes\,\mathcal{R}_\mathrm{sig}(\Delta t'-\Delta t,\sigma_{\Delta t})\;, \end{aligned}$$

where $\langle\mathrm{D}\rangle_\mathrm{c}$ and $\Delta\mathrm{D_c}$ are the tagging-category-specific average and difference of the tagging dilution defined in Sec. 7.3.4.

– **Continuum:** We use a prompt parameterization (δ-function) convolved with the same resolution function as for signal, but with different parameters. All the parameters of the resolution function free to vary in the fit. The initial values have been fitted on a off-peak/sideband sample. $\mathcal{S}$ and $\mathcal{C}$ are set to zero.

– **B-Background:** We use the same form as the signal PDF, with resolution parameters from the *BABAR* tagging group. $\mathcal{S}$ and $\mathcal{C}$ are set to zero and varied for the systematic error estimation.

We split many of the variables in physics and tagging categories. This is a natural choice due the reconstruction from different final states in the detector. The discriminating variables, in particular $\mathrm{m_{ES}}$ and $\Delta\mathrm{E}$, have more tails in $\mathrm{B}^0 \to 2\mathrm{K}^0_\mathrm{s}(\pi^+\pi^-)\mathrm{K}^0_\mathrm{s}(\pi^0\pi^0)$ due to the combinatorics in the reconstruction of the π^0 from photons. The NN is correlated to the tagging category, as the better the tagging category the better the signal B and the $\mathrm{B_{tag}}$ are separated and this reflects in the event-shape variables. The distributions can be found in the appendix B. The $\Delta\mathrm{t}$ resolution function is divided not only in tagging category (as is it is usually done in *BABAR* analyses) but also in physics category. The reason is that the $\mathrm{B}^0 \to 2\mathrm{K}^0_\mathrm{s}(\pi^+\pi^-)\mathrm{K}^0_\mathrm{s}(\pi^0\pi^0)$ channel is less likely to produce a K^0_s in class 1 which is reflected in a broader resolution function. Additionally this choice eases the evaluation of the vertexing systematic uncertainty, see Sec. 8.6. We summarize all the splitted variables in Tab. 8.9.

Species	Variable	Split by:
Signal	Yield	physics
	$\epsilon_{\rm tag}$	tagging
	$\mathrm{P(NN)}$	both
	$\mu(\mathrm{m_{ES}})$	physics
	$\sigma_{\rm R}(\mathrm{m_{ES}})$	physics
	$\sigma_{\rm L}(\mathrm{m_{ES}})$	physics
	$\alpha_{\rm R}(\mathrm{m_{ES}})$	physics
	$\alpha_{\rm L}(\mathrm{m_{ES}})$	physics
	$\mu(\Delta\mathrm{E})$	physics
	$\sigma_{\rm R}(\Delta\mathrm{E})$	physics
	$\sigma_{\rm L}(\Delta\mathrm{E})$	physics
	$\alpha_{\rm R}(\Delta\mathrm{E})$	physics
	$\alpha_{\rm L}(\Delta\mathrm{E})$	physics
	$\langle\mathrm{D}\rangle^{\rm c}$ (mistag)	tagging
	$\Delta\mathrm{D}^{\rm c}$ (mistag-bias)	tagging
	$\mathrm{s}^{\rm b}_{\rm core}$ (Δt resolution core bias)	both
	$\mathrm{s}^{\sigma}_{\rm core}$ (Δt resolution core sigma)	both
	$\mathrm{s}^{\rm b}_{\rm tail}$ (Δt tail bias)	both
	$\mathrm{s}^{\rm f}_{\rm out}$ (Δt outlier fraction)	both
	$\mathrm{s}^{\rm f}_{\rm tail}$ (Δt tail fraction)	both
Continuum	Yield	both
	aNN	physics
	$\mathrm{c_1NN}$	physics
	$\mathrm{b_0NN}$	physics
	$\mathrm{b_1NN}$	physics
	$\mathrm{b_2NN}$	physics
	$\mathrm{c_2NN}$	physics
	$\mathrm{c_3NN}$	physics
	$\mathrm{A_c(m_{ES})}$	physics
	$\mathrm{slope}(\Delta\mathrm{E})$	physics
	All Δt parameters	physics
B-background	$\epsilon_{\rm tag}$	tagging

Table 8.9: List of variables (or PDFs) split by either tagging or physics category or both.

8.4 Validation studies

8.4.1 Fits to MC

We extract the parameters to describe the discriminating variables from fits to resonant MC. High-statistic toys generated from the fit result in comparison with resonant MC for the discriminating variables are shown in Fig. 8.4. In the fit for Δt we also float the parameters of the resolution function described in Eq. 7.9, and the result is shown in Tab. 8.10. We find that the resolution function parameters deviate significantly from the parameters provided by the tagging group[3]. This is an expected behavior (see Sec. 7.4.3) and therefore we use the resolution function from simulation and assign a systematic uncertainty for the MC-data difference using the control sample $B^0 \to J/\psi K^0_S$ (see Sec. 8.6).
We show results of high-statistic fits to different MC samples using the resolution function from MC. These fits have been done separately and combined for both sub-modes in Tab. 8.11. We see that the samples are subject to statistical fluctuation, but are consistent with the generated values.

Parameter	Charmonium	$B^0 \to 3K^0_S(\pi^+\pi^-)$	$B^0 \to 2K^0_S(\pi^+\pi^-)K^0_S(\pi^0\pi^0)$
$s^b_{core;KaonI}$	-0.157 $\pm$ 0.028	-0.151 $\pm$ 0.022	-0.080 $\pm$ 0.029
$s^b_{core;KaonII}$	-0.198 $\pm$ 0.021	-0.220 $\pm$ 0.017	-0.155 $\pm$ 0.022
$s^b_{core;KaonPion}$	-0.194 $\pm$ 0.022	-0.180 $\pm$ 0.017	-0.143 $\pm$ 0.024
$s^b_{core;Lepton}$	-0.070 $\pm$ 0.026	-0.013 $\pm$ 0.022	0.018 $\pm$ 0.028
$s^b_{core;Other}$	-0.176 $\pm$ 0.025	-0.176 $\pm$ 0.021	-0.094 $\pm$ 0.029
$s^b_{core;Pion}$	-0.247 $\pm$ 0.021	-0.178 $\pm$ 0.017	-0.140 $\pm$ 0.023
$s^\sigma_{core;KaonI}$	1.155 $\pm$ 0.045	0.951 $\pm$ 0.033	0.975 $\pm$ 0.040
$s^\sigma_{core;KaonII}$	1.136 $\pm$ 0.034	0.910 $\pm$ 0.024	0.936 $\pm$ 0.029
$s^\sigma_{core;KaonPion}$	1.139 $\pm$ 0.034	0.901 $\pm$ 0.025	0.928 $\pm$ 0.032
$s^\sigma_{core;Lepton}$	1.021 $\pm$ 0.042	0.879 $\pm$ 0.032	0.830 $\pm$ 0.039
$s^\sigma_{core;Other}$	1.074 $\pm$ 0.039	0.922 $\pm$ 0.029	0.978 $\pm$ 0.037
$s^\sigma_{core;Pion}$	1.096 $\pm$ 0.033	0.918 $\pm$ 0.025	0.908 $\pm$ 0.032
f_{out}	0.003 $\pm$ 0.000	0.007 $\pm$ 0.000	0.010 $\pm$ 0.000
s^b_{tail}	-1.051 $\pm$ 0.109	-0.797 $\pm$ 0.031	-0.535 $\pm$ 0.042
f_{tail}	0.117 $\pm$ 0.008	0.237 $\pm$ 0.0044	0.226 $\pm$ 0.005
s^σ_{tail}	3.0 fixed	3.0 fixed	3.0 fixed
s^b_{out}	0.0 fixed	0.0 fixed	0.0 fixed
s^σ_{out}	8.0 fixed	8.0 fixed	8.0 fixed

Table 8.10: Resolution function parameters in B_{reco} data and resolution parameters fitted on the signal MC samples (SP-10045, SP-8996 and SP-6994).

[3]The *BABAR* tagging group provides Δt resolution parameters and tagging information found in a fit to the *BABAR* BFlav sample that consists of $B^0 \to c\bar{c}K^{(*)}$ decays. The tag-side information is the same as in this work and can be used, as it is (almost) independent of the decay on the signal side [16].

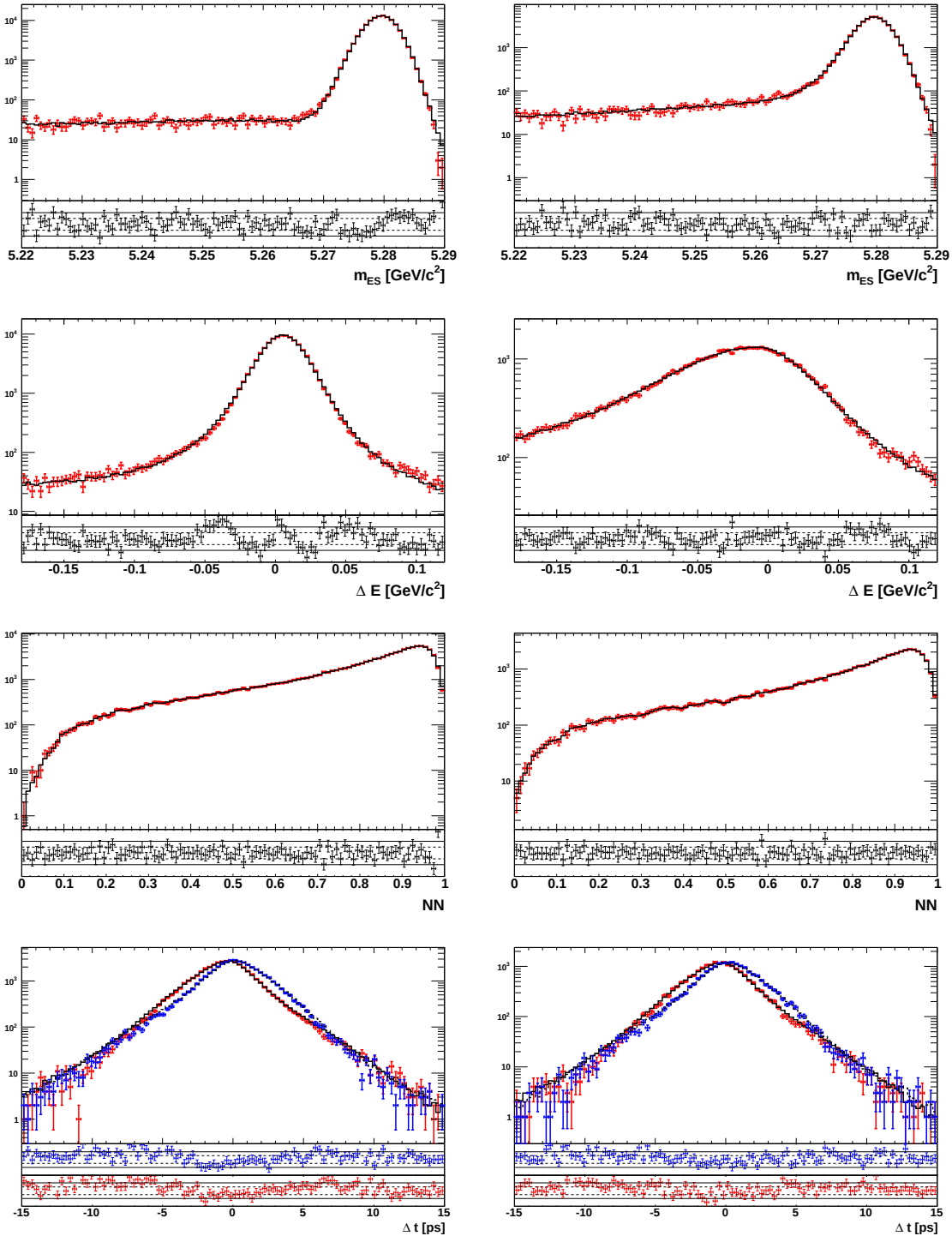

Figure 8.4: Fits to resonant MC (SP-10045). The plots show comparisons between MC (red) and high-statistics toy MC generated from the fit result (black). We find that the parameterizations give a reasonable description. The plots in the left column correspond to the $B^0 \to 3K^0_s(\pi^+\pi^-)$ sub-channel, and the ones on the right to the $B^0 \to 2K^0_s(\pi^+\pi^-)K^0_s(\pi^0\pi^0)$ sub-channel. The first row is the comparison for m_{ES}, the second one to ΔE and the third one to the NN. The last row corresponds to the Δt fit where we have separated the signal events that have been tagged as B^0 (red) from the ones that have been tagged as $\bar{B}^0$ (blue). The residual distributions in units of the statistical error for all fits are shown below the projections.

	Generated	Fitted
SP-6994		
$\mathcal{S}_{pm}$	-0.703	-0.685 $\pm$ 0.022
$\mathcal{C}_{pm}$	0	-0.013 $\pm$ 0.023
$\mathcal{S}_{00}$	-0.703	-0.662 $\pm$ 0.035
$\mathcal{C}_{00}$	0	-0.013 $\pm$ 0.023
$\mathcal{S}_{both}$	-0.703	-0.678 $\pm$ 0.018
$\mathcal{C}_{both}$	0	-0.014 $\pm$ 0.012
SP-8996		
$\mathcal{S}_{pm}$	-0.703	-0.741 $\pm$ 0.014
$\mathcal{C}_{pm}$	0	0.007 $\pm$ 0.009
$\mathcal{S}_{00}$	-0.703	-0.704 $\pm$ 0.022
$\mathcal{C}_{00}$	0	-0.029 $\pm$ 0.014
$\mathcal{S}_{both}$	-0.703	-0.731 $\pm$ 0.012
$\mathcal{C}_{both}$	0	-0.003 $\pm$ 0.007
SP-10045		
$\mathcal{S}_{pm}$	-0.703	-0.719 $\pm$ 0.010
$\mathcal{C}_{pm}$	0	-0.005 $\pm$ 0.007
$\mathcal{S}_{00}$	-0.703	-0.700 $\pm$ 0.016
$\mathcal{C}_{00}$	0	-0.016 $\pm$ 0.010
$\mathcal{S}_{both}$	-0.703	-0.713 $\pm$ 0.008
$\mathcal{C}_{both}$	0	-0.009 $\pm$ 0.005

Table 8.11: Non-combined and combined $\Delta\mathrm{t}$-only-fits to signal MC samples (SP-6994: pseudo-nonresonant generated with a very broad $\mathrm{f}_0(980)\mathrm{K}^0_\mathrm{s}$ resonance, SP-8996:nonresonant MC, SP-10045: resonant MC).

8.4.2 Pure toy studies

In a first step we use pure toy studies (see Sec. 7.6.3) to check for intrinsic biases in our analysis tool. For this we need an estimation of the yields of all species in data to get reliable error estimates of the observables. The expected signal yields are estimated using luminosity, $\mathcal{B}$s from HFAG [15], and efficiencies from Monte Carlo. For continuum, the expected yields are luminosity-scaled from off-peak data. The fractions of different tagging categories in continuum are found by fitting on-peak-$\mathrm{m_{ES}}$ sidebands and off-peak data. The different yields are detailed in Table 8.12. Expected yields for B-background modes have been discussed in Section 8.2.6. We use the same configuration as in the final fit on data;

Yield	$\mathrm{N_{exp}} \pm \sigma(\mathrm{N_{Exp}})$
$\mathrm{N_{sig,pm}}$	193,17 $\pm$ 28.05
$\mathrm{N_{sig,00}}$	86,49 $\pm$ 12.56
$\mathrm{N_{cont,pm,total}}$	2892 $\pm$ 53
$\mathrm{N_{cont,00,total}}$	7211 $\pm$ 85
$\mathrm{N_{cont,pm,notag}}$	978.78 $\pm$ 31.29
$\mathrm{N_{cont,00,notag}}$	2832.03 $\pm$ 53.22
$\mathrm{N_{cont,pm,lepton}}$	19.33 $\pm$ 4.4
$\mathrm{N_{cont,00,lepton}}$	61.04 $\pm$ 7.81
$\mathrm{N_{cont,pm,kaon1}}$	288.75 $\pm$ 16.99
$\mathrm{N_{cont,00,kaon1}}$	477.09 $\pm$ 21.84
$\mathrm{N_{cont,pm,kaon2}}$	492.23 $\pm$ 22.19
$\mathrm{N_{cont,00,kaon2}}$	918.84 $\pm$ 30.31
$\mathrm{N_{cont,pm,kaonpion}}$	344.45 $\pm$ 18.56
$\mathrm{N_{cont,00,kaonpion}}$	861.01 $\pm$ 29.34
$\mathrm{N_{cont,pm,pion}}$	409.25 $\pm$ 20.23
$\mathrm{N_{cont,00,pion}}$	1140.52 $\pm$ 33.77
$\mathrm{N_{cont,pm,other}}$	359.23 $\pm$ 18.95
$\mathrm{N_{cont,00,other}}$	920.45 $\pm$ 30.34

Table 8.12: Expected yields

all yields are as expected and all other values are taken from fits to resonant signal MC or off-peak/side-band data, where $\mathcal{S}$ and $\mathcal{C}$ have the SM expectation values in these studies. We then generate 500 toy datasets and fit them. The resulting pull distributions can be found in Fig. 8.5. We observe no significant biases in all variables.

The previous test was done for a particular configuration of the TDCPV parameters. To ensure that our analysis tool is stable over all the permitted values of $\mathcal{S}$ and $\mathcal{C}$ we perform a "linearity" check using pure toy studies. We generate toys for values of $\mathcal{S}$ between -1 and +1 while keeping $\mathcal{C}$ at zero, and toys with values of $\mathcal{C}$ between -1 and +1 while keeping $\mathcal{S}$ at zero. For each configuration we generate 25 toy data sets (yields according to Tab. 8.12) and fit them. We take the averages of the fitted values for each point and plot them against the generated values, where the error bars indicate the errors on the averages. The result is

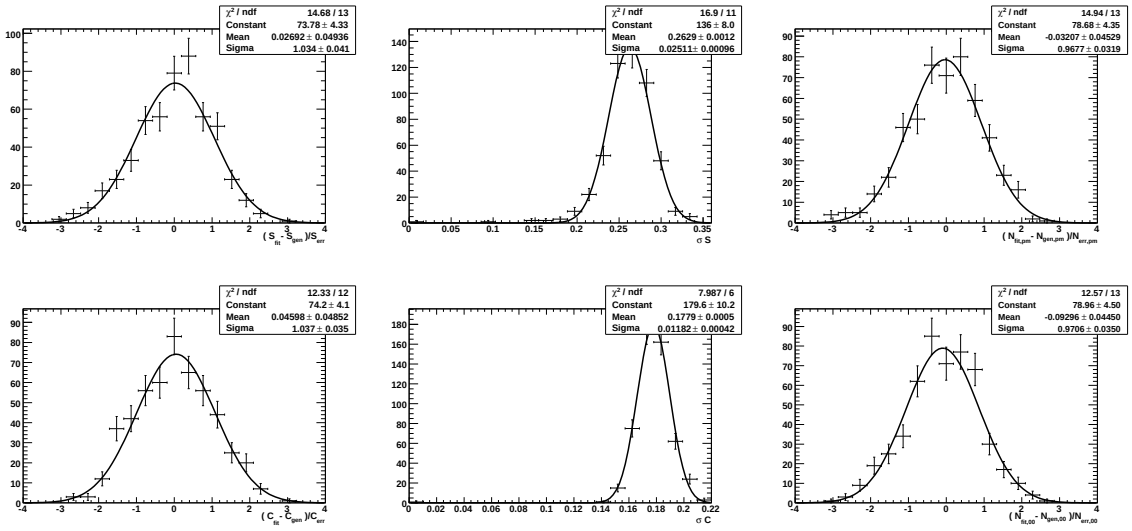

Figure 8.5: Results of the pure toy studies. The plots on the left show the pulls for the S (top) and C (bottom) parameters, the central plots show the fit errors for the same parameters and the plots on the right show the pulls of the signal yields for $\mathrm{B}^0 \to 3\mathrm{K}^0_\mathrm{s}(\pi^+\pi^-)$ (top) and $\mathrm{B}^0 \to 2\mathrm{K}^0_\mathrm{s}(\pi^+\pi^-)\mathrm{K}^0_\mathrm{s}(\pi^0\pi^0)$ (bottom).

shown in Fig. 8.6. It indicates that our analysis tool behaves linearly in the observables.

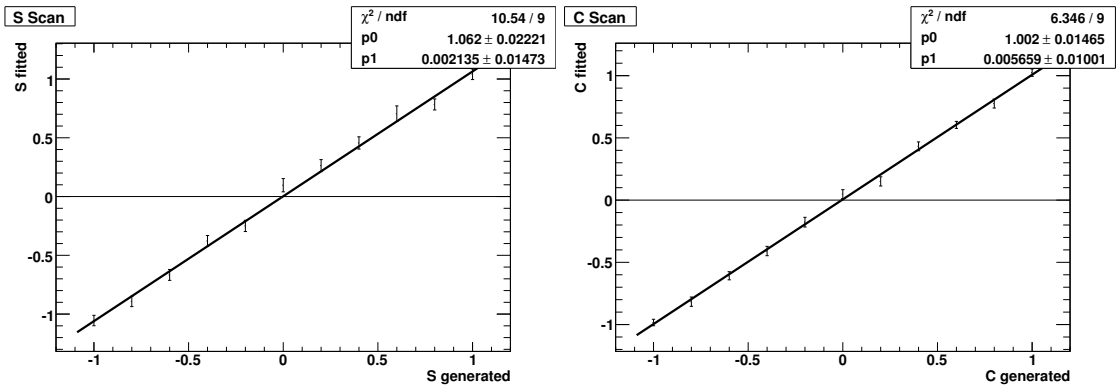

Figure 8.6: Linearity test of TDCPV observables using pure toys

8.4.3 Embedded toys

In the pure toy studies presented above, we have generated and fitted with the same PDF. This procedure is useful to check for intrinsic biases but is not sensitive to reconstruction effects such as correlations between variables, neglected SCF or functional descriptions for the discriminating variables that are not well adapted. In particular, we know that there are non-zero correlations between the variables, as we detail in Table 8.13 that shows the linear correlation

	m_{ES}	ΔE	$\frac{\Delta t}{\sigma(\Delta t)}$	NN
m_{ES}	1	0.186 (0.004)	0.019 (0.041)	0.025 (0.014)
ΔE	-	1	0.022 (0.240)	0.035 (0.021)
$\frac{\Delta t}{\sigma(\Delta t)}$	-	-	1	0.007 (0.015)
NN	-	-	-	1
	m_{ES}	ΔE	$\frac{\Delta t}{\sigma(\Delta t)}$	NN
m_{ES}	1	0.053 (0.004)	0.008 (0.014)	0.045 (0.023)
ΔE	-	1	0.013 (0.059)	0.016 (0.006)
$\frac{\Delta t}{\sigma(\Delta t)}$	-	-	1	0.003 (0.021)
NN	-	-	-	1

Table 8.13: Linear correlation coefficients between likelihood variables in resonant signal MC SP-10045 (continuum background from off-peak and on-peak sideband) for $B^0 \to 3K^0_s(\pi^+\pi^-)$ (top) and $B^0 \to 3K^0_s(\pi^+\pi^-)$ (bottom).

coefficients between the fit variables for signal MC and for continuum background. With the exception of $(\Delta E, \frac{\Delta t}{\sigma(\Delta t)})$ in continuum background for $B^0 \to 3K^0_s(\pi^+\pi^-)$ correlations are small. To evaluate the biases introduced by these effects, we perform embedded toy studies, by fitting 600 pseudo-experiments that are made of signal events from resonant MC and background events generated with the fitting tool. We find no significant biases, except for the signal yield of the $B^0 \to 2K^0_s(\pi^+\pi^-)K^0_s(\pi^0\pi^0)$ sub-mode where a deviation of the order of 20% of the statistical error is observed. As the observables $\mathcal{S}$ and $\mathcal{C}$ are not affected and the bias is relatively small we do not further investigate it and conclude the validation of the TD analysis. The results of embedded toy studies are shown in Fig. 8.7.

8.5 Results

Fits to data are performed in two stages. In the first stage, the blind fit, we do not look at the $\mathcal{S}$ and $\mathcal{C}$ parameters but at yields only. The maximum-likelihood fit of 3261 candidates in the $B^0 \to 3K^0_s(\pi^+\pi^-)$ sub-mode and 7209 candidates in the $B^0 \to 2K^0_s(\pi^+\pi^-)K^0_s(\pi^0\pi^0)$ sub-mode results in the following event yields:

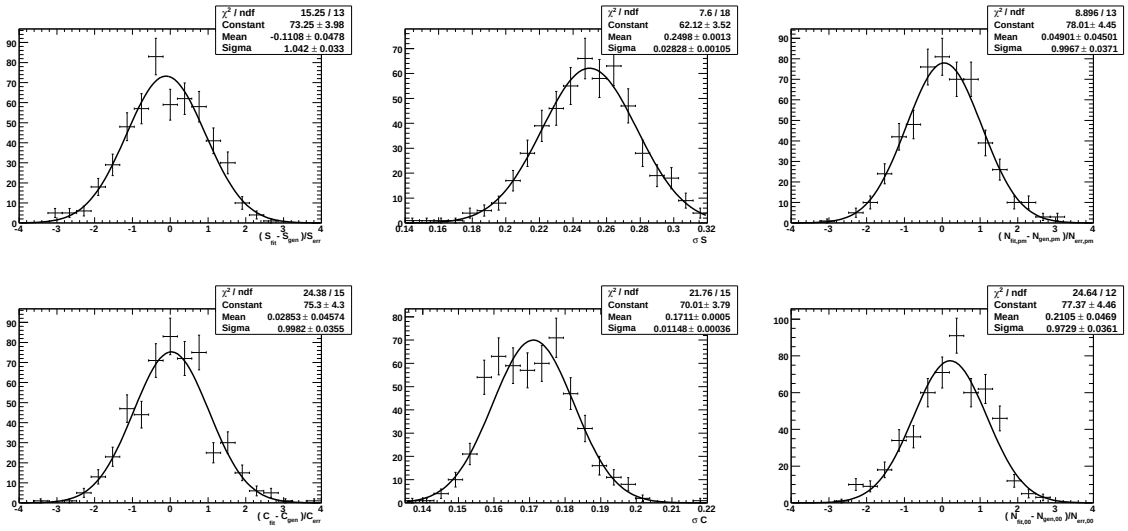

Figure 8.7: Results of the embedded toy studies. The plots on the left show the pulls for the $\mathcal{S}$ (top) and $\mathcal{C}$ (bottom) parameters, the plots in the middle show the fit errors for the same parameters and the plots on the right show the pulls of the signal yields for $B^0 \to 3K^0_S(\pi^+\pi^-)$ (top) and $B^0 \to 2K^0_S(\pi^+\pi^-)K^0_S(\pi^0\pi^0)$ (bottom).

Species	$B^0 \to 3K^0_S(\pi^+\pi^-)$	$B^0 \to 2K^0_S(\pi^+\pi^-)K^0_S(\pi^0\pi^0)$
Signal	201^{+16}_{-15}	62^{+13}_{-12}
Continuum KaonII	516^{+23}_{-22}	870^{+30}_{-29}
Continuum KaonI	322^{+18}_{-17}	457^{+22}_{-21}
Continuum KaonPion	370^{+19}_{-19}	825^{+29}_{-28}
Continuum Lepton	27^{+5}_{-5}	48^{+7}_{-7}
Continuum NoTag	1030^{+33}_{-32}	2862^{+54}_{-54}
Continuum Other	387^{+20}_{-19}	926^{+31}_{-30}
Continuum Pion	434^{+21}_{-20}	1098^{+33}_{-33}
B-bkg B^+B^-	-54^{+29}_{-24}	45^{+34}_{-30}
B-bkg $B^0\bar{B}^0$	9^{+31}_{-30}	4^{+38}_{-29}

These numbers are in acceptable agreement with the expectations. To check the discrimination between signal and background and to check if the model describes the data well, we use the ${}_s\mathcal{P}lots$ technique [67] to weight data and obtain "pure" signal and continuum background distributions using the information from the fit to data. For a given variable, the discriminating information of this variable is not used for the weight evaluation. We then compare the weighted data distribution to a high-statistic toy data sample that has been generated with the values of the fit result. We find that the model provides a good description of the data. The distributions of the discriminating variables for signal are shown in Fig. 8.8 and the same distribution for continuum background (including Δt) are shown in Fig. 8.9. The only variable that does not show a good agreement is the NN for signal in the sub-mode $B^0 \to 2K^0_S(\pi^+\pi^-)K^0_S(\pi^0\pi^0)$. This is due to the fact that the NN is the most discriminating variable and as there is more background in this submode, weighting data with the informa-

tion from the other variables only is not very reliable. To convince ourselves that there is no problem, we look at projection plots, that we enrich with different fractions of signal by cutting on the likelihood ratio for signal defined for the event i as

$$\mathrm{R}^{\mathrm{i}}_{\mathrm{sig}} = \frac{\mathcal{P}^{\mathrm{i}}_{\mathrm{signal}}}{\sum_{\mathrm{j}} \mathcal{P}^{\mathrm{i}}_{\mathrm{j}}} \, . \tag{8.10}$$

Signal-enriched projection plots can be found in the appendix B (Fig. B.9).

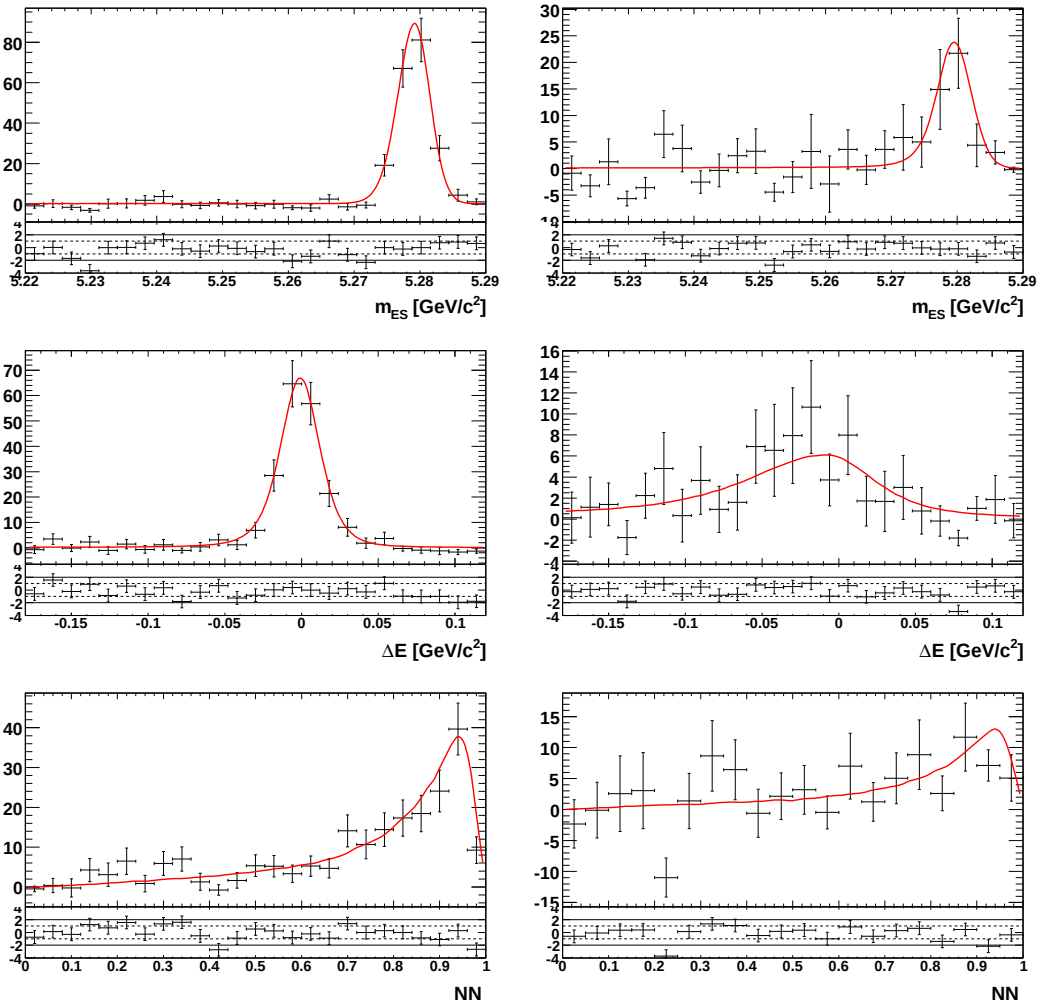

Figure 8.8: Signal ${}_s\mathcal{P}lots$ of the discriminating variables for $\mathrm{B}^0 \to 3\mathrm{K}^0_{\mathrm{s}}(\pi^+\pi^-)$ on the left and for $\mathrm{B}^0 \to 2\mathrm{K}^0_{\mathrm{s}}(\pi^+\pi^-)\mathrm{K}^0_{\mathrm{s}}(\pi^0\pi^0)$ on the right. The first row shows the $\mathrm{m_{ES}}$ distribution, the second row the $\Delta\mathrm{E}$ distribution and the third one the NN output distribution.

The unblinded fit result for the TDCPV parameters S and C yields:

$$\begin{aligned} \mathcal{S} &= -0.935^{+0.238}_{-0.214} \, , \\ \mathcal{C} &= -0.166^{+0.180}_{-0.178} . \end{aligned}$$

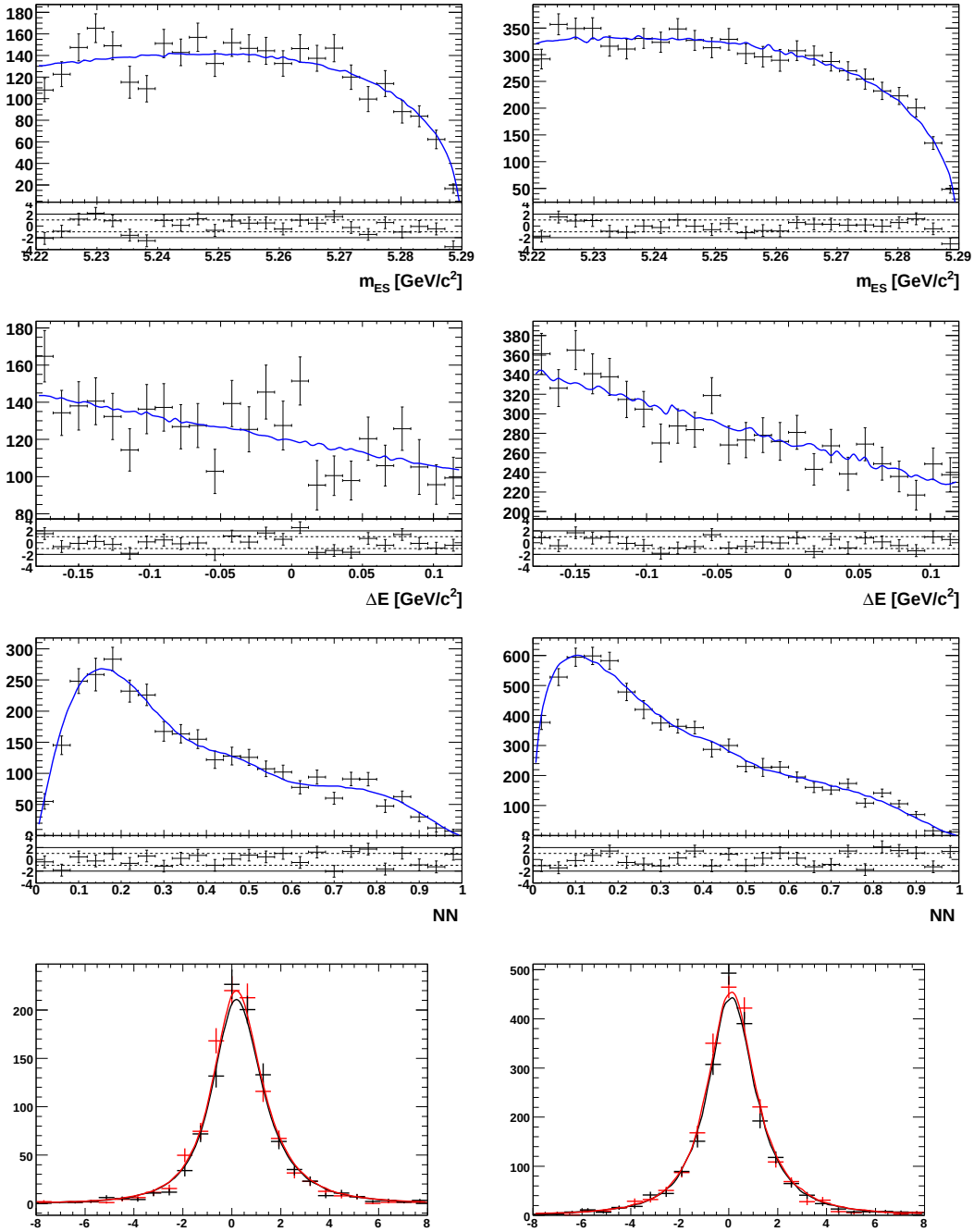

Figure 8.9: Continuum ${}_s\mathcal{P}lots$ of the discriminating variables for $\mathrm{B}^0 \to 3\mathrm{K}^0_\mathrm{s}(\pi^+\pi^-)$ on the left and for $\mathrm{B}^0 \to 2\mathrm{K}^0_\mathrm{s}(\pi^+\pi^-)\mathrm{K}^0_\mathrm{s}(\pi^0\pi^0)$ on the right. The first row shows $\mathrm{m_{ES}}$, the second row $\Delta\mathrm{E}$, the third one the NN output and the forth one $\Delta\mathrm{t}$.

MC_{stat}	0.002	0.000(8)
B_{reco}	0.004	0.003
$B - bkg$	0.031	0.012
$MC - Data : \Delta t$	0.045	0.026
$MC - Data : discr.vars$	0.021	0.003
FitBias :	0.022	0.017
Vetoes :	0.005	0.003
Misc :	0.004	0.015
Sum	0.063	0.038

Table 8.14: Summary of systematic uncertainties on the $\mathcal{S}$ and $\mathcal{C}$ parameters.

The correlation between $\mathcal{S}$ and $\mathcal{C}$ is -0.1583. We use the information of the discriminating variables of the fit result to create ${}_s\mathcal{P}lots$ of the Δt distribution in signal separated by tag flavor and of the asymmetry defined by Eq. 2.31. We produce ${}_s\mathcal{P}lots$ for the combined fit result but also for the individual sub-channels that are shown in Fig. 8.10. We find that the $B^0 \to 3K^0_s(\pi^+\pi^-)$ sub-mode shows a better agreement between model and data. This is expected as the measurement is dominated by the $B^0 \to 3K^0_s(\pi^+\pi^-)$ submode and if the individual values are not the same for both sub-modes (due to statistical fluctuation), we expect to see some disagreement. To better understand the fit result, we scan the likelihood of the $\mathcal{S}$ parameter for both sub-modes and for the combined fit. The result is shown on the left hand side of Fig. 8.11 and we observe a sizable difference between the $\mathcal{S}$ values for both sub-modes preferred by data, and the combination of both likelihoods gives the value found by the combined fit. Clearly the measurement is statistically limited. As there is some correlation between the $\mathcal{S}$ and $\mathcal{C}$ parameters, it is interesting to do a 2-dimensional likelihood scan that is shown on the right hand side of Fig. 8.11. There are several conclusions that can be drawn from this scan. The first is that in the 2-dimensional scan the difference between the fit values and the value from $B^0 \to c\bar{c}K^{(*)}$ is (slightly) more significant than the difference in the $\mathcal{S}$-parameter-alone scan. A second conclusion is that the fit result is close to the physical boundary, given by the constraint $\mathcal{S}^2 + \mathcal{C}^2 <= 1$. Nevertheless, as we assign frequentist errors, this has no consequence on the result (fortunately the fits converge far enough in the non-physical region to get an error estimate). The fact that the individual submodes have quite different values for $\mathcal{S}$ and C and that the value for $B^0 \to 3K^0_s(\pi^+\pi^-)$ is outside the physical region indicate sizable statistical fluctuations.

8.6 Systematic uncertainties

The systematic uncertainties are summarized in Tab. 8.14. We estimate $\delta\mathcal{S} = 0.064$ and $\delta\mathcal{C} = 0.038$. In the following we describe how the individual uncertainties are obtained.

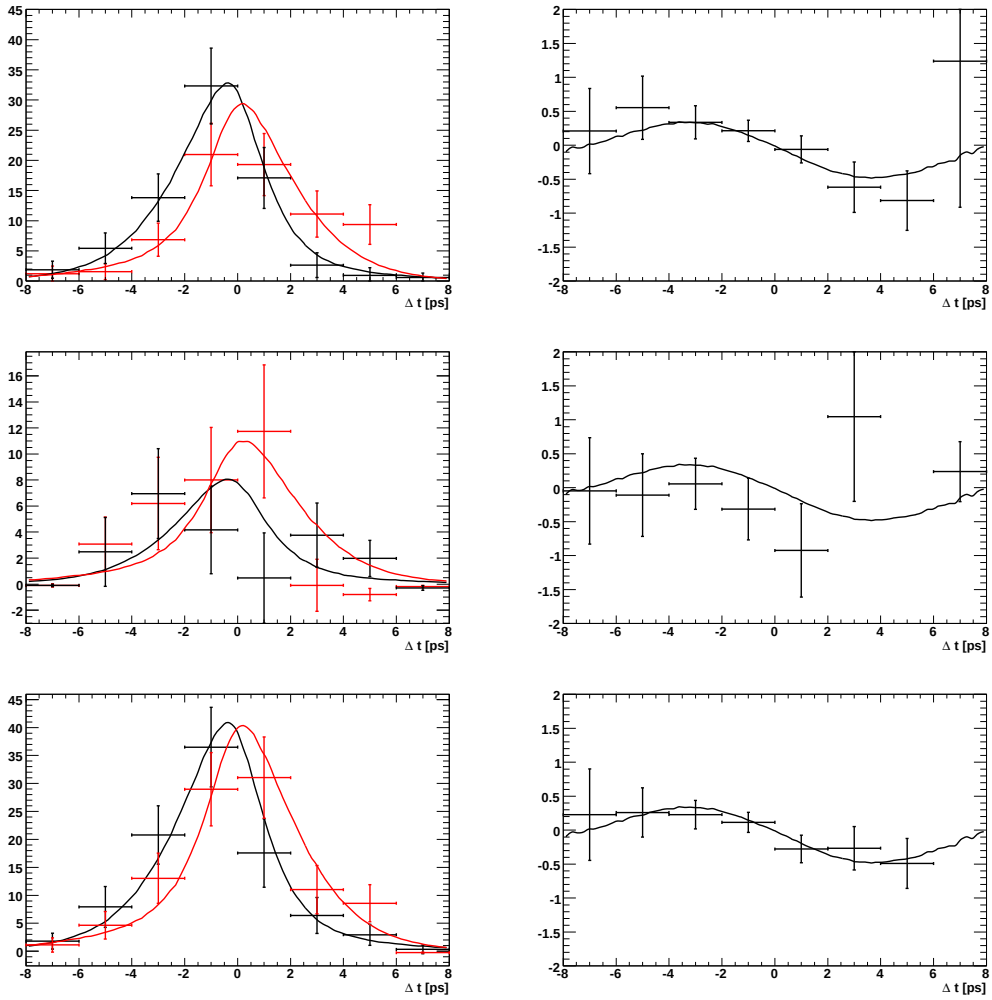

Figure 8.10: ${}_s\mathcal{P}lots$ for signal $\Delta\mathrm{t}$. On the left are shown the proper-time distributions for signal B mesons tagged as B^0 in black and B mesons tagged as $\bar{\mathrm{B}}^0$ in red, on the right are shown the time-dependent CP asymmetry distributions. The data points with error bars in the first row corresponds to $\mathrm{B}^0 \to 3\mathrm{K}^0_\mathrm{s}(\pi^+\pi^-)$, in the second to $\mathrm{B}^0 \to 2\mathrm{K}^0_\mathrm{s}(\pi^+\pi^-)\mathrm{K}^0_\mathrm{s}(\pi^0\pi^0)$ and in the third to both, the smooth lines correspond to the combined fit result in all cases.

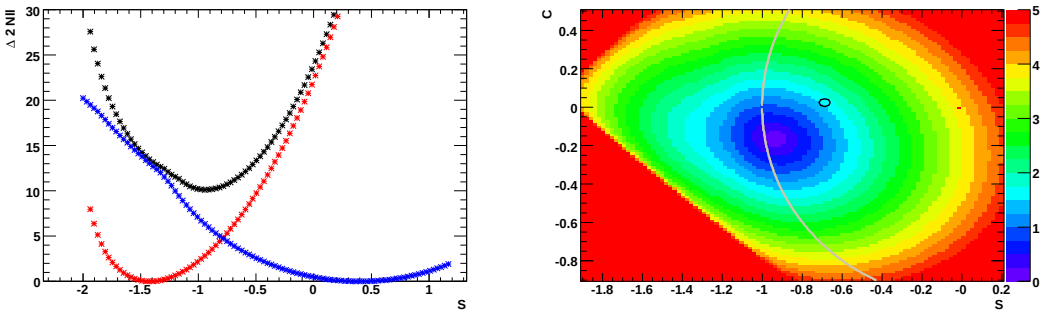

Figure 8.11: Left: Likelihood scans of the $\mathcal{S}$ parameter for the $\mathrm{B}^0 \to 3\mathrm{K}^0_\mathrm{s}(\pi^+\pi^-)$ (red) and $\mathrm{B}^0 \to 2\mathrm{K}^0_\mathrm{s}(\pi^+\pi^-)\mathrm{K}^0_\mathrm{s}(\pi^0\pi^0)$ (blue) sub-channels, and for the combined fit (black).
On the right: two-dimensional likelihood scan of the $\mathcal{S}$ and $\mathcal{C}$ parameters for the combined fit. The z-axis of the two-dimensional scan is given in units of the statistical significance. The SM model value from the *BABAR* analyses of $\mathrm{B}^0 \to \mathrm{c\bar{c}K}^{(*)}$ decays is indicated as a black ellipse and the physical boundary ($\mathcal{S}^2 + \mathcal{C}^2 <= 1$) is marked as a gray line. The two-dimensional plots seems to be trimmed on the lower left. This is due to negative values of the PDF outside the physical region where the fit fails to converge, i.e. the red region does not mean that the scan flattens out at 5σ.

8.6.1 Statistical uncertainty of PDFs taken from simulation

We take most of signal PDF's from simulation that is statistically limited. All parameters that are taken form simulation and fixed in the nominal fit are varied within their statistical uncertainties:

- m_{ES} **and** ΔE: All parameters are varied ("randomized") using Gaussian distributions taking into account the correlations between the parameters.

- **NN**: Contents of the bins of the histograms used to describe the PDF are varied using the Poisson distribution.

- $\Delta\mathrm{t}$ **resolution function**: Same as for $\mathrm{m_{ES}}$ and $\Delta\mathrm{E}$.

We perform 500 fits to data with the randomized values. We use the distribution of the difference between the randomized and nominal fit values for $\mathcal{S}$ and $\mathcal{C}$ and assign the sum in quadrature of the mean and the RMS as systematic uncertainty. We find small uncertainties which indicates that the models give stable descriptions of the simulation and that the generated MC events have been statistically sufficient. The uncertainties for $\mathrm{m_{ES}}$, $\Delta\mathrm{E}$ and NN are included in the "$\mathrm{MC_{stat}}$" systematic in Tab. 8.14. The uncertainty for $\Delta\mathrm{t}$ resolution function is included in "$\mathrm{B_{reco}}/\Delta\mathrm{t_{stat}}$". The distributions of the randomized fits can be found in appendix B. (Fig. B.8).

8.6.2 MC-data differences for PDFs taken from simulation

- **Vertexing technique**: Due to the absence of direct tracks from the decay vertex, the $\Delta\mathrm{t}$ resolution function is different from the standard *BABAR* resolution function from $\mathrm{B} \to \mathrm{c\bar{c}K^{(*)}}$ analyses. We fit the resolution function on MC simulation (see Tab. 8.10). We use the control sample $\mathrm{B^0 \to J/\psi\, K^0_s}$ to estimate the difference between data and MC. We obtain the signal distributions in data with the ${}_s\mathcal{P}lots$ technique using the discriminating information from a fit to $\mathrm{m_{ES}}$ (see appendix B, Fig. B.10). In the $\mathrm{B^0 \to J/\psi\, K^0_s}$ data and MC samples, the vertex has been reconstructed with and without the information from the $\mathrm{J/\psi}$. We use the pull variable $\chi(\Delta\mathrm{t})$ defined as

$$\chi(\Delta\mathrm{t}) = \frac{\Delta\mathrm{t_{w/o}} - \Delta\mathrm{t_w}}{\sqrt{\sigma^2(\Delta\mathrm{t_{w/o}}) - \sigma^2(\Delta\mathrm{t_w})}}\,, \tag{8.11}$$

  that gives an estimation of the resolution function due to the indirect vertexing, where the vertex with the information of the $\mathrm{J/\psi}$ is considered as "true information". For directly vertexed particles, the MC-data difference has been estimated using toy studies[4] and found to be small ($\delta\mathrm{S} \simeq 0.0036$, $\delta\mathrm{C} \simeq 0.0093$). As a result the MC-data difference due to indirect vertexing dominates the uncertainty and we neglect the former. We fit the pull distributions for data and MC for $\mathrm{K^0_s}$ classes 1 and 2 using the sum of two Gaussians; the distributions and the fit result are shown in Fig. 8.12. We use the difference between the fits to data and MC in terms of the means and the widths of these Gaussians to shift the bias and width of the core resolution function and the fraction and the bias of the tail resolution function. The shifts are weighted according to the fraction of Class 1 events (90.1% for $\mathrm{B^0 \to 3K^0_s(\pi^+\pi^-)}$ and 83.6% for $\mathrm{B^0 \to 2K^0_s(\pi^+\pi^-)K^0_s(\pi^0\pi^0)}$), estimated from signal MC. We then perform 500 fits to data where we vary the MC-data correction by randomizing the double-Gaussian fit results according to their statistical uncertainty, taking into account the correlations between the parameters. To estimate the resulting systematic uncertainty, we fill a histogram with the difference between nominal and shifted values of the $\mathcal{S}$ and $\mathcal{C}$ parameters. The sum in quadrature of the mean and the RMS of these distributions is assigned as systematic uncertainty and corresponds to the "$\mathrm{MC - Data : \Delta t}$" systematic in Tab. 8.14. The distributions of the randomized fits can be found in appendix B (Fig. B.8).

- **Discriminating variables**: We estimate the MC-data differences using the control samples $\mathrm{B^0 \to J/\Psi K^0_s(\pi^+\pi^-)}$ and $\mathrm{B^0 \to J/\Psi K^0_s(\pi^0\pi^0)}$. We extract corrections as described for each variable below, apply these corrections, varied within their uncertainties, and perform 500 randomized fits to data. We then assign the systematic uncertainties in the same way as for the statistical uncertainty of PDFs taken from MC simulation.
  For $\mathrm{m_{ES}}$ we fit both MC and data samples, generate high statistics toys with the fit results and compare the mean and the RMS of these distributions to get the shift on the mean and the scale of the RMS between data and MC. We then apply these corrections

[4] Based on the MC-data differences in the *BABAR* $\mathrm{B_{reco}}$ sample.

by shifting the mean and scaling the width of the parameterizations extracted from MC in fits to data. We do not correct the means for $B^0 \to 3K^0_s(\pi^+\pi^-)$ as they are free to vary in the fit.
For ΔE , we use the ${}_s\mathcal{P}lots$ technique to obtain the signal distributions from the m_{ES} fit. For $B^0 \to 3K^0_s(\pi^+\pi^-)$ we then use the same procedure as for m_{ES} to obtain the corrections. For $B^0 \to 2K^0_s(\pi^+\pi^-)K^0_s(\pi^0\pi^0)$ on the other hand, the ΔE distribution is rather different between our MC and for the control sample MC. We therefore use the difference between data and MC in the control sample to reweight our signal MC. We then use the same correcting procedure but based on the difference between nominal and reweighted MC to find the corrections. The differences in terms of mean and RMS for m_{ES} and ΔE can be found in Tab. 8.15 and the corresponding distributions are given in appendix B (Fig. B.11).
For the NN, we use as input the same variables from the control sample, except that we do not use the worst of the K^0_s masses, but just the regular K^0_s mass, as there is only one in the control sample. Given that we are only interested in MC-data differences and that the discriminating power of this variables is small compared to the other inputs of the NN, this should give a good enough estimation. We then use the ${}_s\mathcal{P}lots$ technique to compare the NN output for signal. We use the difference to re-weight the NN histograms in the fit to data. The MC-data comparison can be found in appendix B (Fig. B.11). We see that the data NN output of the control data sample is statistically limited and fluctuates around 4% and in consequence we also vary the weights when applying them by 4%, this variation is done differently for each weight-bin. The corresponding uncertainty is referred to as "$\mathrm{MC} - \mathrm{Data} : \mathrm{disc.vars.}$" systematic in Tab. 8.14.

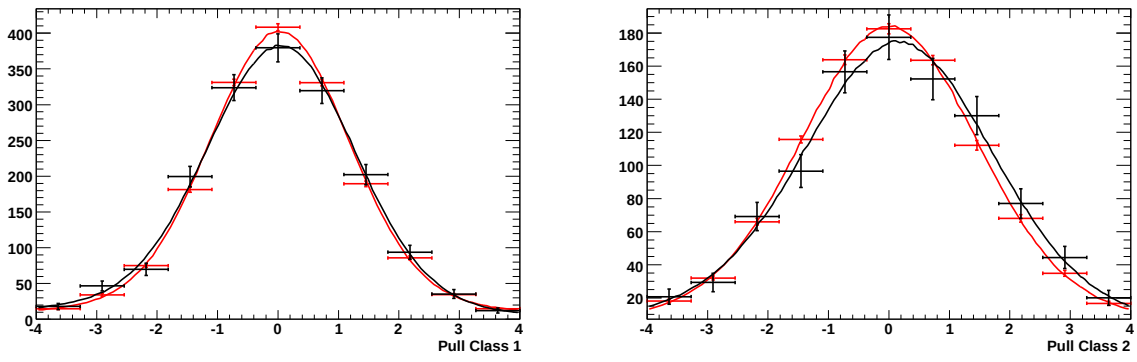

Figure 8.12: Pull distributions for data (black) and MC (red), for K^0_s in Class 1 (left) and K^0_s in Class2 (right). Both samples passed the same selection as the $K^0_sK^0_sK^0_s$ sample.

$B^0 \to 3K^0_s(\pi^+\pi^-)$	MC	Data
Mean m_{ES}[MeV/c^2]	5279.38 ± 0.002	5279.48 ± 0.002
RMS m_{ES}[MeV/c^2]	2.686 ± 0.001	2.64278 ± 0.001
Mean ΔE[MeV/c^2]	$(1.037 \pm 0.435) \times 10^{-2}$	$(-12.3814 \pm 12.0753) \times 10^{-2}$
RMS ΔE[MeV/c^2]	9.70687 ± 0.003	10.0949 ± 0.085
$B^0 \to 2K^0_s(\pi^+\pi^-)K^0_s(\pi^0\pi^0)$	MC	Data
Mean m_{ES}[MeV/c^2]	5278.98 ± 0.003	5279.05 ± 0.003
RMS m_{ES}[MeV/c^2]	3.580 ± 0.002	3.580 ± 0.002
Mean ΔE[MeV/c^2]	-1.527 ± 0.072	3.223 ± 0.679
RMS ΔE[MeV/c^2]	29.170 ± 0.051	28.709 ± 0.480

Table 8.15: Values of means and RMS of m_{ES} and ΔE in the control samples for MC (left) and data (right). The top rows show the values for the control sample $rmB^0 \to J/\psi K^0_s(\pi^+\pi^-)$ and the bottom rows the ones for the control sample $B^0 \to J/\psi K^0_s(\pi^+\pi^-)$

8.6.3 Statistical uncertainty of PDFs taken from data

We take the tagging parameters that are provided by the *BABAR* tagging group as they do not depend on the signal side. These parameters are given in Tab. 7.3 and have statistical uncertainties. As they are fixed in our fit, we overestimate the uncertainty by assuming the parameters to be uncorrelated, and randomize them using a Gaussian distribution whose means are taken as the central values Tab. 7.3 and the widths as corresponding uncertainties. We perform 500 fits to data using the randomized tagging parameters and assign the systematical uncertainty in the same way as for the statistical uncertainty of PDFs taken from MC simulation[5]. The corresponding uncertainty is referred to as "B_{reco}" systematic in Tab. 8.14.

8.6.4 Fit Bias

The fit bias has been estimated using embedded toys. We multiply the statistical errors[6] on $\mathcal{S}$ and $\mathcal{C}$ with the bias shown in Fig. 8.7 to obtain the corresponding systematical uncertainty. The corresponding uncertainty is referred to as "FitBias" systematic in Tab. 8.14.

8.6.5 Uncertainty in the $\mathcal{B}$ and CP content of the B-background

The branching fractions and the CPV parameters for many B decays that we include in our B-background model are unknown or uncertain. In the nominal fit, we assume $\mathcal{S}$=$\mathcal{C}$=0. To estimate the associated systematic uncertainty, we vary these numbers taking random values from a Gaussian centered around zero and with width of 0.5. For the fixed yields we vary the values using the Poisson law. We also randomize the parameters of the resolution function

[5] As we randomize the tagging dilution parameters, and they are the same for B-background and signal, the systematic includes some part of the B-background systematic

[6] symmetric errors from HESSE

and the tagging fractions that we take from the *BABAR* tagging group. The corresponding uncertainty is referred to as "$\mathrm{B}-\mathrm{bkg}$" systematic in Tab. 8.14.

8.6.6 Bias linked with the charmonium vetoes

We apply vetoes to eliminate allowed charmonium events that pass the selection. We apply a veto around the mass, that eliminates 95% of the $\chi_{c0}\mathrm{K}^0_s$ modes as estimated from Monte Carlo. We do not apply a veto on $\chi_{c2}\mathrm{K}^0_s$, as we only expect one such event in $\mathrm{B}^0 \to 2\mathrm{K_S}(\pi^+\pi^-)\mathrm{K_S}(\pi^0\pi^0)$ and a third of an event in $\mathrm{B}^0 \to 3\mathrm{K_S}(\pi^+\pi^-)$. To estimate the bias introduced by remaining charmonium events, we take the results measured in our fit to data, add a signal-like component with SM values, generate 500 toys and fit them. We then fit the same toy data samples without including the SM-signal-like component. We substract the means of the pulls of $\mathcal{S}$ and $\mathcal{C}$ for the two scenarios, multiply this difference by the statistical error and assign the product as a systematic. The generated and poissonized charmonium yields are estimated from Monte Carlo and are 0.79 for $\mathrm{B}^0 \to 3\mathrm{K_S}(\pi^+\pi^-)$ and 1.28 for $\mathrm{B}^0 \to 2\mathrm{K_S}(\pi^+\pi^-)\mathrm{K_S}(\pi^0\pi^0)$. We find a bias of 0.0252 and 0.020 statistical errors for $\mathcal{S}$ and $\mathcal{C}$ respectively. The corresponding uncertainty is referred to as "Vetoes" systematic in Tab. 8.14.

8.6.7 Miscellanea

We take uncertainties due to detector misalignment, beam spot position, the boost of the $\Upsilon(4\mathrm{S})$ and doubly Cabbibo suppressed decays (DCSD) from $\mathrm{B}^0 \to \mathrm{c\bar{c}K}^{(*)}$ analyses [16]. The values are summarized in table 8.16. The corresponding uncertainty is referred to as

Category	$\mathcal{S}$	$\mathcal{C}$
DCSD	0.001	0.014
Svt alignment	< 0.001	< 0.001
beam spot	0.002	0.006
boost	0.003	0.001
total	0.004	0.015

Table 8.16: Systematics from $\mathrm{B}^0 \to \mathrm{c\bar{c}K}^{(*)}$ analyses

"Misc" systematic in Tab. 8.14.

8.7 Summary

We have measured the TDCVP parameters $\mathcal{S}$ and $\mathcal{C}$ simultaneously for the two submodes $\mathrm{B}^0 \to 3\mathrm{K}^0_s(\pi^+\pi^-)$ and $\mathrm{B}^0 \to 2\mathrm{K}^0_s(\pi^+\pi^-)\mathrm{K}^0_s(\pi^0\pi^0)$. The result is:

- $\mathcal{S} = -0.935^{+0.238}_{-0.214} \pm 0.063$
- $\mathcal{C} = -0.166^{+0.180}_{-0.178} \pm 0.038$

and is compatible within uncertainties with the Standard Model prediction. It is also compatible to the 2010 world average of $\mathcal{S}$ measured in charmonium decays [15], $\mathcal{S} = 0.672 \pm 0.023$. The measurement is statistically limited and the dominant systematic uncertainty comes from the vertex measurement. The overall disagreement between the SM prediction and penguin-dominated decays has become much less stringent with recent measurement. A compilation of 2010 summer results from Ref. [15] including the TD analysis presented in this work[7] is shown in Fig. 8.13.

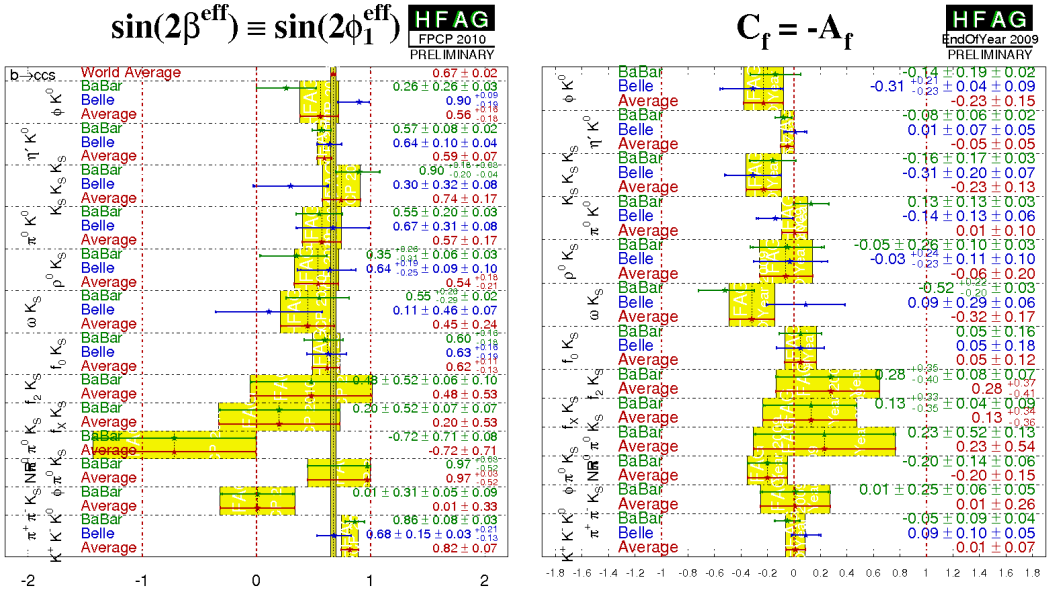

Figure 8.13: Compilation of $\sin(2\beta_{\text{eff}})$ and $\mathcal{C}$ for penguin dominated decays by the HFAG group [15].

[7] The compilation actually shows the preliminary result

9 Amplitude Analysis

9.1 Introduction

Primer: This chapter is intended to be read after the previous one, chapter 8, that describes the TD analysis. For shortness we describe some aspects of the amplitude analysis that are the same or very similar to the TD analysis less extensively.

The selection for the DP analysis is somewhat tighter than in the TD analysis and we only use K^0_s decaying to charged pions (Sec. 9.2). Due to the limited statistics we only measure fit fractions and therefore, as we do not measure CP asymmetries, all events are assumed to be in the `NoTag` category. Details on the likelihood function are given in Sec. 9.3. The analysis is done blindly as far as it is possible, meaning that we validate our fitter before applying it on data. For these validation studies an ad hoc model is used, containing "well established" resonant contributions with arbitrary isobar parameter values, the "baseline-model" (Sec. 9.5.1). We then search for other possible resonant contributions using likelihood scans (Sec. 9.4), and do not look at the fit fractions before the final fit is set up and validated (Sec. 9.5.2). We cannot do a completely blind analysis as this is a first measurement of resonant and non-resonant amplitudes in this mode and in order to understand the different contributions, we have to look at the data.
In the nominal fit (Sec. 9.6) we extract the isobar parameters and the event yields. We translate these parameters into the observables, i.e. the phase differences, fit fractions, product branching fractions and the inclusive branching fraction. Systematic uncertainties are detailed in Sec. 9.7.

9.2 Selection and backgrounds

9.2.1 Selection and Selection Efficiencies

The selection differs from the one of the TD analysis. The most significant change is that we only use K^0_s decaying to charged pions. The advantage of this choice is that the SCF rate becomes negligible, as shown in embedded toy studies (see Sec. 9.5), and this component does not need to be separately taken into account in the DP PDF. Figure 9.1 and Fig. 9.2 show correctly reconstructed and SCF events for the discriminating variables and the DP. It is noteworthy that while the SCF component is continuum-like in $\mathrm{m_{ES}}$ and $\Delta\mathrm{E}$, it differs from the DP continuum PDF (compare Fig. 9.2 and Fig. 9.6).

To remove pathological events we require several very loose criteria that are the same as

in the TD analysis:

- The total energy of the events has to be smaller than 20 GeV.
- The absolute value of the events shape variables L_0 and L_2 has to be inferior to 10.
- The $\Delta\mathrm{t}$ measurement has to be within reasonable limits. We require that the absolute value of the $\Delta\mathrm{t}$ is inferior to 20 ps and that its error is inferior to 2.5 ps.
- The probability of the decay vertex fit of the B candidate has to be non-zero.

A change with respect to the TD analysis is that we apply tighter requirements on $\mathrm{m_{ES}}$ and $\Delta\mathrm{E}$. The tighter requirement on $\mathrm{m_{ES}}$ is necessary as we use the $\mathrm{m_{ES}}$ sideband to model the DP continuum PDF and we cannot use the same data twice.

- Events in the signal peak (fit) region have to satisfy $5.27\,\mathrm{GeV/c^2} < \mathrm{m_{ES}} < 5.29\,\mathrm{GeV/c^2}$. The sideband region is defined as $5.2\,\mathrm{GeV/c^2} < \mathrm{m_{ES}} < 5.27\,\mathrm{GeV/c^2}$. We estimate from non-resonant signal MC that less than 1% of signal passes this sideband requirement.
- $\Delta\mathrm{E}$ has to satisfy $-0.1\mathrm{GeV} < \Delta\mathrm{E} < 0.1\mathrm{GeV}$. As all $\mathrm{K^0_s}$ are reconstructed from charged pions there is no need to use an asymmetric requirement.

Another change with respect to the TD analysis is that we optimize the $\mathrm{K^0_s}$ selection using the `StatPatternRecognition` package, where we optimize simultaneously the selection criteria on the $\mathrm{K^0_s}$ kinematical variables to reject continuum background. We use off-peak data as a continuum sample and non-resonant signal Monte Carlo as a signal sample, and the figure of merit is $\mathrm{S}/\sqrt{\mathrm{S}+\mathrm{B}}$. Each $\mathrm{K^0_s}$ is considered separately, which results in the same selection criteria for all three $\mathrm{K^0_s}$. We find:

- $\alpha < 0.0185\mathrm{rad}$;
- $0.22 < \mathrm{r_{dec}} < 45\,\mathrm{cm}$;
- $|\mathrm{m_{K^0_s}} - \mathrm{m_{PDG}}| < 0.0121\,\mathrm{GeV/c^2}$;

This further optimization with respect to the TD analysis is justified for two reasons. Firstly, as we use very loose requirements on $\mathrm{m_{ES}}$ and $\Delta\mathrm{E}$ in the TD analysis, the gain optimizing the $\mathrm{K^0_s}$ selection would have been minimal. Secondly the modeling of the DP continuum PDF is one of the delicate parts of this analysis and a smaller continuum background results in a smaller associated uncertainty.

9.2.2 Continuum background

We use the $\mathrm{B^0} \to 3\mathrm{K^0_s}(\pi^+\pi^-)$ NN from the TD analysis to discriminate between signal and continuum background. The values of the corresponding PDF parameters are fitted on sideband data, fixed for the nominal fit, and varied for systematic uncertainties. The signal histogram which gives the NN PDF is taken from resonant signal MC.

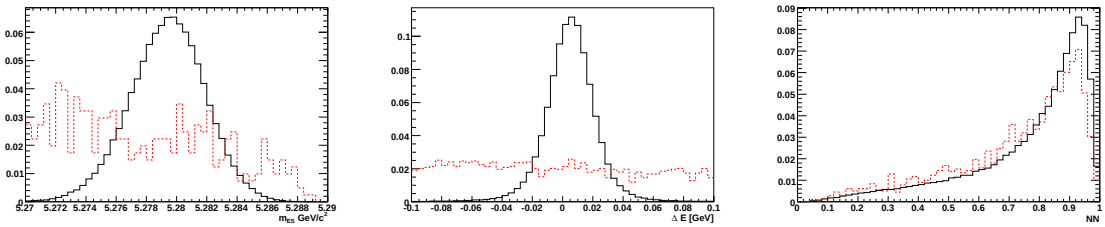

Figure 9.1: Discriminating variables in resonant signal MC SP-10045: $\mathrm{m_{ES}}$ (left), $\Delta\mathrm{E}$ (middle) and NN (right). The red dashed histograms correspond to wrongly reconstructed signal events (SCF). As these correspond to less than 1% of the signal, all distributions have been normalized separately for better visibility.

Selection	relative	absolute	events
			1747000
reconstruction	-	0.135	236324
L0	0.991	0.134	234144
L2	1.000	0.134	234141
$\Delta\mathrm{t}$ & $\sigma(\Delta\mathrm{t})$	0.917	0.123	214775
$\mathrm{E_{tot}}$	0.998	0.123	214306
$\mathrm{m_{ES}(sanity)}$	0.981	0.120	210281
$\mathrm{P}(\chi^2(\mathrm{B}))$	0.860	0.103	180808
$\chi 2(\mathrm{K_s^0})$	0.965	0.100	174509
$\mathrm{r_{dec}}$	0.832	0.083	145218
$\mathrm{m_{K_s^0}}$	0.931	0.077	135245
α	0.945	0.073	127758
$\Delta\mathrm{E}$	0.976	0.071	124720
Cat $\mathrm{K_s^0}$	0.993	0.071	123909
$\mathrm{m_{ES}(signal\ region)}$	0.985	0.070	122053
Efficiency		0.070	
after $\mathrm{K_s^0}$ correction		$0.069\pm0.000(2)\pm0.001$	

Table 9.1: Efficiencies as estimated from resonant MC SP-10045. The last number has been obtained by correcting for data-MC differences in inclusive $\mathrm{K_s^0}$ decays (see Sec. 9.7). The first error is the statistical uncertainty, the second error is associated with the correction.

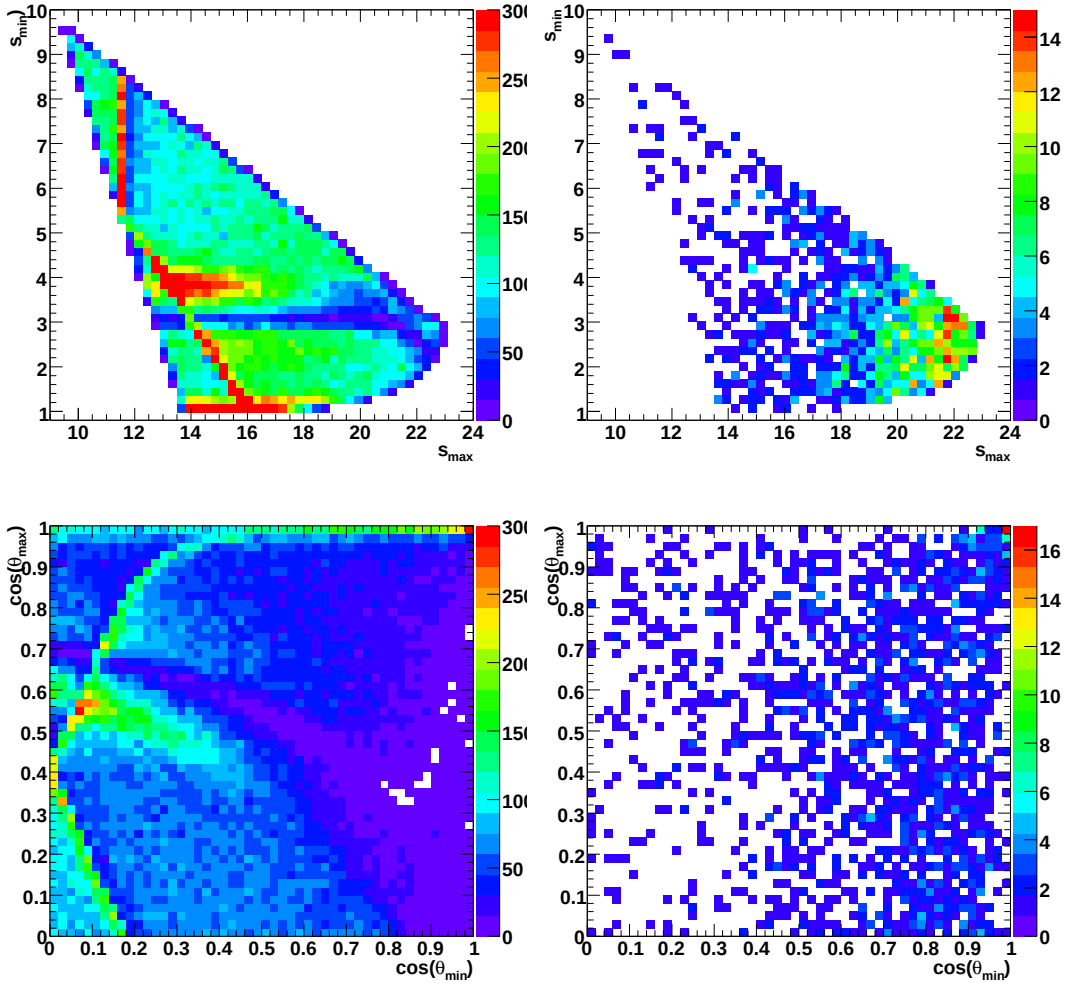

Figure 9.2: Correctly reconstructed (left) and wrongly reconstructed events (SCF - right) in signal MC as a function of the DP and SDP positions. SCF events are concentrated in the corner of the DP, where one of the K^0_s has low momentum.

9.2.3 Background from B decays

We study B-background using generic $\mathrm{B^0\bar{B}^0}$ decays (SP-1237) and generic $\mathrm{B^+B^-}$ decays (SP-1235). The luminosity of the generic samples corresponds approximately to three times the luminosity of the data sample. The number of reconstructed signal events in the neutral generic sample (SP-1237) is 558, which provides the estimation of 186 expected signal events in data. In the same way, the number of expected background events from charmless decays in data is estimated to be 5.1. This number is a combination of the expectation values of 3.4 and 1.7 events, obtained separately from the neutral and charged generic samples, respectively. The distributions of the discriminating variables of these background events compared to signal Monte Carlo and continuum background can be found in Fig. 9.3. Given the small number of expected events and the fact that the distributions suggest that the discriminating variables are not signal-like, we neglect the B-background and assign a systematic uncertainty for it. We also find decays involving charm quarks in the generic samples. For instance, we reconstruct 9 $\mathrm{K^0_s}\chi_{c0}(\rightarrow \mathrm{K^0_s K^0_s})$ decays. As this is a narrow resonance of a non-negligible width, we include it in the signal model. In the TD analysis we use a veto on the invariant mass to suppress this background. We do not consider separately $\mathrm{K^0_s}\chi_{c2}(\rightarrow \mathrm{K^0_s K^0_s})$ decays as we expect only 0.3 such events.

9.3 Maximum likelihood fit

We perform an unbinned extended maximum-likelihood fit to extract the inclusive $\mathrm{B^0} \rightarrow \mathrm{K^0_s K^0_s K^0_s}$ event yield and the resonant and non-resonant amplitudes. The fit uses the variables $\mathrm{m_{ES}}$, $\Delta\mathrm{E}$, the NN output, and the SDP (introduced in chapter 3, Sec. 3.3.7) to discriminate signal from background. The selected on-resonance data sample is assumed to consist of signal and continuum background. Background from B decays (Sec. 9.2.3) and mis-reconstructed signal events (Sec. 9.2) are neglected . Systematic uncertainties account for these events and are estimated using embedded toy studies. When fitting data we randomize the initial parameters of the isobar magnitudes and phases to ensure that the fit finds the global minimum.

9.3.1 Likelihood function

As introduced in chapter 7, Sec. 7.6, the likelihood function $\mathcal{P}^{\mathrm{i}}$ for the event i is the sum of the probability density functions (PDFs):

$$\mathcal{P}^{\mathrm{i}} = \sum_{\mathrm{j}} \mathrm{N_j} \mathcal{P}^{\mathrm{i}}_{\mathrm{j}}(\mathrm{m_{ES}}, \Delta\mathrm{E}, \mathrm{NN}, \mathrm{h_{min}}, \mathrm{h_{max}}) \; , \tag{9.1}$$

where j stands for the species (signal, continuum background) and $\mathrm{N_j}$ is the corresponding yield. The helicities h_{min} and h_{max} have been introduced in chapter 3, Sec. 3.3.7. Each PDF $\mathcal{P}^{\mathrm{i}}_{\mathrm{j}}$ is the product of the four individual PDFs:

$$\mathcal{P}^{\mathrm{i}}_{\mathrm{j}}(\mathrm{m_{ES}}, \Delta\mathrm{E}, \mathrm{NN}, \mathrm{h_{min}}, \mathrm{h_{max}}) = \mathcal{P}^{\mathrm{i}}_{\mathrm{j}}(\mathrm{m_{ES}}) \cdot \mathcal{P}^{\mathrm{i}}_{\mathrm{j}}(\Delta\mathrm{E}) \cdot \mathcal{P}^{\mathrm{i}}_{\mathrm{j}}(\mathrm{NN}) \cdot \mathcal{P}^{\mathrm{i}}_{\mathrm{j}}(\mathrm{h_{min}}, \mathrm{h_{max}}) \; . \tag{9.2}$$

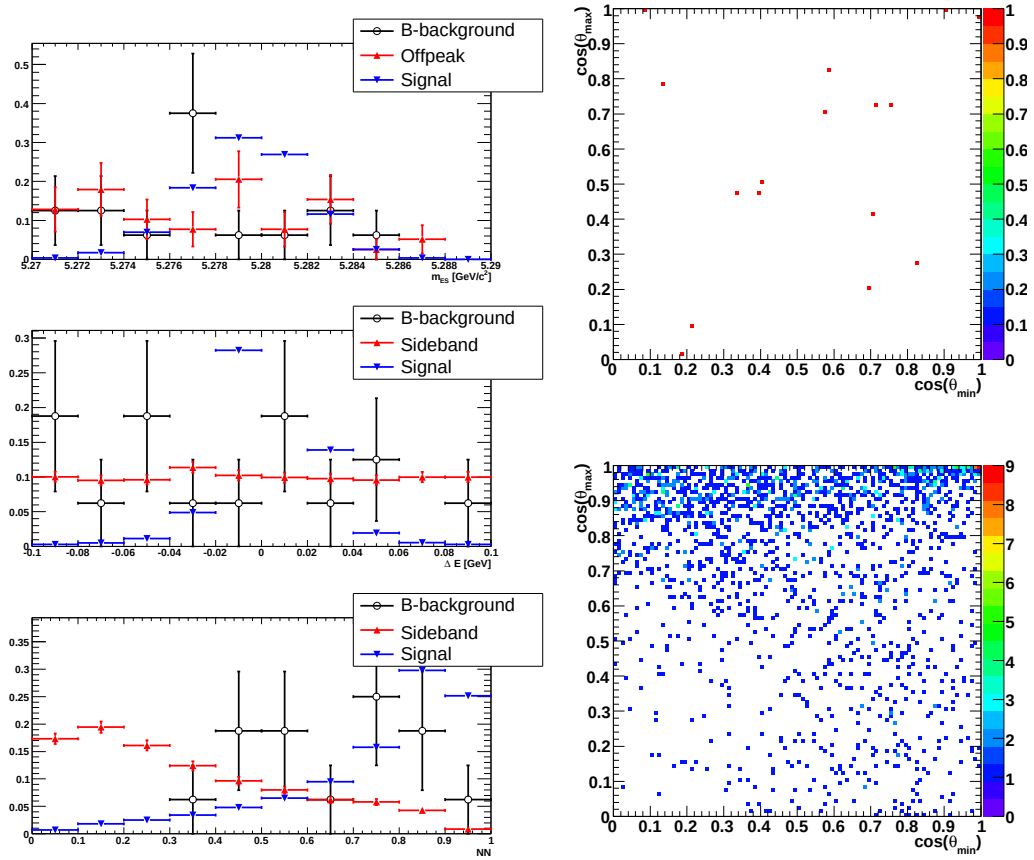

Figure 9.3: On the left are shown the discriminating variables for B-background, continuum and signal: m_{ES} (top), ΔE (middle), NN (bottom). On the right are shown SDP distributions for B-background (top) and continuum (bottom).

The total likelihood is given by

$$\mathcal{L} = \exp(-\sum_{\mathrm{j}} \mathrm{N_j}) \prod_{\mathrm{i}} \mathcal{P}^{\mathrm{i}} \, . \tag{9.3}$$

The parameterizations for the discriminating variables $\mathrm{m_{ES}}$, $\Delta\mathrm{E}$ and NN are same as in the TD analysis except that $\mathrm{m_{ES}}$ and $\Delta\mathrm{E}$ are not separated into physics categories and the NN non-parametric PDFs are not separated in tagging categories:

- $\mathrm{m_{ES}}$:
  - **Signal:** Cruijff function.
  - **Continuum:** ARGUS function.
- $\Delta\mathrm{E}$:
  - **Signal:** Cruijff function.
  - **Continuum:** straight line.
- NN:
  - **Signal:** smoothed non-parametric PDF.
  - **Continuum:** special exponent function.

We take the signal PDFs of the discriminating variables from resonant signal MC. The continuum PDF parameters are found in a fit to sideband data. The continuum background parameters are fixed in the nominal fit and varied for systematics. The means and the widths of $\mathrm{m_{ES}}$ and $\Delta\mathrm{E}$ in the signal PDF are allowed to vary in the nominal fit.
The SDP signal PDFs require as input the DP-dependent selection efficiency, $\varepsilon = \varepsilon(\mathrm{h_{min}}, \mathrm{h_{max}})$ that is described by a histogram and is taken from MC simulation (see Fig.9.4) and has been smoothed using `Roo2DKeysPDF`. The smoothing parameter has been optimized by varying it and fitting fully reconstructed MC. Biases are taken into account in the fit bias systematic uncertainty that is evaluated using embedded toy studies (see Sec. 9.5) and in the efficiency systematic (see Sec. 9.7.4).
For an event i we define the SDP signal PDF as:

$$\mathrm{P_{sig,i}}(\mathrm{h_{min}}, \mathrm{h_{max}}) \propto \varepsilon(\mathrm{h_{min}}, \mathrm{h_{max}}) \cdot |\mathcal{A}(\mathrm{h_{min}}, \mathrm{h_{max}})|^2 \ , \tag{9.4}$$

where $|\mathcal{A}(\mathrm{h_{min}}, \mathrm{h_{max}})|^2$ corresponds to the symmetrized Eq. 3.17. The normalization of the PDF is taken care of by a numerical integration that is performed in the SDP using a grid of 450×450; it has been checked using fits to MC and toy studies that a higher precision was not necessary. We describe the experimental resolution in the SDP variables by convoluting the SDP signal PDFs with a resolution function taken from MC simulation:

$$\mathrm{PDF}(\bar{\mathrm{m}}_{1\mathrm{R}}, \bar{\mathrm{m}}_{2\mathrm{R}}) \sim \int\int \mathrm{F_j F_j^*}(\bar{\mathrm{m}}_{1\mathrm{I}}, \bar{\mathrm{m}}_{2\mathrm{I}}) \mathrm{R}(\bar{\mathrm{m}}_{1\mathrm{R}}, \bar{\mathrm{m}}_{2\mathrm{R}}, \bar{\mathrm{m}}_{1\mathrm{I}}, \bar{\mathrm{m}}_{2\mathrm{I}}) \mathrm{d}\bar{\mathrm{m}}_{1\mathrm{I}} \mathrm{d}\bar{\mathrm{m}}_{2\mathrm{I}} \tag{9.5}$$

where $\bar{m}_{1R} = cos(\theta_{min})|_{Reco}$ and $\bar{m}_{2R} = cos(\theta_{max})|_{Reco}$ are the reconstructed SDP positions and $\bar{m}_{1I}$ and $\bar{m}_{2I}$ are the corresponding integration variables. $R(\bar{m}_{1R}, \bar{m}_{2R}, \bar{m}_{1I}, \bar{m}_{2I})$

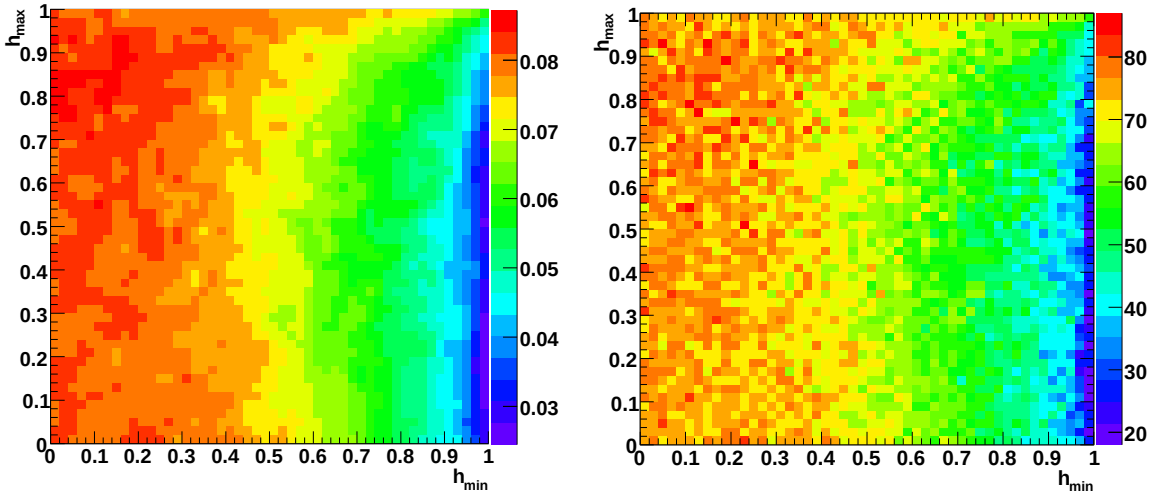

Figure 9.4: Reconstruction efficiency as a function of the SDP position taken from non-resonant and resonant MC simulation. The raw efficiency distribution on a grid of 50×50 is shown on the left hand side. The two-dimensional efficiency map histogram used in the fit is shown on the right hand side and has been smoothed using `Roo2DKeysPDF`.

is the 2-dimensional resolution function that describes the 2-dimensional displacement between true and reconstructed SDP position due to reconstruction and is given by a series of histogram, as described below. The integration limits are chosen to be a 5 RMS interval of the true minus the reconstructed SDP position distribution. As the resolution varies over the SDP, we define a 20×20-matrix of different resolution functions, each of which is a 2-dimensional histogram with 13×13 bins. The bin sizes have been optimized using fits to MC to reproduce the generated value of the isobar parameters, taking into account the limited MC statistics to create the histograms (to avoid empty bins). Figure 9.5 shows the effect of resolution in the invariant mass region where the χ_{c0} is expected, by comparing the true and the reconstructed invariant mass in fully reconstructed MC with the same distributions obtained from toy MC. This region is the most sensitive to resolution effects due to the narrowness of the χ_{c0} state. Note that this state is the main reason for the implementation of the resolution function. The convolution of Eq. 9.5 is done event by event once per fit and cached. Details on the effectiveness of the resolution can also be found in fits to fully reconstructed MC (Sec. 9.5.1). The DP continuum PDF is a two-dimensional non-parametric PDF that is taken from sideband data and is smoothed using `Roo2DKeysPDF`; the smoothing parameter is being varied for systematic uncertainties. Studies using generic MC have shown that the contribution of background from B decays is negligible in the sideband. The continuum background distributions in the regular DP and the SDP are shown in Fig. 9.6.

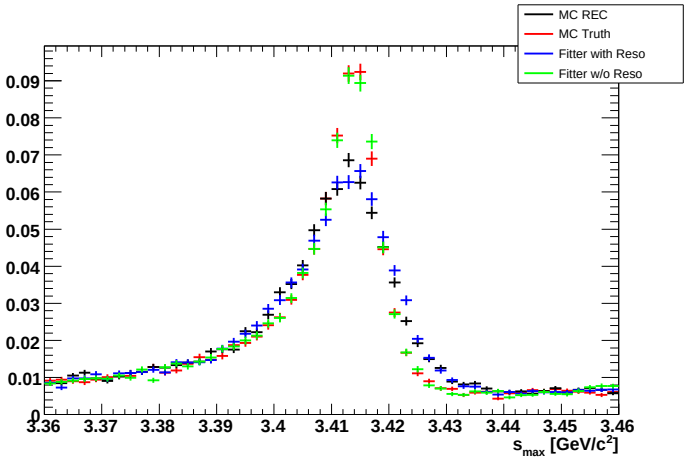

Figure 9.5: The invariant mass region of the χ_{c0} resonance. The comparison between fully reconstructed MC and the corresponding "true" invariant mass with toy MC convoluted with the resolution function and non-convoluted toy MC, shows good agreement between the analysis tool and the MC.

9.4 Determination of the signal model

As we do not know what the resonant contributions to the signal are, we first use an ad-hoc "baseline" model, which includes resonances of even spin that have been found in other 3-body charmless B decays with two Kaons in the final state. We then search for possible additional contributions to the decay by the means of likelihood scans and add them one by one to obtain our nominal model and re-validate the analysis tool (see Sec. 9.5.2) for the nominal model. After each step of this process we validate the tool, as described in Sec. 9.5.1

9.4.1 The "baseline" model

The "baseline" model includes all the even-spin resonances found in Ref. [21], i.e. $\mathrm{f}_0(980)\mathrm{K}^0_\mathrm{s}$, $\mathrm{f}_\mathrm{X}(1500)\mathrm{K}^0_\mathrm{s}$, a non-resonant component and the charmonium background $\chi_{c0}\mathrm{K}^0_\mathrm{s}$. We include the χ_{c0} in the signal model as it is narrow and well measured. This is preferred to applying a veto on the invariant mass that would reduce the reconstruction efficiency and add a systematic uncertainty. Additionally, as this resonance is well measured, our fit can provide a cross-check for the product branching fraction measurements.

9.4.2 Likelihood scans

We investigate possible resonant scalar and tensor contributions by the means of two- dimensional likelihood scans. In a first step, as it is not clear if the $\mathrm{f}_\mathrm{X}(1500)$, seen in other *BABAR* analyses, contributes to $\mathrm{B}^0 \to \mathrm{K}^0_\mathrm{s}\mathrm{K}^0_\mathrm{s}\mathrm{K}^0_\mathrm{s}$, we remove it from the baseline model and include an additional generic scalar resonance instead, using the relativistic Breit-Wigner line-shape. We fix the mean and the width of the additional resonance and fit data. We then change

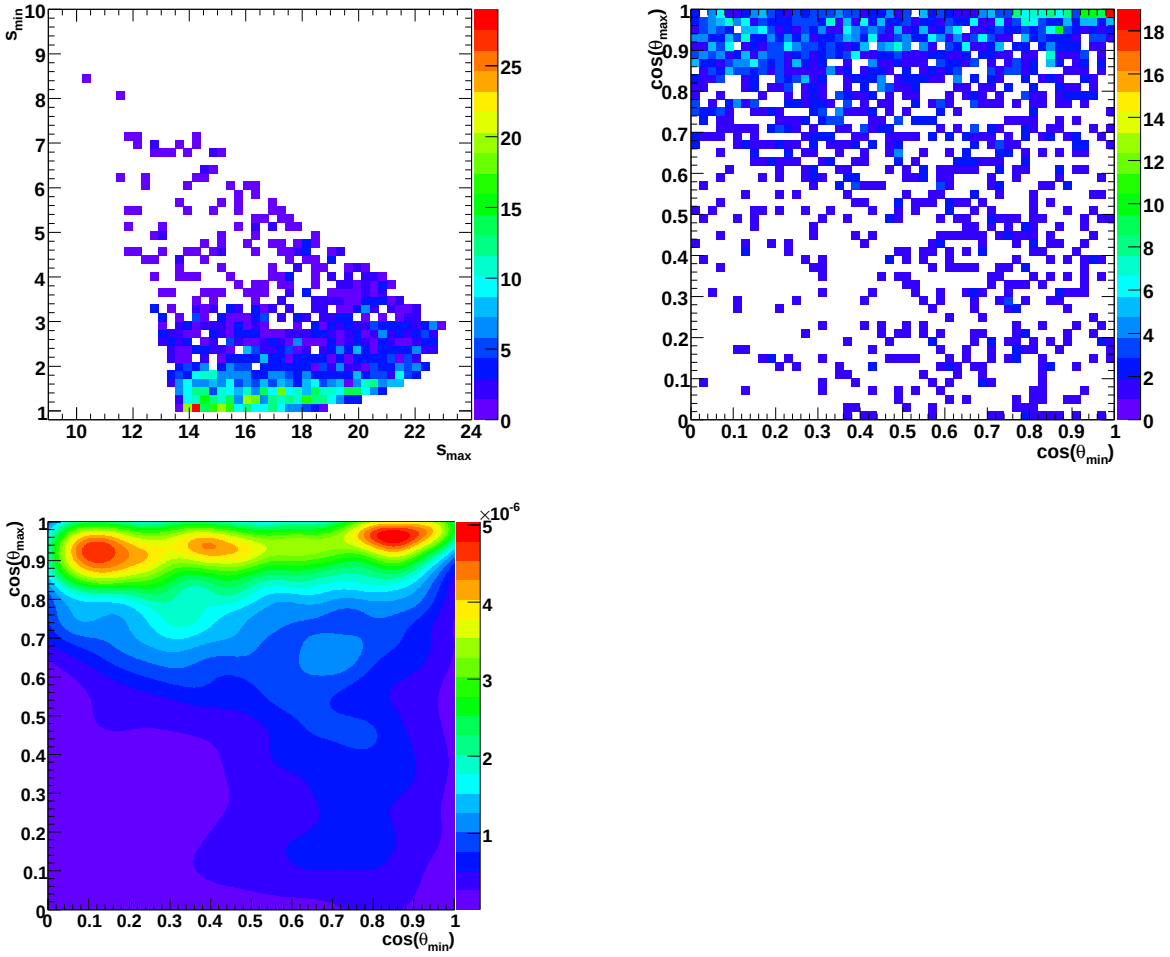

Figure 9.6: DP PDF for continuum obtained from side-band data: regular DP (top left), SDP (top right) and smoothed SDP (bottom left).

the values of the mean and the width and repeat the process. This way we cover the whole range of possible additional scalar resonances in terms of means and widths. All the isobar parameters are free to vary in these fits and for each mean/width point we perform several fits where we vary the initial parameters to ensure that we reach the global minimum. We choose the fits with the highest likelihood for a given point and create a two-dimensional plot of $-2\Delta\log\mathcal{L}$ as a function of the mean and the width. The result is shown in Fig. 9.7. We check for structures that are compatible with known resonances from Ref. [1]. We do not observe any significant increase in the likelihood at the mean and width corresponding to the $\mathrm{f_X}(1500)$ resonance (compare to Tab. 3.1), but find a contribution of the $\mathrm{f_0}(1710)\mathrm{K_s^0}$ and add it to the model. We then repeat the scan procedure for an additional tensor resonance; this time the model includes $\mathrm{f_0}(980)\mathrm{K_s^0}$, $f_0(1710)K_s^0$, non-resonant, $\chi_{\mathrm{c0}}\mathrm{K_s^0}$ and a generic additional tensor resonance. The result in shown in Fig. 9.7. We find a contribution from $\mathrm{f_2}(2010)\mathrm{K_s^0}$. At this stage we establish our nominal DP signal model, which is summarized in Tab. 9.2. To make sure that we did not miss any statistically significant contribution, we

Table 9.2: Parameters of the nominal DP signal model used in the fit. Values are given in $\mathrm{MeV}(/c^2)$, unless mentioned otherwise. The r parameter of the $f_2(2010)$, which has not been measured, is varied by $\pm$ 0.5 GeV^{-1} for the model uncertainty.

Resonance	Parameters	Line shape	Ref. for Parameters
$\mathrm{f_0}(980)$	$\mathrm{m_0} = 965 \pm 10$ $\mathrm{g_\pi} = 165 \pm 18$ $\mathrm{g_K} = 695 \pm 93$	Flatté	[36]
$f_0(1710)$	$\mathrm{m_0} = 1724 \pm 7$ $\Gamma_0 = 137 \pm 8$	RBW	[1]
$f_2(2010)$	$\mathrm{m_0} = 2011^{+60}_{-80}$ $\Gamma_0 = 202 \pm 60$ $\mathrm{r} = 1.5\ \mathrm{GeV}^{-1}$	RBW	[1]
NR decays	$\alpha = -0.14 \pm 0.02\ \mathrm{GeV}^{-2}\mathrm{c}^4$	exponential NR	[24]
χ_{c0}	$\mathrm{m_0} = 3414.75 \pm 0.31$ $\Gamma_0 = 10.2 \pm 0.7$	RBW	[1]

repeat the likelihood scans for additional scalar or tensor resonances on top of the nominal model. The result is shown in Fig. 9.8. We see a broad and not well defined structure in the scan for an additional scalar resonance at low mass, which we cannot match with any known resonance from Ref. [1]. The scan for an additional tensor resonance is basically flat, with the exception of an increase in the likelihood around a mass of 2 $\mathrm{GeV/c^2}$ and small width, this is a manifestation of the fact that our data prefers a narrower width for the $\mathrm{f_2}(2010)$ resonances than the value from Ref. [1].

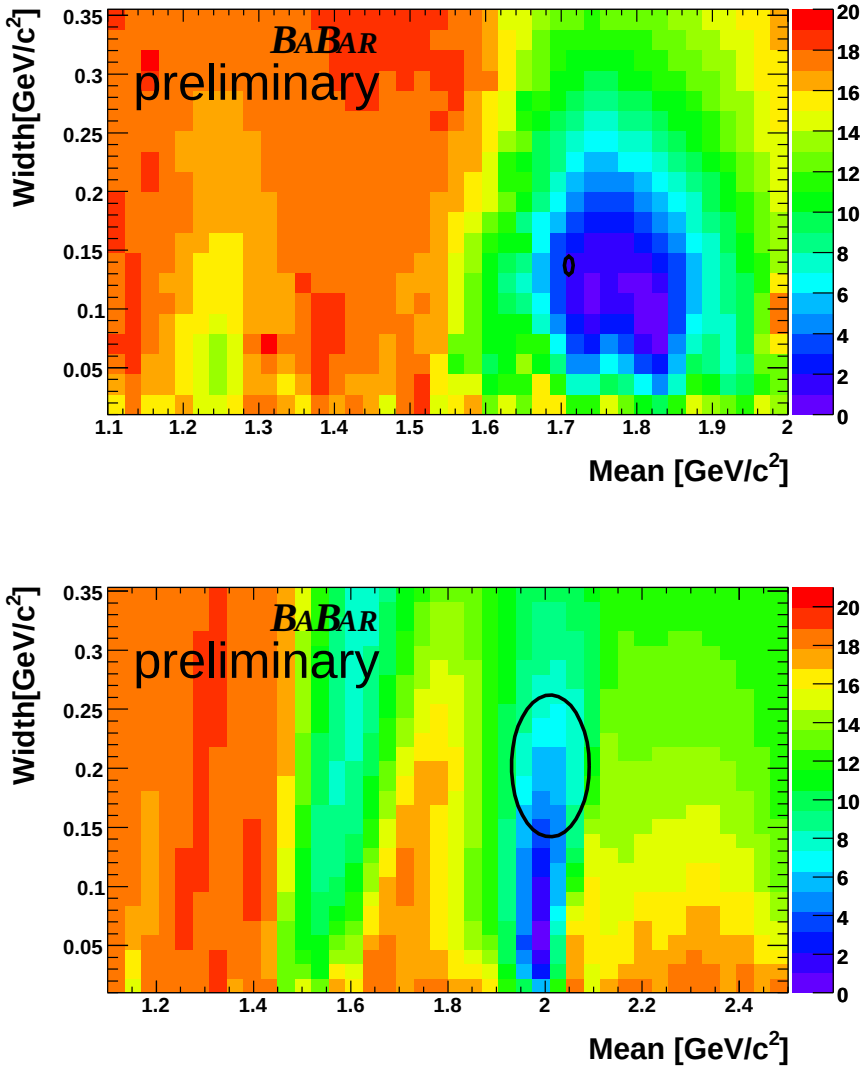

Figure 9.7: Likelihood scans for an additional scalar resonance (top) and additional tensor resonance (bottom). Regions of high likelihood correspond to low values of $-2\Delta\log\mathcal{L}$ (the point with the highest likelihood corresponds to $-2\Delta\log\mathcal{L} = 0$). The ellipses show the measured values and uncertainties of the $\mathrm{f}_0(1710)$ and the $\mathrm{f}_2(2010)$ from Ref. [1].

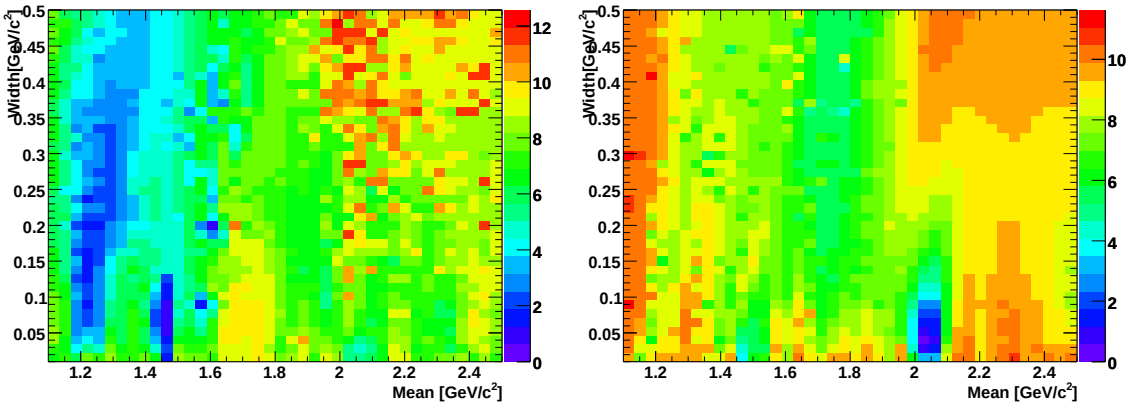

Figure 9.8: Likelihood scans for an additional scalar resonance (left) and additional tensor resonance (right) on top of the nominal model.

9.4.3 Variation of the likelihood as function of single events

Given the small number of events in our dataset, we check if there is some kind of exotic event that contributes significantly more to the likelihood than an average event. To this end, we remove each one of the 505 events at a time from our data sample, fit these reduced data samples using the nominal model, and check how the Nll varies. The result is shown in Fig. 9.9. We see that there are no exotic events, nevertheless we extract some information from this exercise. The average event contributes 13 units of Nll and the fluctuation of this contribution is of the order of 2 units of Nll; this means that an improvement of the Nll by two to three units can be caused by a single (un-)fortunate event.

9.4.4 Add/remove

We start from the nominal model including $\mathrm{f_0(980)K^0_s}$, $\mathrm{f_0(1710)K^0_s}$, $\mathrm{f_2(2010)K^0_s}$, non-resonant and $\mathrm{\chi_{c0}K^0_s}$. We then add one by one all known resonances that might contribute to the resonant structure and check if the likelihood increases. For each added resonance, we perform 500 fits where we vary the initial isobar parameters and use the fit with the highest likelihood that has properly converged. We also estimate the fit fraction of the additional resonance. The result is shown in Tab. 9.3. We know from the fits where we remove single events, that the statistical fluctuation of the Nll is approximately 2 units. Only 3 additional resonances exceed this variation: $\mathrm{a_0(1450)}$, $\mathrm{f_0(1500)}$ and $\mathrm{\chi_{c2}(2P)}$. As the fit fraction of $\mathrm{\chi_{c2}(2P)}$ is compatible with zero we do not consider it any further. For $\mathrm{a_0(1450)}$ and $\mathrm{f_0(1500)}$ on the other hand, the associated fit fractions are considerable. In addition to this, the observed improvement of the likelihood induced by adding a resonance was expected and could be estimated from the likelihood scan of Fig. 9.7, which shows no clear structure for any resonance. As neither of these resonances has been seen in the *BABAR* analyses $B^{\pm} \to K^{\pm}K^{+}K^{-}$ and $B^0 \to K^+K^-K^0_s$ that have much higher statistics, we suppose that any improvement in the Nll by adding these resonances is due to statistical fluctuation.

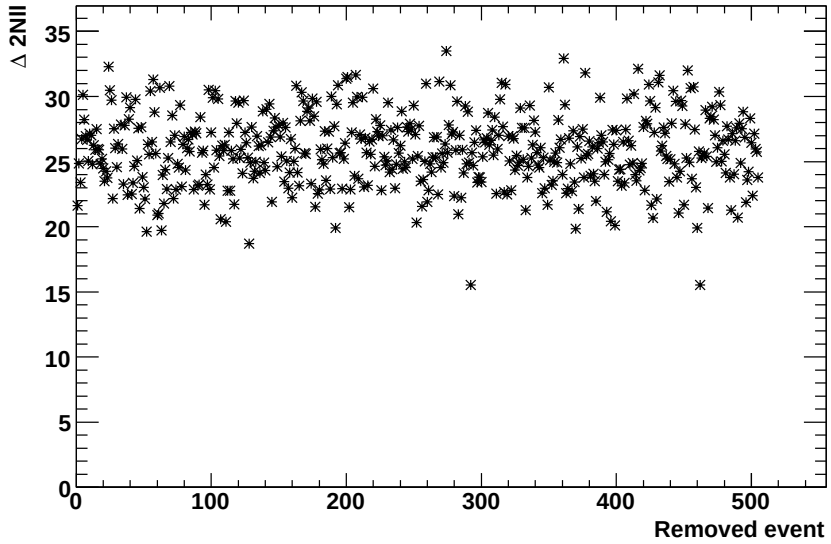

Figure 9.9: Δ2Nll obtained from fits where one event has been removed. The x coordinate corresponds to the number of the removed event. The origin of the y axis corresponds to the nominal likelihood value.

Configuration	Δ2Nll	Fit fraction
$f_2(2010)$,$f_0(980)$,$f_0(1710)$, NR, $\chi_{c0} \equiv$ Nominal	0	-
Nominal + $f_2(1270)$	-4.12	0.039 - 0.023 + 0.035
Nominal + $a_2(1320)$	-2.36	0.041 - 0.018 + 0.026
Nominal + $a_0(1450)$	-6.26	0.823 - 0.249 + 0.187
Nominal + $f_0(1500)$	-6.30	0.407 - 0.071 + 0.087
Nominal + $f_2^{'}(1525)$	-4.56	0.023 - 0.014 + 0.024
Nominal + $f_2(1950)$	-3.18	0.063 - 0.049 + 0.092
Nominal + $f_2(2300)$	-0.64	0.003 - 0.004 + 0.017
Nominal + $f_2(2340)$	-0.78	0.006 - 0.007 + 0.029
Nominal + $\chi_{c2}(1P)$	-0.76	0.002 - 0.003 + 0.012
Nominal + $\chi_{c2}(2P)$	-6.28	0.019 - 0.012 + 0.021
Nominal - $f_0(1710)$ + $f_0(1500)$	+5.66	-
Nominal - $f_2(2010)$	+13.66	

Table 9.3: Add/remove tests for all possible resonant contributions from Ref. [1]. The second and third columns correspond to the change in Δ2Nll with respect to the nominal configuration and to the fit fraction of the additional resonance respectively.

ad-hoc configuration		generator level		reconstr. level w/o resolution		reconstr. level w/ resolution	
Parameter	Generated value	Fitted value	Bias [σ]	Fitted value	Bias [σ]	Fitted value	Bias [σ]
A f0(980)	0,8	0.802 ± 0.016	0.12	0.767 ± 0.017	-1.94	0.775 ± 0.018	-1.38
Φ f0(980)	4,0	4.037 ± 0.045	0.82	4.044 ± 0.052	0.84	4.080 ± 0.055	1.45
A fX(1500)	0,4	0.398 ± 0.007	-0.28	0.383 ± 0.008	-2.12	0.387 ± 0.009	-1.44
Φ fX(1500)	2,0	2.020 ± 0.019	1.05	2.008 ± 0.022	0.36	2.029 ± 0.023	1.26
A χ_{c0}	0,15	0.149 ± 0.001	-1.00	0.138 ± 0.001	-11.9	0.145 ± 0.002	-2.50
Φ χ_{c0}	-0,5	-0.484 ± 0.016	1.00	-0.656 ± 0.017	-9.17	-0.494 ± 0.018	0.33
A NR	1.0	fixed	-	fixed	-	fixed	-
Φ NR	0.0	fixed	-	fixed	-	fixed	-

Table 9.4: High statistics fits to fully reconstructed MC sample (SP-9880), generated with the baseline model. The fit to the truth-part of reconstructed events shows that the reconstruction efficiency map which depends on the position on the square Dalitz plot, is correctly implemented. Results obtained with and without the resolution function show the necessity to implement it.

9.5 Validation tests

The validation of the analysis tool is done in two steps. In a first step, the baseline model is validated, then the nominal signal model is determined as described in Sec. 9.4, and in a second step this nominal model is validated. Here we describe the different stages of validation.

9.5.1 Validation of baseline model

This is a first measurement of the resonant structure of the decay and we do not have any information of the magnitudes and phases. For validation purposes, we use ad-hoc values (listed in the second column in Tab. 9.4), that result in sizable contributions of all included resonances. After a first validation using fully reconstructed MC, we vary the resonant content using pure toy experiments.

Fits to MC

Before fitting fully reconstructed MC, we perform pure toy studies to make sure that there is no intrinsic bias in our fitting tool[1]. We then fit a high statistics signal MC sample to verify that the generated values are reproduced. This fit is sensitive, for instance, to the DP-position-dependent reconstruction efficiency and the accuracy of the numerical integration that is used to normalize the DP PDF. The fit results on the generator ("truth") level and on the reconstructed level with and without resolution function are summarized in Tab. 9.4. These results demonstrate the necessity to include the resolution function in order to correctly describe the narrow χ_{c0} state.

[1] We use the baseline model and actually observe small biases that disappear when we increase the signal yields. We go into detail on this issue for the validation of the nominal model.

Linearity tests using pure toy studies

We use pure toy studies to check the linearity of the isobar magnitudes and phases. For this purpose, we generate several toy MC samples where we vary a single magnitude or phase and fit them. We then check if the generated values have been correctly fitted by comparing them to the fit results. The comparison plot is given is shown in Fig. 9.10, showing rather small biases. In the isobar model, the interference between different resonant contributions can engender geometrical ambiguities that lead to degenerate solutions due to a particular phase-configuration. Also, we have seen in pure toys with an ad-hoc magnitude and phase configuration that there are biases in these variables, that disappear at higher statistics. This bias can depend on the toy configuration. To study these problems, we scan the phases of interest ($\mathrm{f}_0(980)$,$\mathrm{f}_\mathrm{X}(1500)$), while keeping the magnitude and the phase of the χ_{c0} at the ad-hoc pure toy value. The magnitude and phase of the NR are fixed by convention.
We vary the phases in 20 steps from 0 to 360 degrees, which gives 400 scan points with a step width of 18 degrees (the order of magnitude that we expect for the error on the phases). For each point we do 100 toy experiments. We then take the mean of the fitted distribution, subtract the generated value and divide the result by the error on the mean. The result is shown in Fig. 9.11. We expect a flat distribution around zero, but observe biases up to 40% of the statistical error that depend on the values of the magnitudes and phases. We correct for these biases using embedded toys done with fully reconstructed MC that has been generated using the fit result on data.

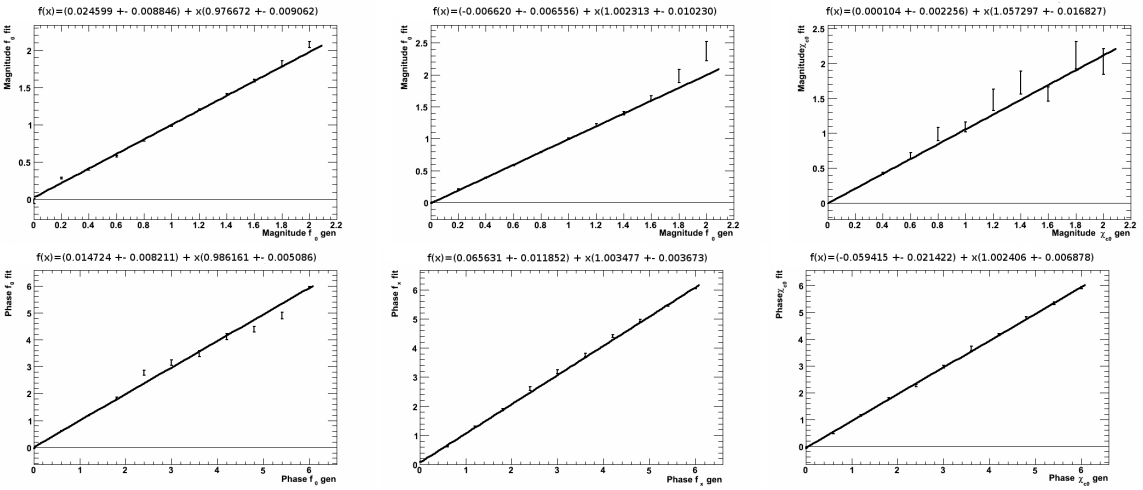

Figure 9.10: Scans of the magnitudes and phases of the baseline model that show a satisfactory linear behavior between generated and fitted values. In an ideal scenario, we would expect the slope to be one and the line to go through the origin. For each point we perform 100 toy experiments. The x-axis corresponds to the generated value and the y-axis is the average of the fitted values. The errorbars indicate the error on the average. The fit using a straight line, shown on each plot, is compatible with the expectation

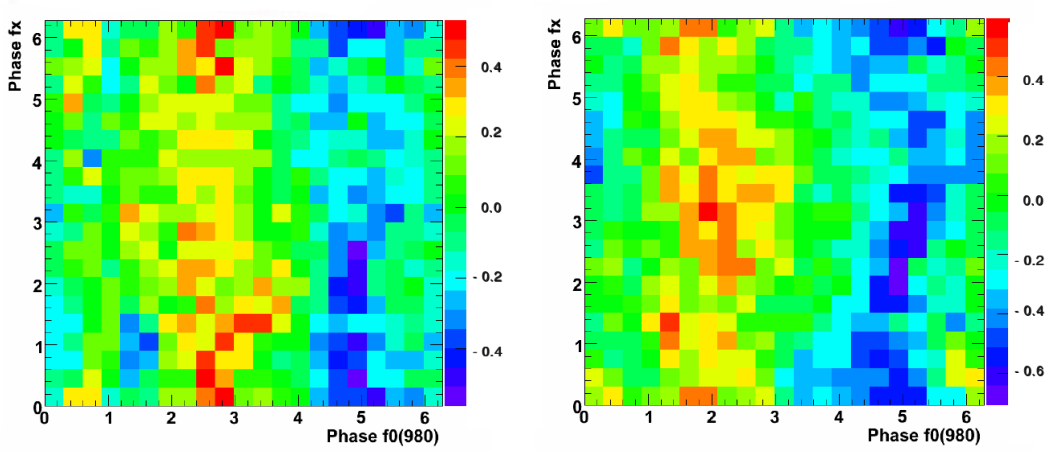

Figure 9.11: Two-dimensional scans of the phases of the $f_0(980)$ and $f_X(1500)$ resonances. For each scan point we generate 100 toy experiments and fit them. The plotted value is the difference between the average of the fitted value and the generated one, divided by the error on the average of the fitted value. This way we get an estimate of the bias in units of the error. The plot on the left (right) shows the bias of the fitted phase of the $f_0(980)$ ($f_X(1500)$).

Validation using embedded toys

Before the first fit to data we use embedded toy studies to validate the model in realistic circumstances. We find that some of the isobar parameters exhibit a small bias. Pure toy studies with the same configuration show a similar bias that disappears when we increase the yields. We conclude that the biases are mainly due to the limited statistics. For shortness, we do not show embedded toys for the baseline model as we redo embedded toys to validate the nominal model (see Sec. 9.5.2). With embedded toys we conclude the validation of the fitter for the baseline model, and proceed to fit the data.

9.5.2 Validation of the nominal model

We fit data using the nominal model before the final validation (without looking at the fit fractions), as we use the values of the isobar parameters found in this fit to generate fully reconstructed MC simulation that we then use for embedded toy studies. This is necessary as we observe biases that range up to 30% of the statistical error on the isobar parameters, and these biases depend on the configuration of the model[2]. We then correct the final result by shifting the isobar magnitudes and phases according to the biases observed in the embedded toy studies, and assign a systematic error for the uncertainty on the shift. We perform pure and embedded toy studies for the nominal model using the isobar- and yield-configuration found in the fit to data. We find that pure and embedded toys yield comparable biases (see.

[2]This is clear from comparison between the results below and the ones from Sec. 9.5.1

Tab. 9.5). The corresponding pull distribution can be found in the appendix (Fig. C.1 for embedded toys and Fig. C.2 for pure toys). Overall, the observed biases are acceptably small

Parameter	Embedded	Pure	Pure $\times$ 100
$\mathrm{N_{signal}}$	-0.024 ± 0.041	-0.042 ± 0.041	0.020 ± 0.042
$\mathrm{N_{cont}}$	0.068 ± 0.040	0.016 ± 0.041	-0.031 ± 0.041
$\phi\ \mathrm{f_0}(980)$	0.242 ± 0.039	0.133 ± 0.038	0.014 ± 0.043
A $\mathrm{f_0}(980)$	0.152 ± 0.039	0.059 ± 0.039	0.112 ± 0.041
$\phi\ \mathrm{f_0}(1710)$	0.068 ± 0.042	0.126 ± 0.041	-0.060 ± 0.040
A $\mathrm{f_0}(1710)$	0.050 ± 0.040	-0.142 ± 0.041	-0.038 ± 0.041
$\phi\ \chi_{\mathrm{c0}}$	-0.029 ± 0.049	-0.068 ± 0.047	-0.352 ± 0.044
A χ_{c0}	-0.014 ± 0.040	0.092 ± 0.039	0.494 ± 0.043
$\phi\ \mathrm{f_2}(2010)$	-0.316 ± 0.039	-0.181 ± 0.039	-0.098 ± 0.042
A $\mathrm{f_2}(2010)$	-0.210 ± 0.039	-0.247 ± 0.043	-0.007 ± 0.043

Table 9.5: Embedded and pure toy biases, where the pure toys in the right column are done with 100 times the event yields of the nominal configuration. The high-statistics toys show some biases, but keeping in mind that the errors are approximately 10 times smaller than for the nominal configuration, these biases are small.

and we conclude the validation of the nominal model.

9.6 Results

The maximum-likelihood fit of 505 candidates results in a $\mathrm{B^0} \to \mathrm{K^0_s K^0_s K^0_s}$ event yield of 200 ± 15 and a continuum yield of 305 ± 18, where the uncertainties are statistical only. The symmetrized and square Dalitz plots of signal DP-model MC sample generated with the result of the fit on data are shown in Fig. 9.12. When the fit is repeated starting from input parameter values randomly chosen within wide ranges around the nominal values for the magnitudes and within the $[-180^\circ,\ 180^\circ]$ interval for the phases, we observe convergence toward two solutions with minimum values of the negative log likelihood function $-2\log\mathcal{L}$, separated by 3.25 units. In Fig. 9.13 we show likelihood scans of the isobar magnitudes and phases of all the resonances, where both solutions can be noticed. As the separation in $-2\log\mathcal{L}$ corresponds to more than one standard deviation (σ), we can use the best solution to calculate the 1σ statistical error. Figure 9.14 shows ${}_s\mathcal{P}lots$ of $\Delta\mathrm{E}$, $\mathrm{m_{ES}}$, and the NN. Figure 9.15 shows projections of the invariant masses $\mathrm{s_{min}}$ and $\mathrm{s_{max}}$. In the fit, we measure directly the relative magnitudes and phases of the different components of the signal model. The magnitude and phase of the NR amplitude are fixed to 1 and 0, respectively, as a reference. The results corresponding to the best solution are given together with their statistical uncertainties in Tab. 9.6. The measured relative amplitudes $\mathrm{c_k}$, where the index represents an intermediate resonance, are used to extract the fit fraction defined in Eq. (3.51). Each fit fraction is a sum of three contributions, one for each pair of $\mathrm{K^0_s}$ that the resonance is allowed to decay to, i.e. the indexes μ and ν run from one to fifteen, as each of the five resonances has

Table 9.6: Summary of measurements of the Q2B parameters. The errors are statistical only. The statistical significance has been estimated from the variation of the likelihood when removing the resonances one by one from the fit ($\mathrm{Significance} = \sqrt{-2\Delta\log\mathcal{L}}$). All the unflavored resonant states have a statistical significance of less than 4 standard deviations.

Mode	Solution 1	Solution 2
FF $\mathrm{f_0(980)K_s^0}$	$0.44^{+0.20}_{-0.19}$	$1.03^{+0.22}_{-0.17}$
Phase [rad]$\mathrm{f_0(980)K_s^0}$	0.09 ± 0.16	1.26 ± 0.17
Significance [σ]$\mathrm{f_0(980)K_s^0}$	3.3	-
FF $\mathrm{f_0(1710)K_s^0}$	$0.07^{+0.07}_{-0.03}$	$0.09^{+0.05}_{-0.02}$
Phase [rad] $\mathrm{f_0(1710)K_s^0}$	1.11 ± 0.23	0.36 ± 0.20
Significance [σ]$\mathrm{f_0(1710)K_s^0}$	3.7	-
FF $\mathrm{f_2(2010)K_s^0}$	$0.09^{+0.03}_{-0.03}$	0.10 ± 0.02
Phase [rad] $\mathrm{f_2(2010)K_s^0}$	2.50 ± 0.20	1.58 ± 0.22
Significance [σ]$f_2(2010)K_s^0$	3.3	-
FF$\chi_{c0}\mathrm{K_s^0}$	$0.07^{+0.04}_{-0.02}$	0.07 ± 0.02
Phase [rad]$\chi_{c0}\mathrm{K_s^0}$	0.63 ± 0.47	-0.24 ± 0.52
Significance [σ]$\chi_{c0}K_s^0$	4.2	-
FF NR	$2.15^{+0.36}_{-0.37}$	$1.37^{+0.26}_{-0.21}$
Phase [rad] NR	0.0	0.0
Significance [σ]NR	8.2	-
Total FF	$2.84^{+0.42}_{-0.41}$	$2.66^{+0.35}_{-0.27}$

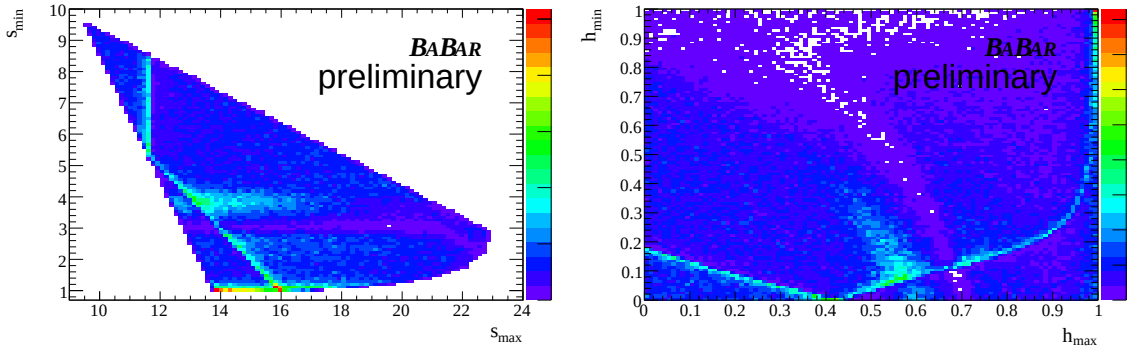

Figure 9.12: Symmetrized (left) and square (right) Dalitz plots for MC simulated data using the amplitudes obtained from the on-resonance data fit. The χ_{c0} resonance can be seen as narrow band that bounces back on the symmetry axes at $\mathrm{h_{min}} = 0$. The $f_0(980)$ is the structure at low mass on the regular DP and on the right border in the SDP. The $\mathrm{f_0}(1710)$ can be seen as destructive interference at $\mathrm{s_{min}} \sim 3(\,\mathrm{GeV/c^2})^2$ and the $\mathrm{f_2}(2010)$ as structure around $\mathrm{s_{min}} \sim 4(\,\mathrm{GeV/c^2})^2$.

contributions of three pairs of $\mathrm{K^0_s}$ in the symmetrized DP. The total fit fraction is defined as the algebraic sum of all fit fractions. This quantity is not necessarily unity due to the potential presence of net constructive or destructive interference. Using the relative fit fractions, we calculate the branching fraction $\mathcal{B}$ for the intermediate mode k as

$$\mathrm{FF(k)} \times \mathcal{B}(\mathrm{B^0} \to \mathrm{K^0_s K^0_s K^0_s}) \,, \tag{9.6}$$

where $\mathcal{B}(B^0 \to K^0_s K^0_s K^0_s)$ is the total inclusive branching fraction

$$\mathcal{B}(\mathrm{B^0} \to \mathrm{K^0_s K^0_s K^0_s}) = \frac{\mathrm{N_{sig}}}{\bar{\varepsilon}\mathrm{N_{B\bar{B}}}} \,. \tag{9.7}$$

We estimate the average efficiency ($\bar{\varepsilon}$) using fully reconstructed DP-model MC sample generated with the parameters found in data. As the fit fractions are not parameters of the PDF itself, we use toy studies to estimate their statistical errors:

- We generate a large number (16 k) of toy experiments with the yields and the isobar parameters obtained from the fit on data, where the isobar parameters are corrected by the corresponding shifts observed in embedded toys.
- For each toy we perform a fit to obtain the isobar parameters, calculate the corresponding fit fractions for all the resonances and dump them into histograms. The fitted isobar parameters are corrected for the intrinsic biases in the toy fits that are due to the limited statistics before calculating the fit fractions.
- We count bin entries in these histograms to the left and to the right of the central values, until the the sum reaches 34.1% of the correclty converged toy fits to each side. We assign the difference to the central value of the corresponding values as asymetric statistical uncertainty.

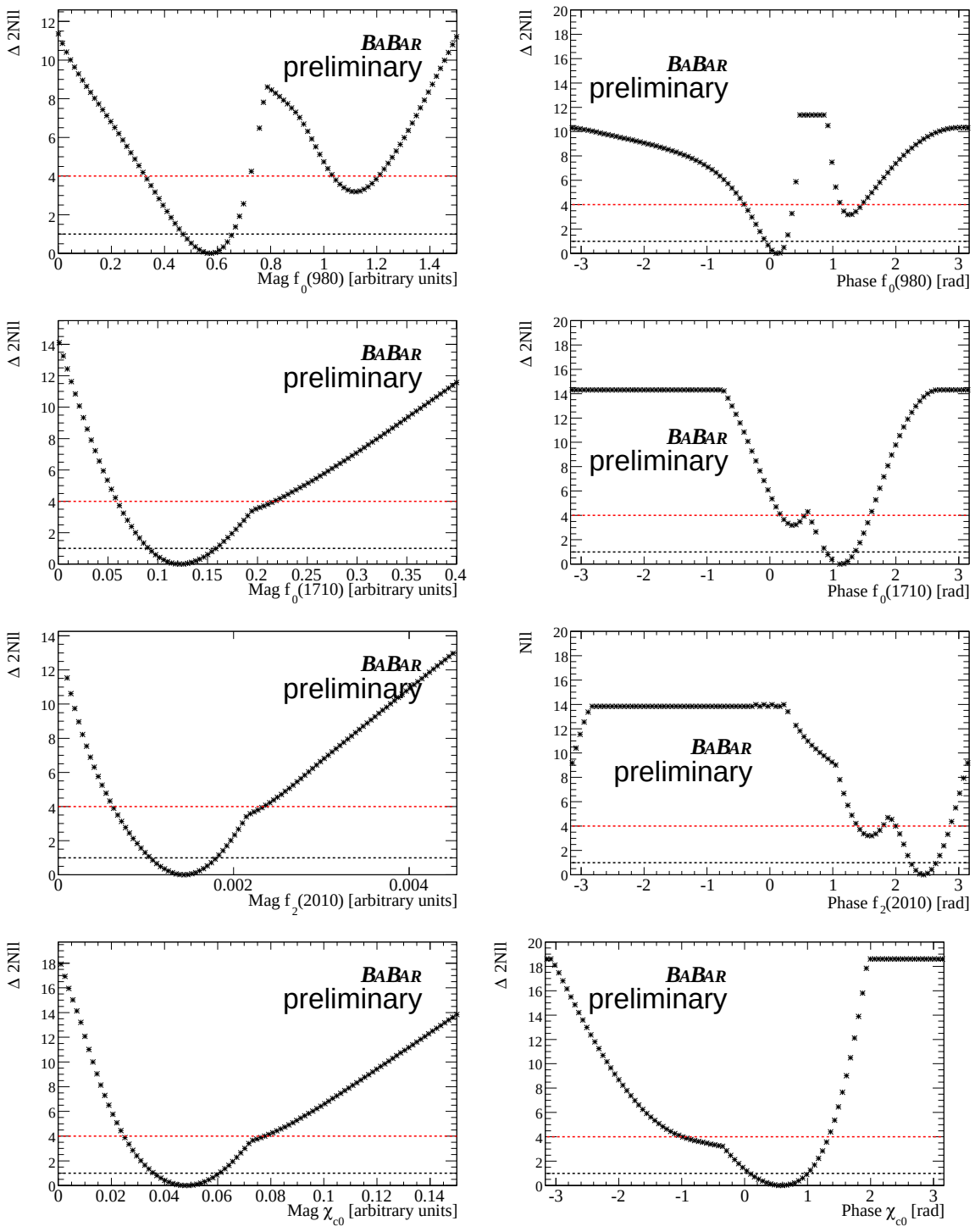

Figure 9.13: Likelihood scans of the magnitudes (left) and phases (right) for all resonances (from top to bottom: $f_0(980)$, $f_0(1710)$, $f_2(2010)$, χ_{c0}). The black (red) dashed line indicates the one (two) standard deviation level.

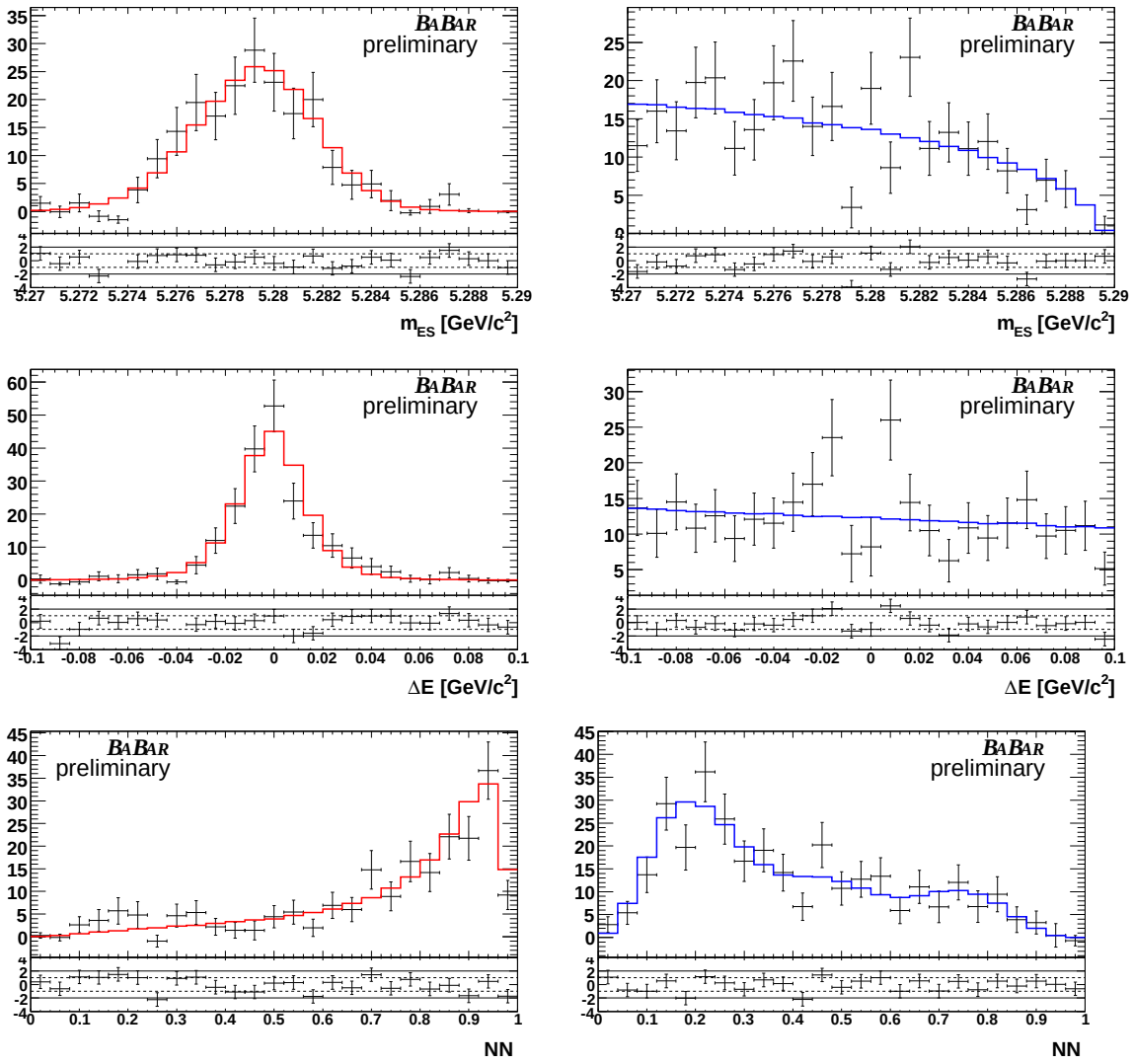

Figure 9.14: ${}_s\mathcal{P}lots$ of the discriminating variables. Top-to-bottom: $\mathrm{m_{ES}}$, ΔE, and NN for signal (left) and continuum (right). The on-resonance data is shown as points with error bars while the PDFs are solid histograms. Below each bin are shown the residuals, normalized in error units.

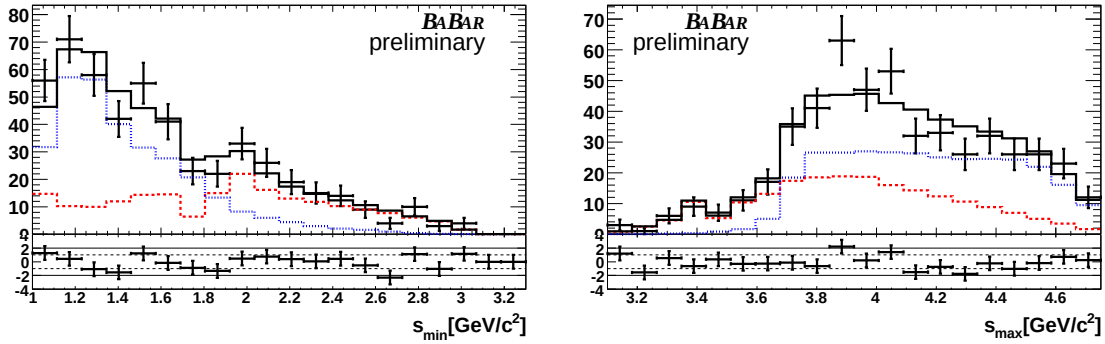

Figure 9.15: Projection plots of the s_{min} (left) and s_{max} (right). On-resonance data are shown as points with error bars while the dashed red (dotted blue) histogram represents the signal (continuum) components. The black histogram is the total PDF. Below each bin are shown the residuals, normalized in error units.

The histograms and the errors obtained by this procedure are shown in Fig. 9.16. The branching fraction measurements are shown in Tab. 9.7. As a cross check we want to compare our branching fraction measurements with results from other measurements; Unfortunately many of the branching fractions for the decay into kaons of the resonances included in our model are not or poorly measured ("seen" in Ref. [1]). An exception is the charmonium state χ_{c0} that has been measured: $\mathcal{B}(\chi_{c0} \to K^0_S K^0_S) = (3.16 \pm 0.18) \times 10^{-3}$ [1]. We can then use the *BABAR* measurement of $\mathcal{B}(B^0 \to \chi_{c0} K^0) = (142^{+55}_{-44} \pm 8 \pm 16 \pm 12) \times 10^{-6}$ [19] to calculate $\mathcal{B}(B^0 \to \chi_{c0}(\to K^0_S K^0_S) K^0_S) = \frac{1}{2} \times \mathcal{B}(B^0 \to \chi_{c0} K^0 \times \mathcal{B}(\chi_{c0} \to K^0_S K^0_S)) = (2.24 \pm 0.78) \times 10^{-7}$, which is consistent with our measurement.

9.7 Systematic uncertainties

The systematic uncertainties are summarized in Tab. 9.8 and the individual contributions are detailed in the following.

9.7.1 PDF parameters and non-parametric PDFs of discriminating variables

We vary all the fixed parameters and the non-parametric PDFs and fit data. We create distributions of the difference with respect to the nominal fit for the fit fractions, the isobar phases and the signal yield and assign the sum in quadrature of the mean and the error on the mean as a systematic uncertainty. Some of the fits converge to the second solution and we do not take them into account when estimating the systematic uncertainty.
There are two types of systematic uncertainty that we take into account in the present category, the first one is due to the limited statistics of either the MC sample or the data sample used to create the PDF, referred to as "Discr. Vars." in Tab. 9.8. The second one is due to differences between data and MC, and is evaluated for the PDFs that have been taken from

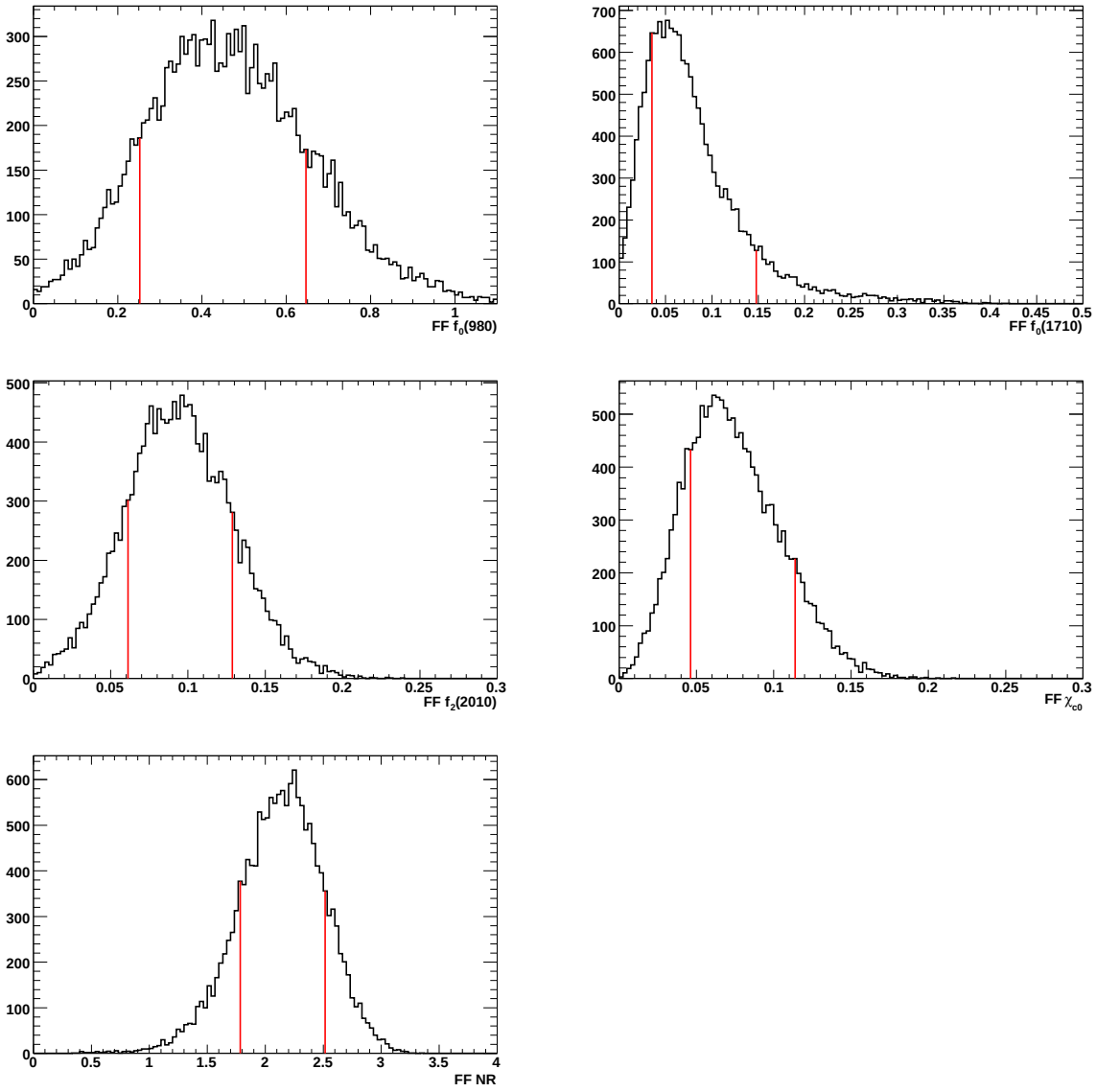

Figure 9.16: Estimation of statistical error on the fit fractions of $\mathrm{f_0}(980)$ (top left), $f_0(1710)$ (top right), $f_2(2010)$ (middle left), χ_{c0} (middle right) and Nonresonant (bottom). The vertical red lines indicate the 68.2% probability intervals, which are used for assigning the errors.

Table 9.7: Summary of measurements of branching fractions. The quoted numbers are obtained by multiplying the corresponding fit fraction from solution 1 by the measured inclusive $\mathrm{B}^0 \to \mathrm{K}^0_\mathrm{s}\mathrm{K}^0_\mathrm{s}\mathrm{K}^0_\mathrm{s}$ branching fraction. The first uncertainty is statistical, the second is systematic and the third represents the signal DP-model dependence.

Mode	$\mathcal{B}(\mathrm{B}^0 \to \mathrm{Mode})[10^{-6}]$
Inclusive $\mathcal{B}(\mathrm{B}^0 \to \mathrm{K}^0_\mathrm{s}\mathrm{K}^0_\mathrm{s}\mathrm{K}^0_\mathrm{s})$	$6.186 \pm 0.475 \pm 0.145 \pm 0.067$
$\mathrm{f}_0(980)\mathrm{K}^0_\mathrm{s}$, $\mathrm{f}_0(980) \to \mathrm{K}^0_\mathrm{s}\mathrm{K}^0_\mathrm{s}$	$2.696^{+1.250}_{-1.188} \pm 0.357 \pm 1.874$
$\mathrm{f}_0(1710)\mathrm{K}^0_\mathrm{s}$, $\mathrm{f}_0(1710) \to \mathrm{K}^0_\mathrm{s}\mathrm{K}^0_\mathrm{s}$	$0.502^{+0.461}_{-0.235} \pm 0.043 \pm 0.129$
$\mathrm{f}_2(2010)\mathrm{K}^0_\mathrm{s}$, $\mathrm{f}_2(2010) \to \mathrm{K}^0_\mathrm{s}\mathrm{K}^0_\mathrm{s}$	$0.543^{+0.214}_{-0.204} \pm 0.034 \pm 0.440$
NR, $\mathrm{K}^0_\mathrm{s}\mathrm{K}^0_\mathrm{s}\mathrm{K}^0_\mathrm{s}$	$13.315^{+2.234}_{-2.302} \pm 0.554 \pm 2.779$
$\chi_{\mathrm{c}0}\mathrm{K}^0_\mathrm{s}$, $\chi_{\mathrm{c}0} \to \mathrm{K}^0_\mathrm{s}\mathrm{K}^0_\mathrm{s}$	$0.462^{+0.252}_{-0.165} \pm 0.015 \pm 0.197$

Table 9.8: Summary of systematic uncertainties. They are dominated by the reconstruction efficiency and the variation of the line-shapes due to the contribution of the poorly measured $\mathrm{f}_2(2010)$.

Parameter	Discr. Vars.	MC-Data	B-bkg	Fit bias	K^0_s reco	$N_{B\bar{B}}$	Sum	Model
$\mathcal{B}_{\mathrm{incl}}[10^{-6}]$	0.053	0.015	0.030	0.011	0.111	0.067	0.145	0.067
FF $\mathrm{f}_0(980)$	0.006	0.001	0.056	0.013	-	-	0.058	0.303
FF $\mathrm{f}_0(1710)$	0.001	0.001	0.001	0.007	-	-	0.007	0.021
FF $\mathrm{f}_2(2010)$	0.003	0.001	0.001	0.005	-	-	0.006	0.071
FF NR	0.023	0.001	0.083	0.024	-	-	0.090	0.449
FF $\chi_{\mathrm{c}0}$	0.001	0.000	0.000	0.002	-	-	0.002	0.032
Ph $\mathrm{f}_0(980)$	0.014	0.000	0.018	0.008	-	-	0.024	0.146
Ph $\mathrm{f}_0(1710)$	0.001	0.003	0.020	0.011	-	-	0.023	0.147
Ph $\mathrm{f}_2(2010)$	0.004	0.002	0.014	0.044	-	-	0.046	0.587
Ph $\chi_{\mathrm{c}0}$	0.010	0.007	0.011	0.039	-	-	0.042	0.437

MC. It is referred to as "MC-Data" in Tab. 9.8. For the MC-data difference, we use exactly the same procedure and the same MC-data differences as in the TD analysis, and therefore we do not go into detail here but refer to Sec. 8.6. The corresponding plots of the variation of the observables are in the appendix (Fig. C.4). The following items describe how the individual PDFs have been varied for the "Discr. Vars." systematic:

- $\mathrm{m_{ES}}$ signal: we vary the parameters that we have found in a fit to resonant signal MC (SP-10045) within their uncertainties. In this process we take the correlations between the variables into account. The mean is free to vary in the fit.

- $\mathrm{m_{ES}}$ continuum: we vary the ARGUS shape parameter by taking random numbers from a Gaussian distribution whose mean corresponds the the central value and the width to the uncertainty found in a fit to sideband data. The ARGUS endpoint is taken as the highest value in the data sample and is varied in the same way as the shape parameter, we take as uncertainty $1\,\mathrm{MeV}$.

- $\Delta\mathrm{E}$ signal: same as $\mathrm{m_{ES}}$ signal.

- $\Delta\mathrm{E}$ continuum: we vary the linear coefficient in the same way as the ARGUS shape parameter in $\mathrm{m_{ES}}$ continuum.

- NN signal: we use the Poisson distribution to vary the bins entries of the histogram.

- NN continuum: we vary all except two parameters in the same way we randomize the $\mathrm{m_{ES}}$ signal PDF. We cannot float all parameters in the fit to sideband data. The two fixed parameters have been fitted in an iterative procedure and are varied within their uncertainties in the same way as the ARGUS shape parameter in $\mathrm{m_{ES}}$ continuum.

- DP signal: see model uncertainties below.

- DP continuum: the Dalitz plot continuum PDF is taken from sideband data. To estimate the uncertainty that is due to the limited number of events we vary the smoothing parameter by $\pm 10\%$.

The shifts of the observables with respect to the nominal fit when varying the PDF parameters and the non-parametric PDFs are shown in the appendix (Fig. C.3).

9.7.2 B background

We add the expected number of B-background events from generic MC to our data sample and fit it. We assign the sum in quadrature of the shifts in each observable as the systematic uncertainty on the inclusive $\mathcal{B}$.

9.7.3 Fit bias

The fit bias is estimated using embedded toys (Sec. 9.5.2). It takes into account the biases due to correlations between the variables, SCF and low statistics. We correct the values of the isobar parameters in the fit to data by the shift observed in embedded toys. We assign, to be conservative, the sum in quadrature of half the shift and the uncertainty of the shift as systematic uncertainty. It is detailed in Tab. 9.8 under "Fit bias".

9.7.4 Reconstruction efficiency

The reconstruction efficiency is obtained from a MC simulation that has been generated with the fit result (SP-10045). There are two main contributions to the uncertainty in the reconstruction efficiency ($\mathrm{K^0_S reco}$ in Tab. 9.8):

- The first one is due to differences between data and MC in the reconstruction of the $\mathrm{K^0_S}$. This is a common problem to many *BABAR* analyses and the "Tracking Efficiency Task Force" provides corrections for the $\mathrm{K^0_S}$ reconstruction efficiency that is based on the data-MC differences in a semi-inclusive sample of $\mathrm{K^0_S}$ candidates. To obtain the correction, bins of three characteristic variables: $\mathrm{r_{dec}}$, $\mathrm{K^0_S}$ momentum and polar angle, are compared between data and MC. This gives a correction factor for each individual $\mathrm{K^0_S}$, which is then averaged for the whole MC sample. The uncertainty of the correction comes from the limited statistics in the semi-inclusive data sample and from the limited statistics of our MC sample that is used to evaluate the correction.
  We divide our resonant MC sample (SP-10045) into three sub-samples, one for each $\mathrm{K^0_S}$. We evaluate the correction for each sub-sample and multiply the results for the three $\mathrm{K^0_S}$ to obtain the total correction, where we propagate the uncertainties of the individual ones. As they originate in statistical uncertainties, we add these uncertainties in quadrature. The correction depends on the selection criteria of the $\mathrm{K^0_S}$ and is provided for several standard $\mathrm{K^0_S}$ selections. The usual approach is to choose the selection closest to the actual selection. As in the present analysis we have only $\mathrm{K^0_S}$ in the final state and we do not want to underestimate the uncertainty, we use all five proposed selection sets that include requirements on the variables that we use for selection. We obtain five corrected efficiencies together with their respective uncertainties. We then assign the interval between the lowest central value minus its error and the largest central value plus its error as an uncertainty and the average of both as the central value of the corrected efficiency. We find

  $$\epsilon = 6.898 \pm 0.102\% \,, \tag{9.8}$$

  which corresponds to a 1.48% relative uncertainty.

- The second contribution is due to the statistical uncertainty in the isobar parameters. To estimate this uncertainty, we generate high statistics (100k events) toy MC samples, where we vary the isobar parameters using the covariance matrix from the fit to data. We then use the efficiency map (see Fig. 9.17) to weight the events of the toy samples

and calculate the overall efficiency for each one of them. We use the distribution of the differences between the toy data efficiencies and the nominal value to estimate the resulting uncertainty. The corresponding distribution is shown in Fig. 9.17.

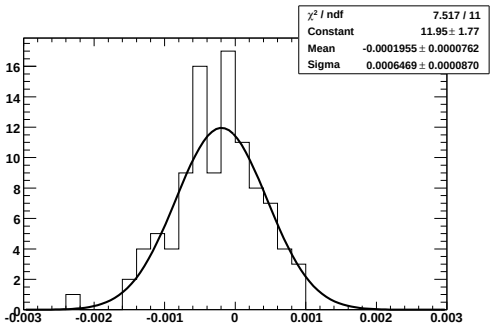

Figure 9.17: Variation of the reconstruction efficiencies obtained when varying the phase-space with respect to the one from the nominal signal MC sample. We assign the sum in quadrature of the mean and the width of the Gaussian fit to the distribution as systematic uncertainty. We find an uncertainty of 0.067% (absolute).

9.7.5 Model uncertainties

In this category we account for the uncertainty on the line-shape parameters and possible contributions of resonances that have not been included in the signal model. We vary the line-shape parameters according to the values given in Tab. 9.2. The barrier factor(s) of the $\mathrm{f}_2(2010)$ has not been measured, but we know from a likelihood scan of the Isobar parameters of the $\mathrm{f}_2(2010)$ with different values of r that the impact of this parameter in small. For the systematic uncertainty we vary it by $\pm 0.5\ \mathrm{GeV}^{-1}$. The result of the line-shape variations is shown in Tab. 9.10. We consider several contributions from other resonances: $\mathrm{f}_0(1370)$, $\mathrm{f}_2(1270)$, $\mathrm{f}_2^{'}(1525)$, $\mathrm{f}_0(1500)$, $\mathrm{a}_0(1450)$ and a scalar $\mathrm{f}_\mathrm{X}(1500)$, and assign their effect on the measured observables as a systematic uncertainty. To this end, we add these resonances one by one to the nominal signal model and fit data. All the amplitudes, except from the one of the additional resonance, are fixed to the values obtained in the nominal fits. Using the resulting isobar parameters of the additional component, we then generate 500 corresponding toy data samples and fit them with the nominal model to get a statistically reliable estimation of the impact. We assign the shifts in the fit fractions, the relative phases and the signal yield with respect to the nominal values as systematic uncertainties. The sum in quadrature of all the model uncertainties is quoted in Tab. 9.8 under "Model"ï£¡. The masses and widths of these additional resonances and the detailed results are given in Tab. 9.9. We chose to consider effects from these particular resonances for the following reasons: the $\mathrm{f}_\mathrm{X}(1500)$ is one of the main motivations for this analysis; the $\mathrm{f}_0(1370)$ as it is a candidate for the large structure seen in the top plot of Fig. 9.7; The tensor resonances $\mathrm{f}_2(1270)$ and $\mathrm{f}_2^{'}(1525)$ have been observed in the $\mathrm{K}_\mathrm{s}^0\mathrm{K}_\mathrm{s}^0$ invariant mass spectrum in other analyses; the $\mathrm{f}_0(1500)$ and $\mathrm{a}_0(1450)$ showed

Table 9.9: Systematic uncertainties from statistically non-significant resonant contributions. For the $f_X(1500)$ we use the line-shape parameters from the ongoing analysis of $B^\pm \to K^+K^-K^\pm$. For the $f_0(1370)$ we use the line-shape parameters from the ongoing analysis $D_s^+ \to K^+K^-\pi^+$ (BAD 2259). The other values are taken from [1].

Parameter	$f_X(1500)$	$f_0(1370)$	$f_2(1270)$	$f_2'(1525)$	$a_0(1450)$	$f_0(1500)$	Sum
Mass [MeV/c^2]	1539	1220	1275	1525	1474	1505	-
Width [MeV/c^2]	257	210	185	73	265	109	-
Signal yield	0.795	1.008	0.731	0.663	0.781	0.894	2.009
FF $f_0(980)$	0.066	0.176	0.061	0.044	0.094	0.108	0.249
FF $f_0(1710)$	0.009	0.002	0.009	0.002	0.010	0.007	0.018
FF $f_2(2010)$	0.001	0.003	0.006	0.011	0.001	0.008	0.016
FF NR	0.095	0.187	0.174	0.017	0.142	0.177	0.356
FF χ_{c0}	0.001	0.003	0.001	0.001	0.001	0.001	0.005
Phase $f_0(980)$	0.086	0.051	0.087	0.019	0.113	0.118	0.211
Phase $f_0(1710)$	0.117	0.013	0.073	0.066	0.082	0.184	0.254
Phase $f_2(2010)$	0.011	0.017	0.068	0.104	0.013	0.571	0.585
Phase χ_{c0}	0.019	0.021	0.053	0.035	0.021	0.022	0.076

an impact on the fit fractions in the add/remove tests. We know from the likelihood scans (Fig. 9.7) that we are not statistically sensitive to any other resonance than the ones included in the model. We add all the model uncertainties in quadrature.

9.7.6 Uncertainty on $N_{B\bar{B}}$

We propagate the uncertainty in the number of produced $B\bar{B}$ pairs, that is provided by the *BABAR* B counting algorithm, into the branching fraction uncertainty.

9.8 Summary

We have performed the first measurement of the resonant content of the decay $B^0 \to K_S^0K_S^0K_S^0$. We make the currently most precise measurement of the inclusive branching fraction for which we find $6.186 \pm 0.475 \pm 0.145 \pm 0.067 \times 10^{-6}$. We find resonant contributions from $f_0(980)K_S^0$, $f_0(1710)K_S^0$, $f_2(2010)K_S^0$, $\chi_{c0}K_S^0$ and also a non-resonant contribution, for which we measure $2.696^{+1.250}_{-1.188} \pm 0.357 \pm 1.874 \times 10^{-6}$, $0.502^{+0.461}_{-0.235} \pm 0.043 \pm 0.129 \times 10^{-6}$, $0.543^{+0.214}_{-0.204} \pm 0.034 \pm 0.440 \times 10^{-6}$, $0.462^{+0.252}_{-0.165} \pm 0.015 \pm 0.197 \times 10^{-6}$ and $13.315^{+2.234}_{-2.302} \pm 0.554 \pm 2.779 \times 10^{-6}$ respectively. We find no significant contribution of the controversial $f_X(1500)$ resonance. The measurement is statistically limited and none of the unflavored resonant states exceeds 4 standard deviations of statistical significance. In the fit we find a second solution that is separated by almost 2 standard deviations from the best solution. The dominant systematic uncertainties are related to the amplitude model. In particular the

Table 9.10: Line-shape systematic

Parameter	$f_0(980)$	$f_0(1710)$	$f_2(2010)$	χ_{c0}	NR	Sum
Signal yield	0.082	0.071	0.743	0.173	0.044	0.772
Phase $f_0(980)$	0.082	0.025	0.116	0.011	0.010	0.146
Phase $f_0(1710)$	0.033	0.095	0.104	0.020	0.000	0.147
Phase $f_2(2010)$	0.015	0.004	0.586	0.001	0.011	0.586
Phase χ_{c0}	0.015	0.018	0.178	0.397	0.004	0.436
FF $f_0(980)$	0.071	0.028	0.149	0.036	0.009	0.172
FF $f_0(1710)$	0.001	0.002	0.007	0.002	0.001	0.008
FF $f_2(2010)$	0.001	0.001	0.069	0.001	0.000	0.069
FF χ_{c0}	0.000	0.001	0.011	0.029	0.000	0.031
FF NR	0.162	0.067	0.184	0.097	0.027	0.273

$f_2(2010)$ is poorly measured, an when varying the mass and the width of this resonance within their uncertainties this leads to sizable shifts not only in the observables of the resonance itself, but also in the $f_0(980)K^0_S$ and non-resonant components. Model uncertainties related to statistically not significant contributions that have not been included in the model are sizable but are the same order of magnitude as the statistical uncertainties on the fit fraction.

Part IV

SuperB prospective of $B^0 \to K^0_S K^0_S K^0_S$

10 Super B-factory prospective

10.1 Introduction

Given that the TD analysis is statistically limited and that the theoretical error for $\mathrm{B}^0 \to \mathrm{K}^0_\mathrm{s}\mathrm{K}^0_\mathrm{s}\mathrm{K}^0_\mathrm{s}$ is very small, it is interesting to investigate the perspectives in a high-luminosity environment. Currently the systematic error of the $\mathcal{S}$ measurement, $\delta\mathcal{S}_{\mathrm{exp}} = 0.064$ (see Sec. 8.6), is several times larger than the theoretical uncertainty, $\delta\mathcal{S}_{\mathrm{theo}} = ^{+0.007}_{-0.018}$ [26]. Right now this not an issue, as the measurement is statistics limited ($\sigma\mathcal{S} \simeq 0.24$, see Sec. 8.5), but the systematic uncertainty will become dominant with accumulated statistics. We investigate how this experimental uncertainty can be reduced to become competitive with the theoretical uncertainty.

Currently there exist two propositions for super B-factories, SuperB and Belle II. In this work we present the SuperB prospective. We study the reconstruction efficiencies, beam backgrounds and the vertex measurement precision for $B^0 \to K^0_s K^0_s K^0_s$ expected at SuperB.

10.2 Error projection using the *BABAR* setup

The fitter setup in the present study is identical to the one in the TD analysis, except that we consider only K^0_s decaying to charged pions. This is a natural choice, because it reduces the background rate considerably but does not reduce significantly the sensitivity. The analysis overestimates the statistical and systematic error by assuming that SuperB will perform as good as *BABAR* in terms of tracking, tagging and PID. We use toy studies to estimate the statistical error of the $\mathcal{S}$ parameter, as following:

- We generate 25 toy samples for a given luminosity and fit them.
- We vary the luminosity by starting with the full *BABAR* data sample size and then increasing this sample in steps of twice the *BABAR* data sample until we reach 350 times the original sample. SuperB is expected to collect data that corresponds to up to $\sim$30 times the *BABAR* luminosity per year. Additionally we can expect an improvement in reconstruction efficiency of 20-30% (see sec. 10.4).
- To estimate the uncertainties on the $\mathcal{S}$ parameter, we use the average of the fit uncertainties obtained in all the properly converged fits for the corresponding step.
- Once the statistical error becomes smaller than the systematic uncertainty, we investigate how the systematic uncertainty can be reduced, for instance, by allowing more parameters to vary in the fit or by using tighter selection requirements. We then start a new scan of the statistical uncertainty.

The result of this procedure is shown in Fig. 10.1. Aside from the projection obtained with the nominal setup, we perform two additional projections:

1. Using the nominal setup, at around 20 times the *BABAR* luminosity the statistical error becomes smaller than the systematic uncertainty. Given the higher statistics, we can now allow some of the initially fixed parameters to vary in the fit procedure, and hence reduce the systematic uncertainty. The largest systematic uncertainty in the TD analysis is due to MC-data differences. We can avoid these uncertainties by allowing all the parameters of the discriminating variables and the $\Delta \mathrm{t}$ resolution function to vary. A problem is that the NN signal PDF is a histogram; as the statistical uncertainty is not dominant, we decide to replace the NN with a Fisher discriminant[1] that can be fitted using analytical functions, for instance bifurcated Gaussians, for both signal and continuum background. This new setup includes many more free parameters and is less discriminant between signal and background, and as a result the statistical uncertainty slightly increases. On the other hand, the systematic uncertainty decreases significantly, resulting in a smaller total error.

2. At around 60 times the *BABAR* luminosity, the statistical error becomes, once again, smaller than the systematic uncertainty. The remaining dominant contributions to the systematic uncertainty are the ones from the fit bias and the non-reducible[2] background from B decays. The latter could be reduced if one have a better knowledge of the branching fractions and the CP content of the contributing modes. We assume that the main background modes that we treat exclusively in the time-dependent analysis will be known at a 10% level in the future, both for branching fractions and CP-violation parameters. We do not make an assumption on the minor contributions that are absorbed in the generic component, but allow the corresponding CP violation parameters and yields to vary in the fit. We also suppose that the fit bias can be reduced by 50%, for instance by taking into account correlations between variables in the PDFs or by using more sophisticated models. The resulting error estimation is given by the blue lines in Fig. 10.1. The statistical uncertainty increases only marginally due to the additional free parameters in the fit.

To summarize, we have shown that the systematic uncertainty can be reduced significantly in a high-luminosity environment. The price to pay in an increase in the statistical error compared to the naive extrapolation. Making the reasonable assumption that the main background modes will be measured more precisely in the future, toy studies indicate that a 2-3% measurement (total error) of the $\mathcal{S}$ parameter is possible after ten years of running of SuperB. This uncertainty is of the same order of magnitude as the current uncertainty on $\sin(\beta)$ from charmonium decays. An improvement in the SuperB reconstruction, for instance in the tagging algorithm or the PID, could further decrease the uncertainties.

[1] We do not actually train a Fisher discriminant but use distributions similar to the ones found in Ref. [68]

[2] This background is non-reducible due tu the fact that the corresponding underlying events are real B decays.

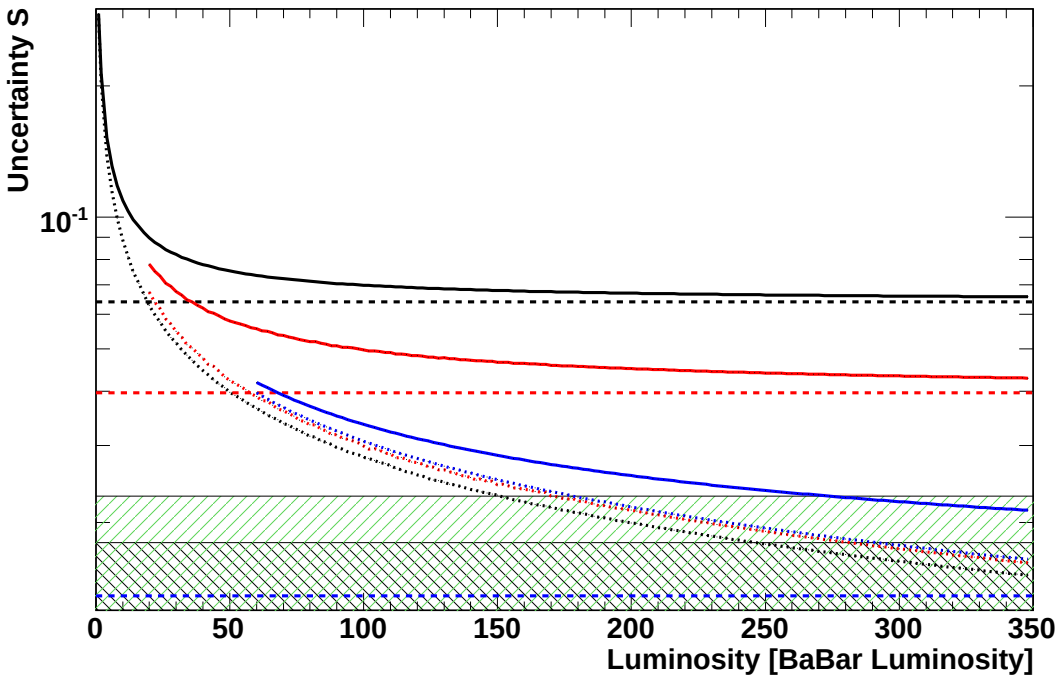

Figure 10.1: Scan of the uncertainty of the $\mathcal{S}$ parameter as a function of the integrated luminosity in units of the complete BABAR $\Upsilon(4S)$ integrated luminosity. The lower dotted lines indicate the statistical errors, the upper solid lines the total error and the dashed lines the systematic uncertainties. The black shaded region shows the theoretical uncertainty and the green shaded region shows the uncertainty of the 2010 average [15] ($\mathcal{S} = 0.670 \pm 0.023$) from charmonium decays. The black lines correspond to the nominal configuration of the TD analysis, the red lines to the configuration where the parameters of the Δt resolution function and the discriminating variables are floating, and the blue lines to the case where we make assumptions on future measurement of background modes.

10.3 The SuperB experiment

SuperB is a next-generation B factory that is aimed to provide information that is complementary to the one obtained in the energy-frontier, from the current LHC experiments. If New Physics particles are discovered at the LHC, detailed understanding of the New Physics phenomena will require data from very sensitive heavy flavor experiments. Determining the flavor structure of the New Physics involved requires information on rare b, c and τ decays, and on *CP* violation in b and c quark decays, which only a very-high-luminosity-asymmetric B Factory can provide [69]. On the other hand, if such signatures of New Physics are not observed at the LHC, the measurements at the luminosity frontier by a next generation super B-factory can constrain New Physics model thanks to loop effects. Such an experiment provides another avenue to observing New Physics at mass scales up to $10\ \mathrm{TeV}$ or more through observation of rare processes involving B and D mesons and studies of lepton flavor violation (LFV) in τ decays. Reaching the above-mentioned sensitivity requires a data sample that is some 50-100 times larger than the existing combined sample from *BABAR* and Belle, or at least $50 - 75\ \mathrm{ab}^{-1}$. Acquiring such an integrated luminosity in a 5 year time frame requires that the collider runs at a luminosity of at least $10^{36}\ \mathrm{cm}^{-2}\mathrm{s}^{-1}$.

10.3.1 The SuperB factory

The SuperB collider uses a new collision scheme, the crab waist [70], to obtain the required luminosities without increasing the beam currents and energy consumption with respect to the existing B factories. This scheme introduces a large crossing angle between beams, which have a reduced horizontal size and a high bunch charge density. The energies of the HER (7GeV) and the LER (4GeV) are chosen to be less asymmetric than in PEP-II , which reduces the boost by approximately a half with respect to PEP-II , and brings it to $\beta\gamma = 0.24$. This leads to a higher containment, but the detector has to be adapted to provide a more precise vertex measurement if TD analyses are to remain feasible (see below). The reduced beam size leads to significantly increased machine backgrounds compared to PEP-II . The background particles can either hit the detector directly or interact with some other material, for instance the beam pipe, and generate secondary particles, which then interact with the detector. For studies, the main contributions of the backgrounds are generated and their impact in the detector and the beampipe is simulated using Geant4. The events can then be embedded in simulated physics events before reconstruction. The main background contributions are:

- **Beam-beam interaction**: Due to the reduced beam size and the high charge density there are strong beam-beam interactions and significant intra-beam scattering. In the SuperB environment these are the dominant background sources. They are larger than single-beam bremsstrahlung or Coulomb scattering and are simulated using the Guinea Pig package[3] [71].

[3] $\mathrm{e}^+\mathrm{e}^-$ pair creation from radiative photons does not work correctly yet and is not included in the simulated events used in this work.

- **Radiative Bhabhas**: The single bremsstrahlung $e^+e^- \to e^+e^-\gamma$ are generated using BBBREM [72]. A large fraction of off-energy electrons and positrons hit the beam-line elements and produce showers; low energy particles from these showers enter all sub-systems of the detector.

- **Touschek Scattering**: Touschek scattering is the source of background that is due to the off-energy particles arising from the elastic scattering of particles within a bunch. This background scales with the bunch charge density. The effect has been studied for the LER using a program developed for DAΦNE. The background can be reduced by inserting collimators, but remaining particles shower electromagnetically in the beam pipe close to the IP (90 kHz per LER bunch).

- **Other sources of background**: Another source of background are particles lost due to Coulomb or bremsstrahlung interactions with the residual gas in the beam pipe. These are the dominant backgrounds at *BABAR*. As an estimate for SuperB, the *BABAR* value has been scaled to the SuperB currents, where it reaches 1-2$\mathrm{MHz\ cm^{-2}}$, and is still negligible with respect to other background sources (see Fig. 10.3 below). Yet another source of background is synchrotron radiation, that can lead to outgassing due to heating and degrade in the local vacuum when photons hit the beam pipe. The expected rate of photons above 10keV that hit the pipe in proximity of the detector is expected to be of the same order of magnitude as in *BABAR* ($\sim$ 1500 γ per bunch crossing) and is negligible.

In Sec. 10.4 we investigate the background composition and its effects when reconstructing $B^0 \to K^0_s K^0_s K^0_s$ events.

10.3.2 The SuperB detector

The SuperB detector [73] concept reuses a number of components from BABAR: the flux-return steel, the superconducting coil, the barrel of the EMC and the fused silica bars of the DIRC. The flux-return will be augmented with additional absorbers to increase the number of interaction lengths (λ) for muons to roughly 7. The DIRC camera will be replaced by a twelve-fold modular camera using multi-channel plate (MCP) photon detectors in a focusing configuration using fused silica optics to reduce the impact of beam related backgrounds and improve performance. The physics benefit from the inclusion of a forward PID (fwdPID) remains under study. The baseline design concept is a fast Cherenkov light based time-of-flight system. The forward EMC (fwdLYSO) will feature cerium-doped LYSO (lutetium yttrium orthosilicate) crystals, which have a much shorter scintillation time constant, a lower Molière radius and better radiation hardness than the current CsI(Tl) crystals, again for reduced sensitivity to beam backgrounds and better position resolution. The tracking detectors for SuperB will be new. The current SVT cannot operate at $\mathcal{L} = 10^{36}\mathrm{cm^{-2}s^{-1}}$, and the DCH has reached the end of its design lifetime and must be replaced. The new DCH is based on the *BABAR* DCH, but adapted in terms of gas and geometry to SuperB requirements. Under study was also the possibility to extend the DCH to the forward side (fwdDCH) and/or to the backward side (bwdDCH) in case the decision would have been not to include the fwdLYSO

or the fwdPID. To maintain a sufficient proper-time difference resolution for time-dependent CP violation measurements with the SuperB boost of $\beta\gamma$ = 0.24, the vertex resolution will be improved by reducing the radius of the beam pipe, and placing the innermost layer of the SVT at a radius of roughly 1.2 cm. A study on the improved resolution for $B^0 \to K^0_S K^0_S K^0_S$ is presented in Sec. 10.4.3. This innermost layer of the SVT will be constructed of either silicon striplets, Monolithic Active Pixel Sensors (MAPS) or other pixelated sensors, depending on the estimated occupancy from beam-related backgrounds. Likewise, the design of the cell size and geometry of the DCH will be driven by occupancy considerations. The hermeticity of the SuperB detector, and, thus, its performance for certain physics channels will be improved by including a backwards "veto-quality" EMC (bwdEMC) detector comprising a lead-scintillator stack. The SuperB detector concept is shown in Fig.10.2. The top portion of this elevation view shows the minimal set of new detector components, with substantial reuse of elements of the current *BABAR* detector; the bottom half shows a configuration with additional new components that would cope with higher beam backgrounds and achieve greater hermeticity.

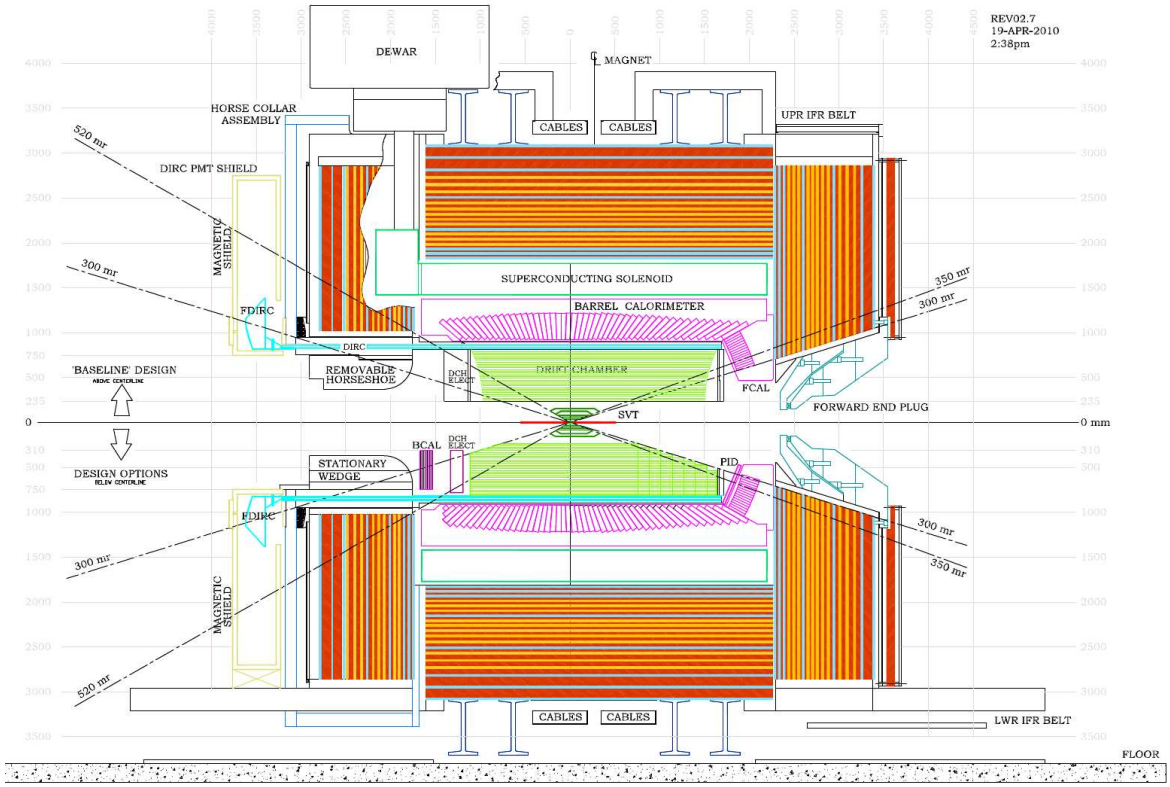

Figure 10.2: The SuperB detector

We investigate the reconstruction efficiencies for the detector geometries (DGs) detailed in Tab. 10.1.

DG	SVT	DCH	PID	EMC	IFR
BABAR	"*BABAR*"	"*BABAR*"	"*BABAR*"	"*BABAR*"	"*BABAR*"
DG0	5 layers+L0	"*BABAR*"	DIRC	"*BABAR*"+fwdLYSO	baseline
DG1	5 layers+L0	"*BABAR*"+bwdDCH+fwdDCH	DIRC	"*BABAR*"+fwdLYSO	baseline
DG2	5 layers+L0	"*BABAR*"+bwdDCH	DIRC+fwdPID	"*BABAR*"+fwdLYSO	baseline
DG3	5 layers+L0	"*BABAR*"+fwdDCH	DIRC	"*BABAR*"+fwdLYSO+bwdEMC	baseline
DG4	5 layers+L0	"*BABAR*"	DIRC+fwdPID	"*BABAR*"+fwdLYSO+bwdEMC	baseline

Table 10.1: Detector configurations studied in this work.

10.4 SuperB studies using FastSim

10.4.1 What is FastSim?

FastSim is a tool aimed to provide simulated data to perform detector optimization and physics studies for SuperB. It is based on the *BABAR* framework and uses EvtGen to simulate the physics events. FastSim generates and reconstructs events in a single sequence, i.e. runs the generation, detector simulation and reconstruction event by event, and the only data that are stored are the reconstructed (or not reconstructed) events. For this to be possible, two main simplifications are used:

1. FastSim detector elements are modeled as quasi two-dimensional objects instead of full volumes. For instance, a layer of the SVT is modeled as a cylindrical section of a given radius and z limits. Furthermore, an effective thickness is assigned to the element defined to be its extent normal to the local surface normal direction. This greatly simplifies the geometric calculations required to determine a particle's interaction with an element.

2. Modeling of a particle's passage through an element starts by computing the intersection between the particle's trajectory and the two-dimensional surface of the element. If that intersection exists and it is within the elements range, the particle's path length through the element is computed using its thickness parameter and the local incidence angle of the trajectory. This simplification thus ignores the "edges" of an element, as a particle may not enter or exit through them. It also ignores the curving of the particle trajectory as it passes through the effective element volume. This approximation is very good for thin elements such as the beampipe and SVT layers. It is reasonably good for the DIRC and the EMC (the thickest element in *BABAR* or SuperB), because the 'edges' of these are outside the region of interest. Several classes of interaction processes are then simulated:

   - "normal" charged particle interactions (energy loss and direction scattering): Energy loss is sampled from a (truncated) Landau distribution, which depends on the material type and the thickness using the *BABAR* `DetMaterial` class, and propagated to the particles momenta. Deflection is sampled from a double-Gaussian. The sampling functions have been tuned using the FastSim implementation of *BABAR* to reproduce the GEANT output.

- EM interactions (pair production, Compton scattering, showering etc.): as a function of the thickness of the material in terms of radiation lengths ($\mathrm{P_{int}} = 1 - \mathrm{e}^{-\mathrm{N}_\lambda}$), it is sampled whether or not a particle interacts. If it does, there is a distinction between thin and thick elements. In thin elements the interaction is considered to be discrete[4] (which means that the particle may or may not survive after the interaction). In thick elements, the result is a shower that corresponds to a parameterization of the average longitudinal electromagnetic shower development described in the Ref. [1].
- Hadronic interactions (nuclear scattering, showering etc.): are simulated in the same way as the EM interactions, except that the showers are hadronic instead of electromagnetic.

As in GEANT, these processes are modeled probabilistically. Unlike GEANT, in FastSim the step size for evaluating the occurrence of a process is set to the actual detector segmentation (i.e. the full thickness of a Si layer), and not to a microscopic size indicated by the process being simulated.

10.4.2 Efficiencies and beam backgrounds

The reconstruction is done with the standard *BABAR* algorithm. We reconstruct three $\mathrm{K^0_s}$ composites from the `KsDefault` list (definded in Sec. 7.3.5) and use the `TreeFitter` vertexing algorithm to combine them to a $\mathrm{B^0}$. Beam backgrounds can be added to the events before reconstruction. The standard backgrounds are the *BABAR* ones (described in Sec. 4.2.2) or the SuperB ones, as describes above.

We study how much the reduced boost and the improved coverage of the SuperB detector benefits to the containment of events by studying the reconstruction efficiency. Due to the simplified detector model we cannot expect to obtain very precise estimations on an absolute scale. This is why we use the FastSim implementation of PEP-II and *BABAR* to compare the reconstruction efficiency of SuperB relative to the the *BABAR* experiment. An aspect that must be taken into account in the reconstruction efficiency is the dependence on the beam backgrounds. As mentioned above, these backgrounds are much more abundant than in the *BABAR* experiment. This is illustrated in Fig. 10.3, where we show the number of generated particles in reconstructed FastSim in several cases. While in *BABAR* most events have less than 200 particles, SuperB events can contain more than 1000 particles. We investigate the compositions of the backgrounds by removing all particles that originate from a $\Upsilon(4S)$ resonance; the remaining particles correspond to background. We then count the average number of each species of background particles; the result is summarized in Tab. 10.2. We do not find any "real" $\mathrm{K^0_s}$, but additional pions can be wrongly reconstructed as $\mathrm{K^0_s}$ daughters. To check this, we compare the number of reconstructed $\mathrm{K^0_s}$ in MC with and without background. The corresponding distributions are shown in Fig. 10.4, where we also show the number of $\mathrm{B^0}$ meson candidates. We do not observe any significant contributions from wrongly reconstructed $\mathrm{K^0_s}$ from background particles. This can be explained with the geometrically-strongly-constrained reconstruction, using the `TreeFitter` algorithm. In average, there

[4] Pair creation is not yet working.

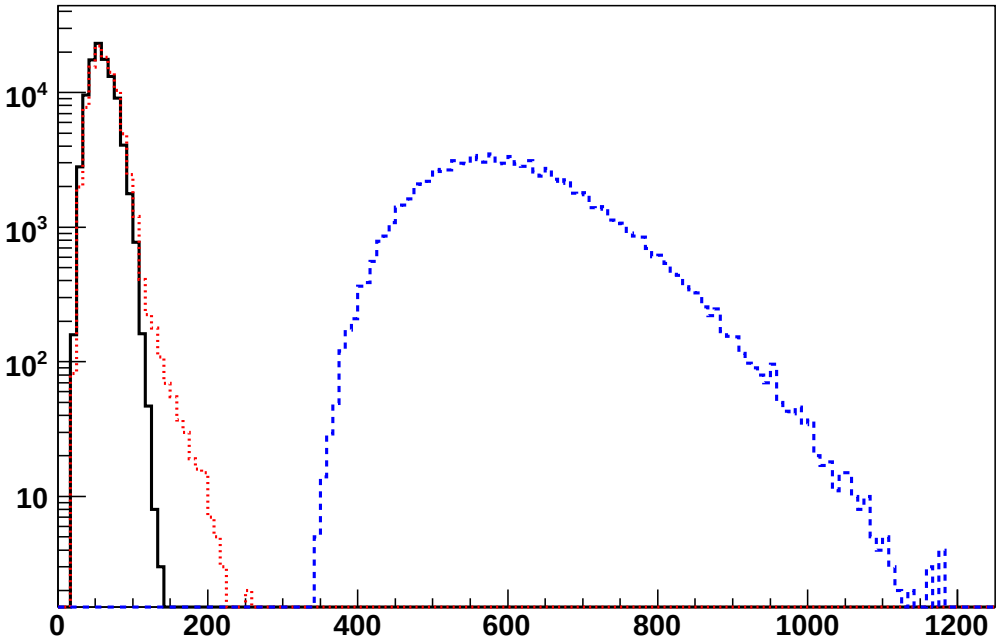

Figure 10.3: Distributions of the numbers of generated particles in reconstructed events for the SuperB baseline detector geometry (DG0). The black solid line corresponds to MC with no beam backgrounds, the red dotted line to MC that includes *BABAR*-like beam backgrounds, and the dashed blue line to MC that includes SuperB backgrounds.

Particle	Average frequency per event
γ	486.72
K_s^0	0
$e^{\pm}$	58.82
μ	0.04
$\pi^{\pm}$	0.10
π^0	0.00(1)
$p/\bar{p}$	0.11

Table 10.2: Composition in terms of average number per event of abundant and/or relevant particles from beam backgrounds.

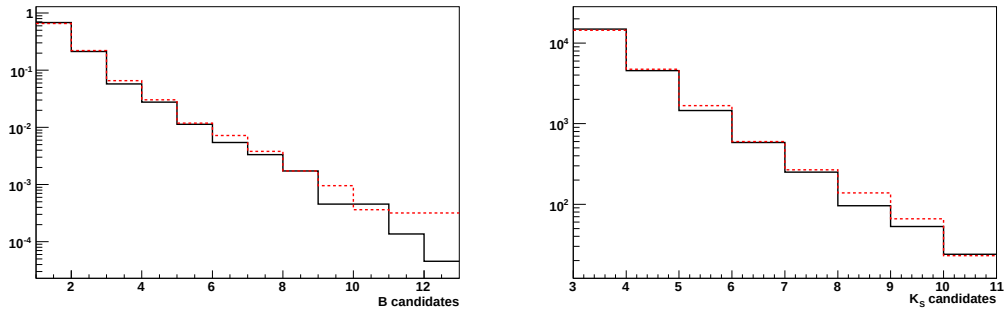

Figure 10.4: Number of reconstructed B candidates (left) and K^0_s candidates (right). The solid black lines correspond to a sample with no background, and the dashed red lines to a sample with SuperB backgrounds.

is only 0.1 charged pion from beam background in an event. The probability that this pion is used in a global fit, where first the K^0_s is reconstructed using geometrical constraints, and then the B^0 is reconstructed in the same way from three K^0_s, is very small. This is also reflected in the reconstruction efficiency, which is almost not influenced by backgrounds. In a less constrained environment one would expect the reconstruction efficiency to increase in the presence of backgrounds.

We compare the reconstruction efficiencies for the different detector geometries that have been introduced earlier. Naturally we find the highest efficiency for DG1, that has the highest coverage due to the additional sub-detector components, but overall the efficiencies are comparable and there is no strong preference for a DG from the point of view of $\mathrm{B}^0 \to \mathrm{K}^0_\mathrm{s}\mathrm{K}^0_\mathrm{s}\mathrm{K}^0_\mathrm{s}$. We also find that the SuperB (DG0) detector has a $\sim 13\%$ higher reconstruction efficiency relative to the *BABAR* detector. This is mainly due to the reduced boost of the SuperB beams and the Layer0 of the SVT. To obtain an estimate of the order of magnitude of the contribution from the reduced boost, we run a test using SuperB beams and the *BABAR* detector; here the increase of the reconstruction efficiency should be only due to the reduced boost. We find 19.5%, that corresponds to a relative increase of 4 %; the remaining increase is then due to the better coverage of the SuperB detector, for instance by the Layer0 of the SVT.

10.4.3 Vertex measurement

We investigate the precision of the vertex measurement by comparing FastSim simulated events with the *BABAR* and the SuperB experiments. We use the distribution of $\delta\mathrm{z}$, the difference between the generated and reconstructed z-position:

$$\delta\mathrm{z} = \mathrm{z}_\mathrm{gen} - \mathrm{z}_\mathrm{rec} \ , \tag{10.1}$$

to estimate the resolution improvement in the SuperB experiment on the signal side of $\mathrm{B}^0 \to \mathrm{K}^0_\mathrm{s}\mathrm{K}^0_\mathrm{s}\mathrm{K}^0_\mathrm{s}$ decays. It has already been shown elsewhere [70], that the vertex precision on the tag-side is sufficient for a time-dependent measurement. The resolution distributions are shown in Fig. 10.5. We use the width of the distribution at half the maximum to compare

Detector	no background	*BABAR* backgrounds	SuperB backgrounds
BABAR	0.188 ± 0.001	0.186 ± 0.001	0.187 ± 0.001
DG0	0.213 ± 0.002	0.216 ± 0.002	0.218 ± 0.002
DG1	0.219 ± 0.002	0.216 ± 0.002	0.220 ± 0.002
DG2	0.217 ± 0.002	0.219 ± 0.002	0.218 ± 0.002
DG3	0.214 ± 0.002	0.217 ± 0.002	0.216 ± 0.002
DG4	0.212 ± 0.002	0.217 ± 0.002	0.216 ± 0.002

Table 10.3: Reconstruction efficiencies for different detector geometries with and without machine backgrounds. The different SuperB detector geometries are detailed in Tab. 10.1.

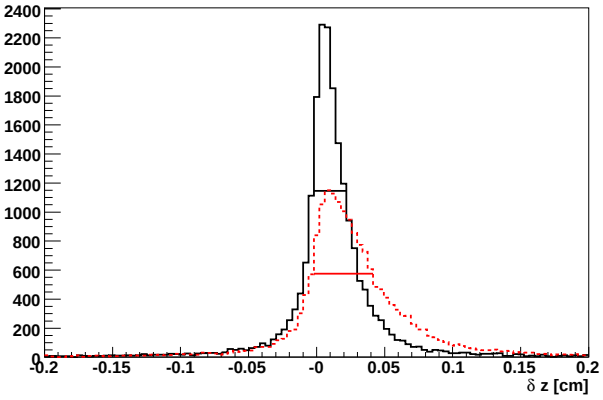

Figure 10.5: Comparison of the resolution δz in the z-position reconstruction for *BABAR* (red dashed) and for the SuperB baseline detector geometry (black solid). The solid horizontal lines show the width at half the maximum.

the resolution functions. We find a width of 44 μm for the *BABAR* configuration and a width of 24 μm for the SuperB configuration. As the boost is reduced approximately by half in SuperB, the precision on the Δt measurement remains approximately the same as in *BABAR* due to the increase by a factor of approximately two in the precision of the Δz measurement. Thanks to this, the TD measurement remains feasible in SuperB.

10.5 Summary

The presented study has reached its two main goals: It has shown that a time-dependent analysis of $B^0 \to K^0_s K^0_s K^0_s$ decays is feasible at SuperB and it provides an estimate of the accuracy of the $\mathcal{S}$ measurement that can be reached. We have projected the experimental uncertainty in the $\mathcal{S}$ parameter of the decay $B^0 \to K^0_s K^0_s K^0_s$ up to the expected integrated luminosity of SuperB after ten years of running. We expect the uncertainty to reach 2-3%, which is of the same order of magnitude as the theoretical uncertainty and the current experimental uncertainty on $\sin(2\beta)$. We have studied the reconstruction efficiency and the vertex measurement of $B^0 \to K^0_s K^0_s K^0_s$ decays at SuperB using FastSim events. We observe, as expected, an increase in efficiency due to the higher containment of SuperB compared to *BABAR*, which is of the order of 13%. This result is almost the same for different SuperB detector geometries, so there is no improvement that is particular to this analysis when adding futher detector components to the baseline geometry. Of course additional compoenent could benefit the tagging efficiency and quality for instance and hence also improve this measurement. We find a vertex resolution that leads to a Δt uncertainty comparable to the one that has been proven sufficient for TD analysis in *BABAR*, from which we conclude that this analysis is feasible at SuperB.

Acronyms

- SM: Standard Model
- CPV: CP violation
- TD: time-dependent
- TDCPV: time-dependent CP violation
- DP: Dalitz plot
- SDP: Square Dalitz plot
- PDF: probability density function
- Nll: negative logarithmic likelihood

Part V

Appendix

A π^0 efficiency

Default Lists

`Pi0VeryLoose`:

- Min Raw Energy: 0.030 GeV
- Min Num of Crystals: 0
- Max Lateral Moment: 0.8
- Mass 0.090:0.165
- Fit: Add4

`GoodTracksVeryLoose`

- Min Transverse Momentum: 0.0 GeV/c
- Max Momentum: 10 GeV/c
- Min # of Dch Hits: 0
- Min Fit Chi-Square Prob.: 0
- Max DOCA in XY plane: 1.5 cm
- Min Z Doca: -10 cm
- Max Z Doca: 10 cm

`Kaon likelihood separators`
Combine following information

- dE/dx: Energy loss in the SVT and DCH
- theta_c: Cerenkov angle in the DRC
- N_gamma: Number of photons in DRC
- N_gamma_exp: Number of photons expected

`Pion likelihood separators`
Combine following information

- dE/dx: Energy loss in the SVT and DCH
- theta_c: Cerenkov angle in the DRC
- N_gamma: Number of photons in DRC
- TrkQual: Track quality
- iselectron: Whether the track passes the LH electron selector
- ismuon: Whether the track passes the MicroVeryTight muon selector

Projection plots

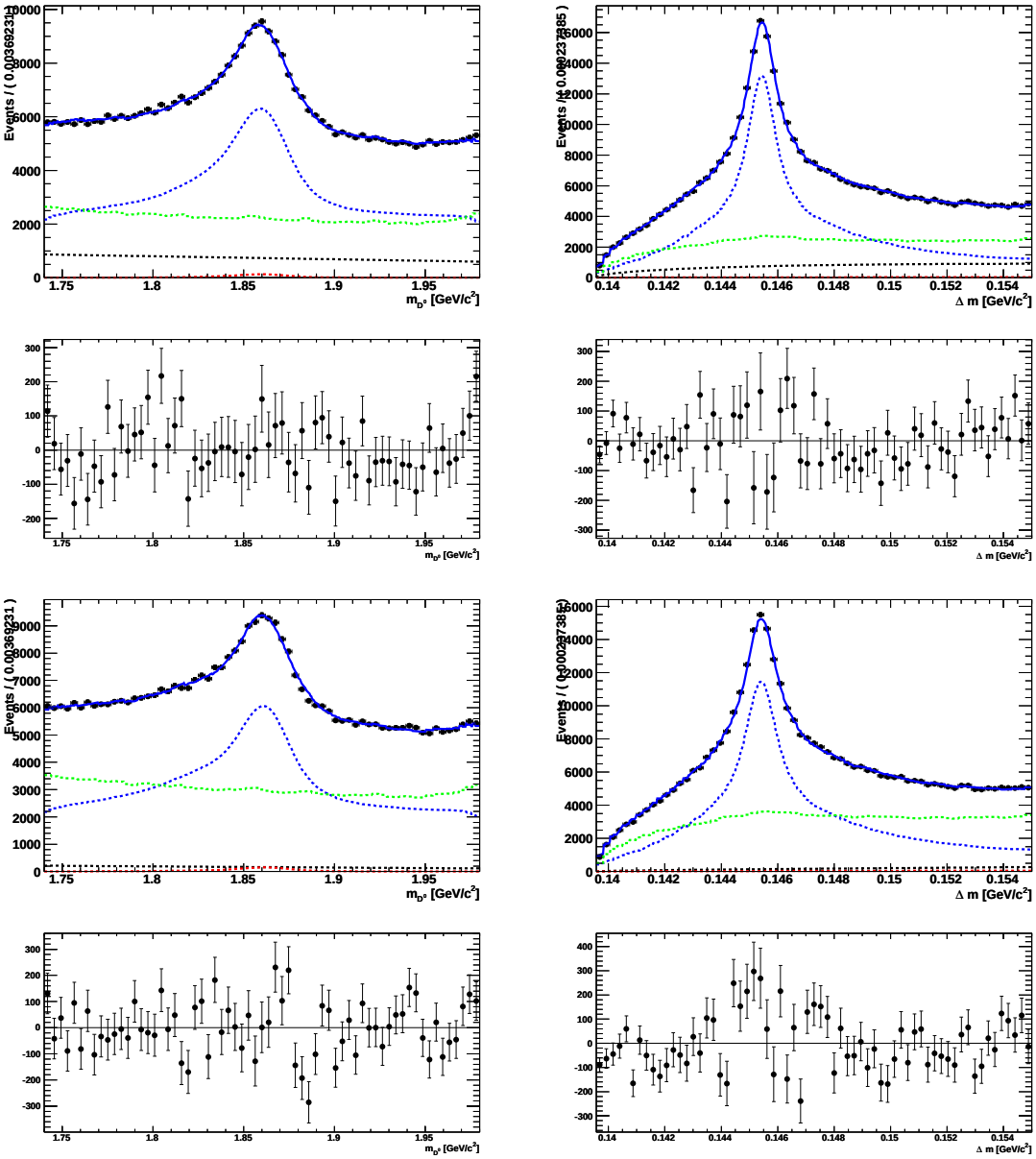

Projections for $\mathrm{p}(\pi^0)$-slice 1. The top plots are fits to MC, the bottom plots fits to data.

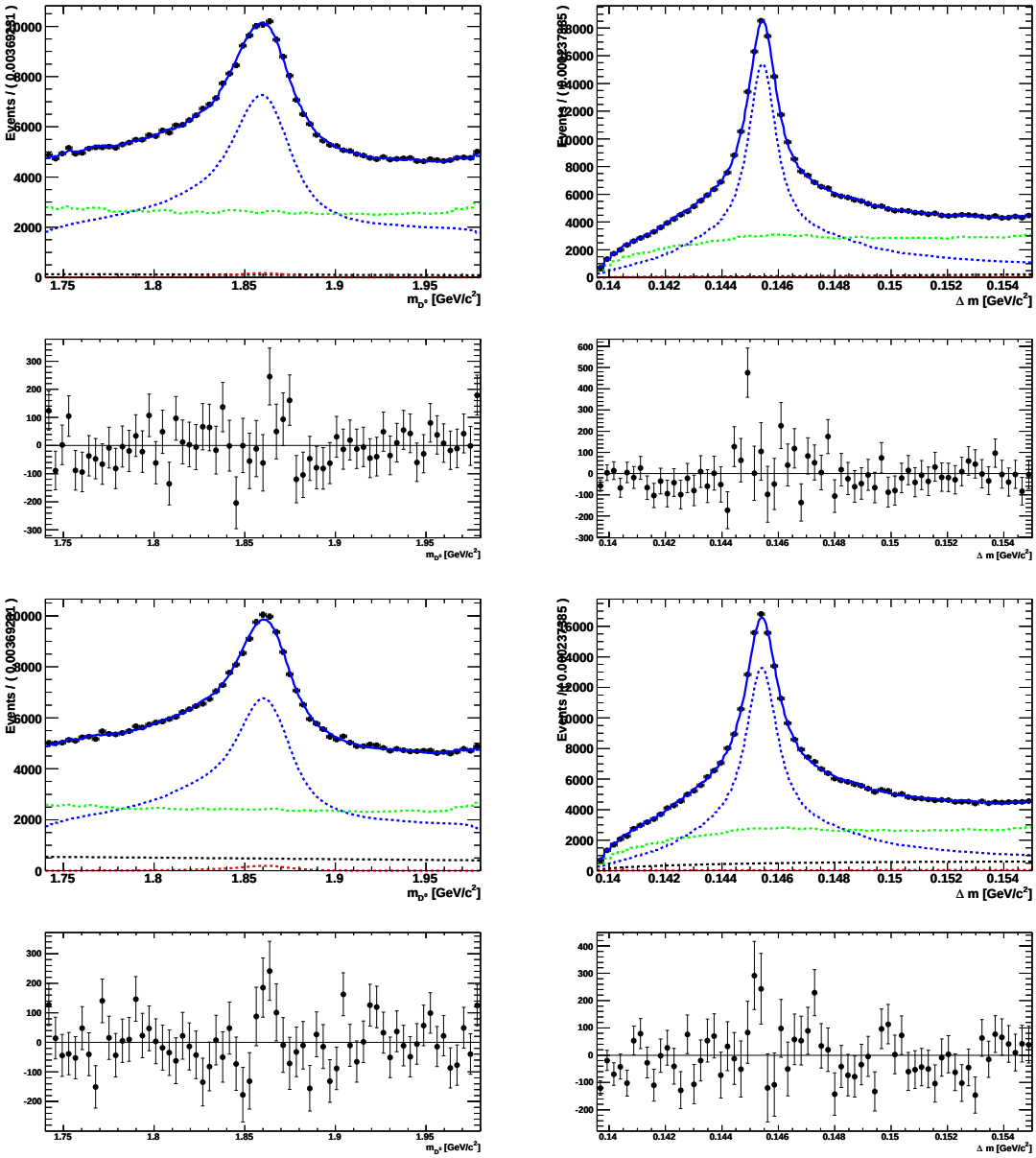

Projections for $\mathrm{p}(\pi^0)$-slice 2. The top plots are fits to MC, the bottom plots fits to data.

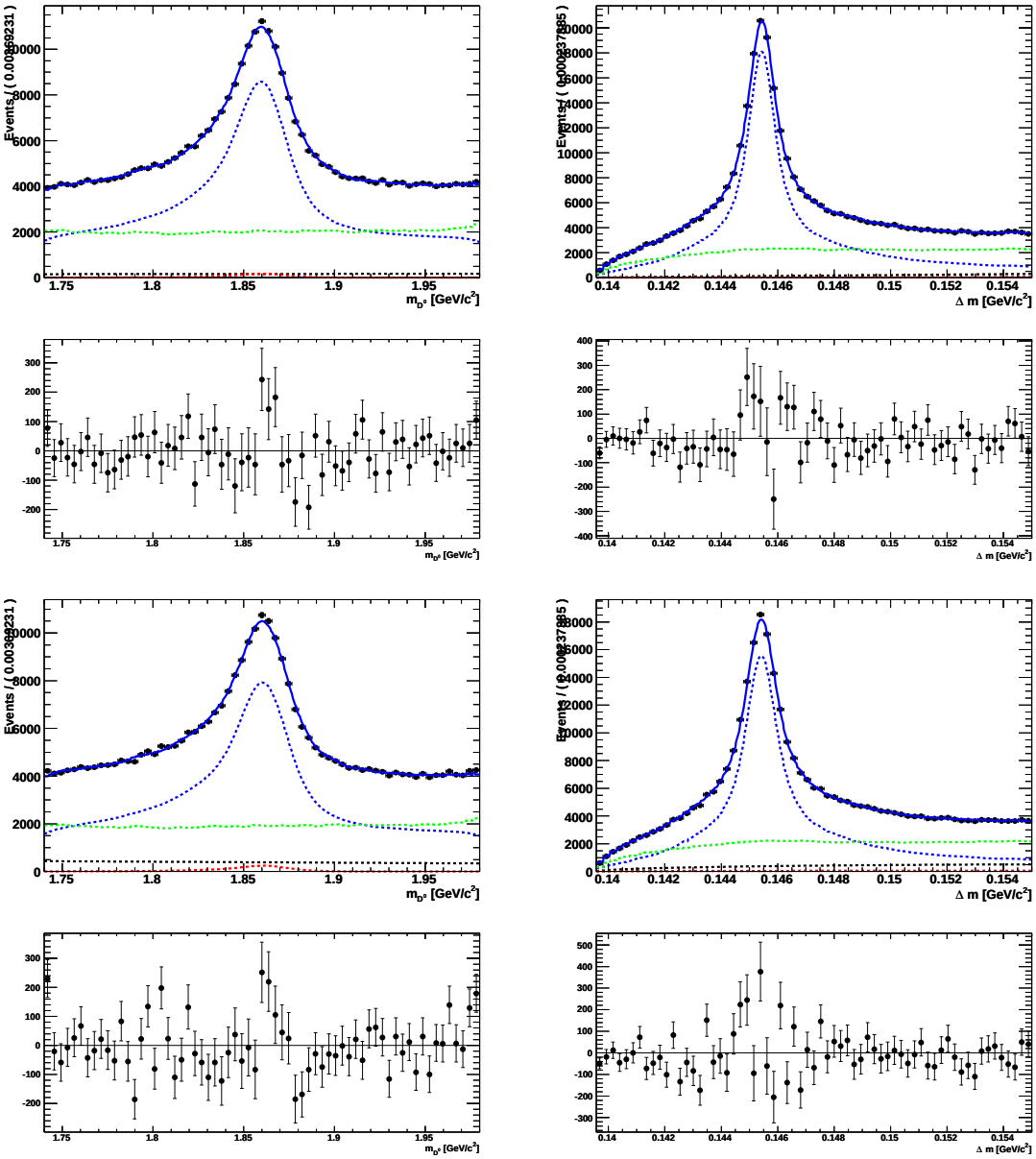

Projections for $\mathrm{p}(\pi^0)$-slice 3. The top plots are fits to MC, the bottom plots fits to data.

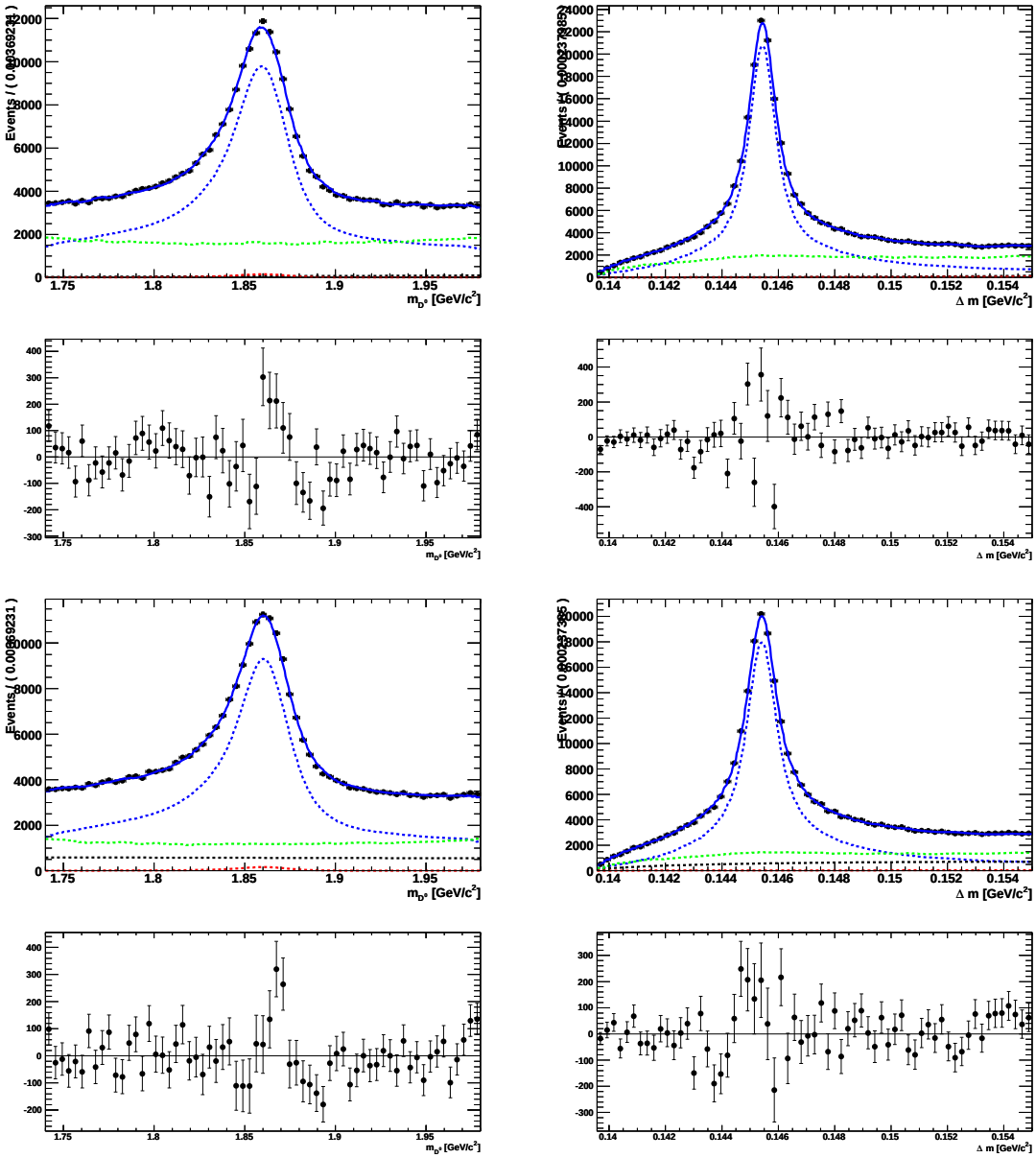

Projections for $\mathrm{p}(\pi^0)$-slice 4. The top plots are fits to MC, the bottom plots fits to data.

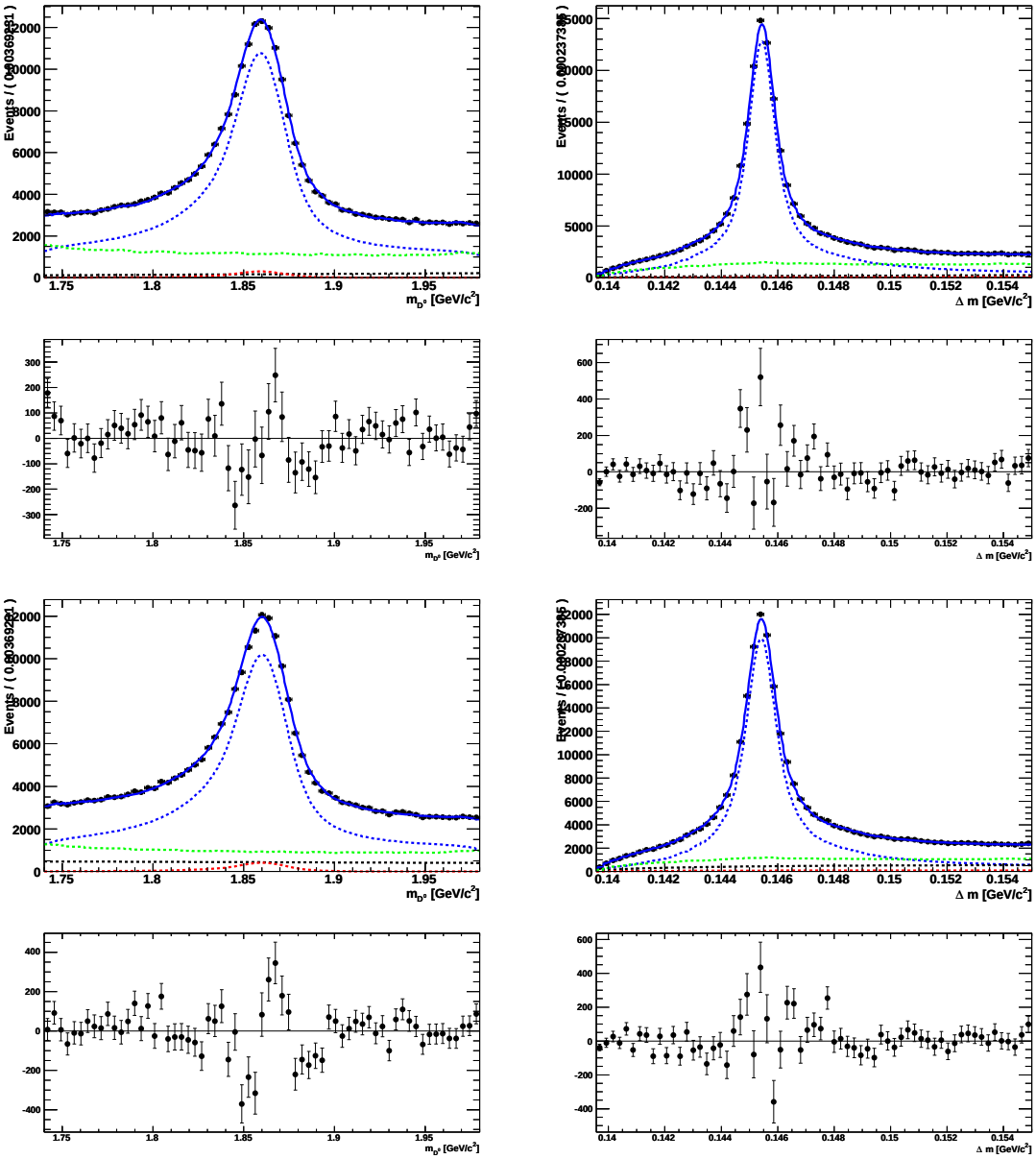

Projections for $\mathrm{p}(\pi^0)$-slice 5. The top plots are fits to MC, the bottom plots fits to data.

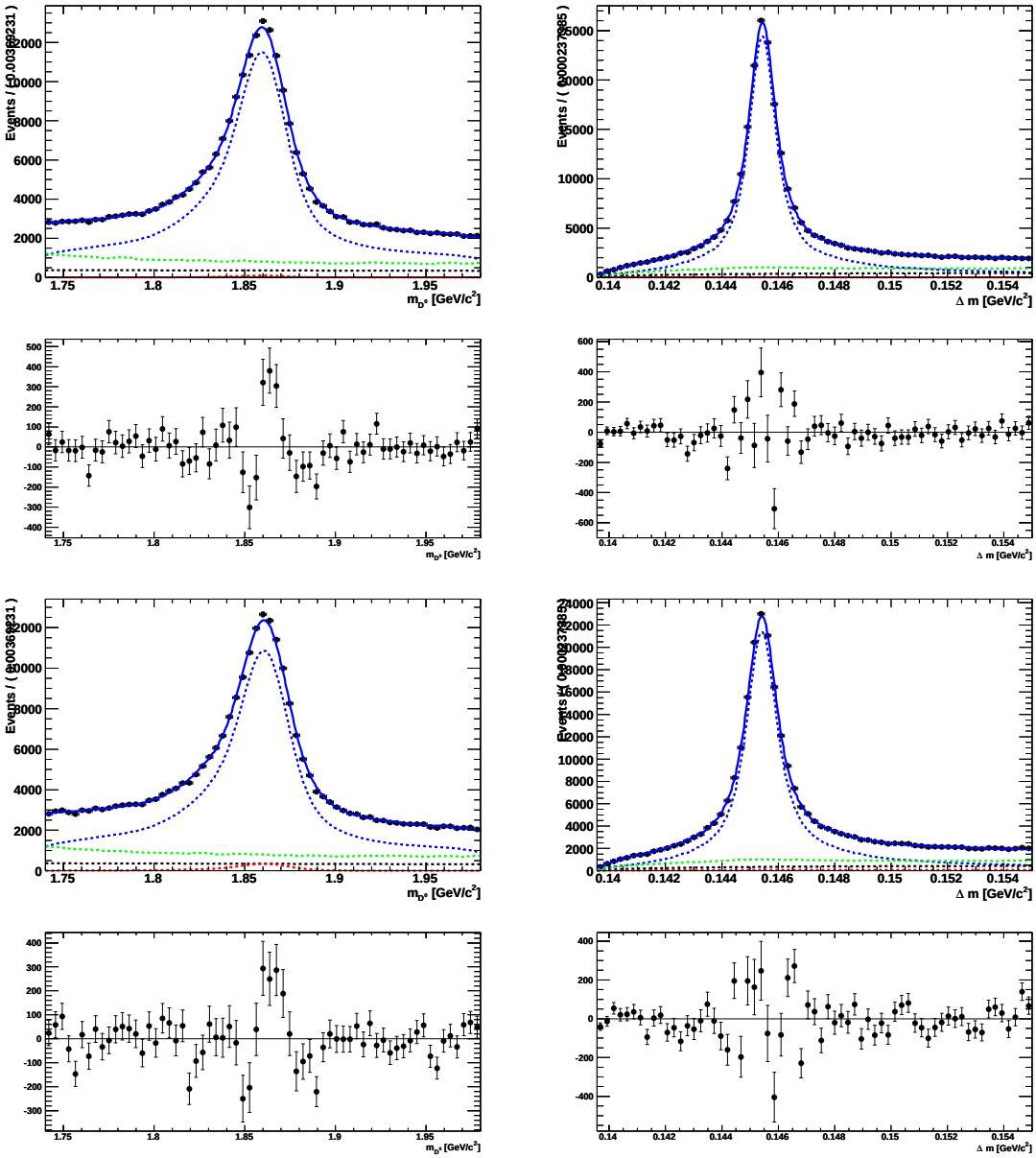

Projections for $\mathrm{p}(\pi^0)$-slice 6. The top plots are fits to MC, the bottom plots fits to data.

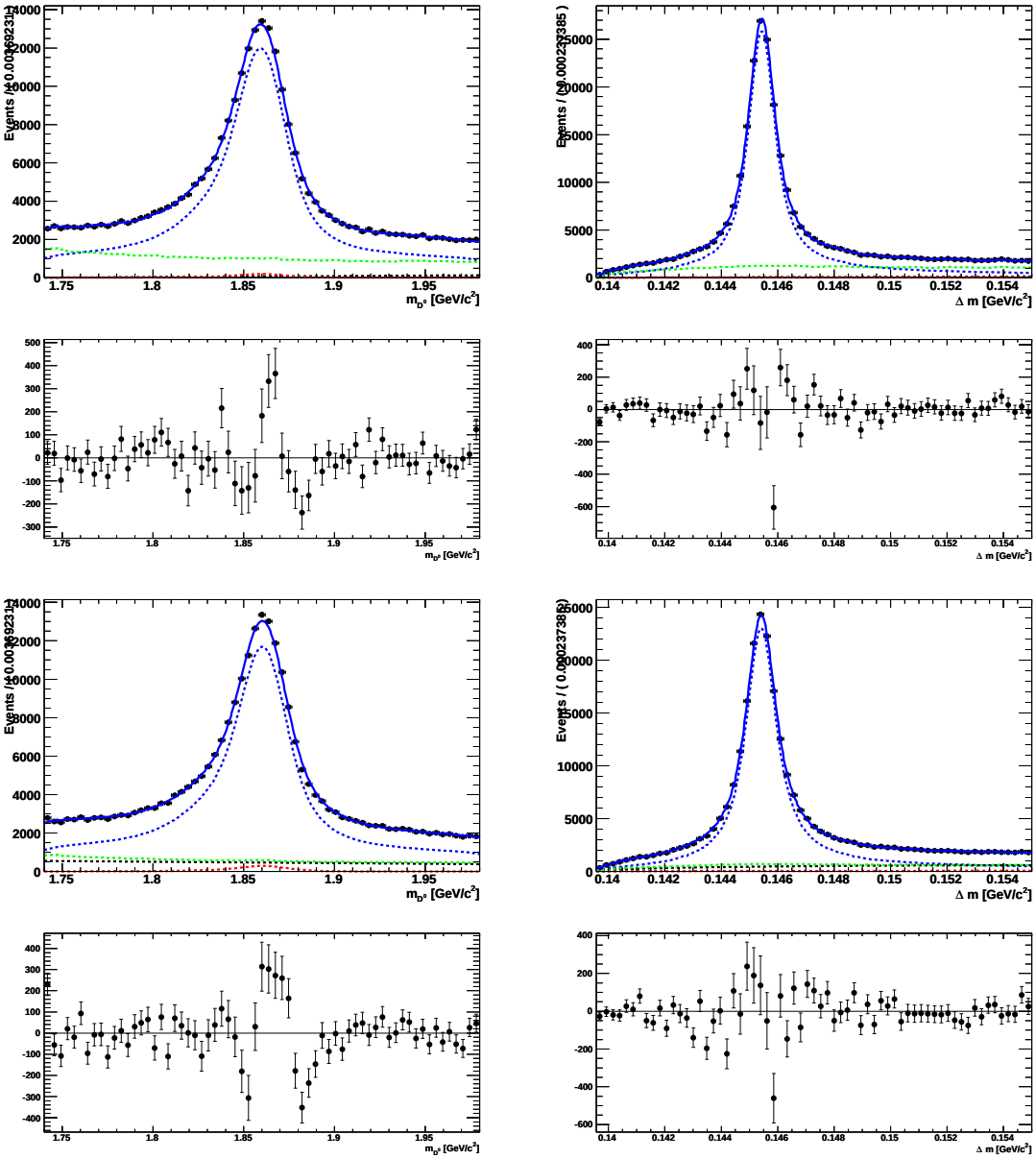

Projections for $\mathrm{p}(\pi^0)$-slice 7. The top plots are fits to MC, the bottom plots fits to data.

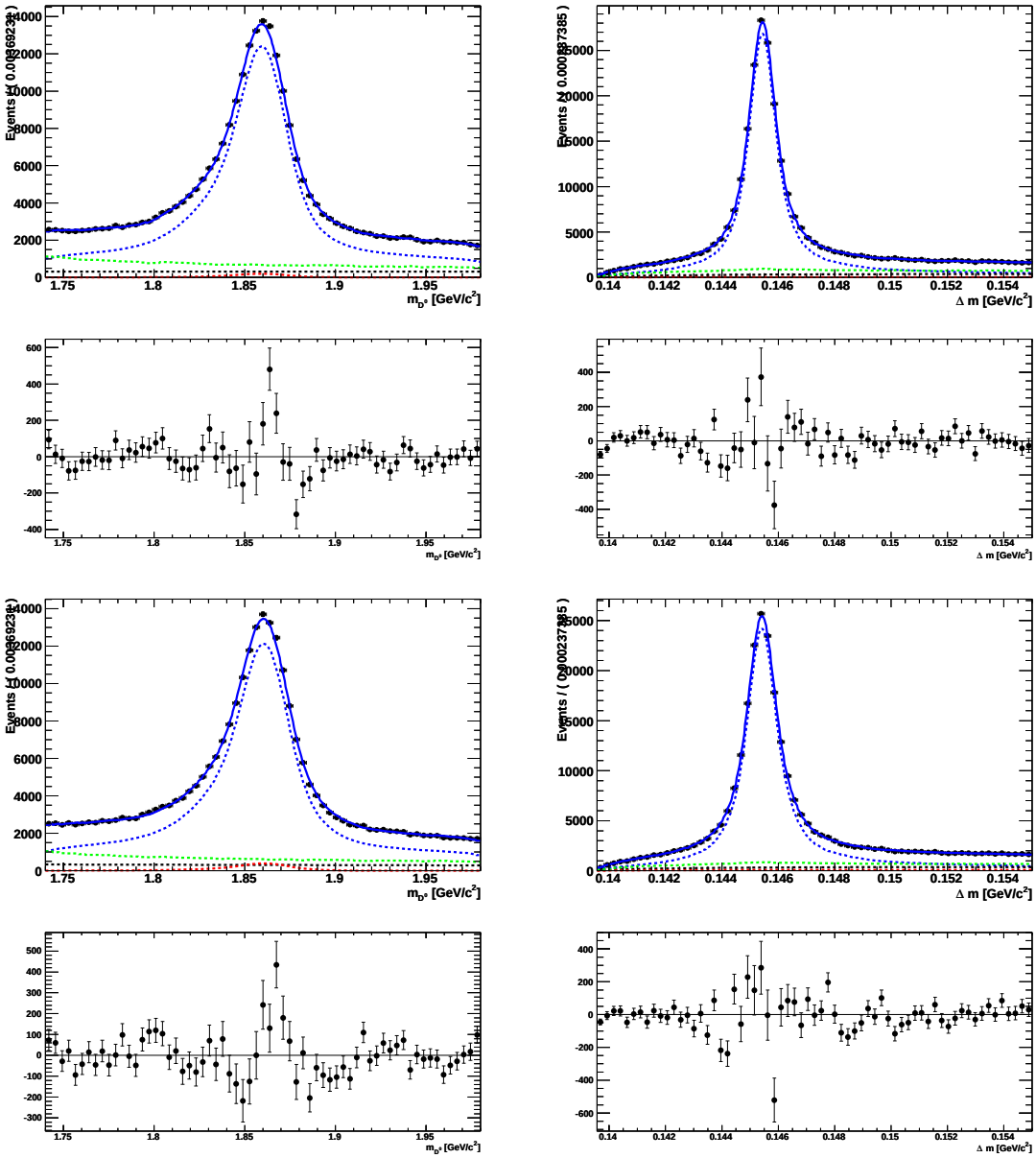

Projections for $\mathrm{p}(\pi^0)$-slice 8. The top plots are fits to MC, the bottom plots fits to data.

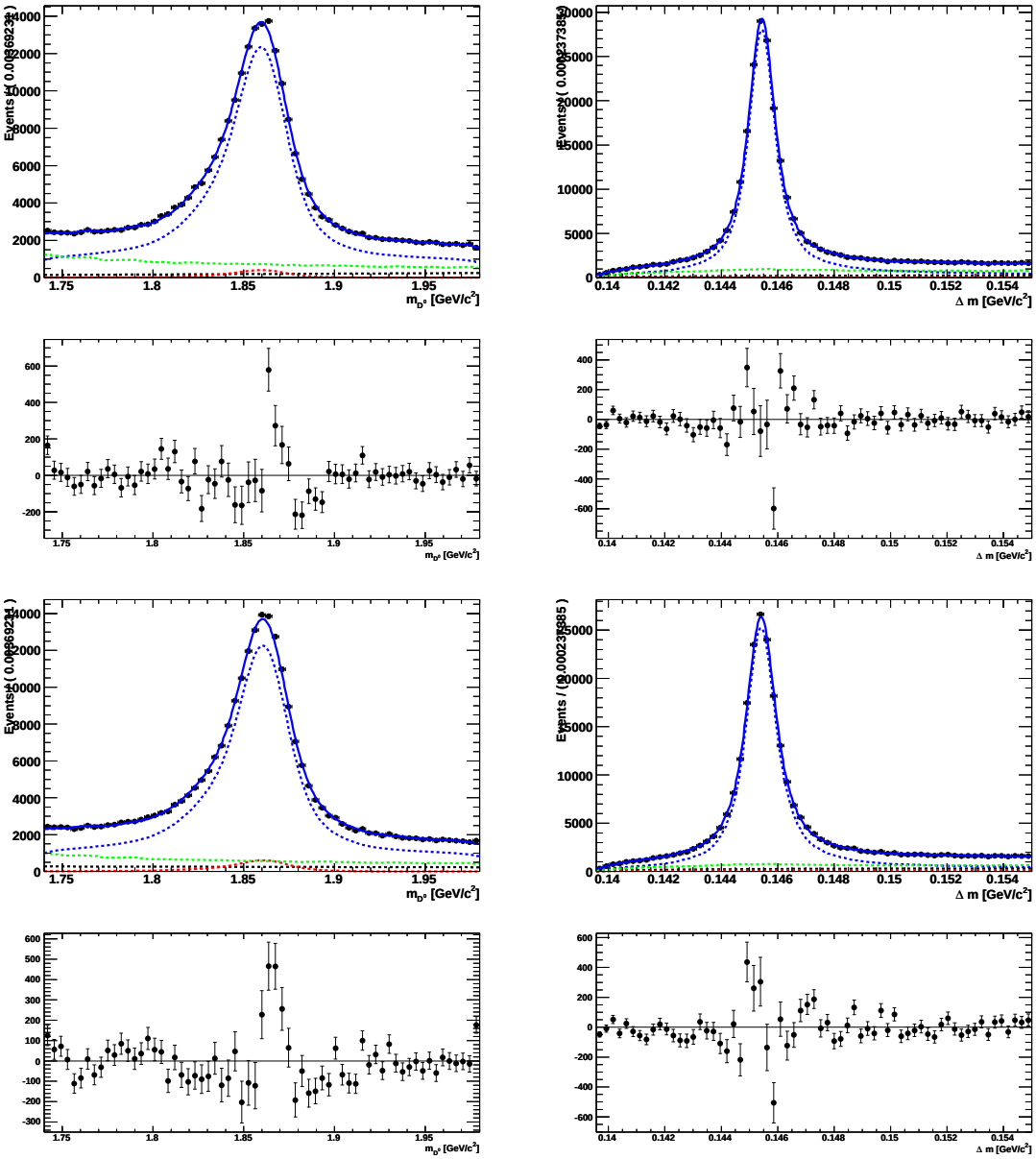

Projections for $\mathrm{p}(\pi^0)$-slice 9. The top plots are fits to MC, the bottom plots fits to data.

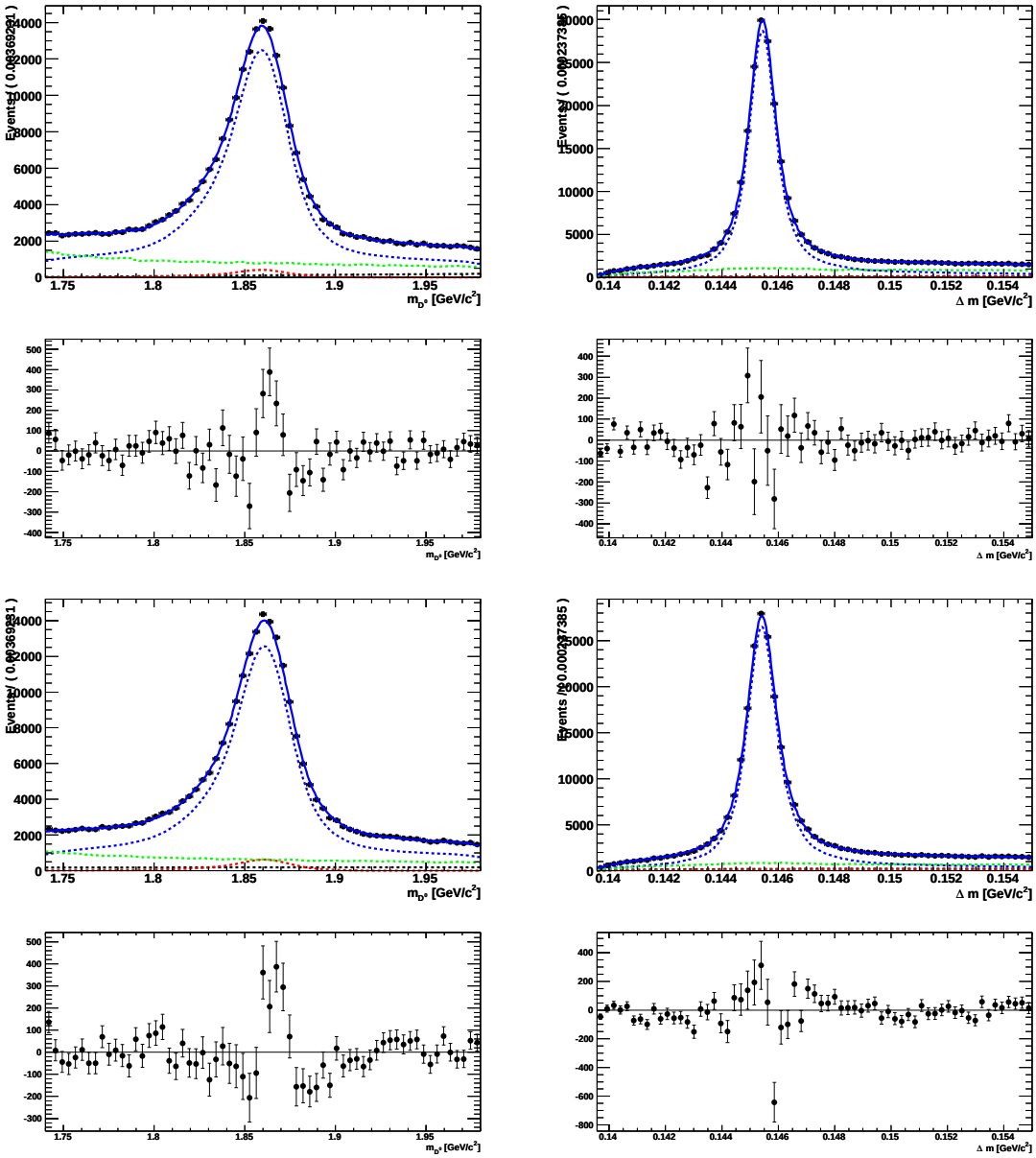

Projections for $\mathrm{p}(\pi^0)$-slice 10. The top plots are fits to MC, the bottom plots fits to data.

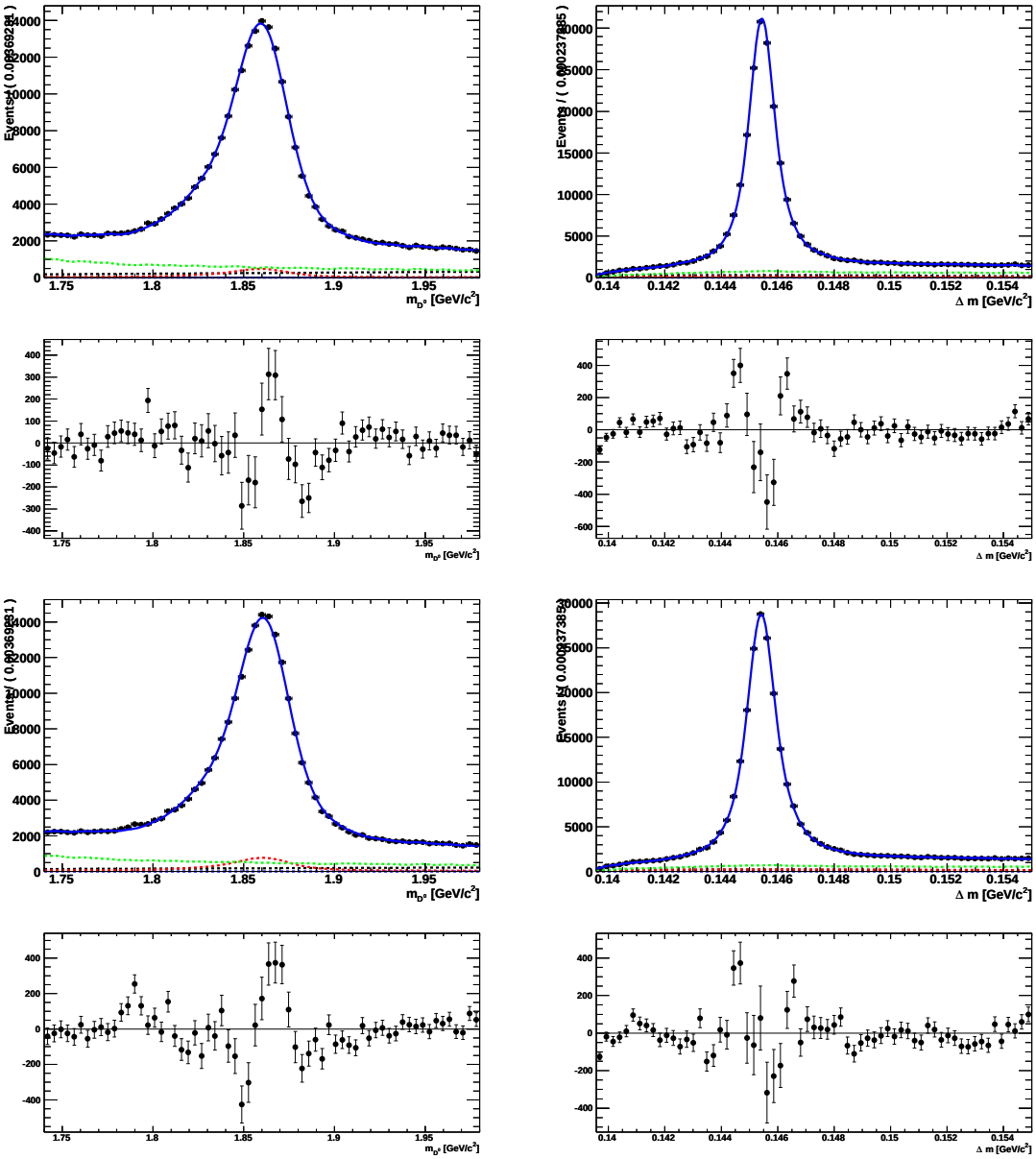

Projections for $\mathrm{p}(\pi^0)$-slice 11. The top plots are fits to MC, the bottom plots fits to data.

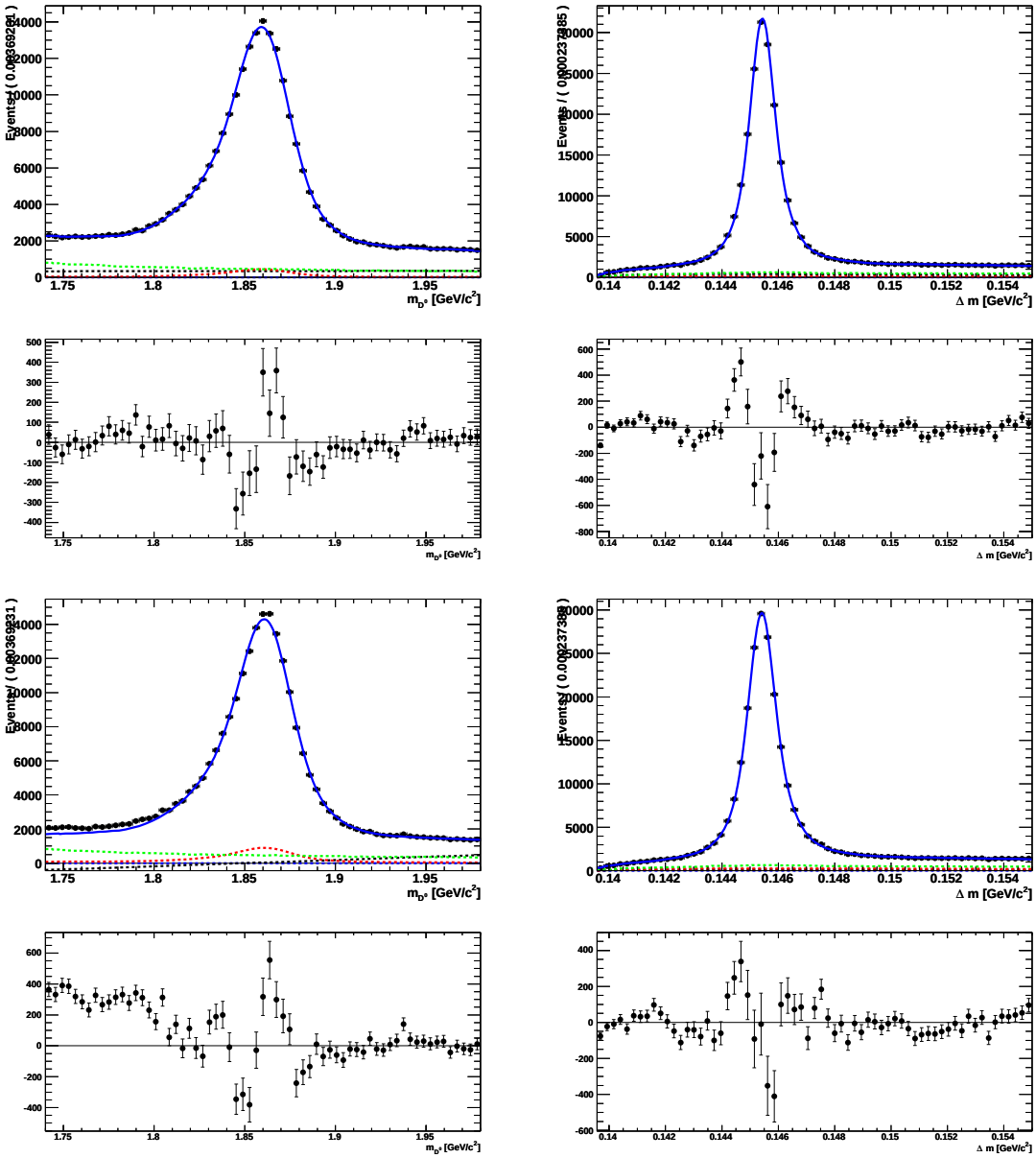

Projections for $\mathrm{p}(\pi^0)$-slice 12. The top plots are fits to MC, the bottom plots fits to data.

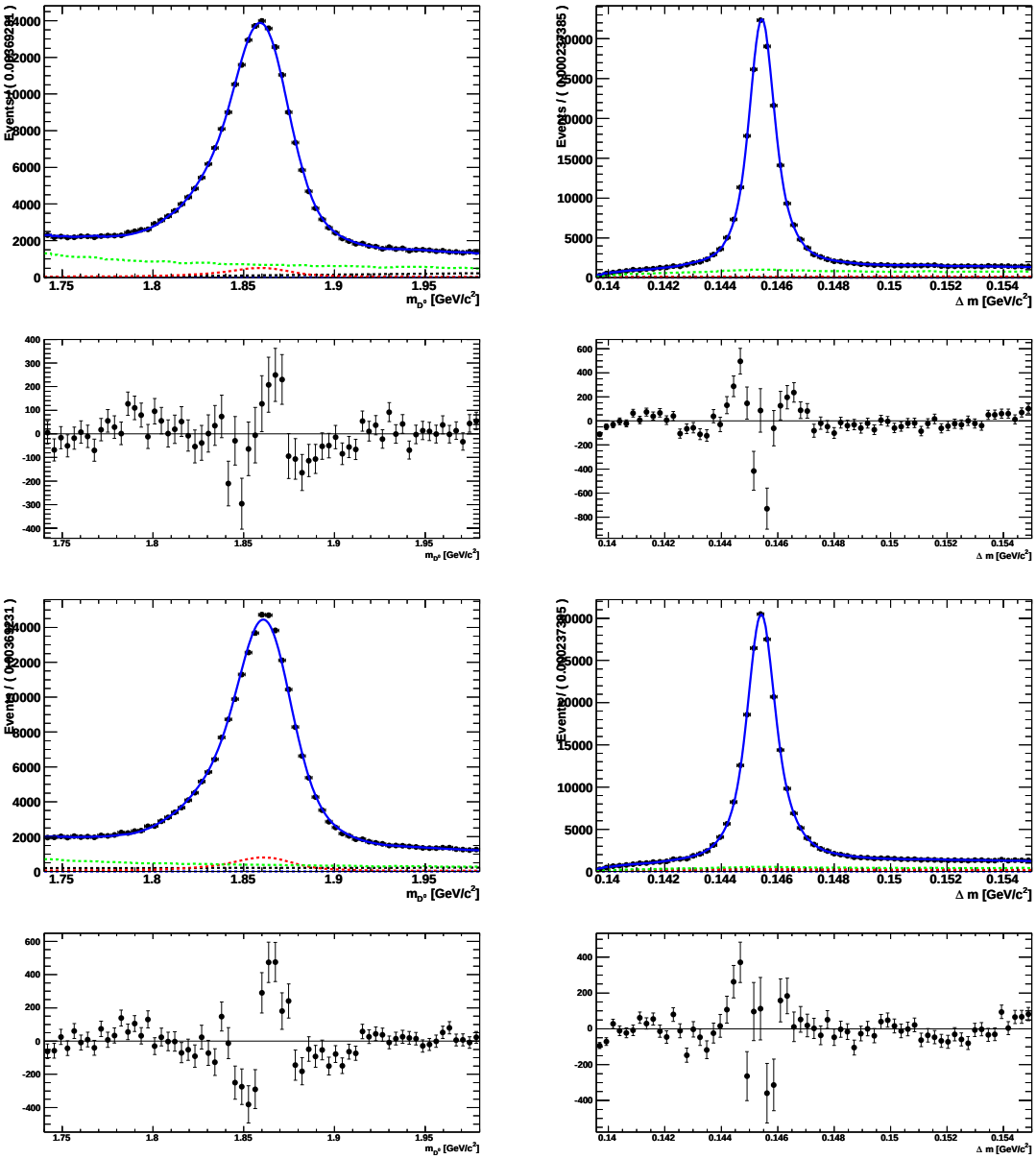

Projections for $\mathrm{p}(\pi^0)$-slice 13. The top plots are fits to MC, the bottom plots fits to data.

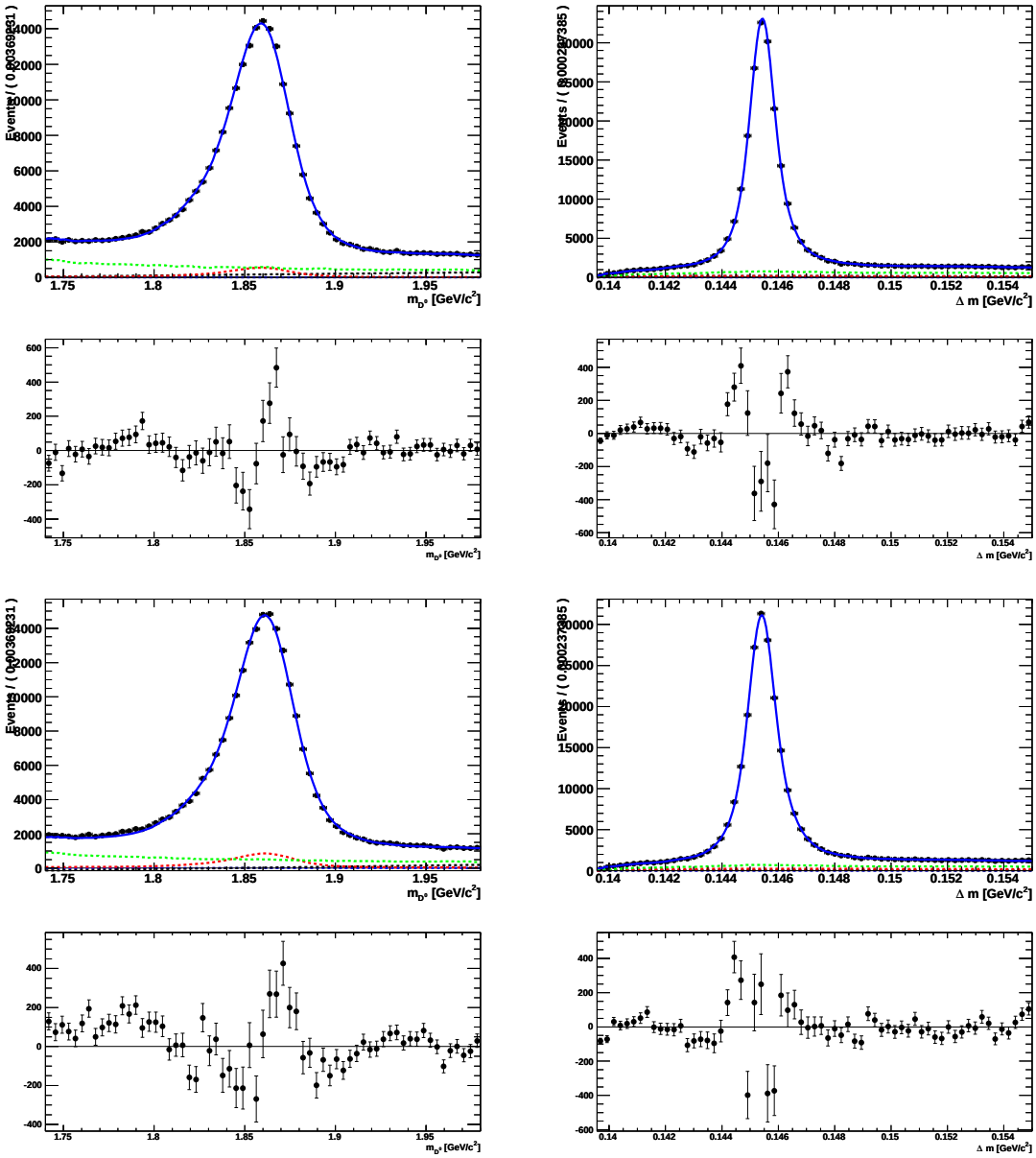

Projections for $\mathrm{p}(\pi^0)$-slice 14. The top plots are fits to MC, the bottom plots fits to data.

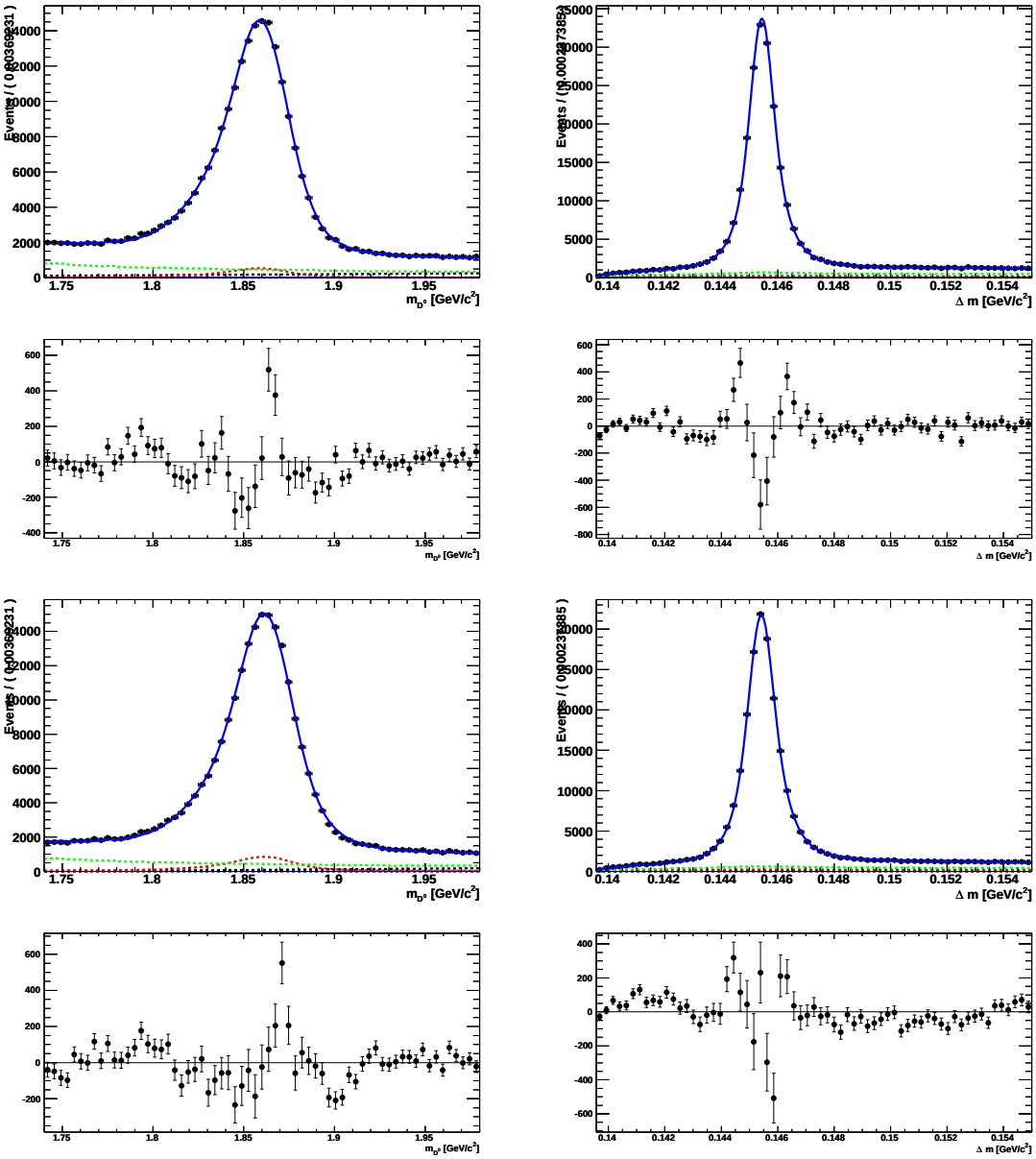

Projections for $\mathrm{p}(\pi^0)$-slice 15. The top plots are fits to MC, the bottom plots fits to data.

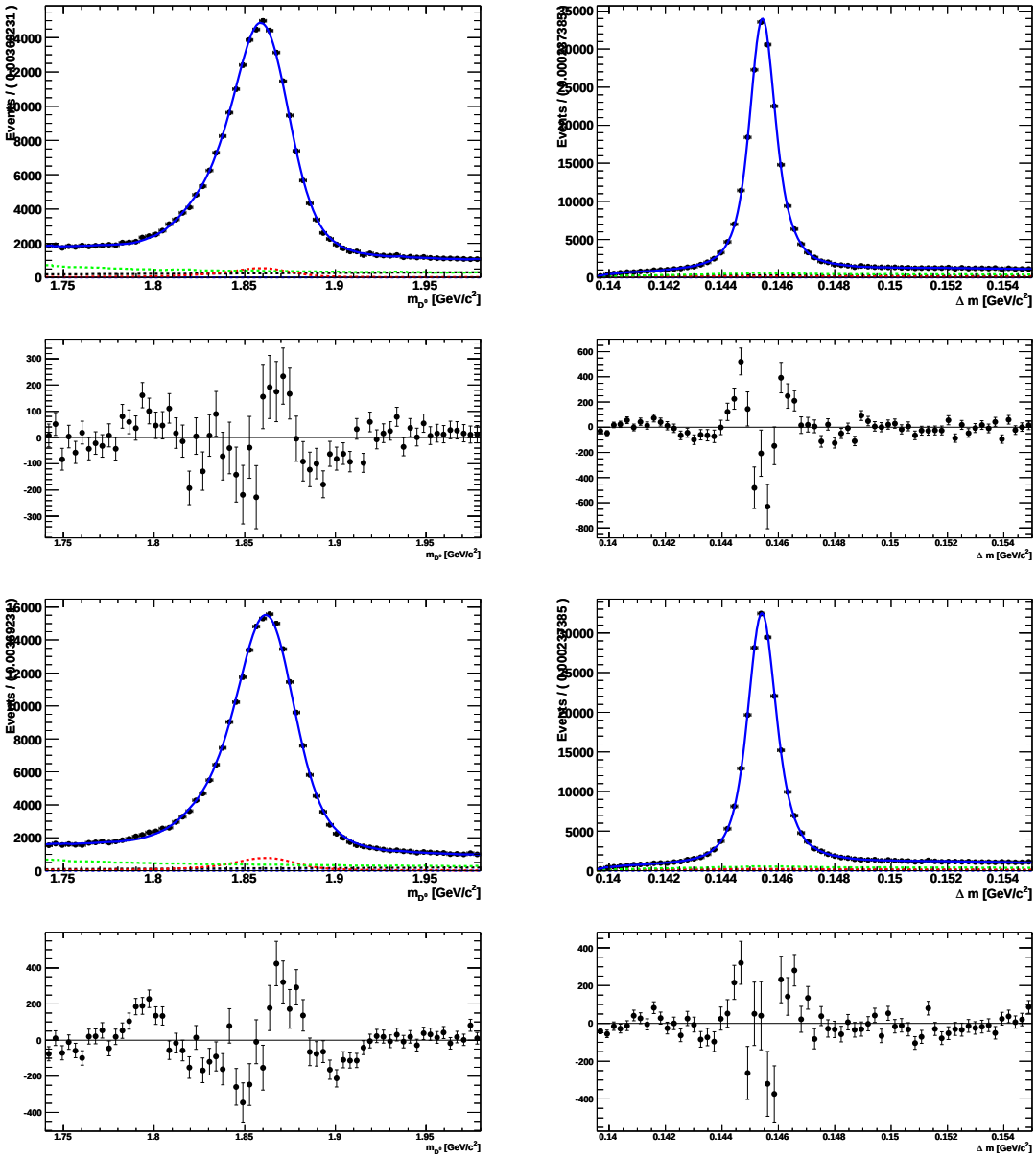

Projections for $\mathrm{p}(\pi^0)$-slice 16. The top plots are fits to MC, the bottom plots fits to data.

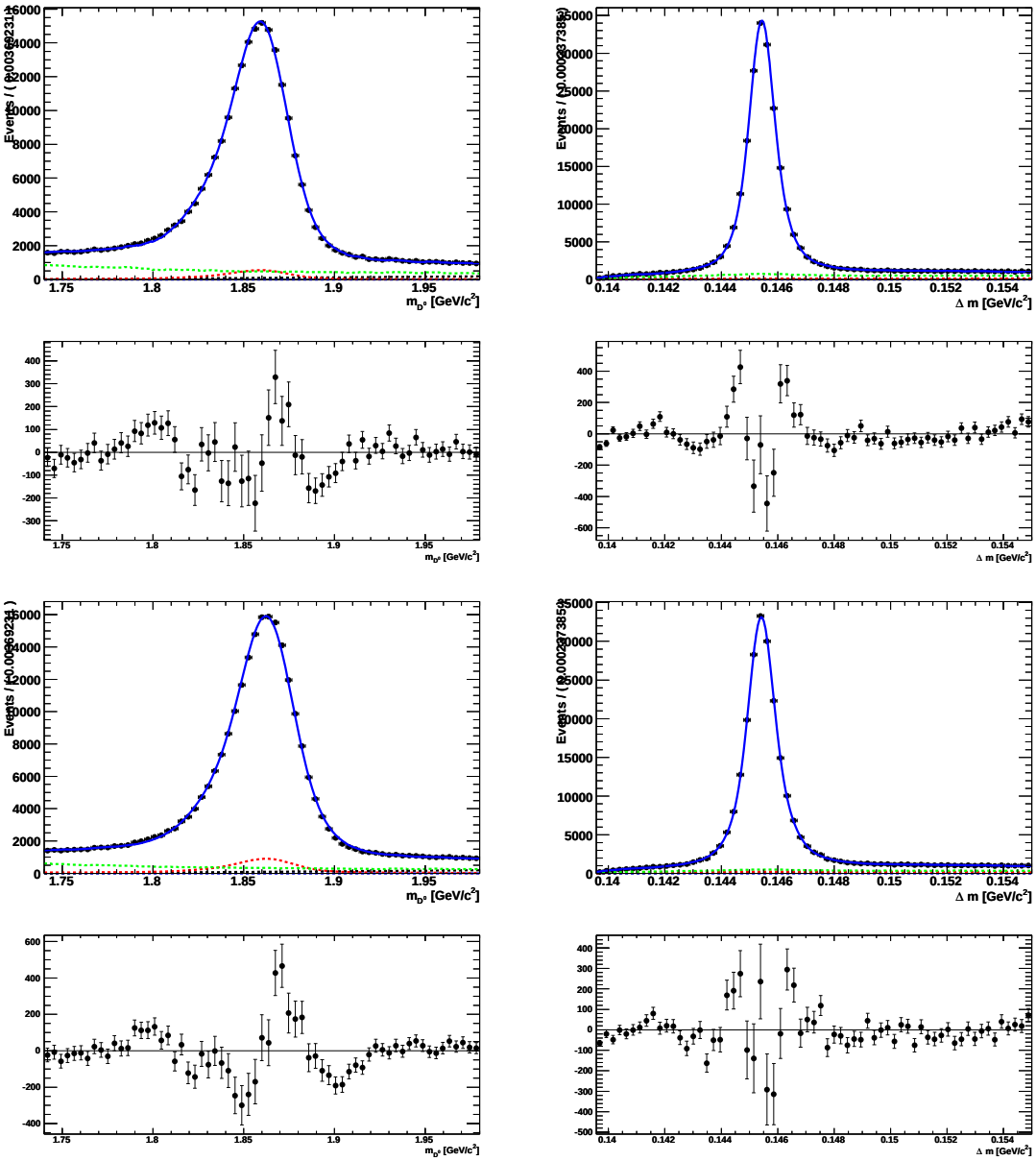

Projections for $\mathrm{p}(\pi^0)$-slice 17. The top plots are fits to MC, the bottom plots fits to data.

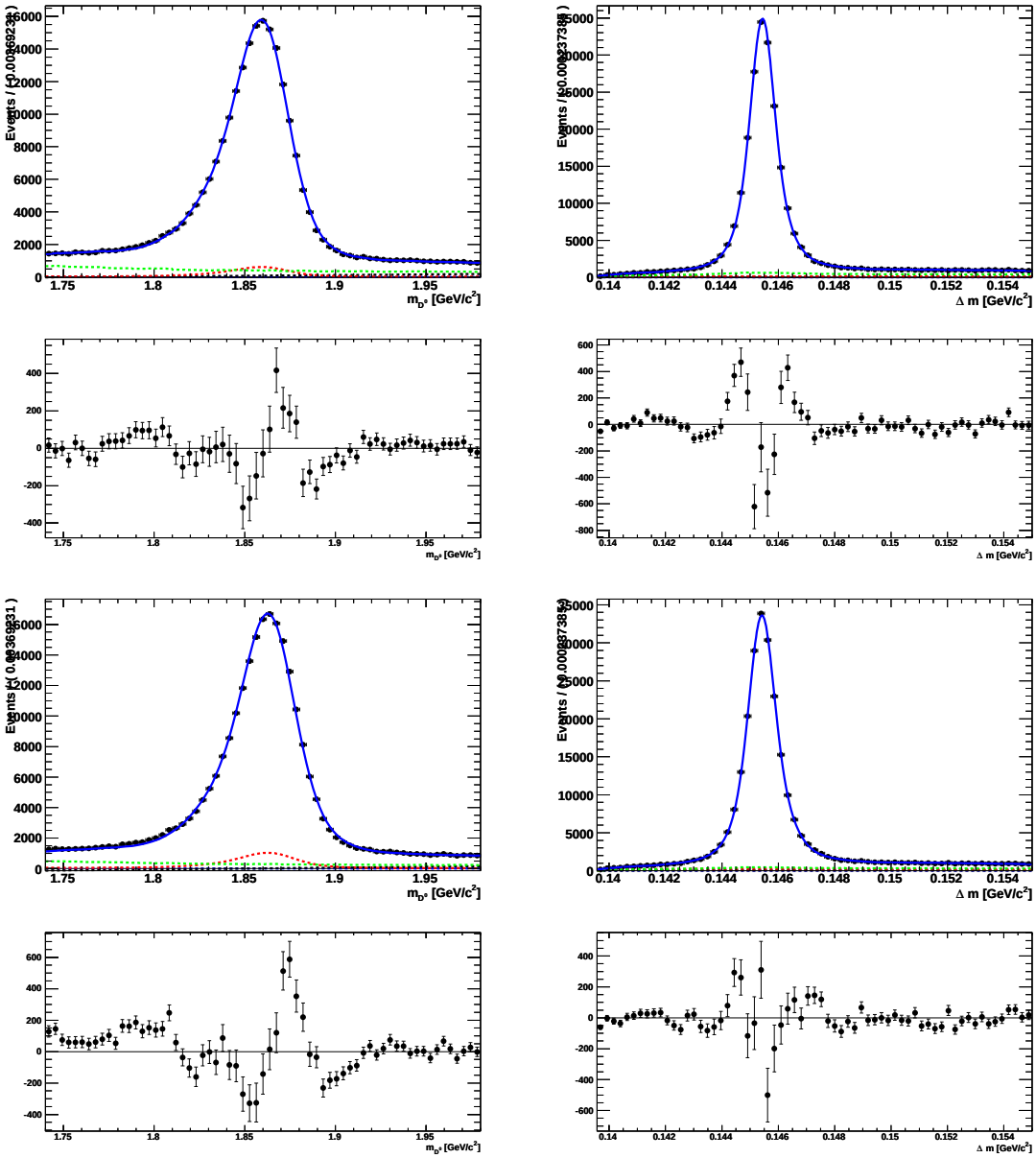

Projections for $\mathrm{p}(\pi^0)$-slice 18. The top plots are fits to MC, the bottom plots fits to data.

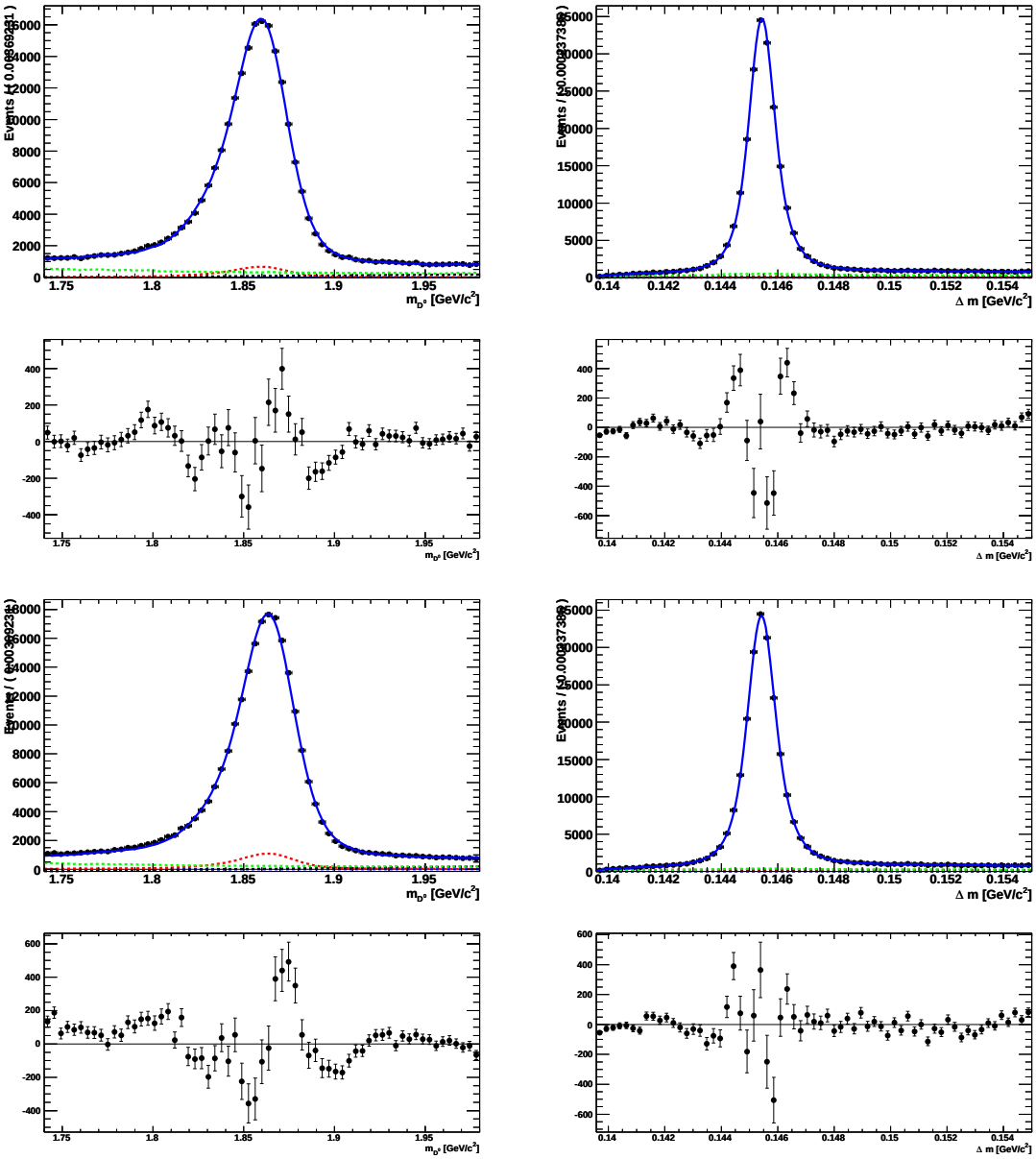

Projections for $\mathrm{p}(\pi^0)$-slice 19. The top plots are fits to MC, the bottom plots fits to data.

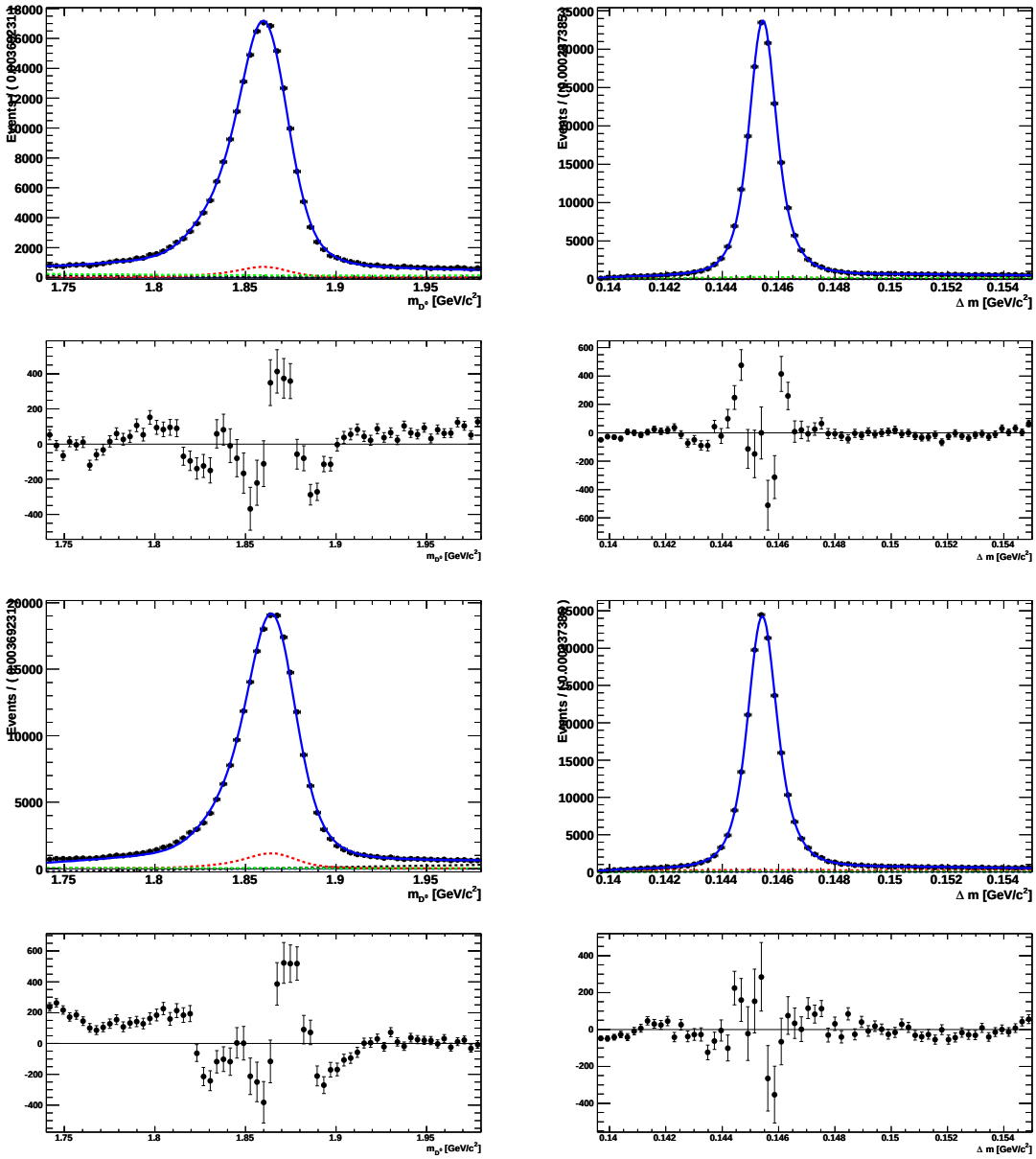

Projections for $\mathrm{p}(\pi^0)$-slice 20. The top plots are fits to MC, the bottom plots fits to data.

B TD analysis

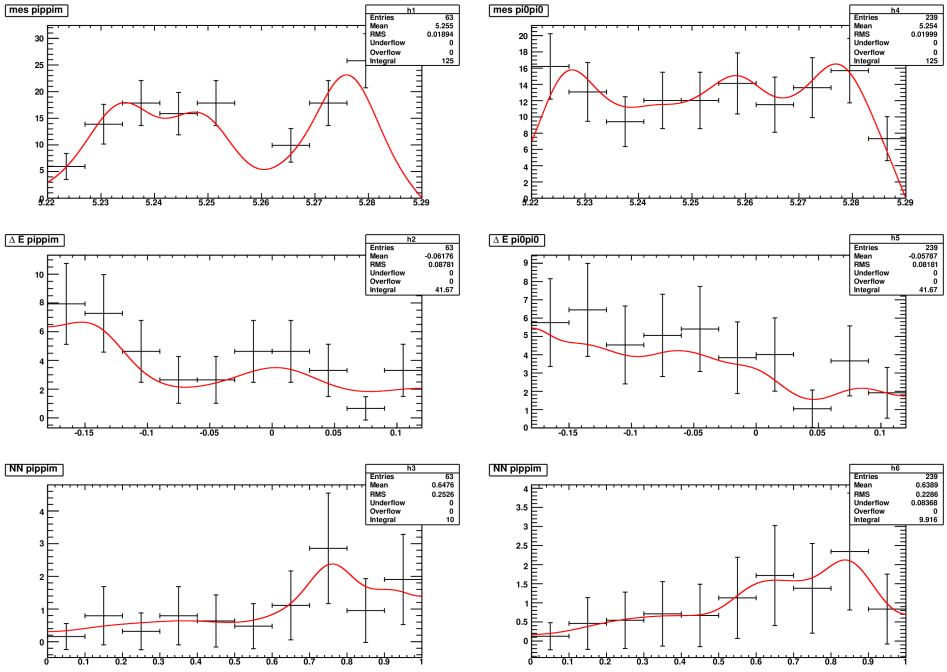

Figure B.1: Neutral generic B background for $\mathrm{B}^0 \rightarrow 3\mathrm{K}^0_\mathrm{s}(\pi^+\pi^-)$ (left) and $B^0 \rightarrow 2K^0_s(\pi^+\pi^-)K^0_s(\pi^0\pi^0)$ (right).

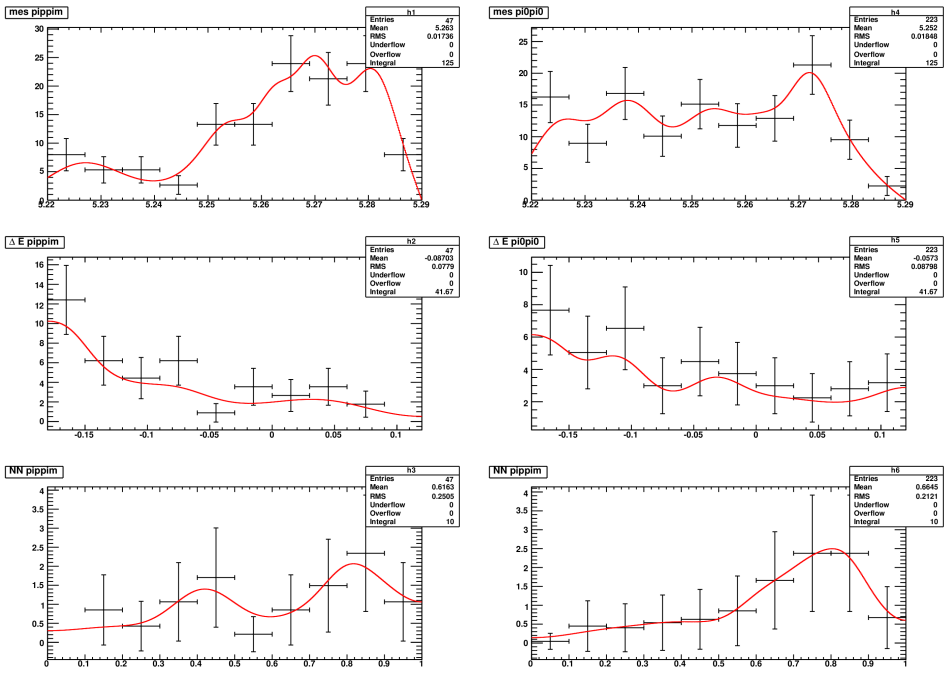

Figure B.2: Charged generic B background for $\mathrm{B}^0 \rightarrow 3\mathrm{K}^0_\mathrm{s}(\pi^+\pi^-)$ (left) and $\mathrm{B}^0 \rightarrow 2\mathrm{K}^0_\mathrm{s}(\pi^+\pi^-)\mathrm{K}^0_\mathrm{s}(\pi^0\pi^0)$ (right).

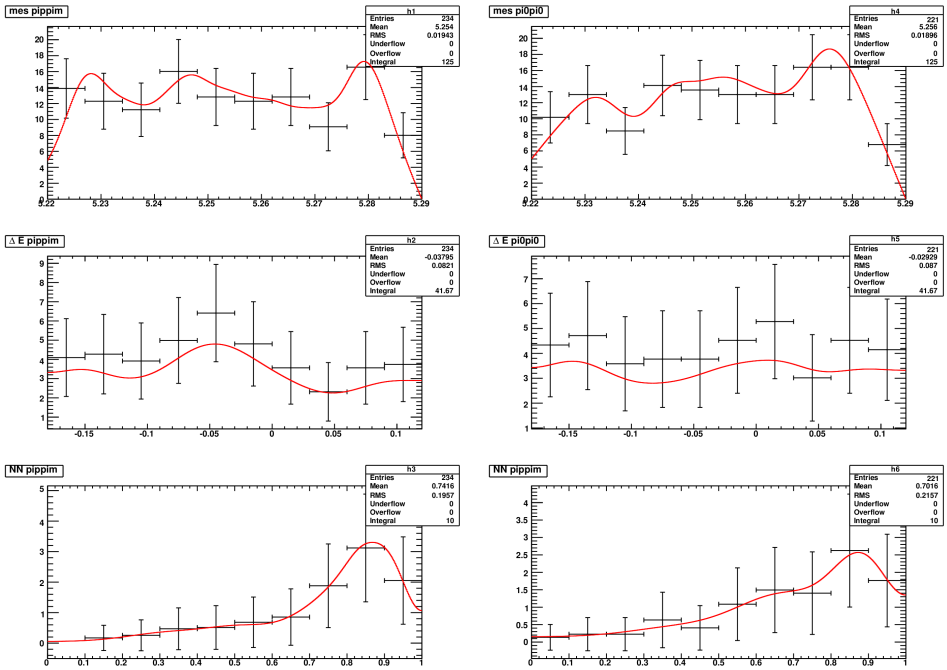

Figure B.3: $\mathrm{K}^0_\mathrm{s}\mathrm{K}^0_\mathrm{s}\mathrm{K}^0_\mathrm{L}$ B background for $\mathrm{B}^0 \rightarrow 3\mathrm{K}^0_\mathrm{s}(\pi^+\pi^-)$ (left) and $B^0 \rightarrow 2K^0_s(\pi^+\pi^-)K^0_s(\pi^0\pi^0)$ (right).

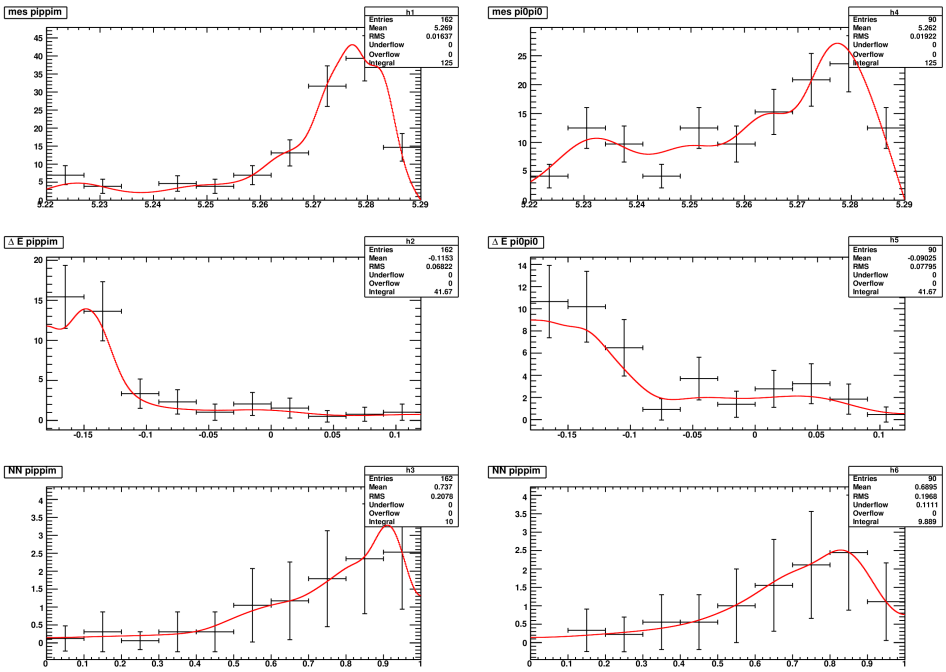

Figure B.4: $K^0_S K^0_S K^{0*}$ B background for $B^0 \to 3K^0_S(\pi^+\pi^-)$ (left) and $B^0 \to 2K^0_S(\pi^+\pi^-)K^0_S(\pi^0\pi^0)$ (right).

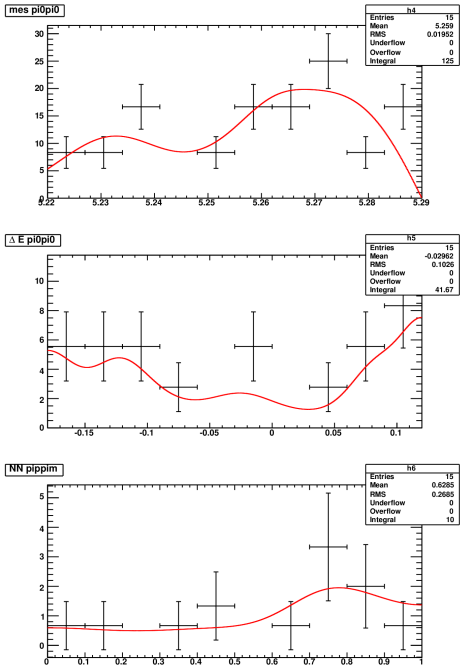

Figure B.5: $K^0_S K^0_L K^{0*}$ B background for $B^0 \to 2K^0_S(\pi^+\pi^-)K^0_S(\pi^0\pi^0)$.

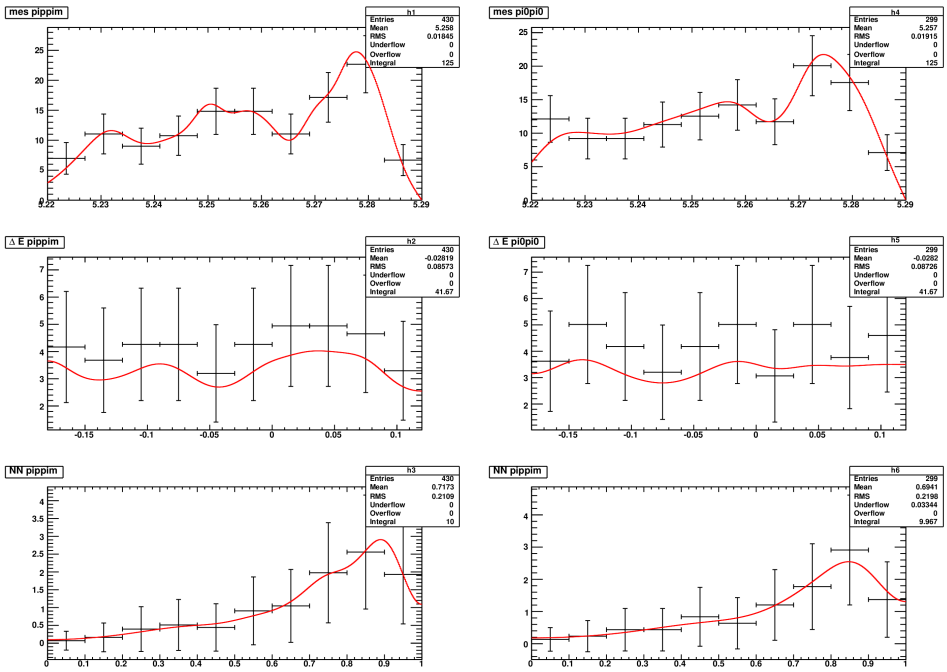

Figure B.6: $K^+K^0_sK^0_s$ B background for $B^0 \to 3K^0_s(\pi^+\pi^-)$ (left) and $B^0 \to 2K^0_s(\pi^+\pi^-)K^0_s(\pi^0\pi^0)$ (right).

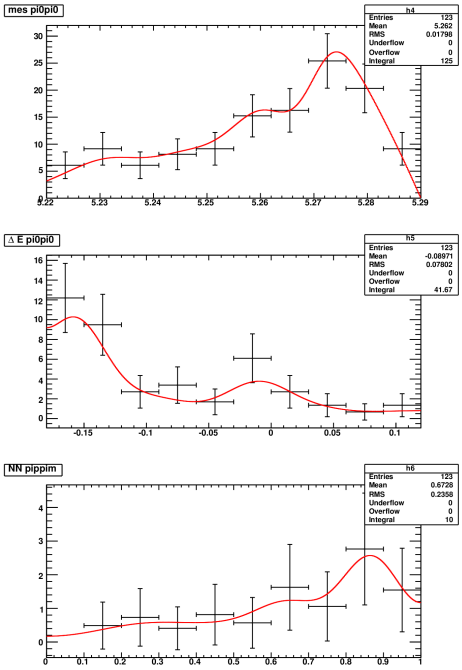

Figure B.7: $K^{+*}K^0_sK^0_s$ B background for $B^0 \to 2K^0_s(\pi^+\pi^-)K^0_s(\pi^0\pi^0)$.

Parameter	generated	$mean_{Gauss-fit}$	$\sigma_{Gauss-fit}$
Signal			
$\mathcal{C}$	0	0.00835857± 0.0481121	0.990382 ± 0.0424254
$\mathcal{S}$	-0.7033	-0.0412034 ± 0.0494202	0.999745 ± 0.0368743
N_{pm}	193.17	-0.00473168 ± 0.0463111	0.954301 ± 0.0326686
N_{00}	86.49	-0.0412075 ± 0.0468025	0.978676± 0.0336913
$m_{ES}mean_{pm}$	5.2772	-0.0769433 ± 0.0435357	0.859489± 0.0338821
$\Delta Emean_{pm}$	-0.000764933	0.0517518 ± 0.0522481	0.97369± 0.0415295
Continuum			
$N_{notag,pm}$	978.78	-0.0317691 ± 0.046889	0.971261 ± 0.0333408
$N_{lepton,pm}$	19.33	0.106027 ±0.0470202	0.894451± 0.0377686
$N_{kaon1,pm}$	288.75	-0.0517638±0.0465272	0.951426± 0.03956
$N_{kaon2,pm}$	492.23	0.00491552±0.0477593	0.997195± 0.0343263
$N_{kaonpion,pm}$	344.45	0.0550192±0.0477309	0.983775± 0.0357926
$N_{pion,pm}$	409.25	-0.00730759±0.0521725	0.949432± 0.0372212
$N_{other,pm}$	359.23	0.0333986±0.0487026	1.01336± 0.0371358
$N_{notag,00}$	2832.03	-0.0256863±0.0475732	0.971492± 0.0394136
$N_{lepton,00}$	61.04	0.0119497±0.0460215	0.939527± 0.0338115
$N_{kaon1,00}$	477.09	0.0173474±0.0509133	1.04833± 0.0380202
$N_{kaon2,00}$	918.84	0.0325718±0.0464365	0.961994± 0.0353892
$N_{kaonpion,00}$	861.01	-0.10059±0.0479542	0.982136± 0.0374445
$N_{pion,00}$	1140.52	0.0434209±0.051519	1.0532± 0.0393291
$N_{other,00}$	920.45	0.0266457±0.0504467	1.03651± 0.0408453
ARGUS-par($m_{ES,pm}$)	-30.892	0.00613475±0.0484304	1.00963± 0.0349377
ARGUS-par($m_{ES,00}$)	-25.144	-0.0323597±0.0514386	0.999737± 0.0382807
Poly-Par($DeltaE_{pm}$)	-1.0917	-0.0577009±0.0512593	1.02939± 0.0390263
Poly-Par($DeltaE_{00}$)	-1.4501	-0.0777566±0.0503457	1.04164± 0.043893
$NNpar1_{00}$)	0.557569	-0.00702153±0.0443683	0.658173± 0.0316174
$NNpar2_{00}$)	0.545081	0.0791056±0.0551378	1.09759± 0.0439093
$NNpar3_{00}$)	4.61274	0.0207806±0.0509456	0.85231± 0.0411782
$NNpar4_{00}$)	2.94361	0.0626806±0.0472311	0.892233± 0.0419154
$NNpar5_{00}$)	1.57656	0.0870328±0.0453204	0.906049± 0.0341674
$NNpar6_{00}$)	0.154671	0.354478±0.0568959	0.820301± 0.0327471
$NNpar1_{pm}$)	0.561204	-0.278034±0.113026	0.873429± 0.0712128
$NNpar2_{pm}$)	1.28643	0.0813185±0.0446069	0.924493± 0.0322544
$NNpar3_{pm}$)	6.81949	0.203472±0.0465349	0.932473± 0.0340021
$NNpar4_{pm}$)	3.50325	0.15927±0.0535836	1.01428± 0.0337363
$NNpar5_{pm}$)	1.47895	-0.0499623±0.0495422	0.978019± 0.0323248
$NNpar6_{pm}$)	0.242551	0.184348±0.0835683	0.799501± 0.052504
TailFrac pm:	0.243127	0.0241999±0.0518261	0.988952± 0.0469698
TailFrac 00:	0.170565	0.0037146±0.0490998	0.927736± 0.0331719
OutlFrac pm:	0.0125658	0.144966±0.0450287	0.835057± 0.0325227
OutlFrac 00:	0.0221525	0.113061±0.0500593	1.00351± 0.038593
CoreBias pm:	0.360908	-0.00713051±0.0468594	0.974028± 0.0325411
CoreBias 00:	0.158698	-0.0285257±0.048389	0.99979± 0.0367433
TailBias pm:	0.505503	-0.0525405±0.0476641	0.926453± 0.0313637
TailBias 00:	0.101235	-0.00343315±0.0459645	0.959796± 0.0366158
CoreSigma pm:	1.43848	-0.0948772±0.0485237	0.990674± 0.0363175
CoreSigma 00:	1.28054	-0.0729561±0.0475572	0.9948± 0.0378663
B background			
$N_{B^0\bar{B}^0}$ pm:	21.7125	-0.135713±0.0555617	1.09171± 0.0491598
$N_{B^0\bar{B}^0}$ 00:	73.62	-0.0214777±0.0519046	1.02261± 0.0418182
$N_{B^+B^-}$ pm:	15.5539	-0.074634±0.0551479	1.10176± 0.0391927
$N_{B^+B^-}$ 00:	73.8	-0.0110317±0.0506484	1.02788± 0.0397902

Table B.1: Fit results of Gaussian fits to pull distributions of all parameters that are free to vary in pure toy studies

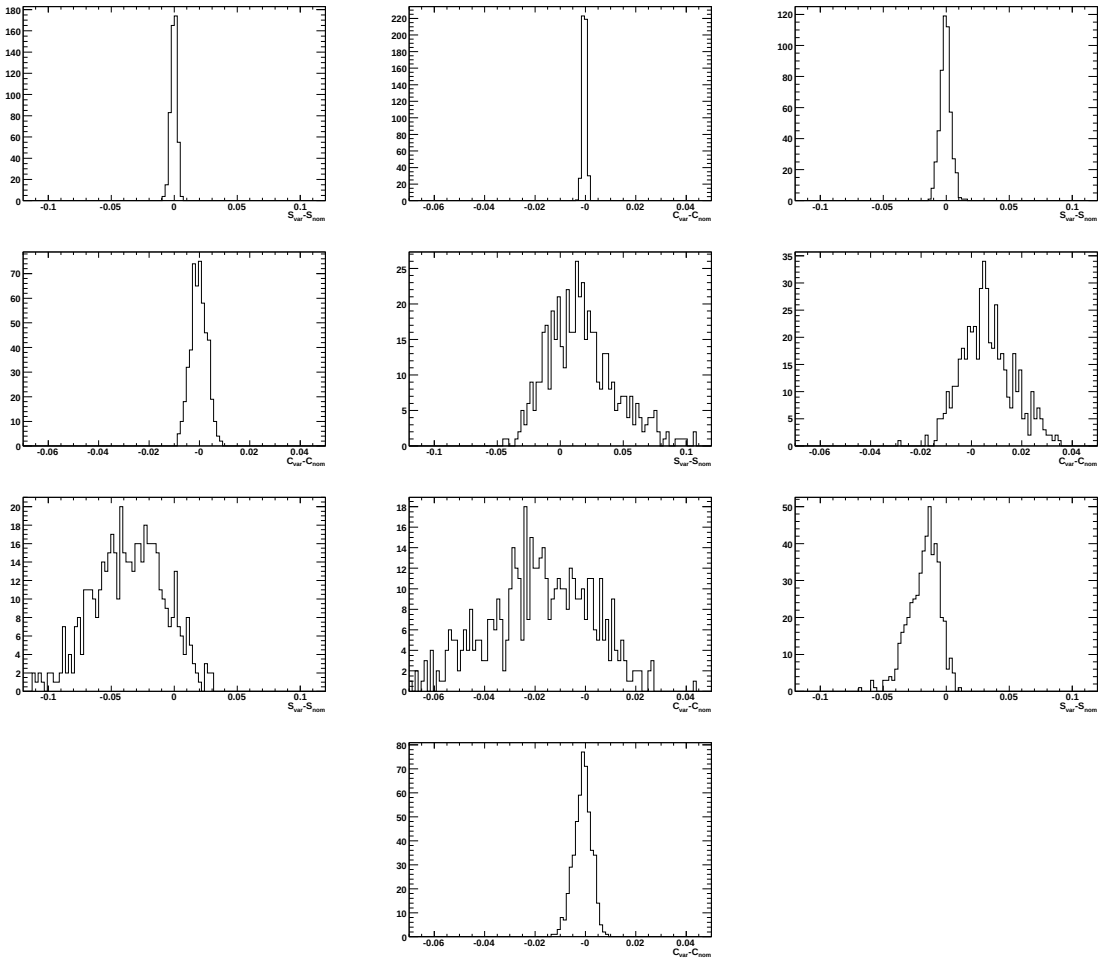

Figure B.8: Differences between the nominal fit values and the varied fits for the S parameter on the left and the C parameter on the right. The first row shows the differences from variations of the MC fit results for the discriminating variables , the second row for the "$\mathrm{B_{reco}}/\Delta\mathrm{t_{stat}}$" parameters, the third for B-background, the forth for MC-data differences in the $\Delta\mathrm{t}$ resolution function and the fifth for the MC-data differences in the discriminating variables.

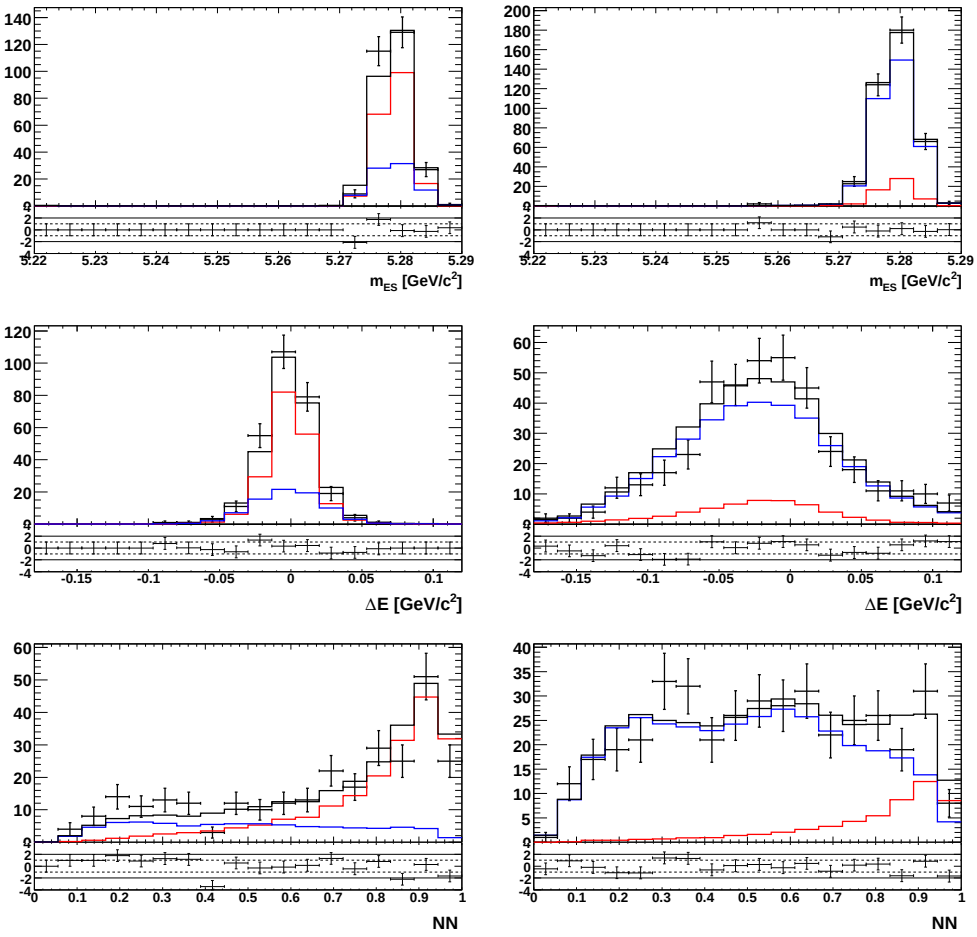

Figure B.9: Projection plots for $\mathrm{B}^0 \to 3\mathrm{K}^0_\mathrm{s}(\pi^+\pi^-)$ (left) and $\mathrm{B}^0 \to 2\mathrm{K}^0_\mathrm{s}(\pi^+\pi^-)\mathrm{K}^0_\mathrm{s}(\pi^0\pi^0)$ (right), $\mathrm{m_{ES}}$ on the top, $\Delta\mathrm{E}$ in the middle and NN in the bottom. The plots include signal (blue), background (red) and the total PDF (black). The plots are signal-enriched by requireing the signal likelihood ratio to larger than 0.3.

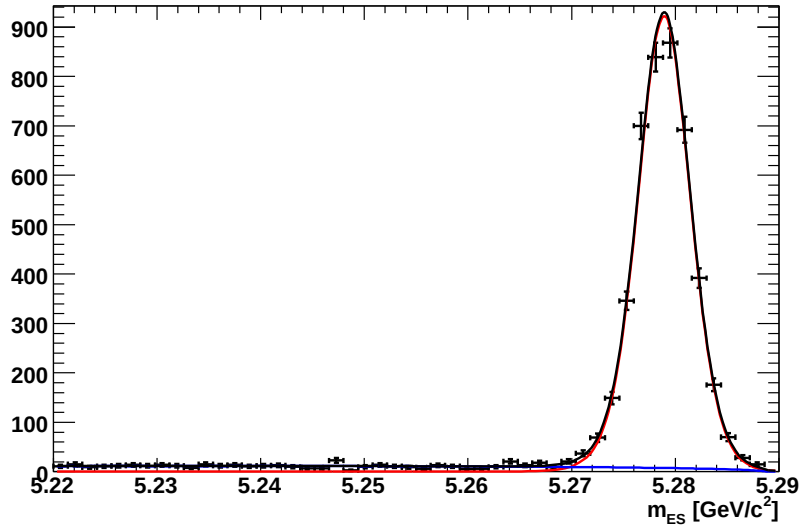

Figure B.10: Projection plots for the $\mathrm{m_{ES}}$ fit of the control sample. The sample is very clean, the plot is not signal-enriched.

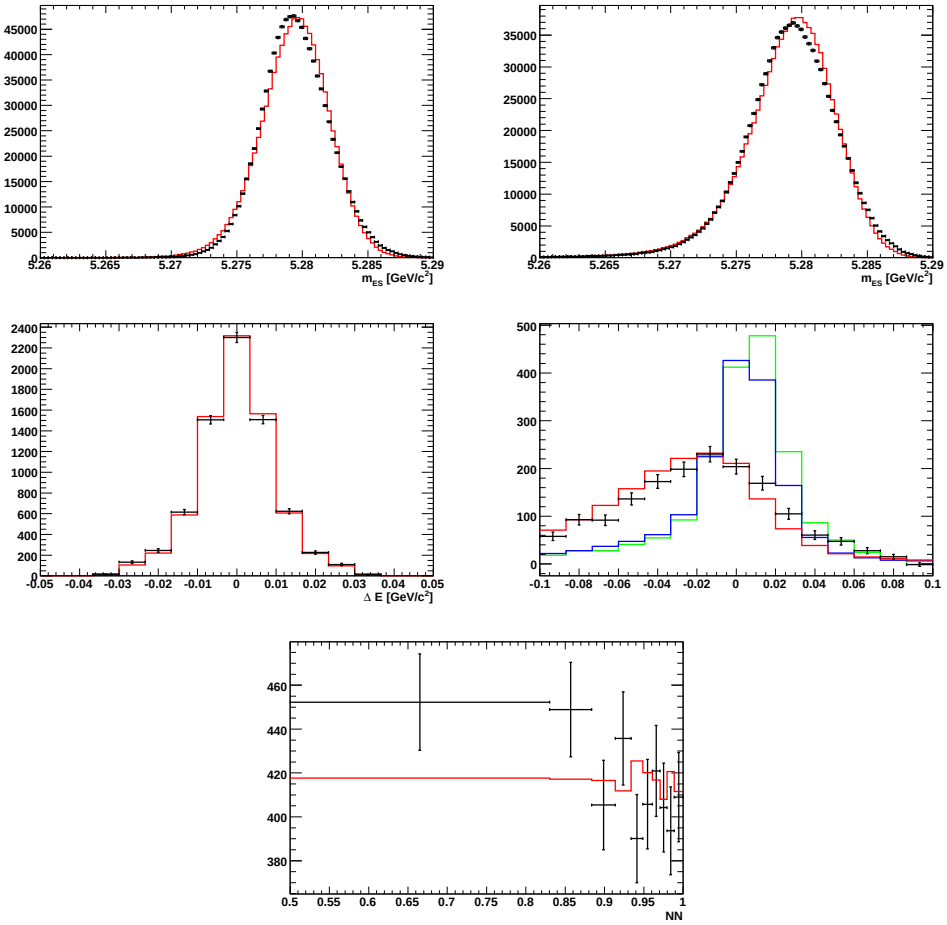

Figure B.11: MC data differences in $\mathrm{B}^0 \to \mathrm{J}/\psi\,\mathrm{K}^0_\mathrm{s}(\pi^+\pi^-)$ (left) and $\mathrm{B}^0 \to \mathrm{J}/\psi\,\mathrm{K}^0_\mathrm{s}(\pi^+\pi^-)$ (right).

C DP analysis

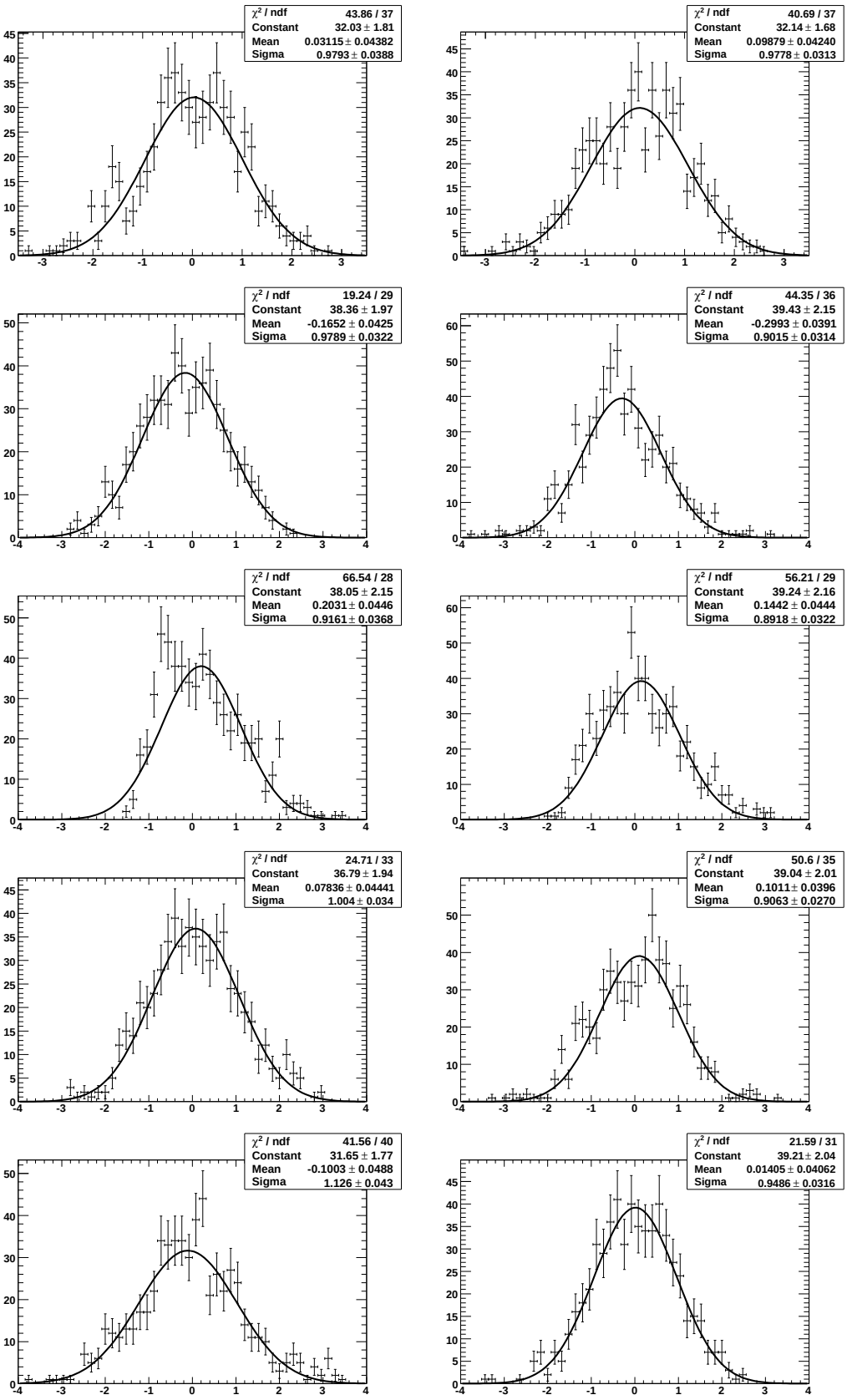

Figure C.1: Pulls of the embedded toy fits for the nominal model. The first row shows the pulls for the signal yield (left) and the continuum yield (right), the second row of the magnitude (left) and the phase (right) of the $\mathrm{f}_2(2010)$, the third row of the $\mathrm{f}_0(980)$, the forth row of the $\mathrm{f}_0(1710)$ and the fifth row of the χ_{c0}.

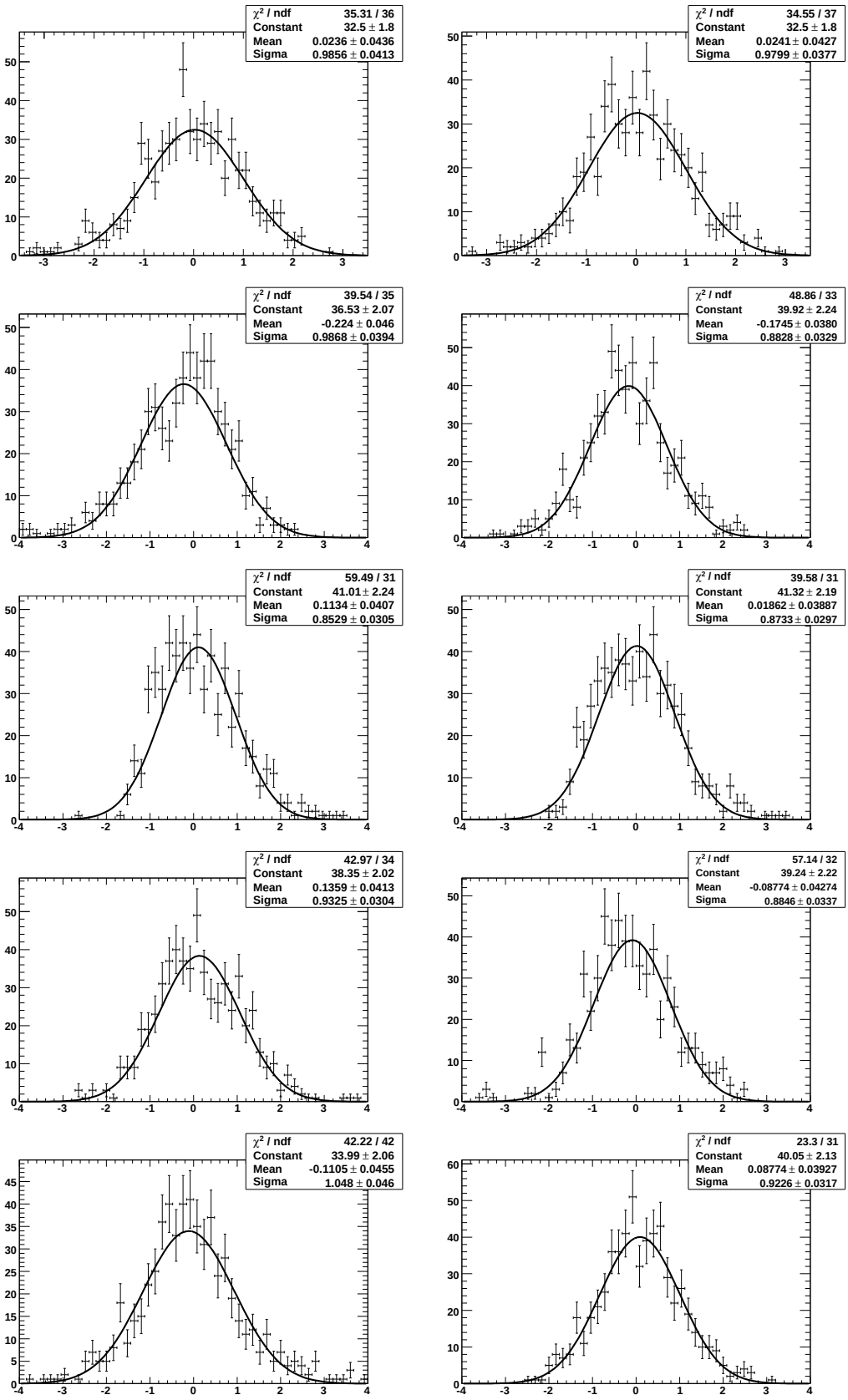

Figure C.2: Pulls of the pure toy fits for the nominal model. The first row shows the pulls for the signal yield (left) and the continuum yield (right), the second row of the magnitude (left) and the phase (right) of the $\mathrm{f}_2(2010)$, the third row of the $\mathrm{f}_0(980)$, the forth row of the $\mathrm{f}_0(1710)$ and the fifth row of the $\chi_{\mathrm{c}0}$.

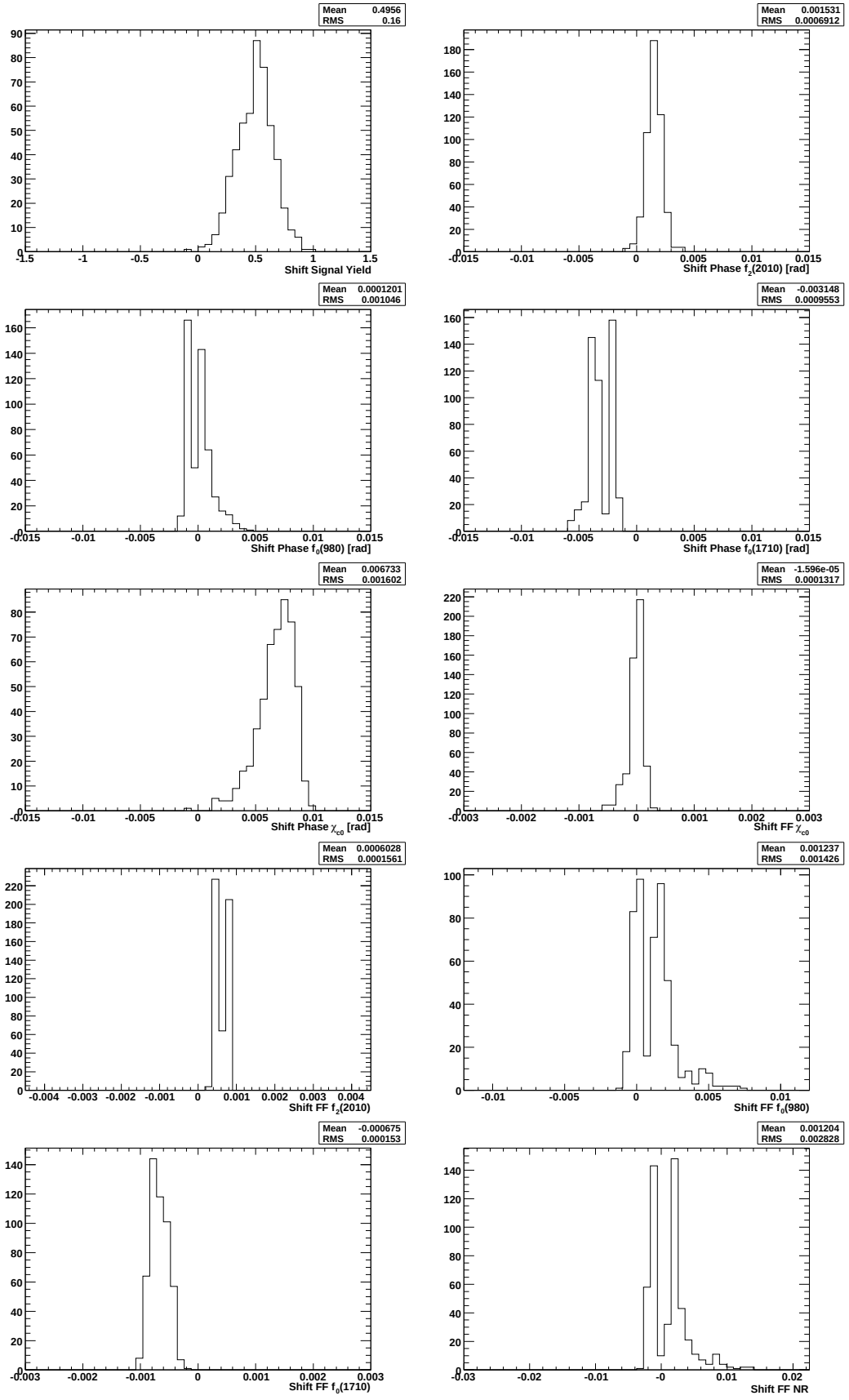

Figure C.3: Shift in the observables when randomizing the PDF parameters. We assign the sum squared of the mean and the error of the mean as systematic uncertainties

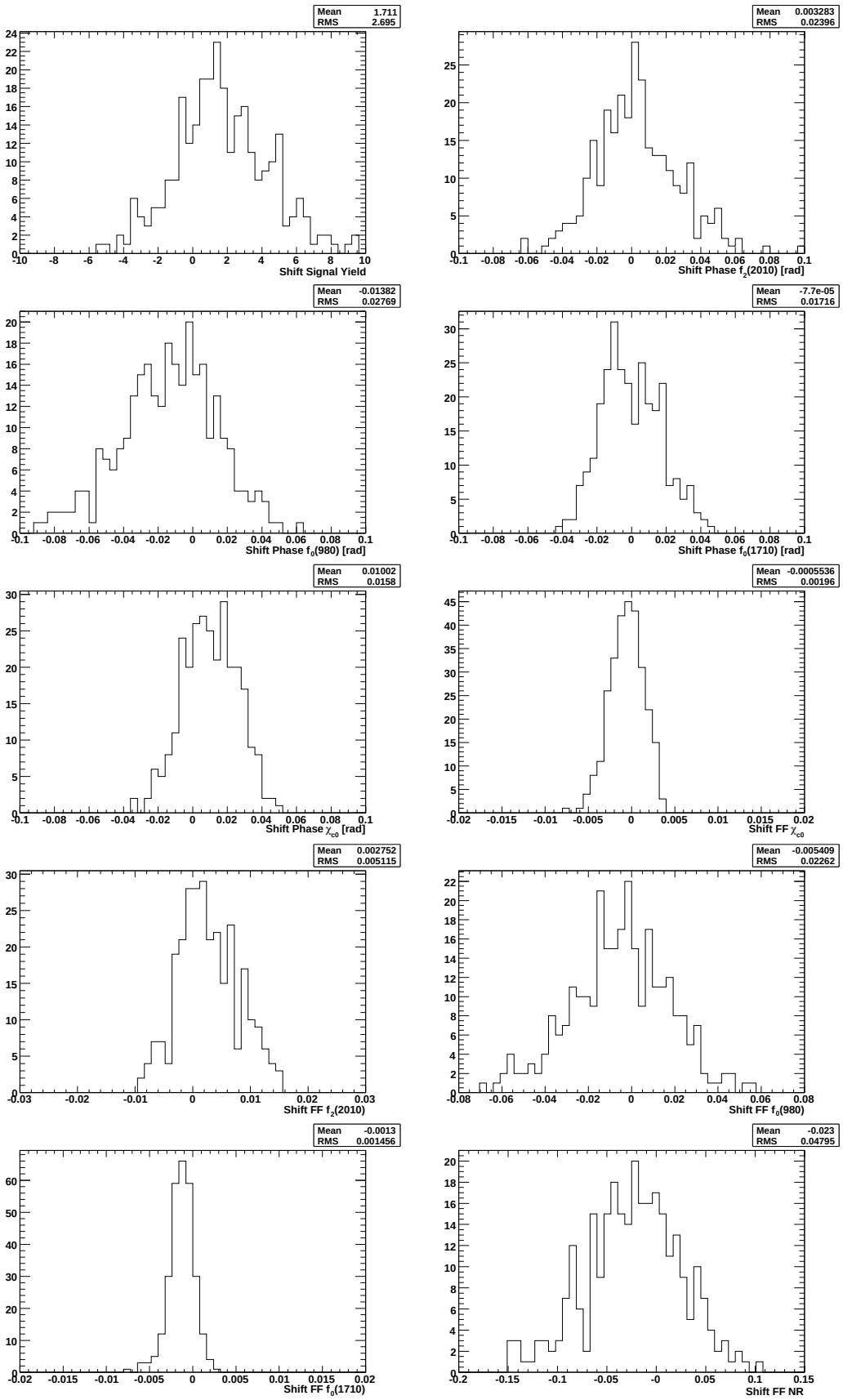

Figure C.4: Shift in the observables when randomizing the PDF parameters. We assign the sum squared of the mean and the error of the mean as systematic uncertainties

Bibliography

[1] Claude Amsler et al. Review of particle physics. *Phys. Lett.*, B667:1, 2008.

[2] J. H. Christenson, J. W. Cronin, V. L. Fitch, and R. Turlay. Evidence for the 2 π Decay of the k(2)0 Meson. *Phys. Rev. Lett.*, 13:138–140, 1964.

[3] A. D. Sakharov. Violation of CP Invariance, c Asymmetry, and Baryon Asymmetry of the Universe. *Pisma Zh. Eksp. Teor. Fiz.*, 5:32–35, 1967.

[4] J. Charles et al. CP violation and the CKM matrix: assessing the impact of the asymmetric B factories. *Eur. Phys. J.*, C41:1–131, 2005.

[5] M. Bona et al. The unitarity triangle fit in the standard model and hadronic parameters from lattice QCD: A reappraisal after the measurements of $\Delta(m(s))$ and BR(B $\rightarrow \tau$ ν/τ). *JHEP*, 10:081, 2006.

[6] B.R. Holstein J.F. Donoghue, E. Golowich. *Dynamics of the Standard Model*. CAMBRIDE UNIVERSITY PRESS, 1992.

[7] Makoto Kobayashi and Toshihide Maskawa. CP Violation in the Renormalizable Theory of Weak Interaction. *Prog. Theor. Phys.*, 49:652–657, 1973.

[8] Ling-Lie Chau and Wai-Yee Keung. Comments on the Parametrization of the Kobayashi-Maskawa Matrix. *Phys. Rev. Lett.*, 53:1802, 1984.

[9] Lincoln Wolfenstein. Parametrization of the Kobayashi-Maskawa Matrix. *Phys. Rev. Lett.*, 51:1945, 1983.

[10] P.F. Harrison and H.R. Quinn (Eds.). *The BABAR physics book*. SLAC-R-504, 1998.

[11] Sliva Branco, Lavoura. *CP violation*. CLARENDON PRESS OXFORD, 1999.

[12] W. M. Yao et al. Review of particle physics. *J. Phys.*, G33:1–1232, 2006.

[13] V. Fitch et R. Turlay J. Christenson, J. Cronin. Evidence for the 2π decay of the K2 meson. *Phys. Rev. Lett.*, 13:138–140, 1964.

[14] P. F. Harrison and Editors H. R. Quinn. *The BABAR Physics Book*. SLAC, 1998.

[15] Heavy Flavor Averaging Group. Averages of b-hadron and c-hadron properties at the end of 2007. 2009.

[16] Bernard Aubert et al. Measurement of Time-Dependent CP Asymmetry in $B^0 \to c\bar{c}K^{(*)0}$ Decays. *Phys. Rev.*, D79:072009, 2009.

[17] Yuval Grossman and Mihir P. Worah. CP asymmetries in B decays with new physics in decay amplitudes. *Phys. Lett.*, B395:241–249, 1997.

[18] Yosef Nir. *B Physics and CP Violation*. Lectures given at the Les Houches Summer School (Session LXXXIV), 2005.

[19] Bernard Aubert et al. Time-dependent amplitude analysis of $B^0 \to K^0_s\pi^+\pi^-$. *Phys. Rev.*, D80:112001, 2009.

[20] Bernard Aubert et al. Measurement of CP-violating asymmetries in $B^0 \to (\rho\pi)^0$ using a time-dependent Dalitz plot analysis. *Phys. Rev.*, D76:012004, 2007.

[21] Bernard Aubert et al. Measurement of CP-Violating Asymmetries in the $B^0 \to K^+K^-K^0_s$ Dalitz Plot. 2008.

[22] Bernard Aubert et al. Dalitz Plot Analysis of $B^\pm \to \pi^\pm\pi^\pm\pi^\pm$ Decays. *Phys. Rev.*, D79:072006, 2009.

[23] B. Aubert et al. Evidence for direct CP violation from Dalitz-plot analysis of $B^\pm \to K^\pm\pi^\pm\pi^\pm$. *Phys. Rev. D*, 78(1):012004, Jul 2008.

[24] B. Aubert et al. Dalitz plot analysis of the decay $B^\pm \to K^\pm K^\pm K^\pm$. *Phys. Rev. D*, 74(3):032003, Aug 2006.

[25] E. Barberio et al. Averages of $b-$hadron and $c-$hadron Properties at the End of 2007. 2008.

[26] Hai-Yang Cheng, Chun-Khiang Chua, and Amarjit Soni. CP-violating asymmetries in B^0 decays to $K^+K^-K^0_{s,l}$ and $K^0_sK^0_sK^0_{s,l}$. *Phys. Rev.*, D72:094003, 2005.

[27] Hai-Yang Cheng, Chun-Khiang Chua, and Amarjit Soni. Effects of Final-state Interactions on Mixing-induced CP Violation in Penguin-dominated B Decays. *Phys. Rev.*, D72:014006, 2005.

[28] T. Gershon and M. Hazumi. Time dependent CP violation in $B^0 \to P^0P^0X^0$ decays. *Phys. Lett. B*, 596, 2004.

[29] A. Garmash et al. Dalitz analysis of the three-body charmless decays $B^+ \to K^+\pi^+\pi^-$ and $B^+ \to K^+K^+K^-$. *Phys. Rev.*, D71:092003, 2005.

[30] Wei Wang et al. Study of scalar mesons $f(980)$ and $f(1500)$ from $B \to f(980)K$ and $B \to f(1500)K$ decays. *Phys. Rev. D*, 74(11):114010, Dec 2006.

[31] Y. Chen et al. Glueball spectrum and matrix elements on anisotropic lattices. *Phys. Rev. D*, 73(1):014516, Jan 2006.

[32] Wei Wang, Yue-Long Shen, and Cai-Dian Lu. The Clean Way to Identify a Scalar Glueball. 2009.

[33] M. Ablikim et al. Observation of a Broad $1--$ Resonant Structure around $1.5GeV/c2$ in the K^+K^- Mass Spectrum in $J/\psi \to K^+K^-\pi$. *Phys. Rev. Lett.*, 97(14):142002, Oct 2006.

[34] D. Herndon, P. Soding, and R. J. Cashmore. A GENERALIZED ISOBAR MODEL FORMALISM. *Phys. Rev.*, D11:3165, 1975.

[35] S. U. Chung et al. Partial wave analysis in K matrix formalism. *Annalen Phys.*, 4:404–430, 1995.

[36] M. Ablikim *et al.* Resonances in $J/\psi \to \phi\pi^+\pi^-$ and ϕK^+K^-. *Phys. Lett. B*, 607:243–253, 2005.

[37] J. Blatt and V. E. Weisskopf. *Theoretical Nuclear Physics*. J. Willey (New York), 1952.

[38] F. Von Hippel and C. Quigg. Centrifugal-barrier effects in resonance partial decay widths, shapes, and production amplitudes. *Phys. Rev.*, D5:624–638, 1972.

[39] Bernard Aubert et al. The BaBar detector. *Nucl. Instrum. Meth.*, A479:1–116, 2002.

[40] Bernard Aubert et al. Measurement of D0-D0bar Mixing using the Ratio of Lifetimes for the Decays $D^0 \to K^-\pi^+$ and K^+K^-. *Phys. Rev.*, D80:071103, 2009.

[41] Bernard Aubert et al. Observation of CP violation in $B^0 \to K^+\pi^-$ and $B^0 \to \pi^+\pi^-$. *Phys. Rev. Lett.*, 99:021603, 2007.

[42] M. Moll. *Radiation Damage in Silicon Particle Detectors*. PhD thesis, University Hamburg (DESY), 1999.

[43] V. Re et al. The BaBar Silicon-Vertex Tracker: Performance, Running Experience, and Radiation-Damage Studies. *IEEE TRANSACTIONS ON NUCLEAR SCIENCE, VOL. 49, NO. 6*, 2002.

[44] S. Bettarini et al. Measurement of the Charge Collection Efficiency After Heavy Non-Uniform Irradiation in BABAR Silicon Detectors. *IEEE TRANSACTIONS ON NUCLEAR SCIENCE*, 52 (4), 2005.

[45] I. Rachevskaia et al. Radiation damage of silicon structures with electrons of 900 MeV. *Nucl. Instrum. Meth. A*, 485:126–132, 2002.

[46] The BaBar Collaboration. *Technical Design Report For The BaBar Detector*. 1995.

[47] Maple. http://www.maplesoft.com/.

[48] V.Re et al. The rad-hard readout system of the BaBar Silicon Vertex Tracker. *Nucl. Instrum. Meth.*, A409:354–359, 1998.

[49] J. Orear. Least squares when both variables have uncertainties. *Am. J. Phys.*, 50(10):912–916, 1982.

[50] Bernard Aubert et al. Measurement of $D^0 - \bar{D}^0$ mixing from a time-dependent amplitude analysis of $D^0 \to K^+\pi^-\pi^0$ decays. *Phys. Rev. Lett.*, 103:211801, 2009.

[51] Bernard Aubert et al. Measurement of $D^0 - \overline{D}^0$ Mixing using the Ratio of Lifetimes for the Decays $D^0 \to K^-\pi^+$ and K^+K^-. *Phys. Rev.*, D80:071103, 2009.

[52] V. Klose. A measurement of the π^0 efficiency using D^0 decays into $K^\pm\pi^\pm\pi^0$. *BABAR Analysis Document # 1194. Unpublished.*

[53] D. J. Lange. The EvtGen particle decay simulation package. *Nucl. Instrum. Meth.*, A462:152–155, 2001.

[54] Torbjorn Sjostrand. PYTHIA 5.7 and JETSET 7.4: Physics and manual. 1995.

[55] S. Agostinelli et al. GEANT4: A simulation toolkit. *Nucl. Instrum. Meth.*, A506:250–303, 2003.

[56] Pierre Billoir. TRACK FITTING WITH MULTIPLE SCATTERING: A NEW METHOD. *Nucl. Instrum. Meth.*, A225:352–366, 1984.

[57] David J. Lange, Gabriella Sciolla, Maria C. Simani, and Yi Zheng. An improved tagging algorithm for CP violation studies. *BABARAnalysis Document # 729. Unpublished.*

[58] W. Hulsbergen. A Kalman Filter for BABAR Decay Chain Fitting, Internal Documentation. *http://www.slac.stanford.edu/BFROOT/www/Physics/Tools/Vertex/treefitter/. Unpublished.*

[59] W. Ford. Choice of Kinematic Variables in B Meson Reconstruction. *BABAR Analysis Document # 53. Unpublished.*

[60] P. Gay, B. Michel, J. Proriol, and O. Deschamps. Tagging Higgs bosons in hadronic LEP2 events with neural networks. Prepared for 4th International Workshop on Software Engineering and Artificial Intelligence for High-energy and Nuclear Physics (AIHENP 95), Pisa, Italy, 3-8 April 1995.

[61] TMVA. http://tmva.sourceforge.net.

[62] F. James. MINUIT, Function Minimization and Error Analysis, Reference Manual. *wwwasdoc.web.cern.ch/wwwasdoc/minuit/minmain.html, unpublished*.

[63] RooFit. http://tmva.sourceforge.net.

[64] B. "Aubert and others". Measurement of CP asymmetries in $B^0 \to K^0_s K^0_s K^0_s$ decays. *Phys. Rev. D*, 76(9):091101, Nov 2007.

[65] O. Long and L. Zhang. A Study of $\mathrm{B}^0 \to \mathrm{K_s K_s K_l}$ Decay. *BABAR Analysis Document # 1193. Unpublished.*

[66] Bernard Aubert et al. Branching fractions and CP asymmetries in $B^0 \to K^+K^-K^0_s$ and $B^+ \to K^+K^0_sK^0_s$. *Phys. Rev. Lett.*, 93:181805, 2004.

[67] Muriel Pivk and Francois R. Le Diberder. sPlot: a statistical tool to unfold data distributions. *Nucl. Instrum. Meth.*, A555:356–369, 2005.

[68] P. del Amo Sanchez. *Time-dependent Dalitz-Plot Analysis of the Charmless Decay $B^0 \to K^0_s\pi^+\pi^-$ at BaBar* . PhD thesis, University of Birmingham, 2007.

[69] D. G. Hitlin et al. Proceedings of SuperB Workshop 6: New Physics at the Super Flavor Factory. 2008.

[70] M. Bona et al. SuperB: A High-Luminosity Asymmetric e^+e^- Super Flavor Factory. Conceptual Design Report. 2007.

[71] D. Schulte. *Study of Electromagnetic and Hadronic Background in the Interaction Region of the Tesla Collider (TESLA-97-08)*. PhD thesis, University of Hamburg, 1996.

[72] R. Kleiss and H. Burkhardt. BBBREM: Monte Carlo simulation of radiative Bhabha scattering in the very forward direction. *Comput. Phys. Commun.*, 81:372–380, 1994.

[73] E. Grauges et al. SuperB Progress Report – Detector. 2010.